On Optics Surface Imperfections and their Effects on the Sensitivity of Speed Meters

Daniela Pascucci

MSci

Submitted in fulfilment of the requirements for the degree of

Doctor of Philosophy

School of Physics and Astronomy
College of Science and Engineering
University of Glasgow

November 2018

Abstract

It took several decades of intense research and development and the effort of thousands of people to reach the detectors sensitivity that allowed the gravitational waves detectors Advanced LIGO and later Advanced Virgo to make the first detection of gravitational waves on September 14th 2015 (and many other after that). This event marks the birth of gravitational wave astronomy and opens a new window on the universe, giving us the ability to gather information otherwise impossible to obtain. However it is still important to further increase the sensitivity of the interferometers in order to extract more accurately the parameters of the observed gravitational wave sources, as well as to discover new classes of gravitational wave emitters.

So research efforts are pursued on all fronts, trying to reduce any relevant sources of noise. One of the proposed methods for the reduction of the quantum noise is based on the concept of quantum non-demolition measurements and speed meters. In this context, a proof-of-concept experiment is underway at the University of Glasgow. The aim of the experiment is to prove that in a Sagnac interferometer, which is *per se* a speed meter, quantum radiation pressure noise is lower than in an equivalent Michelson at audio-band frequencies. The interferometer designed for this experiment is composed by two triangular cavities with 1 g input test masses and 100 g end test masses and a finesse of ~ 8000. In this way the sensitivity at low frequencies will be dominated by quantum radiation pressure noise. However these features make the interferometer very sensitive to loss and high quality surface mirrors are then indispensable. The analysis of how much the mirrors surface imperfections will affect the quantum noise in speed meters is indeed the main topic of this thesis.

The work carried out can be divided in two parts. The first part consists in the derivation of the arm cavity mirrors surface requirements for the Glasgow Sagnac speed meter. Because of the high dependence of its sensitivity from optical loss, the mirror surface requirements must be very stringent and an in-depth analysis to derive them is presented here. This analysis was done performing simulations that give an estimate of the roundtrip loss generated by each kind of mirror surface imperfection. In particular most of the analyses were done using OSCAR (acronym of Optical Simulation Containing Ansys Results), a MATLAB® package that can simulate the behaviour of a cavity with arbitrary mirrors surface profiles. The second part of the thesis is a theoretical analysis of the backscattering effect inside a cavity and how much it affects the quantum noise. The backscattering is a mechanism that arises when the intra-cavity beam has non-zero angle of incidence on the arm cavity mirror. Due to microroughness, in fact, the beam can be scattered back in the same direction as the incident beam. It will then couple with the counter-propagating beam and this coupling causes an increment of the quantum noise. The results are applied to the case of the Glasgow Sagnac speed meter and to future large scale interferometers.

It is worth noting that the analysis of this newly discovered noise coupling caused by backscattering in speed meters featuring triangular cavities can also be applied to the class of speed meters configurations using linear cavities and two different polarisations, where the coupling of the modes is caused by birefringence.

Table of contents

List of tables

List of figures

Acknowledgements

First of all I would like to thank my supervisor Stefan Hild for his enthusiasm and for being a good advisor any time I needed it. Thanks for giving me the opportunity to take part in this amazing project and for making me feel part of the team since the very beginning.

Thanks to Ken Strain for the useful advises and comments on my work and for always having words of encouragement.

Thanks to Stefan Danilishin for his great help. Much of the work presented in this thesis would not have been possible without his guidance.

Thanks to all the present and past members of the IFO-group for the suggestions and comments during the group meetings. All of them helped me to find the right way to proceed with my work in more than one occasion. A special mention goes to Jan for being a friendly officemate for almost four years and to Teng for his help and the useful discussions about backscattering and quantum noise.

Thanks to everyone that made my four years in Glasgow more enjoyable also outside the Kelvin Building. To Marilena for the evenings at the CCA, cinema and concerts. To Sara for the chats, the beers and for being an endless source of information. To Valentina for the ethnic dinners, the game nights and the trips around Scotland.

Thanks to Gabriella, Giorgia and Nadia for being a constant presence through my whole life, even now that we are living so far apart. And thanks to Pierluigi, honorary member of the group.

Finally, thanks to my family. To mum and dad for the constant support and love. To Milena and Federico for the nice time spent together when I go back home. To Ivana and Antonio for the interesting (night) chats on more or less serious topics. And a special thanks to Stefano and Gabriele for making our lives wonderfully chaotic.

Preface

Chapter 1 introduces to gravitational wave astronomy, describing its birth occurred on 14th September 2015 with the first detection of a gravitational wave. A description of the past, present and future detectors is then shown. The data of GW150914 are provided by the open science centre of the LIGO Scientific Collaboration. Other material has been taken from published literature.

Chapter 2 gives an overview of the theoretical concepts used for the input-output (I/O) relations and quantum noise calculations and the softwares used for the measurements, analysis and simulations of the mirror surfaces.

Chapter 3 introduces the quantum non-demolition measurements and the speed meters and describes the Glasgow Sagnac speed-meter (SSM) proof-of concept experiment. The design of the experiment was developed by Stefan Hild, Christian Gräf, Sebastian Steinlechner and Ken Strain. The optical layout was made by Jan-Simon Hennig and Roland Schilling. Additional contribution to the experiment came from Stefan Danilishin, Sean Leavey, Jan-Simon Hennig, Alasdair Houston, Teng Zhang, Peter Dupej and myself.

Chapter 4 shows the mathematical manipulation of the quantum noise for a few interferometer configurations. Even if some of the results are known in literature, all calculations consistent with the conventions used in this thesis were made by myself.

Chapter 5 describes the simulations and the analysis made to derive the surface requirements of the arm cavity mirror of the Glasgow SSM experiment. The simulations were made by myself with the help of Stefan Hild, Kenneth Strain, Christian Gräf and Sebastian Steinlechner. Technical support for OSCAR has been given by Jerome Degallaix. Scattering measurements were made by Laboratoire des Matériaux Avancés (LMA).

Chapter 6 shows the mathematical manipulation of the I/O relations for a Sagnac interferometer with backscattering effect in the cavities. The simulations of the scattering were made by Stefanie Kroker. I made the backscattering calculation with the help of Stefan Danilishin, Teng Zhang, Sergey Vyatchanin, Miroslav Tugolukov and Stefan Hild.

Chapter 7 presents the numerical results of the quantum noise when backscattering effect is present in the cavities, with an analysis and interpretations of the results. The analysis

of the results was made by myself, together with Stefan Danilishin, Teng Zhang, Sergey Vyatchanin, Miroslav Tugolukov and Stefan Hild.

Appendix A shows the symbols and the definitions used in the thesis.

Appendix B contains all the mirror surface measurements. Mirror surface measurements and analysis of the sample mirror were made by myself. Mirror surface measurements of the ITM and ETM were made by Coastline Optics, Inc.

Appendix C reports the specifications documents of the arm cavity mirrors of the Glasgow Sagnac speed meter proof-of-concept experiment. Specifications documents of ITM and ETM were made by myself together with Stefan Hild, Kenneth Strain, Christian Gräf and Sebastian Steinlechner. Drawing of the ETM was made by Liam Cunningham and Russell Jones. Drawings of the ITM were made by Jan-Simon Hennig.

Appendix D describes the measurements of the flatness of the silica ears for the ETM, the polishing procedures to remove the spike from the surfaces and the cleaning and bonding of the test masses. I made the ears flatness measurements. Polishing procedure were made by myself together with Marielle Van Veggel and Stefan Hild with the help of Liam Cunningham. Test masses cleaning and bonding were made together with Jan-Simon Hennig and Marielle Van Veggel. Analysis of the ear position was made by myself together with Jan-Simon Hennig. Drawing of the ear was made by Liam Cunningham and Russell Jones.

Appendix E reports the MATLAB® script for the quantum noise with backscattering calculation. I developed the script starting from a previous script made by Stefan Danilishin.

Chapter 1

Gravitational wave astronomy

1.1 The birth of gravitational wave astronomy

At 09:50:45 UTC on September 14th 2015, the two LIGO interferometers located in Livingston, LA and Hanford, WA, detected for the first time a gravitational wave (GW) signal. It was generated by the merger of two black holes about 1.3 billions light years away [1]. This event marks the beginning of a new era with the birth of the GW astronomy. Einstein predicted gravitational radiation more that 100 years ago, but before that event there were no direct observations[1]. That is the reason why this event is so important. It represents in fact not only the beginning of a new era but also a further proof of the validity of Einstein's theory of General Relativity.

On August 1st 2017 the Virgo detector, located in Cascina, near Pisa, in Italy, joined the two LIGO interferometers in the observation run. Even if this run lasted less than one month, two events were detected, each of them very important for different reasons:

- GW170814 was the first detection made by three interferometers and showed how much the accuracy in the localisation of the source can be increased adding even only one detector in the network;
- GW170817 was generated by a neutron star binary system and, in fact, an electromagnetic (EM) counter part was detected by many telescopes on Earth and in space, giving the chance to combine GW and EM information and marking then the beginning of the multi-messenger astronomy.

[1] With direct observations we mean observations made with instruments able to detect the passage of GW, whereas indirect observations are meant to be observations of astronomical events caused by GW (like the pulsar period measurements described in section 1.2.1). However this distinction is not universally accepted and some scientists consider Hulse and Taylor measurements the first direct observation of GW.

We will describe in this section the details and the outcomes of all the detections announced so far.

1.1.1 GW150914

The GW signal, named GW150914, was produced by two black holes with masses of $36^{+5}_{-4}\,M_\odot$ and $29^{+4}_{-4}\,M_\odot$, which merged and formed a final black hole of $62^{+4}_{-4}\,M_\odot$ with about $3^{+0.5}_{-0.5}\,M_\odot c^2$ of energy emitted in form of gravitational radiation[2]. The signal has been estimated to be at a luminosity distance[3] of 410^{+160}_{-180} Mpc, corresponding to a redshift of $z = 0.09^{+0.03}_{-0.04}$ [1].

The signal was first recorded by LIGO-Livingston and $6.9^{+0.5}_{-0.4}$ ms later by LIGO-Hanford. Each detector can give information about the source localisation in the sky since the detected signal will depend from the relative position of the interferometer arms and the direction of propagation of the wave. The accuracy of the position can be increased combining the information taken from more than one detector. For GW150914, for example, combining the data of the two detectors that received the signal, the location of the source has been estimated to be in an area of the sky of about $610\,\mathrm{deg}^2$ with a 90% probability [4]. This is the reason why is important to have a network of detectors located around the world, as we will explain in details in section 1.2.3.

This discovery has several astrophysical implications and some of them are very significant, among which we can remind:

- first direct observation of GW;
- first direct observation of a black hole;
- first observation of a merger of black holes;
- proof of the existence of high mass black holes ($\geq 25\,M_\odot$)[5];

[2]Here (and in the following sections) the errors have the same units as the measurements. So, for example, with $36^{+5}_{-4}\,M_\odot$ we mean a mass between $32\,M_\odot$ and $41\,M_\odot$.

[3]In Astrophysics the luminosity distance d_L is defined as

$$d_L = \sqrt{\frac{L}{4\pi F}},$$

where L is the luminosity and F the radiant flux emitted by the object [2]. On the other side it can be calculated from the GW signal through the following equation

$$d_L = k\,\frac{\dot{f}}{h f^3},$$

where h and f are the amplitude and the frequency of the GW respectively and k is a constant that depends from the orientation of the source [3]. As we can see the distance can be calculated from the GW signal only, independently from any other calculation of the source properties. This is the reason why GW sources are considered standard candles.

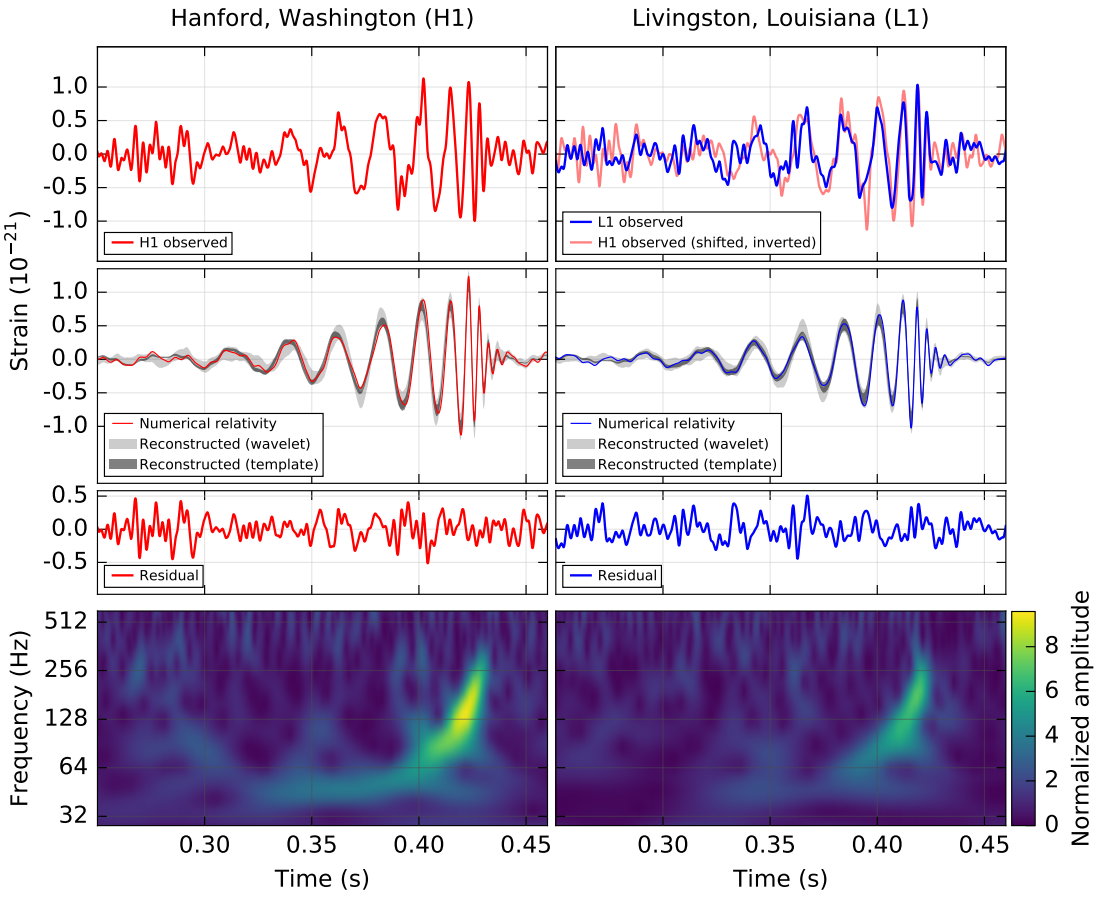

Figure 1.1: Measured signal of the first GW detection made by LIGO Hanford (on the left) and LIGO Livingston (on the right). *First row*: the strain of the measured signal (the Hanford signal on the right has been shifted in time time and inverted in order to take into account the time delay in the observation and the different orientations of the detectors respectively). *Second row*: Numerical relativity waveform obtained from a system with the same parameters of that ones (red line); regions with 90% credibility for the waveform obtained from two independent calculation for the waveform reconstruction (dark and light shaded grey). *Third row*: Residual obtained from the difference between the numerical relativity solutions and the detector observation data. *Fourth row*: Strain amplitude as a function of time and frequency. Figure taken from [1].

- further confirmation of the General Relativity theory [6].

In figure 1.1 the signal detected by the two interferometers is shown, compared with the numerical relativity solution of the waveform.

There are a lot of noise sources that can affect the measurements and then a very careful and rigorous analysis and characterisation is necessary. Apart from the channel that records gravitational wave signals, the two LIGO detectors have over 200 000 other channels, in order to monitor all possible sources of noise. These noises can be uncorrelated, if they occur in each detector independently (like ground motion and laser modulation) or correlated, if they affect both detectors (like electromagnetic signals and cosmic ray showers). Analysing and comparing the data from both detectors makes possible to identify the

sources of noises and to clean up the data [7].

The data are then analysed through an algorithm, with the help of a supercomputer, that compares them with a set of waveforms obtained from numerical relativity solutions. This algorithm is able to check the best waveform that matches with the data, changing all the source parameters, like for example masses, distance and orientations. In this way it is possible to establish which kind of source generated that signal and what are its main physical properties [8].

1.1.2 GW170817

After the first detection a number of other detections were made but the most important between them is certainly the last one, detected on August 17th 2017 and then named GW170817 [9]. The source of this gravitational radiation was the merger of two neutron stars and the event was detected also in the electromagnetic spectrum.

The electromagnetic signal was actually the first one to be detected. The Fermi Gamma-ray Burst Monitor (GBM), in fact, at 12:41:06 UTC received a trigger of a Gamma-ray Burst, named GRB170817A. After about 6 minutes LIGO-Hanford registered a possible candidate signal consistent with a neutron star binary system with merger time (t_c) 12:41:04 UTC. Subsequent analyses showed that the GW signal reached Virgo first, after 22 ms LIGO-Livingston and after 3 ms more LIGO-Hanford. Then an observing campaign was launched and, thanks to the accurate sky localisation reconstructed from the GW, multiple telescopes were able to detect the electromagnetic signal, which gives the exact location of the source in NGC4993 [10].

Figure 1.2 shows the timeline of the observations, taking as reference time the merger time t_c. The central part of the picture reports a table with GW and all electromagnetic spectrum bands and all the instruments that made the observation in each band. On the right of the bands names the following information are reported:

- the solid circles represent the observations with the area of the circle scaled as the brightness;
- the solid horizontal line is the time at which the signal was visible by at least one instrument;
- the shaded vertical lines represent the time when a GCN circular[4] was issued.

[4]The Gamma-ray Burst Coordinate Network (GCN) is a system which distributes information about GRB. Specifically, through the *circulars* they reports the follow-up observations made in all the spectrum bands by both ground-based and space-based observatories [11].

Furthermore in the figure also the first observations in GW and some of the electromagnetic spectrum bands are also shown. On the upper left part of the figure there is the combined spectrogram of the detected GW signals and the γ-ray observations represented with the light curves of the Fermi-GBM and the INTEGRAL/SPI-ACS. Then in the lower part of the figure the X-ray, optical and radio observations are shown. For each of them the instruments that made the observation (top left), the time after the merger time at which the GCN was issued (bottom left) and the observation band (bottom right) is reported. Finally the graph in the upper right part of the figure shows the spectra (each of them normalised to its maximum) of four observations made with SALT, ESO-NTT, SOAR and ESO-VLT, arbitrarily shifted along the *y-axis* in order to have a chronological order.

From the GW signal analysis it was possible to obtain information about the source: it was found to be a binary system with primary component mass between 1.36 and 1.60 $M_\odot$ and secondary component mass between 1.17 and 1.36 $M_\odot$ (low-spin priors), consistent with neutron stars masses, at a luminosity distance of 40^{+8}_{-14} Mpc. Thanks to the fact that three interferometers detected the signal, the sky localisation was more accurate and found to be in a sky region of about 28 deg^2 with a probability of 90%.

The scientific importance of this discovery can be better understood considering the amount of new information that was obtained. The most important aspects are summarised below.

- It was found a connection between at least one class of sGRB and binary neutron stars.
- It was found a kilonova signature, characterised by the presence of *rapid neutron-capture process* and responsible of the creation of heavy elements, like gold and platinum [12].
- An evaluation of the difference between the speed of light v_{EM} and the speed of gravity v_{GW}, which are supposed to be equal according to the Theory of General Relativity, has been done combining the GRB and GW data and obtaining the following result [13]
$$-3 \times 10^{-15} \leq \frac{v_{GW} - v_{EM}}{v_{EM}} \leq +7 \times 10^{-16}. \tag{1.1}$$
This result proves with high accuracy that the assumption made in the Theory of General Relativity is correct.
- A new test of equivalence principle can be done, probing that electromagnetic and gravitational radiation are affected in the same way by the gravitational potential [13].
- A new calculation of the Hubble constant independent from the cosmic distance ladder has been possible. GWs, in fact, can be used as standard sirens and then the

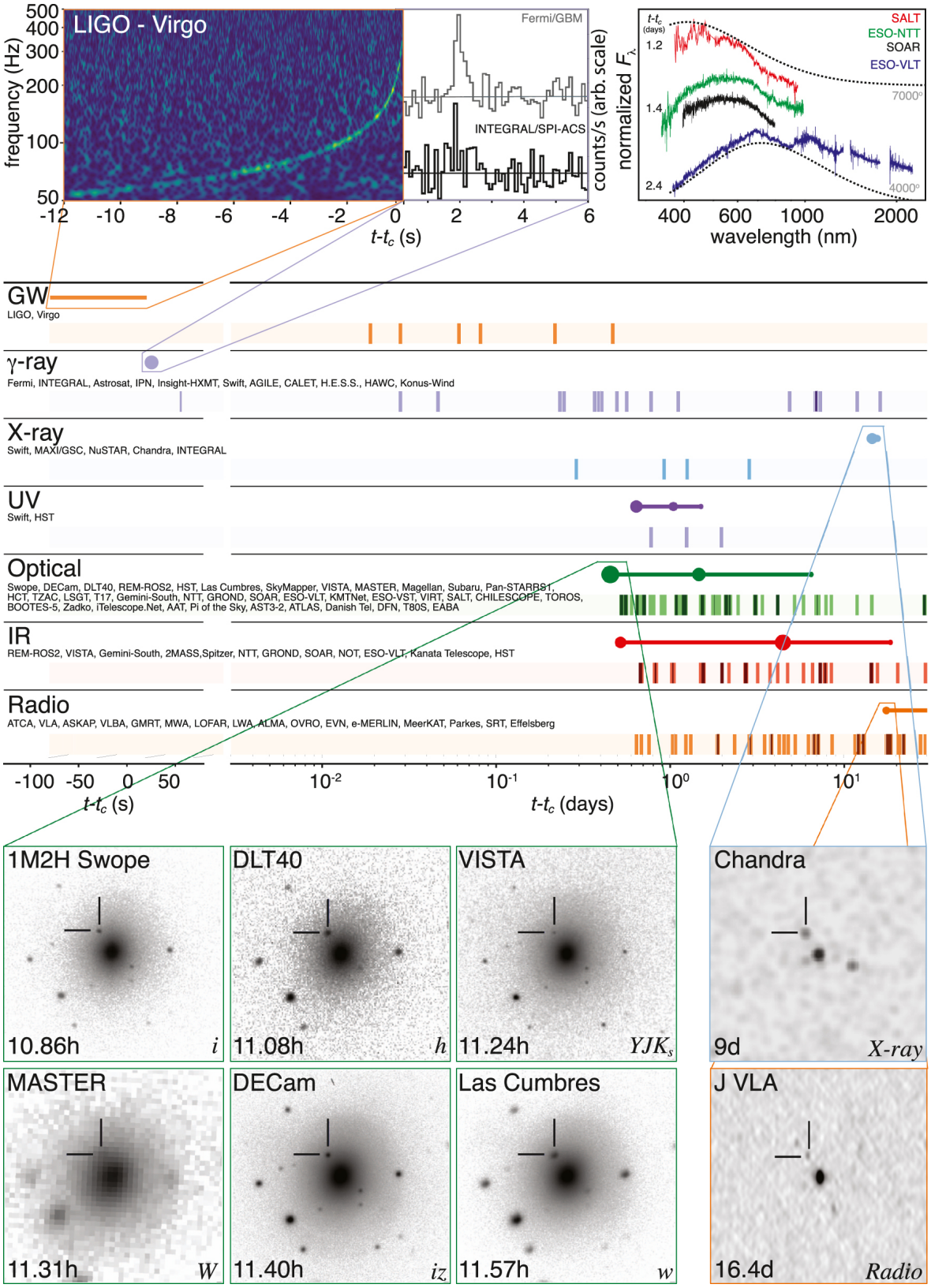

Figure 1.2: Timeline of the observations of GW170817 and its electromagnetic counterpart. As we can see observations were made by about 70 instruments in time span of about two weeks. Refer to the text for a detailed explanation. Figure taken from [10].

distance of the source can be calculated from the GW signal only. The obtained value was $H_0 = 70.0^{+12.0}_{-8.0}\,\mathrm{km\,s^{-1}\,Mpc^{-1}}$, in agreement with the currently accepted values determined with other methods [14].

Furthermore with this event we can state that the multi-messenger astronomy era has officially started.

1.1.3 Other detections

Between the first and the last detections, which are particularly important for the reasons explained in the previous sections, other GWs signals have been detected:

- **GW151226**, also called boxing day event, was a GW signal created by the merging of two black holes with original masses of $14.2^{+8.3}_{-3.7}\,\mathrm{M}_\odot$ and $7.5^{+2.3}_{-2.3}\,\mathrm{M}_\odot$ at a distance of $440^{+180}_{-190}\,\mathrm{Mpc}$ and with a final mass of $20.8^{+6.1}_{-1.7}\,\mathrm{M}_\odot$ [15];
- **GW170104** was produced by the coalescence of two black holes with masses of $31.2^{+8.4}_{-6.0}\,\mathrm{M}_\odot$ and $19.4^{+5.3}_{-5.9}\,\mathrm{M}_\odot$ at a distance of $880^{+450}_{-390}\,\mathrm{Mpc}$ [16];
- **GW170608** was produced by the coalescence of two black holes with masses of $12^{+7}_{-2}\,\mathrm{M}_\odot$ and $7^{+2}_{-2}\,\mathrm{M}_\odot$ at a distance of $340^{+140}_{-140}\,\mathrm{Mpc}$ [17];
- **GW170814** was particularly important since it was the first signal detected by three instruments (the two LIGO and Virgo), which gives a much better accuracy for the sky localisation: we have a sky region of $60\,\mathrm{deg}^2$, compared to $1160\,\mathrm{deg}^2$ that would have been obtained with only the two LIGO detectors. It was produced by two black holes with masses of $30.5^{+5.7}_{-3.0}\,\mathrm{M}_\odot$ and $25.3^{+2.8}_{-4.2}\,\mathrm{M}_\odot$ at a distance of $540^{+130}_{-210}\,\mathrm{Mpc}$ [18].

1.2 Ground-based gravitational wave detectors

1.2.1 From resonant bars to laser interferometers

The discovery of the first binary pulsar PSR1913+16 made by Hulse and Taylor in 1974 [19] and the subsequent analysis of its orbital period made by Taylor and Weisberg [20] gave the first proof of the existence of GW. They in fact found that the orbital period decayed as one would expect if we assume that it is caused by loss of energy through GW emission. However, the direct observation of GW is very difficult and requires extremely high sensitivity detectors, since the strain amplitude of GWs is of the order of 10^{-21} when observed on Earth.

The first experiment to detect GWs was performed in 1969 by Joseph Weber using a resonant bar [21]. The device proposed was composed of an aluminium cylinder with a length of 1.5 m and a resonance frequency of 1660 Hz. On the surface of this cylinder some piezoelectric crystals were bonded, in order to detect any change in the length due to the transit of the GW with an accuracy of the order of 10^{-16} m.

After a few months of observations with two detectors placed 100 km apart, Weber claimed to have detected GWs signals, since he observed some coincident excitations in the two detectors [22]. However no proof of the validity of these results has been found until today, but it seems very unlikely that he was actually observing GW signals, because of some discrepancies between the results and the theory [23].

During the following years the Weber bar detectors were studied and improved by many group around the world, but simultaneously another technique was introduced, which was destined to become the most effective method to detect GWs: laser interferometers.

The proposal of the first laser interferometer for GW detection was made in 1972 by Rainer Weiss[5] [25], based on a previous work of Felix Arnold Edward Pirani[6] [27]. Weiss suggested to use an interferometer with a Michelson configuration, where the beam was split by a beamsplitter and then passed through a hole in a mirror. In this way the beam made multiple reflections between two mirrors before it came out from the arm and came back to the beamsplitter. The transit of GW will change the length of the arms of the interferometer in an opposite way (one arm will become shorter and the other one longer), and when the beams are recombined they will be slightly out of phase. The absolute change of each arm length due to the transit of the GW is given by the equation

$$\Delta L = Lh, \tag{1.2}$$

where L is the length of the arm and h is the amplitude of the GW (also called *strain*). In figure 1.3 the original schematic drawing of the detector proposed by Weiss is shown. He estimated that this detector would be able to measure GW strain of the order of 10^{-17}. The technologies used to reduce the level of the large number of noises which affect the sensitivity of this kind of detectors have been developed during the past 45 years and today we are able to reach a sensitivity $h < 10^{-23}/\sqrt{\text{Hz}}$ (@100 Hz).

Current interferometers have arm lengths of the order of few kilometres, but the optical path is increased using Fabry-Perot cavities. We need, in fact, an optical path as long as

[5] Rainer Weiss will then be awarded, in 2017, with the Nobel Prize in Physics (together with Kip Thorne and Barry Barish) *"for decisive contributions to the LIGO detector and the observation of gravitational waves"* [24].

[6] The very first idea of using an interferometer to detect GWs was actually made by Mikhail E. Gertsenshtein and Vladislav I. Pustovoit in 1963 [26].

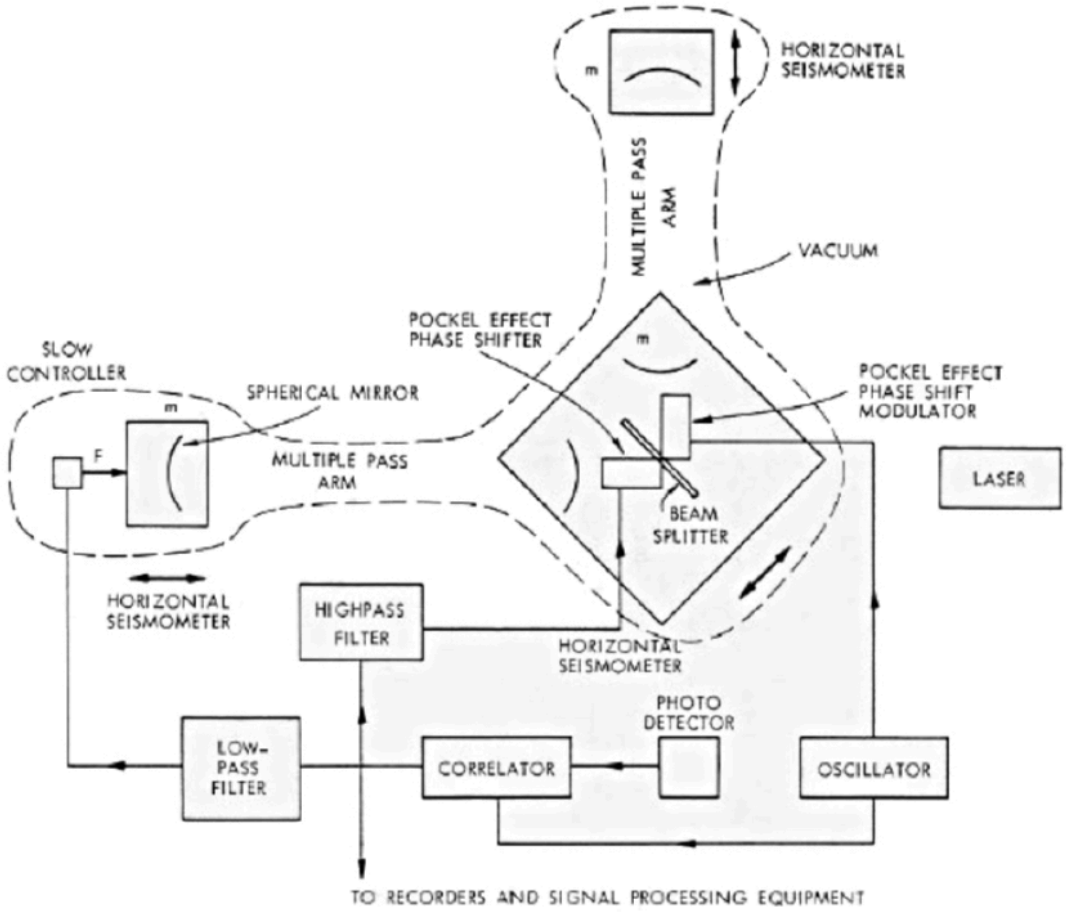

Figure 1.3: Original schematic drawing of the first interferometric GW detector proposed by Rainer Weiss in 1972. Figure taken from [25].

possible[7] in order to have a change in its length great enough to be detectable. However is not so simple to build big interferometer, both economically and logistically. Moreover the Earth curvature introduces further source of error, since the gravity force acting on the mirrors has different directions. This means that if the two mirrors that compose the cavity are arranged in order to be parallel to each other, then they will not be perpendicular to the local Earth surface. The number of degrees of freedom will then increase, since we have to care about the vertical motion of the mirrors too. However a Fabry-Perot cavity can be the solution to this problem, because it can increase the effective optical path without increasing the physical size of the device. It is composed by two mirrors, named input test mass (ITM) and end test mass (ETM). The input beam is partially transmitted through the ITM and then it reaches the ETM, which has a high reflectivity and sends it again towards the ITM. Since the ITM is partially reflective some of the light is reflected from the ITM and is incident on the ETM and so on. Since part of the power is lost through the ITM, there is

[7]It must be noted that the length of the arms of the interferometer cannot be too big. The increase of sensitivity with length, in fact, is in principle limited to about the GW wavelength (which has typical values between a hundred and a thousand kilometers).

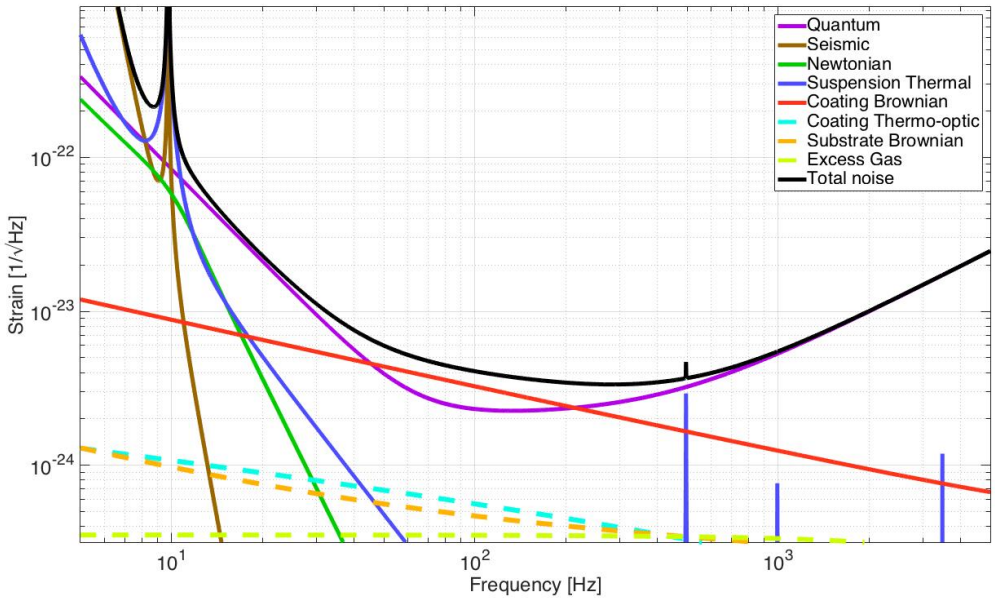

Figure 1.4: Sensitivity plot of Advanced LIGO made with GWINC [29], where the contributions of all the most important noises are shown.

a mirror before the beamsplitter (power recycling mirror), which reflects the exit light and send it again into the cavities.

The behaviour of a lossless Fabry-Perot cavity is described by the so called finesse, defined as [28]

$$\mathcal{F} = \frac{\pi\sqrt{r_1 r_2}}{1 - r_1 r_2}, \tag{1.3}$$

where r_1 and r_2 are the amplitude reflectivities of the ITM and ETM, respectively. From this parameter it is possible to deduce the optical path and the circulating power of the beam inside the cavity. For example Advanced LIGO has a finesse of 450, arms 4 km long and input power of 125 W, which gives an optical path of $\sim$ 1150 km and a circulating power of $\sim$ 60 kW, which is further increased by the power recycling mirror up to 730 kW.

1.2.2 Fundamental noises

In order to reach the required sensitivity to be able to detect the GW signal, a lot of noises must be analysed and minimised. In figure 1.4 the spectral density of the sensitivity of Advanced LIGO with some of the most important noises contributions is shown. In this section we will explain the meaning and the way to estimate the dominant noises in the spectrum: seismic, Newtonian, thermal and quantum noise.

Seismic noise

Seismic noise originates from ground vibrations and it is dominant at low frequencies (below 10 Hz). In a quiet site the value of the spectrum is expected to be $\sim 10^{-7}\, f^{-2}\,\mathrm{m}/\sqrt{\mathrm{Hz}}$ [30]. In order to reduce it, some techniques were developed through the years and can be divided in the two kinds described below.

- Passive isolations are that ones that do not require energy from the outside. They include for example the use of many stages pendulum structure which reduces the horizontal motion by a factor $1/f^2$ at each stage [23]. The transfer function for a single pendulum between the ground motion x_g and the mirror motion x_m is

$$\frac{x_m}{x_g} = \frac{\omega_0^2}{\sqrt{\left(\omega_0^2 - \omega^2\right)^2 + \gamma^2\omega^2}}, \tag{1.4}$$

  where $\omega = 2\pi f$ is the angular frequency, ω_0 is the resonance angular frequency and γ is the damping constant [30].

- Active isolations, on the other side, use an external force to damp or attenuate the motion of the mirrors. This can be done for example using inertial sensors combined to feedback.

The mirror suspensions of all current interferometers are based on these principles, even though each of them is developed in a different way. In Advanced LIGO, for example, the seismic isolation is composed by one hydraulic stage outside the vacuum system and two stages in vacuum with active isolation [31]. For Advanced Virgo instead the pendulum has seven stages: an inverted pendulum and a chain of six seismic filters, all of them acting like a low pass filters [32]. With these techniques it is possible to reduce the seismic noise by more than 10 orders of magnitude.

Another possible way to reduce seismic noise is to use underground detectors as has been done for KAGRA and it will be done for 3^{rd} generation GW detectors like the Einstein Telescope.

Newtonian noise

The Newtonian noise, also called gravity gradient noise, is the displacement noise of the interferometer's test masses due to local fluctuations of the gravitational potential. It can be caused by different factors: fluctuating seismic fields, atmospheric pressure and temperature fluctuations, but also by anthropogenic sources. It has been estimated that it will limit the sensitivity at low frequencies [33]. Direct measurements of this kind of noise are very

difficult, but recent studies showed that it might be possible to detect it in the near future [34].

Different approaches have been proposed with the aim to reduce this kind of noise in future GW detectors. The first one is to use a monitor and subtraction method, composed by seismometers placed around each mass and a subtraction signal which will correct the observed gravity fluctuations. The other one is to choose very quiet location and build underground detectors [23]. For the Einstein Telescope, for example, we might need both approaches together.

Thermal noise

Thermal noise includes any noise related to the temperature and it can affect both mirrors and suspensions. Mirror thermal noise can be divided in two types: thermo-optic noise, which is the sum of thermo-elastic and thermo-refractive noise, and Brownian thermal noise. Thermo-refractive noise is due to the change of refractive index with the change of temperature, thermo-elastic noise is due to the thermal expansion and Brownian thermal noise is due to Brownian motion. Furthermore each of them affects both the substrates and the coating.

In general the spectral density of the thermal noise is given by the following equation

$$S_{th}(\omega) = \frac{4k_B T}{\pi\omega}\frac{W_{diss}}{F_0} \quad \left[\frac{\mathrm{m}^2}{\mathrm{Hz}}\right] \tag{1.5}$$

where k_B is the Boltzmann constant, T the temperature, W_{diss} the dissipated power and F_0 the amplitude of the oscillatory force acting on the mass [35].

Between all thermal noises the most dominant in the current GWs detectors are the coating Brownian thermal noise and the suspension thermal noise. For the coating Brownian thermal noise equation 1.5 becomes

$$S_{cbt}(\omega) = \frac{4k_B T \phi_{eff}(1-\sigma)}{\sqrt{\pi}\,\omega\, w_m Y}, \tag{1.6}$$

where σ is the Poisson ratio, w_m is the beam radius, Y is the Young modulus of the substrate and

$$\phi_{eff} = \phi + \frac{d}{w_m\sqrt{\pi}}\left(\frac{Y}{Y_\perp}\phi_\perp + \frac{Y_\parallel}{Y}\phi_\parallel\right), \tag{1.7}$$

with ϕ the mechanical loss of the substrate and $Y_\perp$, $\phi_\perp$, $Y_\parallel$ and $\phi_\parallel$ are the perpendicular and parallel components of the Young's modulus and the mechanical loss of the coating. For

the suspension thermal noise, on the other hand, the spectral density can be written as

$$S_{susp}(\omega) = \frac{4k_B T \omega_0^2 \phi_{tot}}{m\omega^5}, \tag{1.8}$$

where, in this case, ϕ_{tot} is the mechanical loss of the pendulum, m its mass and ω_0 its resonant angular frequency.

Quantum noise

Quantum noise is one of the most dominant sources of noise in the interferometric GW measurements. It is composed of photon shot noise and radiation pressure noise [28]. The shot noise is due to the fluctuations on the count of the photons that reach the photodetector. Radiation pressure noise, on the other side, is the noise due to the random radiation pressure force created by the amplitude fluctuations of the incident light, which cause a recoil of the mirror.

The quantum noise is composed by these two components. While the signal-to-noise ratio of shot noise decreases when the input power increases, the radiation pressure noise increases. So it is not possible to improve both at the same time, changing only the power. A more detailed analysis of the quantum noise will be provided in chapter 4, where we will describe the quantum noise calculations for some interferometer configurations. One of the proposed approaches aimed to reduce this kind of noise in future generations of GW detectors is the introduction of a speed meter configuration, as will be explained in chapter 3 in more details .

1.2.3 A worldwide network

It is very important to be able to localise the sources of the GWs in order to alert telescopes to point in the right direction and looking for an electromagnetic counterpart. However, GW detectors are not like optical telescopes. Whereas the directivity of a telescope is associated with its large dimension compared to an optical wavelength, the GW detector has dimensions much smaller than a GW wavelength. This results in a very limited directional discrimination and the localisation of the source is then not easy to deduce from the detected signal. So, in order to be able to do that we need to place detectors around the world in appropriate positions and with determined orientations. In this way we can combine the signal arrival time at each interferometer and the information obtained from the relative position of the arms and the GW direction of propagation in order to derive the position of the source in the sky.

Today there are four operative detectors :

- Advanced LIGO-Hanford, which has 4 km long arms and is located in Hanford, WA (USA);
- Advanced LIGO-Livingston, with the same dimensions and located in Livingston, LA (USA);
- Advanced Virgo, with 3 km long arms and located in Cascina, near Pisa (Italy);
- GEO600, with an arm length of 600 m and located in Ruthe, near Hanover (Germany).

For the first four detections only the two LIGO interferometers were active and the sky localisation of the sources were found to be between 500 and 1200 $\deg^2$, while for the first one detected by three interferometers (two LIGO and Virgo) the position has been estimated in area of 60 $\deg^2$, a factor ~ 20 better than it would be with only two detectors[8]. So having a worldwide network of detectors can further increase the accuracy.

In an effort to further improve the sky localisation, two more detectors are expected to join the observations in the near term future. One is currently under construction in Japan and it is called KAGRA (the name is a combination of its location, Kamioka, and Gravity). It is an underground (to reduce seismic noise) cryogenic (to reduce thermal noise) GW detector with 3 km arm length [36]. It is expected that with this additional detector the sky localisation area will be reduced by a factor between 2.5 and 10 [37].

The last detector that is in program to join the network is LIGO-India. The construction is expected to start in 2019 and the detector is planned to start observations in 2025 [38].

In figure 1.5 the location on the world map of all these detectors is shown.

1.2.4 Future generations

Detecting GWs was only the beginning of a new chapter in the study of the universe. The search of technologies able to improve the sensitivity of the detectors is still in progress. For the future, in fact, many proposals have been made and many experiments are currently underway trying to figure out what are the best solutions for the future upgrades of the current detectors and for the design and construction of what is called the 3$^{\text{rd}}$ generation of GW detectors.

For example, for the near future an upgrade of Advanced LIGO, called A+, is funded by NSF. It does include only moderate changes in the infrastructure and the total cost will be then limited. The most important changes are [39]:

[8] GEO600 did not help with the sky localisation because it did not have a signal-to-noise ratio good enough to detect the signal.

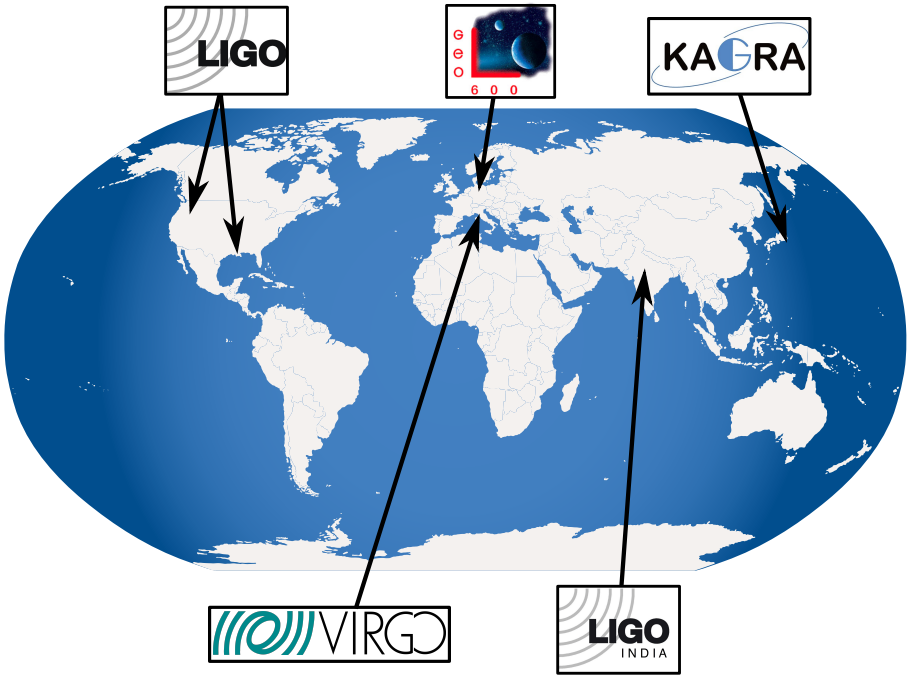

Figure 1.5: World map with the location of the detectors that will compose the worldwide network in the next future.

- it will be implemented frequency dependent squeezing using a 300 m filter cavity in order to reduce the quantum noise;
- the optical coatings will be optimised in order to have a reduction of the mechanical loss by a target factor of 4, which will reduce the displacement noise from coating thermal noise by a factor 2 [40];
- there will be a balanced homodyne readout[9] with suspended mirrors;
- it will be used a larger beamsplitter, which will reduce the loss;
- new test masses obtained with improved welding and fibres pulling systems will be installed, in order to lower the test masses bounce mode frequency [41].

The observations with A+ are planned to start in 2024.

Another upgrade under consideration for the future of LIGO is called Voyager. It is a 4 km interferometer with cryogenic 200 kg silicon mirrors, operating at a temperature of 123 K. This will potentially enable the increase of the intra-cavity power to 3 MW, without affecting too much the thermal noise (at 123 K in fact the silicon has low mechanical loss and zero thermal expansion). Another big change will be the laser wavelength that will be

[9]Details on the homodyne readout method will be given in section 3.4.3.

	aLIGO	A+	Voyager	Cosmic Expl.	ET-LF	ET-HF
Arm length [km]	4	4	4	40	10	10
Mirror mass [kg]	40	40	200	320	211	200
Mirror diameter [cm]	34	34	45	>70	>45	62
Temperature [K]	295	295	123	123	10	290
Input power [W]	125	125	140	220	3	500
Arm power [kW]	710	750	3000	2000	18	3000
Wavelength [nm]	1064	1064	2000	1550	1550	1064

Table 1.1: List of the parameters of the future GW detectors compared with that ones of Advanced LIGO [39, 44].

2 μm, instead of the usual 1064 nm. The sensitivity is expected to be improved by a factor 2 at 100 Hz respect to A+ [39].

Apart from the upgrade of the current detectors, a 3rd generation is planned to join the worldwide network, which will require new facilities because of their bigger dimensions. These detectors will have significant differences from the current ones and the research to define all their features is still underway. The most important detectors that will form the 3rd generation are listed below.

- **Cosmic Explorer** will have 40 km arms and the test masses weight will be further increased to 320 kg. Like Voyager, it will use cryogenic mirrors and high intra-cavity power (2 MW). This detector has expected to have a sensitivity improved by a factor >10 respect to Advanced LIGO [42].
- **Einstein telescope** (ET) is an underground observatory composed by three 10 km long detectors nested in a triangular shape. Each detector will be composed by two interferometers, one optimised at low frequency (ET-LF) and the other one at high frequency (ET-HF) [43].

The parameters of each of these detectors are listed in table 1.1 and the expected sensitivity curves are shown in figure 1.6.

1.3 Elements of gravitational wave theory

GWs are a direct consequence of the theory of General Relativity introduced by Albert Einstein in 1916 [46]. They are ripples in the space-time propagating at the speed of light,

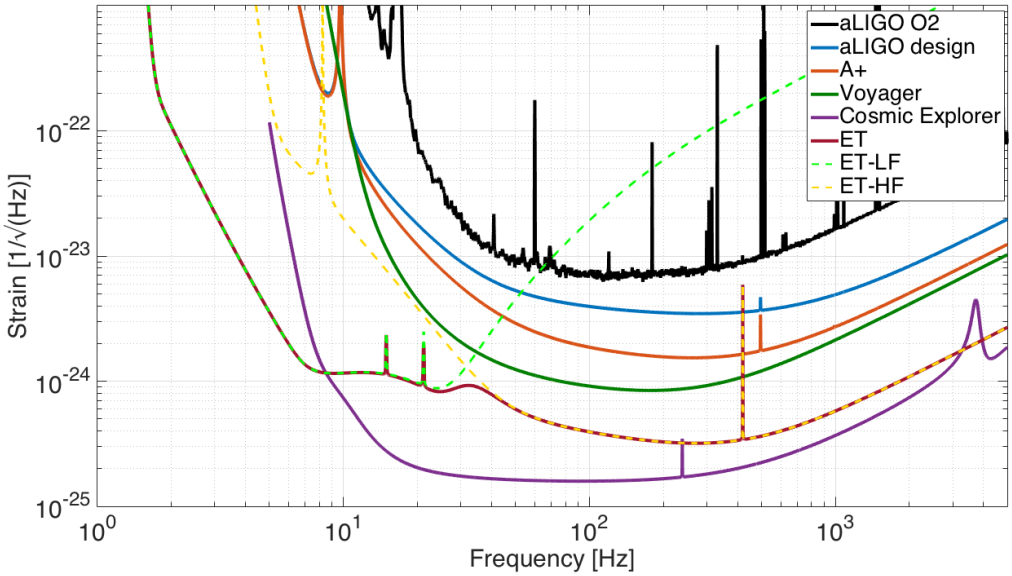

Figure 1.6: Sensitivity curves (created with GWINC [29]) of the 3rd generation GW detectors Cosmic Explorer and Einstein Telescope (LF, HF and the sum of the two), compared with the designed and real (for the second observation run) of Advanced LIGO and with the expected sensitivity for Advanced LIGO upgrades A+ and Voyager [45].

created by a sudden and great change of mass distribution. Their equation is obtained by linearising the Einstein equations of field considering a Minkowski space with a small perturbation. There are two possible solutions, giving two possible polarisation, named *plus* (+) and *cross* (×) [47].

Unlike of what happens for the electromagnetic radiation, created by the dipole momentum, the lowest order for the gravitational emission is the quadrupole momentum, defined by the equation [28]

$$I_{\mu,\nu} = \int dV \left(x_\mu x_\nu - \frac{1}{3}\delta_{\mu\nu} r^2 \right) \rho(r), \tag{1.9}$$

where r is the size of the source and ρ is the mass density. From this equation we obtain the amplitude of the GW, that is

$$h_{\mu\nu} = \frac{2G}{Rc^4} \ddot{I}_{\mu\nu}, \tag{1.10}$$

where G is the gravitational constant and R is the distance of the source.

The passage of a GW will squeeze and stretch the space-time in the plane transverse to its direction of propagation with opposite effect in the two directions and h represent the relative change in length, according to equation 1.2 and this the basic working principle of interferometric GW detectors (see figure 1.7).

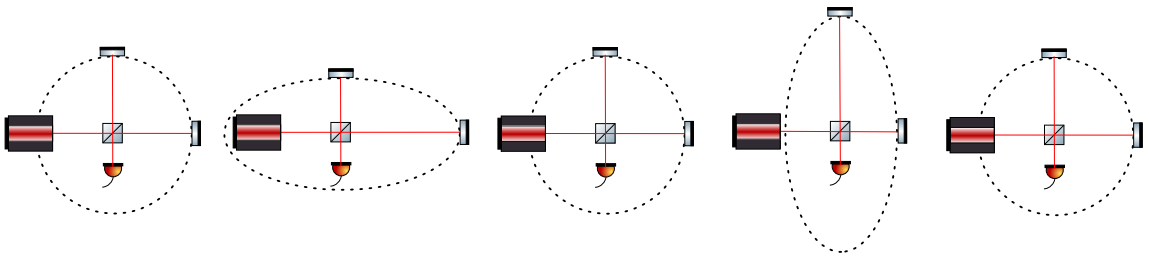

Figure 1.7: Representation (amplified) of how the arms of a Michelson interferometer will be affected by the passage of a GW propagating in the direction perpendicular to the plane of the paper.

1.4 Conclusions

In this chapter we gave an overview of the past, present and future of ground based GW detectors. In the first section we described the detections announced so far. We gave particular relevance to the most important ones: the first detection, which marked the birth of the GW astronomy, and the detection of the GW generated by a binary neutron star merger, which marked the start of the multi-messenger astronomy. The main outcomes and physical implications of these two detections are also described. In the second section, then, we described the history of ground-based GW detectors. We explained what are the fundamental noises that limit the sensitivity of the detectors and what are the tecniques used to reduce these noises in the current and future detectors. Finally in the last section we gave a brief overview of the gravitationa wave theory.

Chapter 2

Methodology

In this chapter an overview of the tools and methods used to make the analyses and obtain the results shown in the following chapters are given.

In the first section the theory at basics of the calculations of the I/O relations and the quantum noise of an interferometer is shown. The results of this calculations are described in chapters 4 and 6.

The last two sections of this chapter are about the tools used for the measurements and analyses of the map of the mirror surfaces and the computer programs used for the simulations. Specifically, in the first part we show the softwares used for the analysis of the surfaces imperfections of the arm cavity mirrors of the Glasgow SSM and the cavity loss associated with them. This analysis, described in details in chapter 5, was made performing simulations with the help of two MATLAB® packages, *SimTools* and OSCAR.

The meaning of the symbols and some definitions used in this chapter and all the later ones can be found in appendix A.

2.1 Basic theory for quantum noise calculation

In an optomechanical system the equations that describe the linear transformations of the input fields into the output fields are called input-output (I/O) relations. In this section we show the theoretical basis and the mathematical framework that will be used for the derivation of the I/O relations of the interferometers and the calculation of the quantum noise that will be shown in chapters 4 and 6.

In the first section the two-photon formalism is introduced. This formalism, developed in the 1980's, is commonly used for the analysis of quantum noise of gravitational wave detectors. In the second section the definition and the properties of the vacuum state of

an optical field are shown. Finally, in the last two sections, the derivation of the transfer matrix of a lossless and a lossy optical element is shown.

2.1.1 Two-photon formalism

In chapter 4 the calculations of the I/O relations for several interferometer configurations relevant in the context of this thesis are shown. The calculations are made using the two-photon quadrature formalism, developed by Caves and Schumaker in 1985 [48] [49]. It was developed modifying the one-photon formalism in order to analyse the so called two-photon devices. Two-photon devices are systems that produce as output a radiation composed by pairs of modes independently excited.

Something similar happens in the interferometers for gravitational waves detection, since the gravitational wave signal produces a pair of sideband fields in the output of the interferometer. This is the reason why this formalism is commonly used for the description of quantum noise of interferometric gravitational wave detectors.

In quantum field theory, a freely propagating electromagnetic wave is described in every point of the space (x, y, z) and at any time t by the Heisenberg operator, that for a wave propagating along the positive direction of the z-axis can be written as [50] [51]

$$\mathcal{A}(x, y, z, t) = u(x, y, z) \int_0^\infty \frac{d\omega}{2\pi} \sqrt{\frac{2\pi\hbar\omega}{A_q c}} \left(\hat{a}_\omega e^{-i\omega t} + \hat{a}_\omega^\dagger e^{i\omega t}\right) \tag{2.1}$$

where ω is the frequency, A_q is the beam cross-sectional area, $u(x, y, z)$ is the spatial mode shape and the single photon annihilation and creation operators $\hat{a}$ and $\hat{a}^\dagger$ satisfies the commutation relations

$$\left[\hat{a}_\omega, \hat{a}_{\omega'}^\dagger\right] = 2\pi\delta(\omega - \omega'), \quad \left[\hat{a}_\omega, \hat{a}_{\omega'}\right] = \left[\hat{a}_\omega^\dagger, \hat{a}_{\omega'}^\dagger\right] = 0. \tag{2.2}$$

As said, in GW interferometric detectors a pair of sidebands is created by the signal with frequencies $\omega_p + \Omega$ and $\omega_p - \Omega$, so it is useful to define the sideband operators

$$\hat{a}_+ = \hat{a}_{\omega+\Omega}, \quad \hat{a}_- = \hat{a}_{\omega-\Omega}. \tag{2.3}$$

These operators are used to define the quadrature operators, which will be

$$\hat{a}_c(\Omega) = \frac{\hat{a}_+ + \hat{a}_-^\dagger}{\sqrt{2}}, \quad \hat{a}_s(\Omega) = \frac{\hat{a}_+ - \hat{a}_-^\dagger}{i\sqrt{2}} \tag{2.4}$$

in frequency domain and

$$\hat{a}_c(t) = \int_{-\infty}^{\infty} \frac{d\Omega}{2\pi} \frac{\hat{a}_+ + \hat{a}_-^\dagger}{\sqrt{2}} e^{-i\Omega t}, \quad \hat{a}_s(t) = \int_{-\infty}^{\infty} \frac{d\Omega}{2\pi} \frac{\hat{a}_+ - \hat{a}_-^\dagger}{i\sqrt{2}} e^{-i\Omega t} \tag{2.5}$$

in time domain.

Through these definitions the commutation relations 2.2 become

$$\left[\hat{a}_c(\Omega), \hat{a}_s(\Omega')\right] = 2\pi\delta(\Omega + \Omega'), \quad \left[\hat{a}_c, \hat{a}_c(\Omega')\right] = \left[\hat{a}_s, \hat{a}_s(\Omega')\right] = 0. \tag{2.6}$$

In order to make the calculation simpler, each of these components can be split in a constant part and a time dependent part, i.e.

$$\hat{a}_c^{old} \rightarrow A_c + \hat{a}_c^{new}, \qquad \hat{a}_s^{old} \rightarrow A_s + \hat{a}_s^{new}, \tag{2.7}$$

which represent the classical amplitude and the time varying part, e.g. the quantum fluctuation of the field[1].

Now we can define the vectors of quadrature for both components (from now on the superscript *new* will be omitted) as

$$\boldsymbol{A} = \begin{bmatrix} A_c \\ A_s \end{bmatrix} \qquad \hat{\boldsymbol{a}}(\Omega) = \begin{bmatrix} \hat{a}_c \\ \hat{a}_s \end{bmatrix} \tag{2.8}$$

and with these definitions we can finally write the electric field in equation 2.1 in terms of

[1]Here we made the assumption that since we control the interferometers and they are stable, then the DC part is constant

a cosine and a sine component. So, approximating ω as ω_p, equation 2.1 becomes

$$\begin{aligned}
\mathcal{A}(x,y,z,t) =& u(x,y,z)\sqrt{\frac{2\pi\hbar\omega_p}{A_q c}}\int_0^\infty \frac{d\Omega}{2\pi}\left(a_+\, e^{-i(\omega_p+\Omega)t} + a_-^\dagger\, e^{i(\omega_p-\Omega)t}\right)\\
=& u(x,y,z)\sqrt{\frac{2\pi\hbar\omega_p}{A_q c}}\int_0^\infty \frac{d\Omega}{2\pi}\left(e^{-i\omega_p t}\, a_+\, e^{-i\Omega t} + e^{i\omega_p t}\, a_-^\dagger\, e^{-i\Omega t}\right)\\
=& u(x,y,z)\sqrt{\frac{2\pi\hbar\omega_p}{A_q c}}\int_0^\infty \frac{d\Omega}{2\pi}\left(a_+\, e^{-i\omega_p t} + a_-^\dagger\, e^{i\omega_p t}\right)\, e^{-i\Omega t}\\
=& u(x,y,z)\sqrt{\frac{2\pi\hbar\omega_p}{A_q c}}\int_0^\infty \frac{d\Omega}{2\pi}\left[a_+\left(\cos\omega_p t - i\sin\omega_p t\right) + a_-^\dagger\left(\cos\omega_p t + i\sin\omega_p t\right)\right]\, e^{-i\Omega t}\\
=& u(x,y,z)\sqrt{\frac{4\pi\hbar\omega_p}{A_q c}}\int_0^\infty \frac{d\Omega}{2\pi}\left(\frac{a_+ + a_-^\dagger}{\sqrt{2}}\cos\omega_p t + \frac{a_+ - a_-^\dagger}{i\sqrt{2}}\sin\omega_p t\right) e^{-i\Omega t}.
\end{aligned} \tag{2.9}$$

Finally, using equation 2.5 we have

$$\boldsymbol{A} = u(x,y,z)\sqrt{\frac{4\pi\hbar\omega_p}{A_q c}}\left(\left(A_c + \hat{a}_c(t)\right)\cos\omega_p t + \left(A_s + \hat{a}_s(t)\right)\sin\omega_p t\right). \tag{2.10}$$

In the end any relation between two electric fields of the form $\hat{\mathbf{b}}(\omega) = f(\Omega)\,\hat{\mathbf{a}}(\omega)$ can be written in terms of two-photon formalism transforming the function $f(\Omega)$ according to the following rule

$$\hat{\boldsymbol{b}}(\Omega) = \frac{1}{2}\begin{bmatrix} \left(f_+ + f_-^*\right) & i\left(f_+ - f_-^*\right) \\ -i\left(f_+ - f_-^*\right) & \left(f_+ + f_-^*\right)\end{bmatrix}\cdot\hat{\boldsymbol{a}}(\Omega), \tag{2.11}$$

where f_+ and f_- are defined as in equation 2.3 and

$$\hat{\boldsymbol{a}}(\Omega) = \begin{bmatrix}\hat{a}_c \\ \hat{a}_s\end{bmatrix}, \qquad \hat{\boldsymbol{b}}(\Omega) = \begin{bmatrix}\hat{b}_c \\ \hat{b}_s\end{bmatrix} \tag{2.12}$$

are the fields in the two-photon formalism.

2.1.2 Vacuum state of the optical field

In classical physics the vacuum is a region of the space where no particle are present. However this is not true in quantum mechanics, where, because of the Heisenberg's uncertainty

principle, in each point there must be a fluctuation of energy. To explain that, it has been supposed that in the vacuum there are temporary particles which continuously and quickly create and annihilate.

So the vacuum state $|0\rangle$ of an optical field is by definition the ground state, i.e. the lowest state of energy (equal to $\hbar\omega/2$) with no excitation. This means that it must satisfy the following relations

$$\hat{a}_\omega |0\rangle_\omega = 0, \tag{2.13}$$

$$\langle 0|_\omega \hat{a}^\dagger_\omega = 0, \tag{2.14}$$

$$\langle 0| \hat{a}_\omega |0\rangle = \langle \hat{a}_\omega \rangle = \left\langle \hat{a}^\dagger_\omega \right\rangle = 0 \Rightarrow \langle \hat{a}_c(\Omega) \rangle = \langle \hat{a}_s(\Omega) \rangle = 0, \tag{2.15}$$

$$\langle 0| \hat{a}(t) |0\rangle = \langle \hat{a}(t) \rangle = \left\langle \hat{a}^\dagger(t) \right\rangle = 0 \Rightarrow \langle \hat{a}_c(t) \rangle = \langle \hat{a}_s(t) \rangle = 0, \tag{2.16}$$

where $|0\rangle$ is defined as the vacuum state of all modes[2] over all frequencies ω [50]. The first two equations represent the fact that $|0\rangle$ has the lowest energy and no excitation at every frequency. The last two, instead, represent the fact that, because of its statistical properties the mean value is zero, in both frequency and time domain.

Furthermore for the quantum noise calculation it is useful to define the symmetrised single-sided spectral density $S_{ij}(\Omega)$ as

$$2\pi\delta(\Omega - \Omega')S_{ij}(\Omega) = \frac{1}{2}\left\langle \hat{\boldsymbol{a}}_i(\Omega)\,\hat{\boldsymbol{a}}_j(\Omega') + \hat{\boldsymbol{a}}_j(\Omega')\,\hat{\boldsymbol{a}}_i(\Omega) \right\rangle \quad (i, j = c, s) \tag{2.17}$$

and the associated quadrature amplitude matrix of spectral densities

$$\mathbb{S}(\Omega) = \begin{bmatrix} S_{cc}(\Omega) & S_{cs}(\Omega) \\ S_{sc}(\Omega) & S_{ss}(\Omega) \end{bmatrix}. \tag{2.18}$$

For the vacuum state, this matrix of spectral densities can be obtained form the commutation relations 2.6 and it is

$$\mathbb{S}(\Omega)_{vac} = \begin{bmatrix} 1 & 0 \\ 0 & 1 \end{bmatrix}, \quad S_{cc}(\Omega) = S_{ss}(\Omega) = 1, \quad S_{cs}(\Omega) = 0. \tag{2.19}$$

2.1.3 Transfer matrix of a lossless optical element

In order to be able to write the relations between the input and output fields of a general optical element (e.g. mirror, lens, beamsplitter, etc.) its optical transfer matrix must be defined.

[2] A quantum state of a travelling wave comprises a continuum of modes and each of them can be viewed as a quantum oscillator.

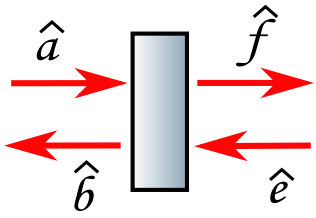

Figure 2.1: Optical element with two input beams $\hat{\boldsymbol{a}}(\Omega)$ and $\hat{\boldsymbol{e}}(\Omega)$ and two output fields $\hat{\boldsymbol{b}}(\Omega)$ and $\hat{\boldsymbol{f}}(\Omega)$.

Let us consider for example an optical element with power transmissivity T and power reflectivity R and suppose that there are two beams $\hat{\boldsymbol{a}}(\Omega)$ and $\hat{\boldsymbol{e}}(\Omega)$ incident on its surface (cf. figure 2.1). The relation between these beams and the output beams $\hat{\boldsymbol{b}}(\Omega)$ and $\hat{\boldsymbol{f}}(\Omega)$ can be written as

$$\begin{bmatrix} \hat{\boldsymbol{b}}(\Omega) \\ \hat{\boldsymbol{f}}(\Omega) \end{bmatrix} = \begin{bmatrix} \sqrt{R}\, e^{i\phi_r} & \sqrt{T}\, e^{i\phi_t} \\ \sqrt{T}\, e^{i\phi_t} & \sqrt{R}\, e^{i\phi_r} \end{bmatrix} \cdot \begin{bmatrix} \hat{\boldsymbol{a}}(\Omega) \\ \hat{\boldsymbol{e}}(\Omega) \end{bmatrix}, \tag{2.20}$$

where ϕ_r and ϕ_t are the phases of the reflected and transmitted fields respectively.

Because of the energy conservation law, the optical transfer matrix must be unitary and that means that the following relation must be true

$$\begin{bmatrix} \sqrt{R}\, e^{i\phi_r} & \sqrt{T}\, e^{i\phi_t} \\ \sqrt{T}\, e^{i\phi_t} & \sqrt{R}\, e^{i\phi_r} \end{bmatrix} \cdot \begin{bmatrix} \sqrt{R}\, e^{-i\phi_r} & \sqrt{T}\, e^{-i\phi_t} \\ \sqrt{T}\, e^{-i\phi_t} & \sqrt{R}\, e^{-i\phi_r} \end{bmatrix} = \begin{bmatrix} 1 & 0 \\ 0 & 1 \end{bmatrix}. \tag{2.21}$$

This gives us the following conditions:

$$\begin{cases} R + T = 1, \\ \sqrt{RT}\left(e^{i(\phi_r - \phi_t)} + e^{i(\phi_t - \phi_r)}\right) = 0. \end{cases} \tag{2.22}$$

The first one is the the energy conservation law itself and from the second condition we have

$$\cos(\phi_r - \phi_t) + i\sin(\phi_r - \phi_t) + \cos(\phi_t - \phi_r) + i\sin(\phi_t - \phi_r) = 2\cos(\phi_r - \phi_t) = 0, \tag{2.23}$$

which means that must be $\phi_r - \phi_t = \pm\frac{\pi}{2}$. There are several solutions that satisfy this condition. In this thesis , unless otherwise specified, we will always use the convention

$$\phi_r = 0, \quad \phi_t = \frac{\pi}{2}. \tag{2.24}$$

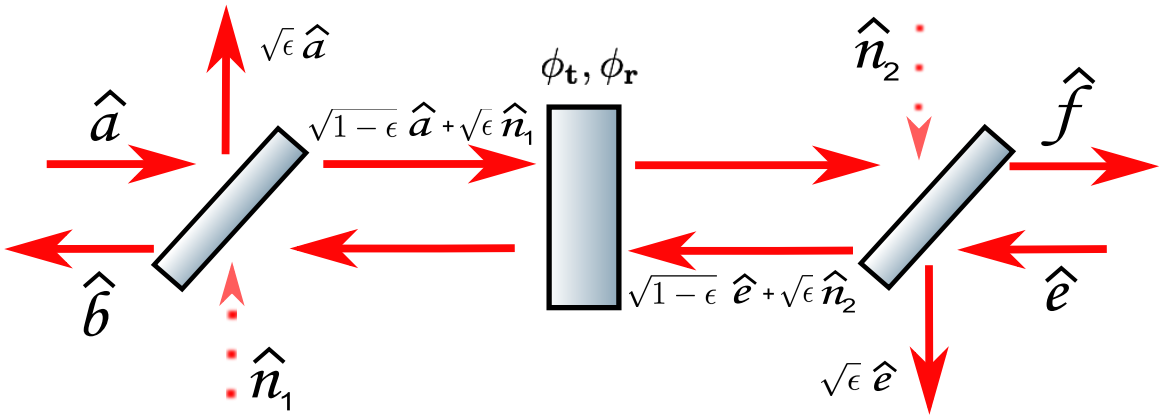

Figure 2.2: System equivalent to a mirror with a power loss equal to ϵ. In order to take into account the loss and the additional noise related to it, two imaginary asymmetric beamsplitters with reflectivity equal to the loss are added before the two input fields. The two vacuum fields $\hat{\boldsymbol{n}}_1(\Omega)$ and $\hat{\boldsymbol{n}}_2(\Omega)$ gives the contribution of the additional noise.

So equation 2.20 become

$$\begin{bmatrix} \hat{\boldsymbol{b}}(\Omega) \\ \hat{\boldsymbol{f}}(\Omega) \end{bmatrix} = \begin{bmatrix} \sqrt{R} & i\sqrt{T} \\ i\sqrt{T} & \sqrt{R} \end{bmatrix} \cdot \begin{bmatrix} \hat{\boldsymbol{a}}(\Omega) \\ \hat{\boldsymbol{e}}(\Omega) \end{bmatrix}. \tag{2.25}$$

which describe the relations between the input and the output beams acting on the mirror.

2.1.4 Transfer matrix of a lossy optical element

The case of a lossy mirror is more complex but it is required to analyse realistic systems. Let us consider for example a mirror with power transmissivity T, power reflectivity R and a loss described by a coefficient ϵ that could be due to scattering, absorption, any other mechanism that creates a loss or a combination of these. According to the Fluctuation Dissipation Theorem [52] there is a connection between any kind of a dissipative mechanism (i.e. the loss) and some kind of fluctuation. This means that the optical loss must always introduce an additional noise.

In order to take into account this additional noise, we can consider an equivalent system where two imaginary beamsplitters are introduced (see figure 2.2). Each of these beamsplitters will have a reflectivity ϵ, so the reflected light is equal to the loss, and a second input field, which is a vacuum field and represent the additional noise associated to the loss.

The relations between the input fields $\hat{\boldsymbol{a}}(\Omega)$ and $\hat{\boldsymbol{e}}(\Omega)$ the output fields $\hat{\boldsymbol{b}}(\Omega)$ and $\hat{\boldsymbol{f}}(\Omega)$ can

then be written as follow [50]

$$\begin{bmatrix} \hat{\boldsymbol{b}}(\Omega) \\ \hat{\boldsymbol{f}}(\Omega) \end{bmatrix} = (1-\epsilon) \begin{bmatrix} \sqrt{R} & i\sqrt{T} \\ i\sqrt{T} & \sqrt{R} \end{bmatrix} \cdot \begin{bmatrix} \hat{\boldsymbol{a}}(\Omega) \\ \hat{\boldsymbol{e}}(\Omega) \end{bmatrix} + \sqrt{\epsilon(1-\epsilon)} \begin{bmatrix} \sqrt{R} & i\sqrt{T} \\ i\sqrt{T} & \sqrt{R} \end{bmatrix} \cdot \begin{bmatrix} \hat{\boldsymbol{n}}_1(\Omega) \\ \hat{\boldsymbol{n}}_2(\Omega) \end{bmatrix} \quad (2.26)$$

where $\hat{\boldsymbol{n}}_{1,2}(\Omega)$ are vacuum fields. It is worth noting that in this case the energy conservation law becomes $R + T + \epsilon = 1$. The additional noises sources associated to the loss are uncorrelated with the input field and one with each other and that means that they must satisfy the following condition:

$$\left\langle \hat{n}_1(t), \hat{n}_2(t') \right\rangle = 0. \quad (2.27)$$

Furthermore, because of the arbitrariness of the noise fields introduced, we can redefine them as

$$\begin{bmatrix} \hat{\boldsymbol{n}'}_1(\Omega) \\ \hat{\boldsymbol{n}'}_2(\Omega) \end{bmatrix} = \begin{bmatrix} \sqrt{R} & i\sqrt{T} \\ i\sqrt{T} & \sqrt{R} \end{bmatrix} \cdot \begin{bmatrix} \hat{\boldsymbol{n}}_1(\Omega) \\ \hat{\boldsymbol{n}}_2(\Omega) \end{bmatrix} \quad (2.28)$$

keeping the condition of uncorrelation expressed in equation 2.27 still valid. In this way equation 2.29 can be simplified

$$\begin{bmatrix} \hat{\boldsymbol{b}}(\Omega) \\ \hat{\boldsymbol{f}}(\Omega) \end{bmatrix} = (1-\epsilon) \begin{bmatrix} \sqrt{R} & i\sqrt{T} \\ i\sqrt{T} & \sqrt{R} \end{bmatrix} \cdot \begin{bmatrix} \hat{\boldsymbol{a}}(\Omega) \\ \hat{\boldsymbol{e}}(\Omega) \end{bmatrix} + \sqrt{\epsilon(1-\epsilon)} \begin{bmatrix} \hat{\boldsymbol{n}'}_1(\Omega) \\ \hat{\boldsymbol{n}'}_2(\Omega) \end{bmatrix}, \quad (2.29)$$

which gives the equations of the output beams for a lossy optical elements as a function of the input beams and the vacuum fields associated to the loss.

This method will be used in chapter 6 for the calculation of quantum noise of an interferometer with a lossy ITM.

2.2 Measurements and analysis of the mirror surface

The surface requirements of the arm cavity mirrors of the Glasgow SSM are defined performing simulations in order to evaluate the loss that each kind of surface imperfection produces. There are several kinds of surface imperfections that cause loss or beam distortion. They will be analysed in details in chapter 5, where we will describe the results of the measurements and the simulations that led us to the derivation of the mirrors requirements.

In this section we will describe the most important mirror surface errors and the tools used to measure and analyse them.

2.2.1 Mirror surface imperfections

There are a lot of imperfections a mirror surface can have that can create additional sources of noise in the interferometers. The effects they have on the interferometer performance are different for each of them, but one of the most important is the scattering, which will be described in details in chapter 6.

Here there is a list of the most important surface errors.

Point defects

A point defect is defined as a randomly placed defect with dimensions of the order of the microns. A theoretical study of the effects of this kind of anomalies was made by Yamamoto [53] and can be summarised as follow.

According to the Huygens principle any point of the wavefront can be considered as a source of the electromagnetic field. So, if we consider the field $E_0(x_0, y_0, z_0)$ as the field in the source point (x_0, y_0, z_0), then the electromagnetic field in a generic point of the space (x, y, z) in the Fresnel approximation can be written as [54]

$$E(x, y, z) \equiv \frac{i}{L\lambda} \int\int dx_0\, dy_0\, E_0(x_0, y_0, z_0)\, e^{-ik\frac{\Delta x^2+\Delta y^2}{2L}}, \tag{2.30}$$

where $L = z - z_0$, λ is the wavelength, k is the wave number, $\Delta x = x - x_0$ and $\Delta y = y - y_0$.

In our case we want that the source is a gaussian beam reflected by a point defect placed in the centre of the reflection point. The effects of the point defect is a perturbation of the gaussian field TEM_{00} described by a factor $\exp[2i\,k\,f(x_0, y_0)]$, i.e.

$$E_0(x_0, y_0, z_0) = TEM_{00}\, e^{2i\,k\,f(x_0,y_0)} = \sqrt{\frac{2}{\pi w_0^2}}\, e^{-\frac{x_0^2+y_0^2}{w_0^2}}\, e^{2i\,k\,f(x_0,y_0)}, \tag{2.31}$$

with w_0 the beam waist (which is supposed to be on the mirror surface) and $f(x_0, y_0)$ a function that describe the geometry of the point defect. Inserting equation 2.31 in equation 2.30 and expanding the exponential in f until the first order, we can write the Huygens integral as the sum of an unperturbed field $F_0(x, y)$ and a perturbation $dF(x, y)$:

$$\begin{aligned} E(x, y, z) &= F_0(x, y, z) + dF(x, y, z) \\ &= \sqrt{\frac{2}{\pi w_0^2}}\, \frac{i}{L\lambda} \int\int dx_0\, dy_0\, e^{-ik\frac{\Delta x^2+\Delta y^2}{2L}}\, e^{-\frac{x_0^2+y_0^2}{w_0^2}} \\ &+ \sqrt{\frac{2}{\pi w_0^2}}\, \frac{i}{L\lambda} \int\int dx_0\, dy_0\, 2ik\, f(x_0, y_0)\, e^{-ik\frac{\Delta x^2+\Delta y^2}{2L}}\, e^{-\frac{x_0^2+y_0^2}{w_0^2}}. \end{aligned} \tag{2.32}$$

The perturbed field $dF(x, y)$ can be simplified using the Fraunhofer approximation (then $x_0 << x$ and $y_0 << y$) and assuming that the beam size is much more bigger than the point defect ($x << w_0$ and $y << w_0$) and then we have

$$dF(x,y) = \sqrt{\frac{2}{\pi w_0^2}}\,\frac{i}{L\lambda}\,e^{-ik\frac{x^2+y^2}{2L}}\,2ik\int\int dx_0\,dy_0\,f(x_0,y_0)\,e^{-ik\frac{x\cdot x_0+y\cdot y_0}{L}}. \tag{2.33}$$

Finally, the relative power loss due to the point defect is found by calculating the power of the perturbed field

$$Loss = \int\int dx\,dy\;|dF(x,y,z)|^2 = \frac{32\pi a^2 h^2}{(w_0\lambda)^2}, \tag{2.34}$$

where we have supposed that the point defect has a gaussian shape with area on the mirror surface equal to a^2 and maximum height h.

Since the loss is proportional to the power that hits the point defect, the final equation for the total loss is obtained performing the integral of the loss due to a point defect described in equation 2.34 multiplied by the gaussian beam's function and the surface density N of point defects:

$$Loss_{tot} = \int\int dxdyLoss\exp(-2(x^2+y^2)/w^2)N. \tag{2.35}$$

Astigmatism

Astigmatism is an optics aberration that causes a distortion of the image and the creation of a secondary image. For example, in case of a point source reflected (or propagating) through an astigmatic mirror (or lens) the image will be two perpendicular lines [55]. The surface of an astigmatic optical element can be described by the Zernike polynomial (2,2) [56].

Zernike polynomials are a set of polynomials which are a complete orthogonal base over a unit disk. This means that every circular surface (or wavefront) can be described as a sum of Zernike polynomials and this is the reason why they are often used to describe the mirror surface.

In a polar coordinate system (ρ, ϕ), they are defined through two indexes m and n as [57]

$$\begin{cases} Z_n^m(\rho,\phi) = R_n^m(\rho)\cos(m\phi) & \text{for } m > 0, \\ Z_n^m(\rho,\phi) = R_n^m(\rho)\sin(m\phi) & \text{for } m < 0, \\ Z_n^m(\rho,\phi) = R_n^m(\rho) & \text{for } m = 0, \end{cases} \tag{2.36}$$

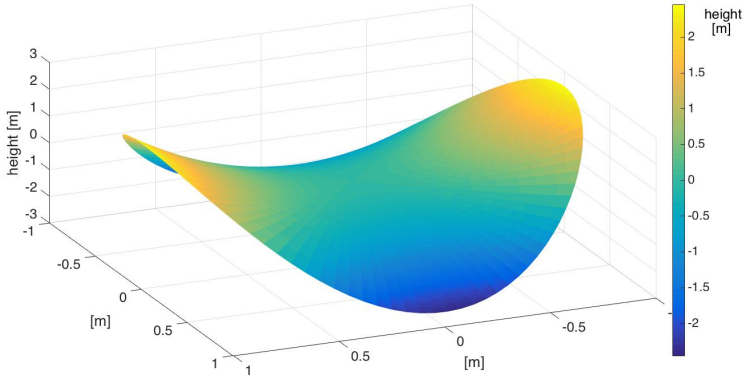

Figure 2.3: Example of a surface described by Zernike polynomial $Z_2^2(\rho, \phi)$.

with

$$R_n^m(\rho) = \sum_{k=0}^{(n-m)/2} \frac{(-1)^k (n-k)!}{k! \left(\frac{n+m}{2} - k\right)! \left(\frac{n-m}{2} - k\right)!} \rho^{n-2k}. \tag{2.37}$$

From this definition we have that the polynomial $Z_2^2(\rho, \phi) = \sqrt{6}\,\rho^2 \cos(\phi)$ represents the astigmatism (see figure 2.3).

Flatness and microroughness

Spatially periodic surface imperfections can be defined considering their spatial frequencies. In general errors with low spatial frequencies are defined as flatness, and errors with high spatial frequencies as microroughness. There is not a fixed rule to define the limit of the spatial frequency range for each kind and their effects depend from different parameters like beam size and mirror diameter. Usually the spatial period of flatness is of the order of the mm or cm and that one of microroughness of the order of the microns.

They are usually measured in *rms*, which stands for *root mean square*, and it is defined as

$$h_{rms} = \sqrt{\frac{\sum_{n=1}^{N} \left|h_n - \bar{h}\right|^2}{N}}, \tag{2.38}$$

where h_n is the measure of the height of each of the N points of the surface map and $\bar{h}$ is the mean value of the heights.

A very useful tool to describe the periodic surface errors is the power spectral density (PSD). The PSD of a random time series $s(t)$ is defined as the Fourier transform of the autocorrelation function [28]

$$PSD(f) = \frac{1}{\sqrt{2\pi}} \int_{-\infty}^{\infty} s \star s(\tau)\, e^{2\pi i f \tau}\, d\tau, \tag{2.39}$$

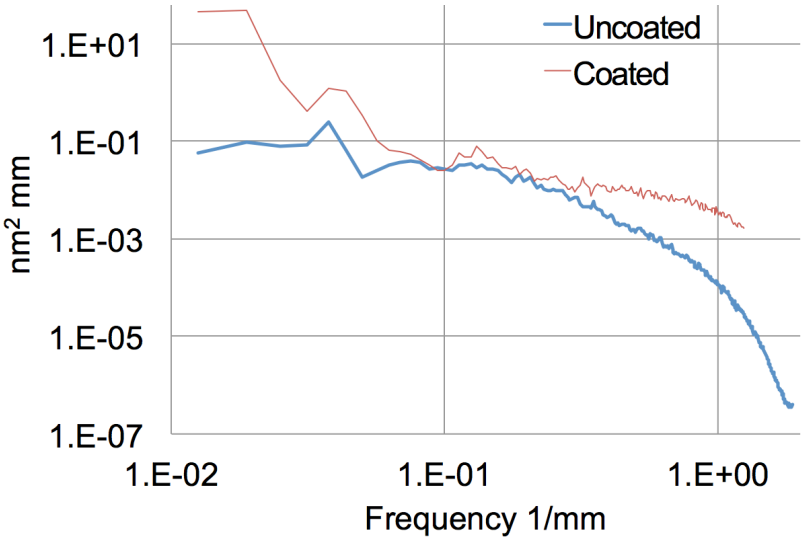

Figure 2.4: Example of the PSD of a mirror surface. Specifically it is the measurements of the surface of one of LIGO's ETM, made before and after the coating. The units of the *y-axis* are expressed in this way in order to highlight the scale of the error (nm) and the spatial frequency units (1/mm). It must also be noticed that at low frequencies the convolution gives non-physical results. Figure taken from [58].

where the autocorrelation function is defined as

$$s \star s(\tau) = \int_{-\infty}^{\infty} s(t)\, s(t+\tau)\, dt, \tag{2.40}$$

and it gives the frequency distribution of the time series amplitude.

This definition can be extended to a surface replacing the time with the space coordinates and the frequencies with the spatial frequencies. In this way we have a detailed description of the periodic surface errors relatively to their spatial frequencies. An example of the PSD of a mirror surface can be seen in figure 2.4, where it is shown the PSD of one of the LIGO ETM before and after the coating.

The spatial frequencies are usually measured in 1/mm and the lower limit is defined by the mirror diameter, because at lower frequencies we do not have enough statistics (it would mean to have less than one defect per mirror size). The microroughness, on the other side, has usually a spatial scale greater than 1/mm, which set the upper limit. The PSD, then, is measured in $[\mathrm{nm}^2 \cdot \mathrm{mm}]$ or $[\mathrm{nm}^2 \cdot (1/\mathrm{mm})^{-1}]$, in order to highlight the scale of the errors (nm) and the spatial frequency units (1/mm).

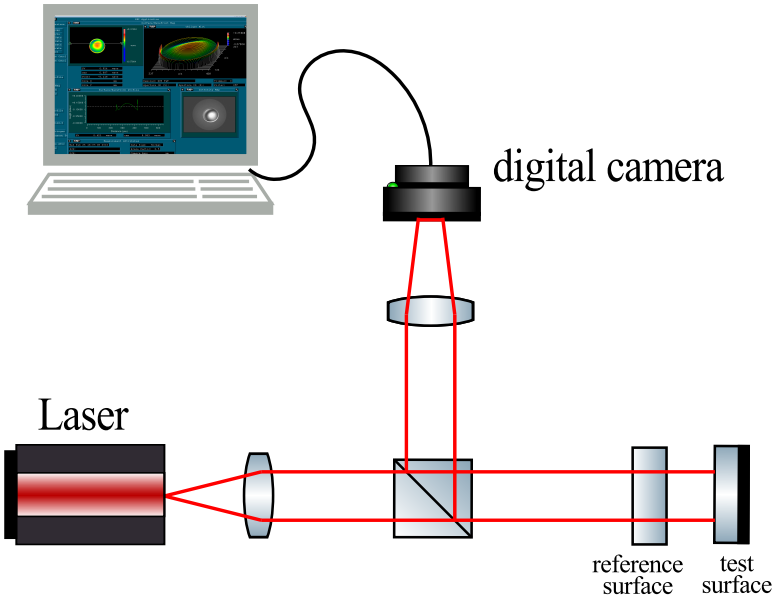

Figure 2.5: Schematic draw of a Fizeau interferometer.

2.2.2 Flatness measurements through phase shifting interferometry

The measurements of the flatness were done with Zygo GPI XP/D™ interferometer [59], which allows to measure flatness of a mirror without touching its surface. This model is a phase shifting interferometer with a Fizeau configuration.

The optical configuration of a Fizeau interferometer can be seen in figure 2.5. The laser beam passes through a beamsplitter and reaches the reference flat, placed in front of the test surface that we want to measure. At this point part of the light is reflected back to the beamsplitter creating a reference wavefront and part is transmitted and reaches the test mirror. The two wavefronts are then recombined at the beamsplitter and the phase difference between the two creates an interference pattern of dark and light fringes.

The relation of the height of the surface $h(x, y)$ and the phase difference $\phi(x, y)$ in each point (x, y) of the surface is described by the following equation

$$h(x, y) = \frac{\phi(x, y)\lambda}{4\pi}, \tag{2.41}$$

where λ is the laser wavelength.

The phase shifting interferometry technique is based on the introduction of a time dependent phase shift, added with the help of some piezoelectric transducers, that change the position of the reference flat [60]. According to this method, the reflected fields from the

reference flat and the test surface will be respectively

$$E_r(x,y,t) = A_r(x,y)\, e^{i(\phi_r(x,y)-\delta(t))}, \tag{2.42}$$

$$E_t(x,y) = A_t(x,y)\, e^{i\phi_t(x,y)}, \tag{2.43}$$

where A_r, A_t, ϕ_r and ϕ_t are the amplitudes and the phases of the reference flat and the test surface respectively and $\delta(t)$ is the time-varying phase. The intensity of the interference pattern is given by the squared sum of the two fields, i.e.

$$\begin{aligned} I(x,y,t) &= \left|E_r(x,y,t) + E_t(x,y)\right|^2 \\ &= A_r^2(x,y) + A_t^2(x,y) + A_r(x,y)\, A_t(x,y) \left(e^{i(\phi(x,y)+\delta(t))} + e^{-i(\phi(x,y)-\delta(t))}\right) \\ &= I'(x,y) + I''(x,y)\, \cos\left(\phi(x,y) + \delta(t)\right), \end{aligned} \tag{2.44}$$

where we have defined $I'(x,y) = A_r^2(x,y) + A_t^2(x,y)$ the average intensity and $I''(x,y) = A_r(x,y)\, A_t(x,y)$ the intensity modulation.

At this points there are several algorithms that can be used to take the measurements, whose major differences are the number of times and the rate at which the interference patterns are measured. In order to have an idea of how these algorithms work, we will show here the simplest one, the so called *four step algorithm*.

As the name suggests, with this algorithm we consider four changes of the phase

$$\delta_i = 0, \pi/2, \pi, 3\pi/2; \qquad i = 1,2,3,4, \tag{2.45}$$

which give the following measured intensities for the interference patterns

$$I_1(x,y) = I'(x,y) + 2I''(x,y)\, \cos\left(\phi(x,y)\right), \tag{2.46}$$

$$\begin{aligned} I_2(x,y) &= I'(x,y) + 2I''(x,y)\, \cos\left(\phi(x,y) + \pi/2\right) \\ &= I'(x,y) - 2I''(x,y)\, \sin\left(\phi(x,y)\right), \end{aligned} \tag{2.47}$$

$$\begin{aligned} I_3(x,y) &= I'(x,y) + 2I''(x,y)\, \cos\left(\phi(x,y) + \pi\right) \\ &= I'(x,y) - 2I''(x,y)\, \cos\left(\phi(x,y)\right), \end{aligned} \tag{2.48}$$

$$\begin{aligned} I_4(x,y) &= I'(x,y) + 2I''(x,y)\, \cos\left(\phi(x,y) + 3\pi/2\right) \\ &= I'(x,y) + 2I''(x,y)\, \sin\left(\phi(x,y)\right), \end{aligned} \tag{2.49}$$

This is a system of four equations in three unknowns $I'(x, y)$, $I''(x, y)$ and $\phi(x, y)$, but what we only need for our measurements is the value of $\phi(x, y)$ in each point of the map. It can be found subtracting in pairs the equations with odd and the even subscripts, in order to eliminate the average intensity and making the ratio of the obtained equations to eliminate the intensity modulation

$$\frac{I_4(x, y) - I_2(x, y)}{I_1(x, y) - I_3(x, y)} = \frac{\sin(\phi(x, y))}{\cos(\phi(x, y))} = \tan(\phi(x, y)). \tag{2.50}$$

Finally the value of the phase shift is

$$\phi(x, y) = \tan^{-1}\left(\frac{I_4(x, y) - I_2(x, y)}{I_1(x, y) - I_3(x, y)}\right) \tag{2.51}$$

and replacing this equation in equation 2.41, we obtain the height of the surface map.

In Zygo GPI XP/D™ a digital camera with a 640x480 pixels resolution is used for the acquisition. The camera takes a set of snapshots of the interference pattern when the two wavefronts has a predetermined phase difference, with an algorithm similar to that one described above, and the data are then processed and combined in order to find the phase of the wavefront at each point of the surface map. The data can be then visualised through the MetroPro™ software, provided with the instrument. An example of the output is shown in figure 2.6.

2.2.3 SimTools

SimTools is a collection of MATLAB® functions useful for optical simulations. It has been developed by *gwoptics* since 2006 and it includes functions made by several people. It does not have a manual, but the list of available functions can be found on the website [61].

A few of these functions will be used in chapter 5 for the correction of the flatness measurements of some mirrors surfaces. These maps will be then used for the simulations performed to derive the arm cavity mirrors requirements. Specifically we will use the following functions:

`FT_recenter_mirror_map.m`

It finds the centre of the map (x_0, y_0) by computing the centre of gravity, i.e.

$$x_0 = \frac{\sum_i x_i}{x_{max}}, \quad y_0 = \frac{\sum_i y_i}{y_{max}} \tag{2.52}$$

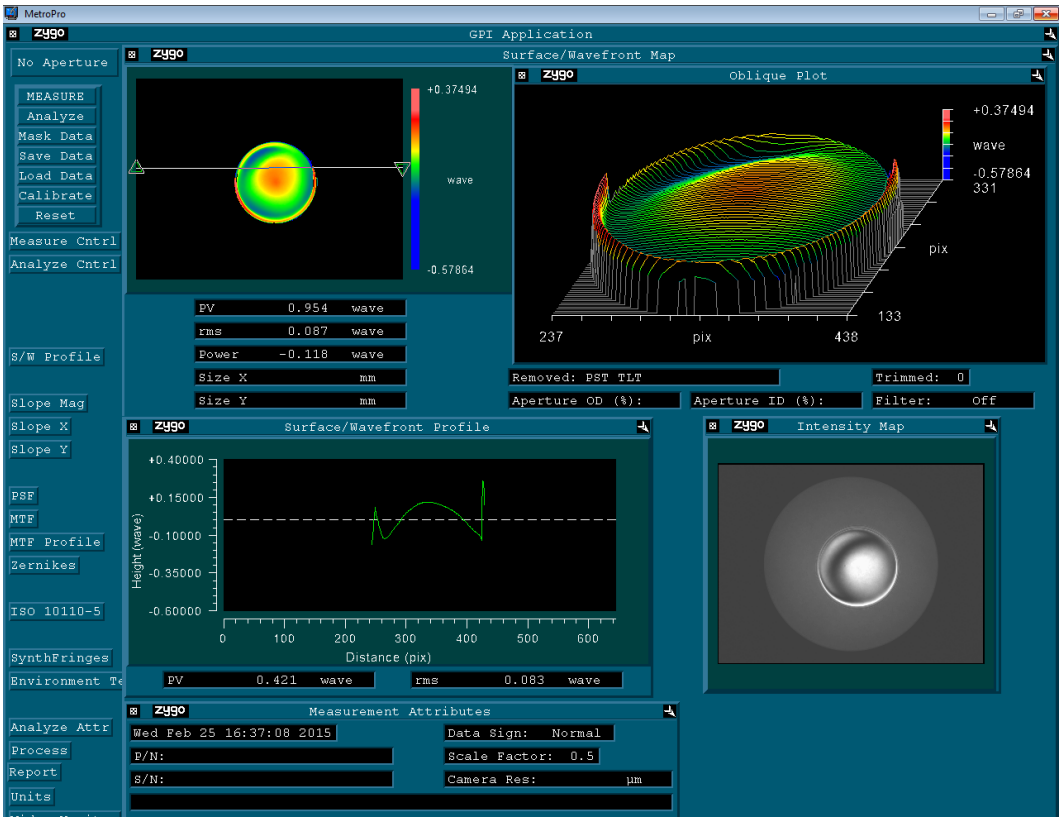

Figure 2.6: Example of a measurement with Zygo interferometer. In the top part of the figure we have the surface profile (in 2D on the left and in 3D on the right) and the values of the flatness. In the bottom part we have 1D surface profile on the left (the direction where this measurement is taken can be chosen by the user) and the intensity map on the right. On the far left we have a list of other possible analyses that can be made on the map.

where x_i and y_i are the indices and x_{max} and y_{max} are the number of element in x and y respectively.

`FT_remove_offset_from_mirror_map.m`

This function is used to remove any offset on the map. It calculates the average value of the central region of the map and then it removes it from the whole map, in order to have the average value of the central region equal to zero. The size of the central area can be chosen by the user, according to the accuracy required.

`FT_remove_piston_from_mirror_map.m`

This function is used to remove any tilt in x and y directions. In order to do that a perfect map is defined and modified adding a tilt in x and y directions. Finally the most likely value of the tilt of the measured map is found testing for which values of the x and y tilt the measured map has minimum difference respect to the perfect map. The output of the

function is a new map with the tilt removed and the values of the tilt.

FT_map_rms.m

This function computes the *rms* value of the surface distortion using equation 2.38. It can be applied to the whole mirror surface or to a selected area. The latter can be done defining the radius over which the calculation should be made.

FT_remove_curvature_from_mirror_map.m

This function gives an estimate of the radius of curvature of the mirror surface. This is done finding the spherical surface which best fit to the surface map. The output is the radius of curvature and a new map with the curvature removed.

FT_zernike_map_convolution.m

This function performs a convolution between a mirror map and a Zernike polynomial and it is used to define the astigmatism as the amplitude of $Z_2^2(\rho, \phi)$ polynomial. The amplitude c of the Zernike polynomial is found through the following equation

$$c = \frac{\sum_{x,y}\left(Z_{x,y} \cdot D^*_{x,y}\right)}{\sum_{x,y}\left(Z_{x,y} \cdot Z^*_{x,y}\right)}, \tag{2.53}$$

where $Z_{x,y}$ and $D_{x,y}$ are the map defined through one of the Zernike polynomials and the measured map respectively.

2.3 OSCAR

In order to find the arm cavity mirrors requirements for the Glasgow SSM, we need to evaluate how the surface imperfections will affect the performance of the cavity. As we will explain in detail in chapter 5, the loss is a critical factor for the sensitivity of this particular experiment. Therefore, we need to consider any possible source of loss and evaluate its impact. This analysis was done in MATLAB® with the help of OSCAR (acronym of *Optical Simulation Containing Ansys Results*), a MATLAB® code that uses the fast Fourier transform (FFT) method [62] to simulate cavities with arbitrary mirror profiles [63]. However, since its calculations are limited to the steady state solution, it cannot be used to calculate quantum effects, like radiation pressure.

The details and the results of these simulations are shown in chapter 5.

2.3.1 Field propagation

The FFT simulations base on the fact that the propagating field can be represented by adding a phase to the FFT of the original field. That means that a transverse electric field $E(x, y, 0)$, which propagates in the z direction from $z = 0$ to $z = d$, can be evaluated as follow [64].

First we make the Fourier transform of the original field

$$\tilde{E}(\nu_x, \nu_y, 0) = \int_{-\infty}^{\infty} \int_{-\infty}^{\infty} E(x, y, 0) e^{2i\pi(\nu_x x + \nu_y y)} dx dy, \tag{2.54}$$

where $\nu_{x,y}$ is the spatial frequency in the basis of x or y.

If we consider that the wave is propagating along the direction z, or close to it, then the z-component of the wave number can be written as

$$k_z \approx k - \frac{k_x^2 + k_y^2}{2k} \approx k - \lambda\pi(\nu_x^2 + \nu_y^2), \tag{2.55}$$

where $k = \sqrt{k_x^2 + k_y^2 + k_z^2} = 2\pi/\lambda$ is the wave number. Substituting equation 2.55 in 2.54 we have

$$\tilde{E}(\nu_x, \nu_y, d) = \tilde{E}(\nu_x, \nu_y, 0)\, e^{-ik_z d} = \tilde{E}(\nu_x, \nu_y, 0) e^{-i(k - \lambda\pi(\nu_x^2 + \nu_y^2))d}. \tag{2.56}$$

Finally, the field after the propagation can be obtained making the inverse Fourier transform of equation 2.56:

$$E(x, y, d) = \int_{-\infty}^{\infty} \int_{-\infty}^{\infty} \tilde{E}(\nu_x, \nu_y, d) e^{-2i\pi(\nu_x x + \nu_y y)} d\nu_x d\nu_y. \tag{2.57}$$

In order to use this method for a computer simulation, we need to consider that the optical field is not a continuous but a discrete function. So the integrals will become sums over a discrete 2D grid and the multiplications are meant as element by element multiplications of two matrices. It is important to highlight the FFT requires square grids with the number of elements for each side being a power of 2 [65]. The reason for this condition can be explained through the Danielson-Lanczos Lemma.

In 1942 Gordon Danielson and Cornelius Lanczos showed that a discrete FFT of length N can be written as the sum of two FFT of length N/2 each. This lemma is of great importance for digital computing since it can be used recursively reducing the computation time. But in order to be able to do that it is necessary that the number of elements will always be even at each iteration and this can be guaranteed by using as number of elements a power of two. [66]

2.3.2 Realistic optics and wavefront distortion

One of the most important features of OSCAR is the possibility to simulate realistic optical elements, e.g. optics with curvature or surface profile defined by the user. The method used to calculate the wavefront distortion is the same in both cases. In fact once we have defined the surface profile of the optics, the calculation is done pixel by pixel, despite the fact that the surface has a perfect shape or not. We will see now in detail how this calculation is made.

The mirror surface curvature or imperfections cause a difference in the optical path of the beam. In order to calculate this difference, consider a frame of reference (x, y) with the origin in the centre of the mirror, which has a radius of curvature R_c. The change in the value of the *sagitta* in each point will be

$$\Delta s(x, y) = R_c - \sqrt{R_c^2 - (x^2 + y^2)} \tag{2.58}$$

and the difference of path length will simply be twice this value.

From this value the wavefront distortion can be evaluated considering that this change in the optical path will add a phase shift in the original field. So the field affected by this distortion can be described performing the following calculation pixel by pixel

$$E(x, y) = E_0(x, y)\, e^{-2ik\,\Delta s(x,y)}. \tag{2.59}$$

2.3.3 Clipping and round trip loss

With the term clipping loss we mean the loss that occurs in a cavity due to the finite size of the mirrors [64]. It is always present in a cavity since a gaussian beam has by definition an infinite wavefront area, but usually the beam radius is chosen much smaller than the mirror radius and then it can be neglected. On the other side, it becomes important when other mechanisms occur in the cavity, like scattering or generation of higher order modes.

The clipping loss is found considering that, for the energy conservation law, the sum of all the output powers and the loss must be equal to the input power, i.e. [67]

$$P_{in} = P_r + P_t + P_{lost}, \tag{2.60}$$

where P_{in} is the incidence power, P_r is the reflected power, P_t is the transmitted power and P_{lost} is the lost power, as shown in figure 2.7. Dividing the previous equation for the

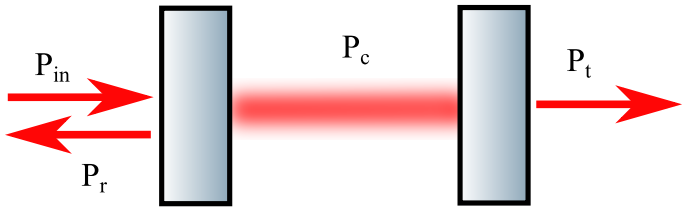

Figure 2.7: Drawing of a cavity where we show the definition of incidence power P_{in}, reflected power P_r, circulating power P_c, and transmitted power P_t, used for the calculation of the clipping loss.

circulating power P_c we obtain

$$\begin{aligned}
\frac{\left(1-r_1r_2\sqrt{1-\mathscr{L}}\right)^2}{t_1^2} &= \frac{\left(r_1-r_2\sqrt{1-\mathscr{L}}\right)^2}{t_1^2} + t_2^2 + \frac{P_{lost}}{P_c} \\
\frac{1-r_1^2-r_2^2+r_1^2r_2^2+\left(r_2^2-r_1^2r_2^2\right)\mathscr{L}}{t_1^2} &= t_2^2 + \frac{P_{lost}}{P_c} \\
\frac{\left(1-r_1^2\right)\left(1-r_2^2\right)+r_2^2\left(1-r_1^2\right)\mathscr{L}}{1-r_1^2} &= t_2^2 + \frac{P_{lost}}{P_c} \\
\left(1-r_2^2\right)+r_2^2\mathscr{L} &= t_2^2 + \frac{P_{lost}}{P_c},
\end{aligned} \tag{2.61}$$

where r is the amplitude reflectivity and t the amplitude transmissivity of the cavity input mirror (subscript 1) and end mirror (subscript 2) and $\mathscr{L}$ is the total loss at each round trip, which will be then

$$\mathscr{L} = \frac{P_{lost}}{r_2^2 P_c} = \frac{P_{in}-P_r-P_t}{r_2^2 P_c} \approx \frac{P_{in}-P_r-P_t}{P_c} \tag{2.62}$$

since the factor r_2^2 in the denominator is usually close to one.

We can also calculate the loss projected on the TEM00 mode

$$L_{00} = \frac{P_{in}-P_r^{00}-P_t^{00}}{P_c}, \tag{2.63}$$

where P_r^{00} and P_t^{00} are the powers in the TEM00 mode of the reflected and transmitted fields. In this way we take into account, apart from the clipping loss due to the finite size of the mirrors, also the loss due to the coupling due to the generation of higher order modes. In this case we will talk about round trip loss, i.e. the total loss that we have at each round trip [68].

2.3.4 Fundamental functions

In order to be able to perform simulations of a cavity, we first need to define its necessary feature, like the input field, the mirrors and the shape and the length of the cavity itself. In this section we will describe the fundamental functions used to do that. These functions are used to define new classes of objects that OSCAR introduce in order to simplify the calculation.

`Grid(Num_point,Length)`

Before performing any simulation, we need to define the grid, setting the number of points `Num_point` and the physical size `Length` of each side. It will be used for both the mirrors and the fields wavefront and it defines the resolution of the calculation. So it is important to choose a number of points high enough to avoid to lose any information, but not too high that entails a very long computational time. The better solution is to define a different grid for each simulation, finding a good compromise between the resolution needed for that particular simulation and a reasonable running time of the code. A wrong choice of the resolution, for example, could cause aliasing, which will entail an underestimation of the loss [65].

It is important to remember that the number of points must always be a power of two, as explained in section 2.3.1.

The output of this function will be an object of the class *Grid* with the following properties:

```
      Num_point:  512
         Length:  1
           Step:  0.0020
  Half_num_point:  256
         Vector:  [1x512 double]
           Axis:  [1x512 double]
       Axis_FFT:  [1x512 double]
           D2_X:  [512x512 double]
           D2_Y:  [512x512 double]
      D2_square:  [512x512 double]
           D2_r:  [512x512 double]
       D2_FFT_X:  [512x512 double]
       D2_FFT_Y:  [512x512 double]
```

where we have used as an example 512 point over a length of 1 metre. Apart of these two values, the function have calculated and stored in the object some properties useful for the simulations. Specifically we have

- `Step` is the resolution, i.e. the physical size of one pixel, given by the ratio of the length and the number of points;
- `Half_num_point`, as the name suggests, is simply half the number of points;
- `Vector` is an array with values from 1 to `Num_point`;
- `Axis` is a vector representing the x and y physical coordinates (in metres), from `-Length/2` to `Length/2`, so centred in zero, and it is calculated as

$$\texttt{Axis} = -\frac{\texttt{Length}}{2} + \frac{\texttt{Step}}{2} + \texttt{Vector} \cdot \texttt{Step}; \tag{2.64}$$

- `Axis_FFT` are the spatial frequency coordinates calculated as

$$\texttt{Axis\_FFT} = -\frac{1}{2\texttt{Step}} + \texttt{Vector} \cdot \texttt{Step}; \tag{2.65}$$

- `D2_X` and `D2_Y` are the grids of the coordinates x and y defined in `Axis`;
- `D2_square` is a 2D matrix with the square of the distances from the centre of each point, so

$$\texttt{D2\_square} = \texttt{D2\_X}^2 + \texttt{D2\_Y}^2 \tag{2.66}$$

- `D2_r` is the square root of `D2_square`, so it is the distance of each point from the centre;
- `D2_FFT_X` and `D2_FFT_Y` are the grids of the spatial frequencies coordinates.

`E_Field(Grid,`*`options`*`)`

This function is used to defined the electromagnetic field. There are two mandatory parameters: the first is an object of the class *Grid*, which is defined as described above, and the second could be either the waist radius[3] , the beam size and the radius of curvature or the waist radius and the distance from the waist or the complex radius of curvature q, defined as [54]

$$\frac{1}{q} = \frac{1}{R} - i\frac{\lambda}{\pi w_0^2} \tag{2.67}$$

with R the radius of curvature, λ the wavelength and w_0 the waist radius. In this way, if no other options are set, a gaussian beam is created.

Additionally other optional parameters can be added, like the power (otherwise set to 1 W by default) and the mode order (otherwise set to the fundamental mode).

[3]The waist radius of Gaussian beam is defined as the minimum beam radius, which occurs where the radius of curvature of the wavefront is zero [54].

The objects of the class *Field* will have the following properties:

```
             Grid  :  [1x1 Grid]
            Field  :  [512x512 double]
        Field_SBl  :  []
        Field_SBu  :  []
 Refractive_index  :  1
       Wavelength  :  1.0640e-06
 Frequency_Offset  :  0
        Mode_name  :  'HG 0 0'
           k_prop  :  5.9052e+06
```

where

- `Field` is a 2D matrix with the values of the field in each point;
- `Field_SBl` and `Field_SBu` are the lower and upper sidebands (they will be defined only in some simulations);
- `Refractive_index` is the refractive index of the medium set to 1 by default;
- `Wavelength` is the laser wavelength set to 1064 nm by default;
- `Frequency_Offset` is the frequency of the sidebands;
- `Mode_name` is the family (HG or LG) and order of the mode;
- `k_prop` is the laser wavenumber, i.e. $2\pi/$`Wavelength`.

`Interface(Grid)`

This function is used to create an interface between two media. The only required parameter is an object of the class *Grid*. In this way a flat, infinite interface with a power transmissivity of 0.1 is defined. However it is possible to change these features setting the optional parameters like radius of curvature, the diameter, the transmissivity, the loss and the angle of incidence of the input beam.

The properties of an object of the class *Interface* are:

```
    Grid  :  [1x1 Grid]
 surface  :  [512x512 double]
    mask  :  [512x512 double]
       T  :  0.1
       L  :  0
      n1  :  1
      n2  :  1.4500
       t  :  0.0000 + 0.3162i
       r  :  0.9487
```

where

- `surface` is a 2D matrix with the height of the surface in each point;
- `mask` is a 2D matrix with only 1 and 0 that describe the aperture of the optic;
- `T` is the power transmissivity, set by default to 0.1;
- `L` is the loss, set by default to zero;
- `n1` and `n2` are the refractive index of the two media (set as default to 1 and 1.45, i.e. air and silica);
- `t` and `r` are the amplitude transmissivity and reflectivity respectively.

If needed is also possible to define thick substrates using the class *Mirror*. However, since we will not use it for our simulations, we will not talk about it.

`Cavity1(I_input,I_end,Length,Laser_in)` and `CavityN(I_array,d_array,Laser_in)`

Once we have defined the grid, the input field and the interfaces, we are able to define the cavity. The simplest option is the linear cavity, which is defined by the function `Cavity1`. In this case we just have to put as the function options the two objects of the class *Interface* interface `I_input` and `I_end`, the length of the cavity `Length` and an object of the class *E_Field* (`Laser_in`), that represent the input field.

If needed it is also possible to define more complex cavities, with an arbitrary number of mirrors. In this case the function `CavityN` must be used, with the input variables an array `I_array` with all the interfaces, an arrays `d_array` with the distances between the mirrors and the input field `Laser_in`. Setting appropriate values of the distance between the mirrors in the array `d_array` and the angles of incidence of the beams in the options of each interface it is possible to define a cavity with any geometrical shape.

The properties of this two class are similar: for `Cavity1` the output will be an object with the following properties

```
                I_input  :  [1x1 Interface]
                  I_end  :  [1x1 Interface]
                 Length  :  1
               Laser_in  :  [1x1 E_Field]
    Laser_start_on_input  :  0
         Resonance_phase  :  []
   Cavity_scan_all_field  :  []
       Cavity_scan_param  :  [1000 500 2.0000e-09 1000]
      Cavity_phase_param  :  200
           Cavity_scan_R  :  []
          Cavity_scan_RZ  :  []
           Cavity_EM_mat  :  []
         Propagation_mat  :  [1x1 Prop_operator]
              Field_circ  :  []
               Field_ref  :  []
             Field_trans  :  []
       Field_reso_guess  :  []
               Loss_RTL  :  []
```

and for `CavityN` we have

```
                I_array  :  [1x3 Interface]
                d_array  :  [1 0.5000 1]
              Nb_mirror  :  3
               Laser_in  :  [1x1 E_Field]
    Laser_start_on_input  :  1
         Resonance_phase  :  []
   Cavity_scan_all_field  :  []
       Cavity_scan_param  :  [1000 500 2.0000e-09]
      Cavity_phase_param  :  100
           Cavity_scan_R  :  []
          Cavity_scan_RZ  :  []
           Cavity_EM_mat  :  []
  Propagation_mat_array  :  [1x3 Prop_operator]
       Field_reso_guess  :  []
             Field_circ  :  []
              Field_ref  :  []
            Field_trans  :  []
               Loss_RTL  :  []
```

As we can see the only differences between the two classes are the first three properties, because we have the input and end interface and the length of the cavity in the first case and the array with the interfaces, the array of the distances and the number of mirrors in the second one. Furthermore, most of other properties are empty vectors that will be fill during the simulations. We will see now in details what are all these properties:

- `Laser_start_on_input` is a logical value (1 for true and 0 for false) which specifies where the input field is defined;
- `Resonance_phase` is a complex number used to adjust the phase and bring the cavity on resonance;
- `Cavity_scan_all_field` stores all the fields after each round trip;
- `Cavity_scan_param` is an array with the number of points used for `Cavity_scan_R`, the number of points for `Cavity_scan_RZ`, the span of the zoom and the max number of iteration in case of high finesse cavity;
- `Cavity_phase_param` is the number of roundtrips used to find the resonance;
- `Cavity_scan_R` and `Cavity_scan_RZ` are the cavity circulating power scan over one FSR[4] and the zoom of the scan around the resonance frequency;
- `Cavity_EM_mat` is the kernel for one round trip in the cavity (it is used to calculate the eigen modes);
- `Propagation_mat` and `Propagation_mat_array` describe the propagation rules of the field in the cavity through a new class of objects introduced by OSCAR and called `prop_operator`;
- `Field_reso_guess` is a first approximation of the cavity resonant field used for the calculation of the resonance phase of the cavity;
- `Field_circ`, `Field_ref` and `Field_trans` are the circulating, reflected and transmitted fields respectively;
- `Loss_RTL` is the round trip loss.

[4]The free spectral range (FSR) is defined as the frequency difference between two consecutive intensity maxima (or minima) and it is equal to $c/(2L)$, with L the length of the cavity [54].

2.4 Conclusions

In this chapter we described the tools and methods that are used to obtain the results shown in the next chapters for the calculation of the quantum noise and for the analysis of the mirror surfaces. Specifically, in the first part we introduced a new formalism, called two-photon formalism, which is used for the calculation of the quantum noise. In the second part of the chapter, then, we described how the measurements of the mirror surface can be done and analysed. Finally we have given an overview of the MATLAB® package OSCAR, which is a code that simulates the behaviour of a cavity with arbirtrary mirror surface profiles. This code is used for the simulations of the cavity with the aim to estimate the optical loss as a function of the mirror surface imperfections and to derive the surface requirements of the arm cavity mirrors of the Glasgow Sagnac proof-of-concept experiment described in the next chapter.

Chapter 3

Speed meters as sub-SQL interferometers

In this chapter we introduce the concepts of the standard quantum limit (SQL) and quantum non-demolition (QND) measurements, which represent respectively a limitation in the quantum measurements and a possible way-out to this limitation, which can be applied to the gravitational wave detectors. It will be shown that an example of QND observable is the velocity (or momentum) and then measuring the speed instead of the position of test masses in gravitational wave detectors can reduce the quantum noise.

At the end of the chapter we will describe the features of the Glasgow Sagnac speed meter (SSM) proof-of-concept experiment, which has the purpose to asses the validity of the theoretical predictions and then the quantum noise of a SSM is actually lower than an equivalent Michelson.

3.1 Linear quantum measurements

The description of a linear quantum measurement can be obtained considering the scheme shown in figure 3.1, where we have a probe mass on which a force G, that we want to measure, is acting. The measurement of the mass motion[1] $\hat{x}$ due to this force is done through a generic meter or detector (for gravitational wave detection it is the interferometer). The force $\hat{F}$ represents the back-action force, i.e. the radiation pressure fluctuations. Furthermore, the meter will have also an additional readout noise $\hat{O}_{fl}$, i.e. the shot noise.

The Hamiltonian that describes the system is given by the sum of the Hamiltonian of the probe $\hat{H}_P$, the Hamiltonian of the detector $\hat{H}_D$ and an interaction term $V(t) = -\hat{x}\left(\hat{F} + G(t)\right)$,

[1] The hat symbol (ˆ) is used to denote quantum operators.

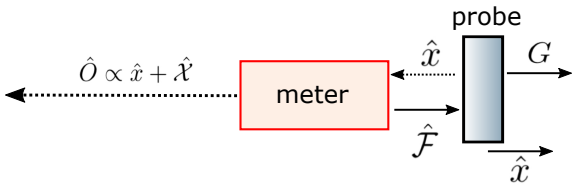

Figure 3.1: Schematic drawing of a linear measurement of the motion due to a force G of a probe mass, through a generic meter. The output signal will include the displacement $\hat{x}$ and the measurement noise $\hat{\chi}$.

i.e.

$$\hat{H}(t) = \hat{H}_P + \hat{H}_D + V(t). \tag{3.1}$$

The evolution in time of the readout observable $\hat{O}$, the back-action force $\hat{F}$ and the probe displacement $\hat{x}$ can be found using the Heisenberg operators[2] and they are found to be [50, 70]

$$\hat{O}(t) = \hat{O}^{(0)}(t) + \int_{t0}^{t} dt'\, \chi_{OF}(t-t')\hat{x}(t'), \tag{3.2}$$

$$\hat{F}(t) = \hat{F}^{(0)}(t) + \int_{t0}^{t} dt'\, \chi_{FF}(t-t')\hat{x}(t'), \tag{3.3}$$

$$\hat{x}(t) = \hat{x}^{(0)}(t) + \int_{t0}^{t} dt'\, \chi_{xx}(t-t')\left(G(t') + F(t')\right), \tag{3.4}$$

where the so called susceptibilities χ are defined through the Heisenberg equations of motion as

$$\chi_{OF}(t-t') = \frac{i}{\hbar}\left[\hat{O}^{(0)}(t), \hat{F}^{(0)}(t')\right], \tag{3.5}$$

$$\chi_{FF}(t-t') = \frac{i}{\hbar}\left[\hat{F}^{(0)}(t), \hat{F}^{(0)}(t')\right], \tag{3.6}$$

$$\chi_{xx}(t-t') = \frac{i}{\hbar}\left[\hat{x}^{(0)}(t), \hat{x}^{(0)}(t')\right], \tag{3.7}$$

with the superscript (0) denoting the free evolution of the observable, i.e. without coupling between the probe and the detector. Here the probe displacement $\hat{x}$ is composed by three terms: the motion due to the signal force $x_s(t)$, the displacement due to the back-action force that the meter exerts on the probe $x_{b.a.}(t)$ and the free evolution of the probe $\hat{x}^{(0)}(t)$.

[2]In the Heisenberg representation the state function do not depend explicitly on time and all the time dependences are given by the operators corresponding to physical variables [69].

Defining the spectral susceptibility as

$$\chi_{AB}(\Omega) = \int_0^\infty d\tau\, \chi_{AB}(\tau)\, e^{i\Omega\tau}, \tag{3.8}$$

equations 3.2, 3.3 and 3.4 can be rewritten in frequency domain as

$$\hat{O}(\Omega) = \hat{O}^{(0)}(\Omega) + \chi_{OF}(\Omega)\hat{x}(\Omega), \tag{3.9}$$

$$\hat{F}(\Omega) = \hat{F}^{(0)}(\Omega) + \chi_{FF}(\Omega)\hat{x}(\Omega), \tag{3.10}$$

$$\hat{x}(\Omega) = \hat{x}^{(0)}(\Omega) + \chi_{xx}(\Omega)\left(G(\Omega) + F(\Omega)\right), \tag{3.11}$$

which gives[3]

$$\hat{O}(\Omega) = \hat{O}^{(0)}(\Omega) + \frac{\chi_{xx}(\Omega)\chi_{OF}(\Omega)}{1 - \chi_{xx}(\Omega)\chi_{FF}(\Omega)}\left(G(\Omega) + \hat{F}^{(0)}(\Omega)\right), \tag{3.12}$$

$$\hat{F}(\Omega) = \frac{1}{1 - \chi_{xx}(\Omega)\chi_{FF}(\Omega)}\left(\chi_{xx}(\Omega)\chi_{FF}(\Omega)G(\Omega) + \hat{F}^{(0)}(\Omega)\right), \tag{3.13}$$

$$\hat{x}(\Omega) = \frac{\chi_{xx}(\Omega)}{1 - \chi_{xx}(\Omega)\chi_{FF}(\Omega)}\left(G(\Omega) + \hat{F}^{(0)}(\Omega)\right). \tag{3.14}$$

We can define now two new observables $\hat{\chi}$ and $\hat{\mathcal{F}}$ as

$$\hat{\chi}(\Omega) \equiv \frac{\hat{O}^{(0)}(\Omega)}{\chi_{OF}(\Omega)}, \tag{3.15}$$

$$\hat{\mathcal{F}}(\Omega) \equiv \hat{F}^{(0)}(\Omega) - \frac{\chi_{FF}(\Omega)}{\chi_{OF}(\Omega)}\hat{O}^{(0)}(\Omega). \tag{3.16}$$

The first of these two new variables, $\hat{\chi}(\Omega)$, represents the output fluctuation that does not depend on the probe, which in the gravitational wave detectors is identified as the shot noise. The second one, $\hat{\mathcal{F}}(\Omega)$, on the other side, represents the response of the probe to the back-action force, i.e. the radiation pressure noise. Furthermore, we have that the doubled-sided spectral densities of these two variables are defined as

$$S_{\chi\chi}(\Omega) = \int_{-\infty}^{\infty} dt\, \langle \hat{\chi}(t) \circ \hat{\chi}(t') \rangle\, e^{i\Omega(t-t')}, \tag{3.17}$$

$$S_{\mathcal{F}\mathcal{F}}(\Omega) = \int_{-\infty}^{\infty} dt\, \langle \hat{\mathcal{F}}(t) \circ \hat{\mathcal{F}}(t') \rangle\, e^{i\Omega(t-t')}, \tag{3.18}$$

[3]Here the terms $\hat{x}^{(0)}(\Omega)$ can be omitted because it only depends on the initial value of position and momentum of the probe.

$$S_{\chi F}(\Omega) = \int_{-\infty}^{\infty} dt \, \langle \hat{\chi}(t) \circ \hat{F}(t') \rangle \, e^{i\Omega(t-t')}, \tag{3.19}$$

and they must satisfy the Schrödinger-Robertson uncertainty relation:

$$S_{\chi\chi}(\Omega) S_{FF}(\Omega) - \left| S_{\chi F}(\Omega) \right|^2 \geq \frac{\hbar^2}{2}, \tag{3.20}$$

which is the equivalent of the Heisenberg uncertainty principle for correlated variables.

3.2 Standard quantum limit

The results described in the previous section, and specifically the condition set by equation 3.20, imply a lower limit in the value of the shot noise and the radiation pressure noise. In case of the two noise sources are non-correlated the condition becomes

$$S_{\chi\chi}(\Omega) S_{FF}(\Omega) \geq \frac{\hbar^2}{2}, \tag{3.21}$$

since $S_{\chi F}(\Omega) = 0$.

Furthermore, under this conditions, $\hat{\chi}$ and $\hat{F}$ are simply the fluctuation of the displacement and the force and then we can rename their spectral density as

$$S_{\chi\chi}(\Omega) = S_x(\Omega), \qquad S_{FF}(\Omega) = S_F(\Omega). \tag{3.22}$$

Using this condition is possible to minimise the quantum noise in the measurements, i.e. the sum of these two noises. In order to do that, it is useful to normalise the output described in equation 3.12 by the unit signal. However there are different options depending on which aspect of the signal we want to consider. The most common normalisation for gravitational wave detectors are the follows:

- *F-normalisation*: in this case we consider as signal the force of the gravitational wave;
- *x-normalisation*: we consider as signal the mirror motion due to the gravitational wave force;
- *h-normalisation*: the signal considered is the gravitational wave amplitude.

Let first consider the *F-normalisation*. In this case the coefficient of $G(\Omega)$ will be equal to 1

and the output described in equation 3.12 becomes [50]

$$\begin{aligned}\hat{O}^F(\Omega) &= \frac{1-\chi_{FF}(\Omega)\chi_{xx}(\Omega)}{\chi_{OF}(\Omega)\chi_{xx}(\Omega)}\,\hat{O}(\Omega)\\ &= \frac{\hat{O}^{(0)}(\Omega)}{\chi_{OF}(\Omega)\chi_{xx}(\Omega)} + \left(\hat{F}^{(0)}(\Omega) - \frac{\chi_{FF}(\Omega)}{\chi_{OF}(\Omega)}\,\hat{O}^{(0)}(\Omega)\right)\\ &= \frac{\hat{\chi}(\Omega)}{\chi_{xx}(\Omega)} + \hat{\mathcal{F}}(\Omega) + G(\Omega)\end{aligned} \tag{3.23}$$

and then its power spectral density will be

$$S^F(\Omega) = \frac{S_x(\Omega)}{\left|\chi_{xx}(\Omega)\right|^2} + S_F(\Omega) = \frac{S_x(\Omega)}{\left|\chi_{xx}(\Omega)\right|^2} + \frac{\hbar^2}{4S_x(\Omega)}. \tag{3.24}$$

The minimum of the sum of these two noises is called standard quantum limit (SQL) and is achieved when they are equal, i.e.

$$S^F_{SQL}(\Omega) = \frac{\hbar}{\left|\chi_{xx}(\Omega)\right|}, \tag{3.25}$$

with

$$S_x(\Omega) = \frac{\hbar}{2}\left|\chi_{xx}(\Omega)\right|, \qquad S_F(\Omega) = \frac{\hbar}{2\left|\chi_{xx}(\Omega)\right|}. \tag{3.26}$$

The relations between the SQL in the other normalisations is given by the following equations

$$S^h_{SQL}(\Omega) = \frac{4S^F_{SQL}(\Omega)}{M^2L^2\Omega^4}, \tag{3.27}$$

$$S^x_{SQL}(\Omega) = \left|\chi_{xx}(\Omega)\right|^2 S^F_{SQL}(\Omega), \tag{3.28}$$

where M is the mass and L the cavity length.

The explicit form of the noises, and then of the SQL, change depending on the properties of the system. We can consider for example two common cases: the free mass and the harmonic oscillator. In the first case we have

$$\chi_{xx} = -\frac{1}{M\Omega^2}, \tag{3.29}$$

$$S^F_{SQL}(\Omega) = \hbar M\Omega^2, \tag{3.30}$$

$$S^x_{SQL}(\Omega) = \frac{\hbar}{M\Omega^2}, \tag{3.31}$$

$$S^h_{SQL}(\Omega) = \frac{2\hbar}{ML^2\Omega^2}, \tag{3.32}$$

while in the latter we obtain

$$\chi_{xx} = -\frac{1}{M(\Omega_0^2 - \Omega^2)}, \tag{3.33}$$

$$S^F_{SQL}(\Omega) = \hbar M|\Omega_0^2 - \Omega^2|, \tag{3.34}$$

$$S^x_{SQL}(\Omega) = \frac{\hbar}{M|\Omega_0^2 - \Omega^2|}, \tag{3.35}$$

$$S^h_{SQL}(\Omega) = \frac{4\hbar|\Omega_0^2 - \Omega^2|}{ML^2\Omega^4}, \tag{3.36}$$

where Ω_0 is the oscillator mechanical eigenfrequency.

3.3 Speed meters

The SQL, described in the previous section, is a fundamental limitation in quantum measurements. However, it is important to remark that it is a direct consequence of the Heisenberg uncertainty principle that is valid only for conjugate variables.

The SQL, in fact, can be avoided through the quantum non-demolition (QND) measurements, defined in 1980 by Braginsky *et al.* [71]. A physical quantity A is said to be a QND observable if and only if it commutes with itself when measurements are made in two different times t_1 and t_2, i.e.

$$[A(t_1), A(t_2)] = 0, \tag{3.37}$$

and if this is true for all times. This condition is satisfied if the observable A is conserved during the system evolution, i.e. $\frac{dA}{dt} = 0$. This means that energy and momentum are QND observables, but position is not. So a way to avoid SQL is to make measurements of QND observables.

There are some observables that are intrinsically QND variables and than they can be measured without being limited by the SQL. An example of such kind of observables is the momentum (or the speed), because it is well known that, since it is a conserved quantity, is not affected by the Heisenberg principle [72]. This can be applied also in gravitational wave detectors in order to increase the sensitivity reducing the radiation pressure noise.

The first attempt to convert a Michelson interferometer for gravitational wave detection in a speed meter was done in 2000 by Braginsky *et al.* [73] and after that many other approaches have been theorised (cf. for example [74–76]). However in 2003 Chen showed

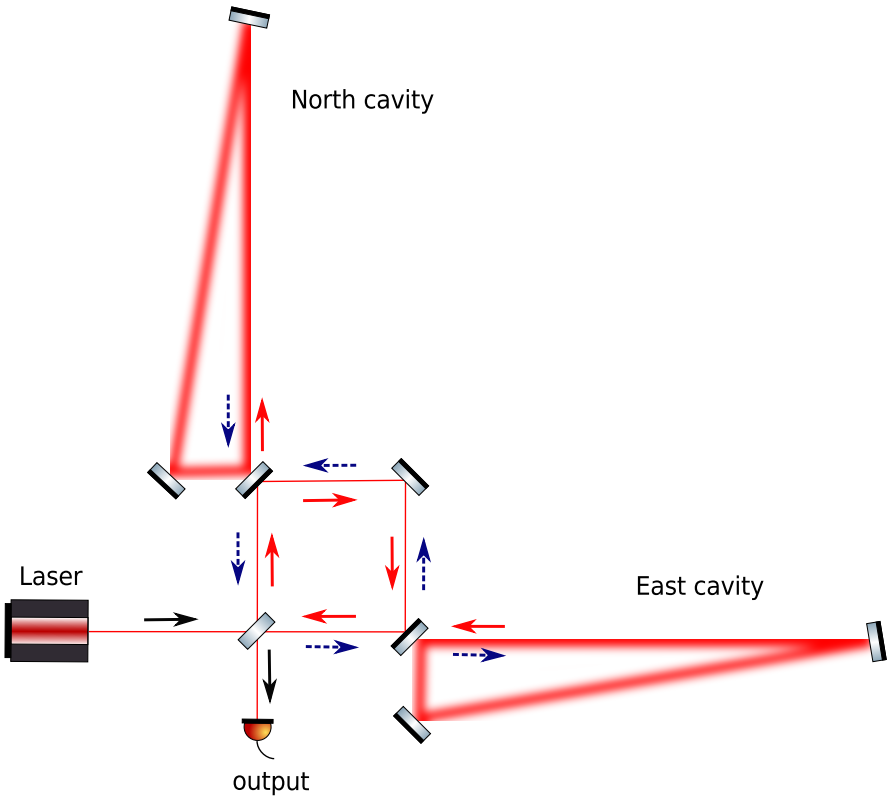

Figure 3.2: Optical layout of a Sagnac interferometer with triangular cavities.

theoretically that a *zero area* Sagnac interferometer is a speed meter as it is, without any change in the basic configuration [77].

3.3.1 The Sagnac speed meter

The working principle of a Sagnac speed meter (SSM) is based on the fact that in this configuration the two beams that come out from the beamsplitter will travel in both arms before being recombined again. We have in fact that the beam is split by the beamsplitter in two different beams: one goes into the North cavity and one into the East cavity. The first beam measures the positions of the mirror at time t and then goes into the East cavity and measures the position of the mirror at time $t+2\tau$, where τ is half the cavity roundtrip time. The second beam, instead, follows the reverse path, so it measure the position of the mirror of the East cavity at time t and the position of the mirror of the North cavity at time $t+2\tau$. So the measurements of the mirrors positions are made at different times and this means that the test mass velocity is actually measured. In figure 3.2 the layout of Sagnac interferometer with triangular arm cavities is shown. We will describe now in details how it works.

The phase shift of the clockwise propagating beam (R) and the counterclockwise (L) at the

output port are [77]

$$\delta\phi_R \sim x_N(t) + x_E(t+2\tau), \tag{3.38}$$

$$\delta\phi_L \sim x_E(t) + x_N(t+2\tau), \tag{3.39}$$

where x_N and x_E are the measurements of the displacements of the mirrors in the North and East cavity respectively. At the output port the amplitude of the beam is proportional to the difference of the phases of the two beams[4], i.e.

$$\delta\phi_R - \delta\phi_L \propto \left(x_N(t) - x_N(t+2\tau)\right) - \left(x_E(t) - x_E(t+2\tau)\right). \tag{3.40}$$

The two terms on the right hand side of the equation are simply the velocity of the test masses and then in this way the output will give a measurement of the speeds instead of the positions, as happens for the Michelson interferometer.

The reason why we need a *zero area* configuration can be explained considering that the Sagnac interferometer is sensitive to the rotation of the Earth, because the relative phase of the two beams depends on the angular velocity of the instrument (Sagnac effect). Specifically, the relative phase of the two beams is given by the following equation

$$\phi = \frac{4A}{c^2}\,\Omega\,\omega_p, \tag{3.41}$$

where A is the enclosed area, Ω is the angular frequency of the interferometer rotation and ω_p is the laser angular frequency. So the Sagnac effect can be suppressed with a *zero area* configuration, obtained when the total area enclosed in the beam path is zero, i.e. it travels in two equal cavities with opposite directions. However, in gravitational wave detectors, even if the rotation of the Earth could be considered negligible in the time span of one measurement, we still need a *zero area* configuration. From equation 3.41 we can see that any fluctuation of the area or the laser frequency could affect the relative phase of the beams. This means that also the laser frequency noise, the seismic noise and the beam misalignement can couple into optical phase noise, affecting the performance of the detector. An estimation of the noise due to these effects has been made, showing that it can be minimise using a *zero area* configuration [78].

A detailed calculation of the I/O relations and the quantum noise for a Sagnac interferometer with and without cavities will be shown in chapter 4.

[4] As we will see in chapter 4, for this particular configuration the output port will be the dark port, i.e. where we have the destructive interference between the two beams.

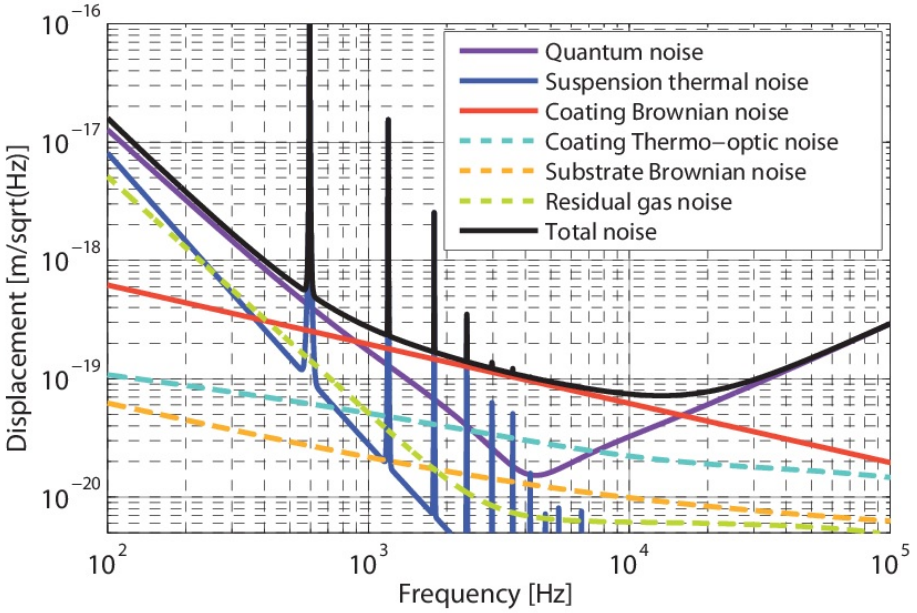

Figure 3.3: Expected noise budget of the Glasgow SSM. In the plot all the main sources of noise are included and, as we can see, the spectrum is dominated by quantum noise for frequencies between 100 and 800 Hz. Figure taken from [79].

3.4 The SSM proof-of-concept experiment

With the aim to prove experimentally the validity of the theory introduced by Chen, a proof-of-concept experiment has been designed and is currently in commissioning at the University of Glasgow [79, 80]. An input beam of 1.7 W with a wavelength of 1064 nm is used. Since the purpose of the experiment is to prove the reduction of radiation pressure noise compared to an equivalent Michelson, we need that the sensitivity of the interferometer is limited by quantum noise. In order to do that a cavity finesse of $\sim$ 8000, which gives an intra-cavity power of $\sim$ 5 kW and very small arm cavity mirrors have been chosen (as e can see from the noise budget plot shown in figure 3.3). In figure 3.4 a plot of the expected quantum noise limited sensitivity (red line) and total noise (orange line) of the Glasgow SSM compared with an equivalent Michelson (dark and light blue lines) are shown. The goal of the experiment is to reach a sensitivity better than the Michelson's, i.e. in the green area of the plot.

The whole system is placed in a vacuum chamber, with a stack of tables for seismic isolation, as shown in figure 3.5. The data acquisition and control of the Glasgow SSM is based on the Advanced LIGO Control and Data System (CDS) [81]. More information about the control system of the Glasgow SSM can be found in [82].

In this section we will give an overview of the main features of the experiment.

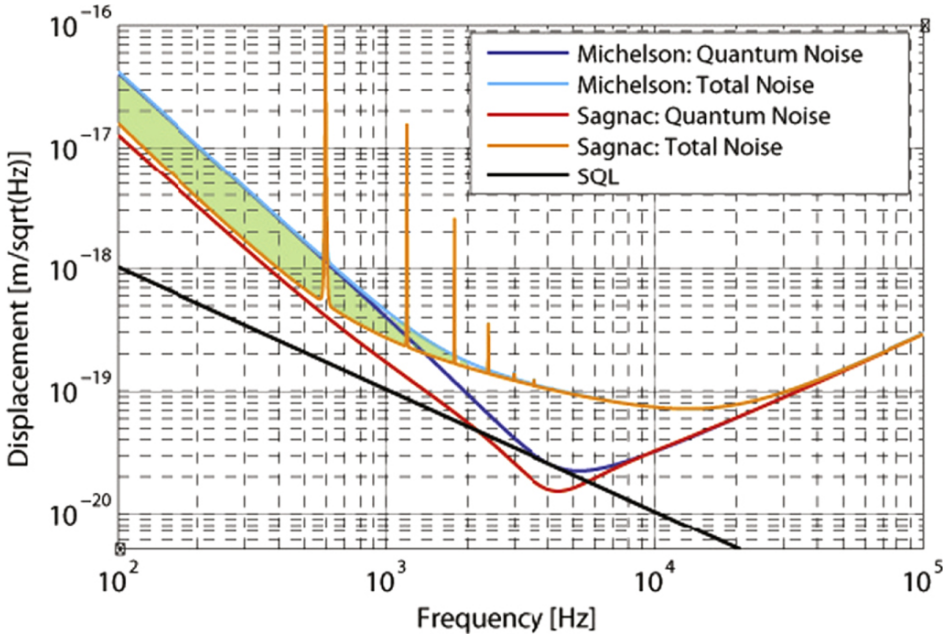

Figure 3.4: Plot of the expected sensitivity of the Glasgow SSM compared with an equivalent Michelson. The aim of the experiment is to reach a sensitivity in the green area of the plot, in order to prove that the radiation pressure noise is smaller than an equivalent Michelson. Figure taken from [79].

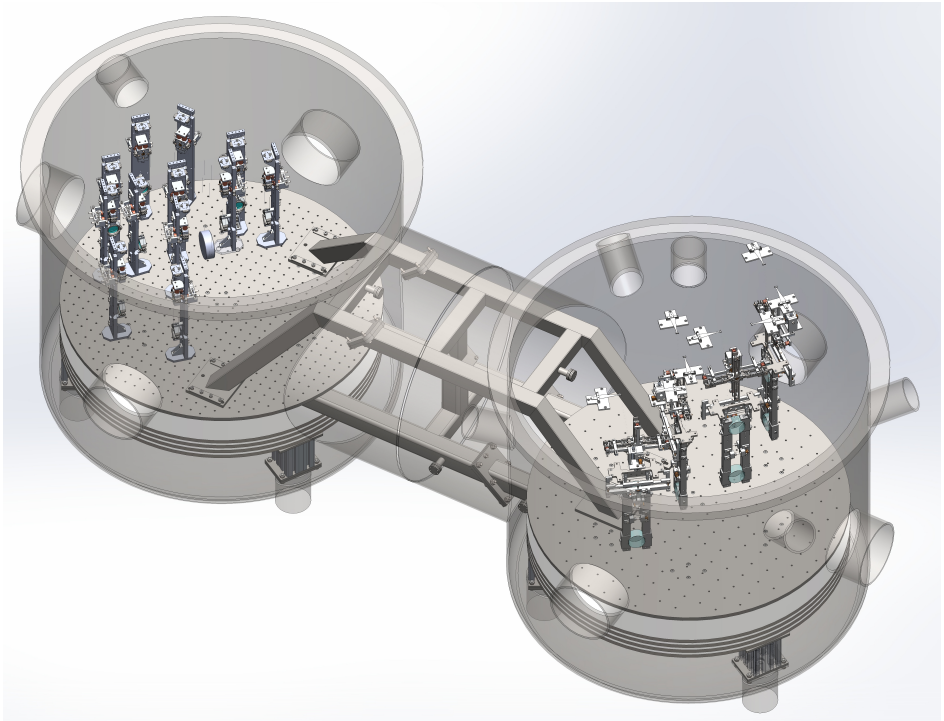

Figure 3.5: Image of the vacuum chamber used for the SSM experiment. It is composed by two tanks of 1 m diameter connected through a tube. In each tank there is a seismic isolation stack of tables connected to each other with a bridge structure.

3.4.1 Optical layout

The optical layout of the Glasgow SSM is shown in figure 3.6. The most important mirrors are

- M_{1a} and M_{1b} are the input test masses (ITM) of the cavities a and b, respectively. They are 1 g mirrors with a diameter of 1 cm and a curvature of 7.91 m[5]. The value of the radius of curvature has been chosen in order to avoid the resonance of higher order modes in the cavities, as shown in figure 3.7.
- M_2 and M_3 are the cavities end test masses (ETM) mirrors, which are 100 g mirrors with 5 cm diameter. More details of the ITM and ETM can be found in chapter 5 and Appendix C.
- M_6 is the main beamsplitter.
- M_9 is a curved steering mirror and its purpose is to mode match the cavities.
- M_{16} is the beamsplitter of the balanced homodyne detector, which will be described in section 3.4.3.

More information about the optical layout can be found in [83].

3.4.2 Suspensions and actuation

In order to have a quantum noise limited sensitivity all the other noises must be reduced as much as possible. Seismic noise is one of the most critical ones and this is the reason why all the mirrors will be suspended by multiple pendulum systems. Three different kind of suspensions are used:

- the auxiliary suspensions are two stages pendulum with coils actuation on the top mass and they will be used for all mirrors except for the arm cavity mirrors;
- the 100 g suspensions, which will be used for the four ETM, are triple pendulum with monolithic last stage and electrostatic actuators;
- the 1 g suspensions, used for the ITM, are four stages pendulums with monolithic last stage and switchable Eddy current damping [84].

More information about the suspensions used for the Glasgow SSM experiment can be found in [83].

[5]The value of the curvature reported here is that one established in the design [79], but it has been changed to 8 m during the progression of work, because of manufacturing difficulties (cf. section 5.3.2).

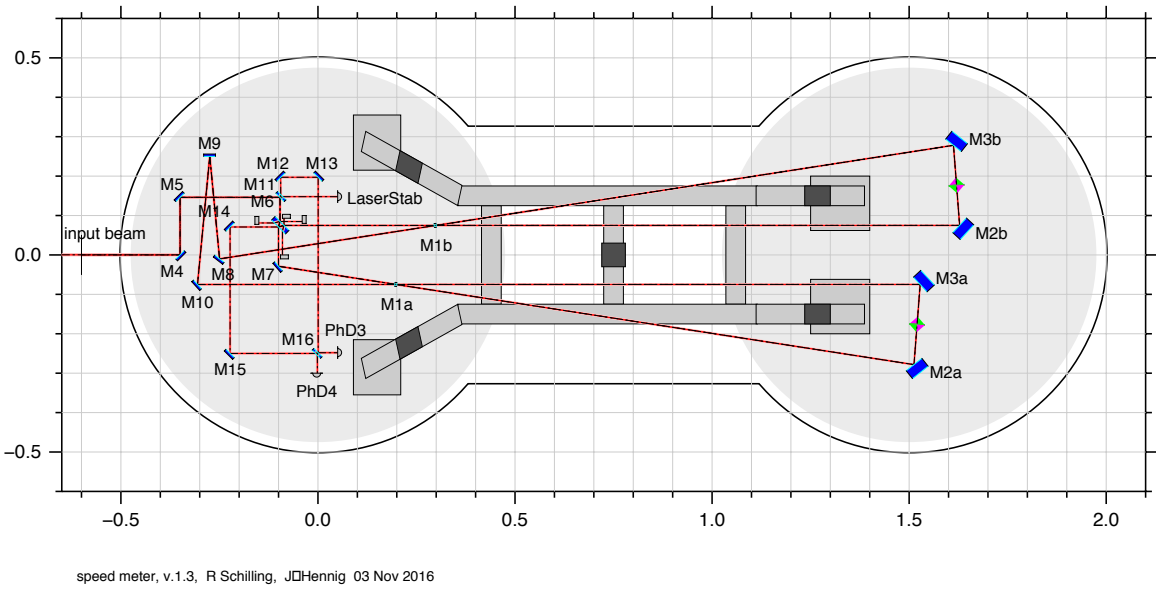

Figure 3.6: Layout of the Glasgow SSM experiment.

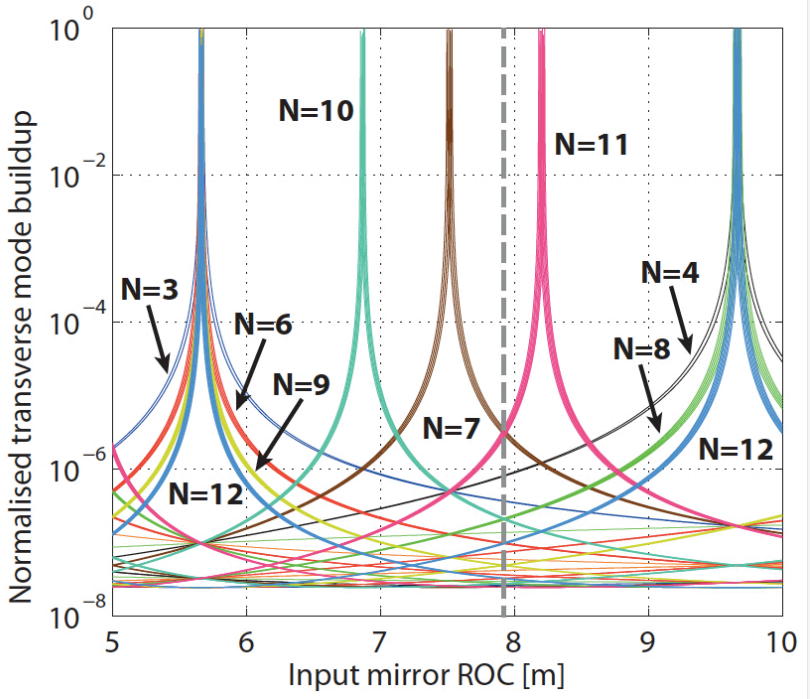

Figure 3.7: Normalised power buildup of the higher order modes inside the cavity as a function of the radius of curvature of the ITM, which has been chosen to be 7.91 m, in order to avoid the resonance of modes 7 and 11 (dashed grey line). Figure taken from [79].

3.4.3 Balanced homodyne readout

The output of the Glasgow SSM is read out using a balanced homodyne detector (BHD) [85]. In this kind of detector the output signal is overlapped with another laser beam called local oscillator (LO) through a 50:50 beamsplitter (M_{16}). If $\boldsymbol{a}$ is the LO and $\boldsymbol{b}$ the output signal, the two outputs from the beamsplitter will be

$$\boldsymbol{c}^\dagger\boldsymbol{c} = \frac{1}{2}\left[\boldsymbol{a}^\dagger\boldsymbol{a} + \boldsymbol{a}^\dagger\boldsymbol{b}\,\mathrm{e}^{-i\phi} + \boldsymbol{a}\boldsymbol{b}^\dagger\,\mathrm{e}^{i\phi} + \boldsymbol{b}^\dagger\boldsymbol{b}\right], \tag{3.42}$$

$$\boldsymbol{d}^\dagger\boldsymbol{d} = \frac{1}{2}\left[\boldsymbol{a}^\dagger\boldsymbol{a} - \boldsymbol{a}^\dagger\boldsymbol{b}\,\mathrm{e}^{-i\phi} - \boldsymbol{a}\boldsymbol{b}^\dagger\,\mathrm{e}^{i\phi} + \boldsymbol{b}^\dagger\boldsymbol{b}\right], \tag{3.43}$$

where the phase shift ϕ between the two signals is called homodyne angle. Both output signals $\boldsymbol{c}$ and $\boldsymbol{d}$ are then detected with high efficiently photodetectors and subtracted to each other in order to remove the DC part:

$$\boldsymbol{i}_- = \boldsymbol{c}^\dagger\boldsymbol{c} - \boldsymbol{d}^\dagger\boldsymbol{d} = \boldsymbol{a}^\dagger\boldsymbol{b}\,\mathrm{e}^{-i\phi} - \boldsymbol{a}^\dagger\boldsymbol{b}\,\mathrm{e}^{i\phi} + \boldsymbol{a}\boldsymbol{b}^\dagger\,\mathrm{e}^{-i\phi} - \boldsymbol{a}\boldsymbol{b}^\dagger\,\mathrm{e}^{i\phi}. \tag{3.44}$$

For the Glasgow SSM the output of the bright port of the main beamsplitter has been chosen as LO. It has been recently shown analytically that this choice can significantly reduce the laser fluctuations noise [86].

3.5 Conclusions

In this chapter we explained the concept of SQL, which is direct consequence of the Heisemberg uncertainty principle and then a fundamental limit in linear quantum measurements. However this limit can be surpassed with the introductionof QND variables, such as momentum (or speed). The use of speed meter instead of position meter can then increase the sensitivity of GW detectors, reducing the radiation pressure noise. We described in this chapter a proof-of-concept experiment that is underway at the University of Glasgow which has the aim to asses the validity of this theory.

We will explain in the next chapter how the quantum noise can be calculated for both position meters (like a Michelson interferometer) and speed meters (like a Sagnac interferometer), showing why in the second case we will have a lower radiation pressure noise. So the speed meter might be a valid alternerative for future generations of GW detectors, like ET. An example of the sensitivity of a speed meter with the same scale of ET will be shown in section 5.1, where we will also show how the loss, that has an important role in the performance of a speed meters, will affect the sensitivity of the Glasgow SSM and ET-LF.

Chapter 4

Introduction to quantum noise for lossless interferometers

In this chapter an introduction to the calculation of the quantum noise is shown. Quantum noise is one of the most dominant noises in interferometric gravitational waves detectors. It include noises due to two different effects: quantum radiation pressure and shot noise. We have already explained in chapter 3 the physical meaning and the consequences of these two effects for the sensitivity of interferometric gravitational wave detectors. In this chapter we will focus on how they can be evaluated mathematically and how the quantum noise limited sensitivity can be calculated for a few exemplary interferometer configurations.

In the first section we explain how the radiation pressure force can be calculated starting from the equation of motion of the mirror. We will see that, in order to calculate it, we need the equations of the output fields in terms of the input fields. So in the second section we show how these fields can be calculated and what are the input/output (I/O) relations for different interferometer configurations. All these calculations are made for lossless interferometer and then we will assume that all the mirrors have reflectivity equal to 1 (apart from the ITM when arm cavities are present). In the third section we will introduce the optical rigidity, which plays an important role for the radiation pressure contribution when we have to deal with detuned cavities. Finally in the last section we show how the quantum noise limited sensitivity of the interferometer is obtained.

The meaning of the symbols used and some definitions can be found in appendix A.

4.1 Radiation pressure force

Radiation pressure noise is the noise due to the amplitude fluctuations of the incident photons which cause a recoil of the mirror. The contribution of the radiation pressure in the

mirror motion is found from the equation of motion

$$m\ddot{x}(t) = F(t) + G(t), \tag{4.1}$$

which states that the total force acting on a mirror with mass m that makes it move by x is given by the sum of the radiation pressure force F and the signal force G.

We know that the radiation pressure force is given by the ratio between the power incident on the mirror and the speed of light, that can be written as [50]

$$\tilde{F}(t) = \frac{P_c}{c} = \frac{\hbar\omega_p}{2c}\,\mathcal{E}\,(t)^2 = \frac{\hbar\omega_p}{2c}\left(\boldsymbol{E} + \hat{\boldsymbol{e}}(t)\right)^2, \tag{4.2}$$

where the field $\mathcal{E}\,(t)$ is defined in equation 2.9 and then we have considered the field as the sum of the classical amplitude $\boldsymbol{E}$ and the quantum fluctuation $\hat{\boldsymbol{e}}(t)$.

This equation can be simplified keeping only the terms of the first order in the quantum fluctuation and performing the Fourier transform averaged over a time much shorter than the signal period and much longer than $1/\omega_p$:

$$\tilde{F}(\Omega) \approx \frac{\hbar\omega_p}{2c}\left(\boldsymbol{E}^\dagger\boldsymbol{E} + 2\boldsymbol{E}^\dagger\,\hat{\boldsymbol{e}}(\Omega)\right). \tag{4.3}$$

Furthermore we can ignore the first term because it is constant and so we are able to correct it adding an opposite force on the mirror. So we can write

$$\tilde{F}(\Omega) \approx \frac{\hbar\omega_p}{c}\boldsymbol{E}^\dagger\,\hat{\boldsymbol{e}}(\Omega). \tag{4.4}$$

Transforming the equation of motion in frequency domain we have

$$-m\Omega^2\tilde{x}(\Omega) = \tilde{F}(\Omega) + \tilde{G}(\Omega) \tag{4.5}$$

and splitting the mirror motion x into two terms: the motion due to the radiation pressure (which is noise and it can be calculated from the radiation pressure force $\tilde{F}^E(\Omega)$) and the motion due to signal (which is the one we want to measure) we have

$$\tilde{x}(\Omega) = \tilde{x}^{rp}(\Omega) + \tilde{x}^{GW}(\Omega) = \chi_E(\Omega)\tilde{F}^E(\Omega) + \tilde{x}^{GW}(\Omega), \tag{4.6}$$

where we have defined the mechanical susceptibility as

$$\chi(\Omega) = -\frac{1}{m\Omega^2}. \tag{4.7}$$

Replacing equation 4.4 in the I/O relations we are able to explicitly include the radiation

pressure contribution relative to each input field.

4.2 I/O relations

In this section we will show how the I/O relations of an interferometer are calculated. First we will do it for a simple Michelson configuration (without cavities) and then we will do the same for a simple Sagnac. After having shown the results for a single cavity, at the end of the section we will show the solution for a Michelson with linear arm cavities and a Sagnac with triangular cavities, a configuration similar to that one used for the Glasgow SSM proof-of-concept experiment described in chapter 3.

The method is similar for all cases, so we will show the full calculation only for the Michelson interferometer, since for the other cases it is easy to deduce following the same steps, which can be summarised as follow.

1. The first thing to do is to write the relations between all the fields involved using the optical transfer matrix that we showed in section 2.1.3. In our case we will assume that all the mirrors have reflectivity equal to 1, apart from the ITM for cases where the arm cavities are considered. Furthermore we are using the convention that the phases will not change in reflection, but only in transmission (by $\pi/2$), so the optical transfer matrix in equation 2.25 is just the identity matrix and then we have that the reflected field is equal to the incoming field. Of course this is not true for the beamsplitter, for which we have to write and solve the full transfer matrix.

2. Apart from the equations obtained from the transfer matrix we also need to consider other conditions that take into account the phase change due to the propagation. This is done considering that when a field $\mathcal{E}(t)$ propagates for a distance s, the value of the field in s will be $\mathcal{E}(t + s/c)$, which can be evaluated after the FFT, as described in the next point.

3. In order to solve the equations obtained we need to transform them in frequency domain. Since neither the reflectivity nor the transmissivity depends on time, this transformation is quite immediate for the relations obtained from the transfer matrix. For the equations that describe the propagation, on the other hand, we need a further step. The equation of the field in the position s, namely $\mathcal{E}(t + s/c)$, in frequency domain becomes

$$\hat{\mathbf{E}}(\omega)\, e^{2i\omega\frac{s}{c}} \approx \left(\mathrm{E} + \hat{\mathbf{e}}(\omega)\right)\left(1 + 2i\omega\frac{S}{c}\right) \approx \mathrm{E} + \hat{\mathbf{e}}(\omega) + 2i\omega\mathrm{E}\frac{S}{c}, \tag{4.8}$$

since for GW detectors we have $\omega \sim 10^{15}$ Hz and $s \sim 10^{-18}$ m.

4. At this point of the calculation it is useful to split the fields in a classical and a quantum fluctuation part, as described in 2.7, since they will have different roles in the quantum noise calculation.

5. For the quantum noise calculation we need to transform the results obtained so far in two-photon quadrature using the rule described in equation 2.11.

6. In order to obtained the final I/O relations, with both shot noise and radiation pressure noise explicitly included in the equations, we have to replace equation 4.6 in the I/O relations.

7. We have now obtained the I/O relations in two-photon quadrature formalism with the shot noise and radiation pressure transfer matrix explicitly expressed in the equations. So we are able to calculate the quantum noise, as we will describe in the next section. However, when arm cavities are present, a further step is required with the purpose to write the solutions in a more compact way. From the definition of the cavity bandwidth, we obtain that the transmissivity of the ITM can be written as a function of the arm half roundtrip time τ and the half-bandwidth γ, i.e. $T_{ITM} = 4\gamma\tau$. In this way we have all terms written as a function of τ and they can be expanded in Taylor series:

$$\begin{aligned} \sqrt{T_{ITM}} &= \sqrt{4\gamma\tau}, \\ \sqrt{R_{ITM}} &= \sqrt{1-4\gamma\tau} \approx 1 - 2\gamma\tau, \\ e^{2i\Omega\tau} &\approx 1 + 2i\Omega\tau. \end{aligned} \tag{4.9}$$

   Replacing these equations in the I/O relations, keeping only the first non-vanishing terms, we can rewrite the relations as a function of τ and γ.

In all these calculations we will consider as phase reference the phase of the intra-cavity fields. This is done because it makes the equations much more easier to write and much more clearer to understand, without changing in any way the outcome of the analysis. Of course this entails that the input fields have components in both quadratures.

4.2.1 Simple Michelson

The Michelson interferometer is probably the most famous and used interferometry configurations. It was invented by Albert Abraham Michelson in 1881 and it was first used to measure the speed of light in different directions, obtaining the first proof against the aether theory [87]. Because of its high potential in high precision measurements despite the

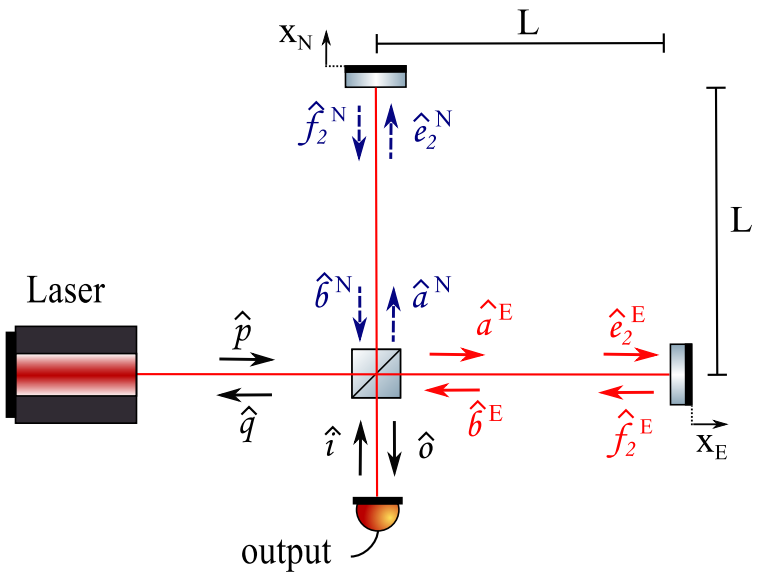

Figure 4.1: Simple Michelson interferometer.

simplicity of the configuration, it is largely used in different field, including gravitational wave detection.

The layout of a Michelson interferometer is shown in figure 4.1: the input beam $\mathcal{P}(t)$, that comes from the laser, is split in two beams that go into the two arms, are reflected by the end mirrors and then they are recombined again at the beamsplitter. Since both end mirrors are at the same distance L from the beamsplitter, the two output beams will be the results of the destructive interference ($\mathcal{Q}(t)$) and the constructive interference ($\mathcal{O}(t)$). These two outputs are named respectively dark and bright port of the interferometer for obvious reasons[1].

From equation 2.25 we can deduce the optical transfer matrix that relates the input and output beams at the beamsplitter, which can be written as follows

$$\begin{bmatrix} \mathcal{O}(t) \\ \mathcal{Q}(t) \\ \mathcal{A}^E(t) \\ \mathcal{A}^N(t) \end{bmatrix} = \begin{bmatrix} i\sqrt{T_{BS}} & \sqrt{R_{BS}} & 0 & 0 \\ \sqrt{R_{BS}} & i\sqrt{T_{BS}} & 0 & 0 \\ 0 & 0 & i\sqrt{T_{BS}} & \sqrt{R_{BS}} \\ 0 & 0 & \sqrt{R_{BS}} & i\sqrt{T_{BS}} \end{bmatrix} \times \begin{bmatrix} \mathcal{B}^N(t) \\ \mathcal{B}^E(t) \\ \mathcal{P}(t) \\ \mathcal{I}(t) \end{bmatrix}. \tag{4.10}$$

This is a system of four equations that describes the relations of the input and output fields in time domain. However for the calculation that we are going to do the transformation in frequency domain is necessary. Then we have

$$\mathcal{O}(t) = i\sqrt{T_{BS}}\,\mathcal{B}^N(t) + \sqrt{R_{BS}}\,\mathcal{B}^E(t) \Rightarrow \hat{\mathbf{O}}(\omega) = i\sqrt{T_{BS}}\,\hat{\mathbf{B}}^N(\omega) + \sqrt{R_{BS}}\,\hat{\mathbf{B}}^E(\omega), \tag{4.11}$$

[1]Interferometric gravitational wave detectors actually are set in order to have all the injected power exiting toward the laser and then the dark port is on the side of the photodiode.

$$\mathcal{Q}(t) = \sqrt{R_{BS}}\,\mathcal{B}^N(t) + i\sqrt{T_{BS}}\,\mathcal{B}^E(t) \Rightarrow \hat{\mathbf{Q}}(\omega) = \sqrt{R_{BS}}\,\hat{\mathbf{B}}^N(\omega) + i\sqrt{T_{BS}}\,\hat{\mathbf{B}}^E(\omega), \quad (4.12)$$

$$\mathcal{A}^N(t) = \sqrt{R_{BS}}\,\mathcal{P}(t) + i\sqrt{T_{BS}}\,\mathcal{I}(t) \Rightarrow \hat{\mathbf{A}}^N(\omega) = \sqrt{R_{BS}}\,\hat{\mathbf{P}}(\omega) + i\sqrt{T_{BS}}\,\hat{\mathbf{I}}(\omega), \quad (4.13)$$

$$\mathcal{A}^E(t) = i\sqrt{T_{BS}}\,\mathcal{P}(t) + \sqrt{R_{BS}}\,\mathcal{I}(t) \Rightarrow \hat{\mathbf{A}}^E(\omega) = i\sqrt{T_{BS}}\,\hat{\mathbf{P}}(\omega) + \sqrt{R_{BS}}\,\hat{\mathbf{I}}(\omega). \quad (4.14)$$

Furthermore we can define the field incident on the end mirrors as the field that comes from the beamsplitter multiplied by a propagation factor which takes into account the change of the phase

$$\mathcal{E}_2^E(t) = \mathcal{A}^E\left(t + \frac{L}{c}\right) \Rightarrow \hat{\mathbf{E}}_2^E(\omega) = \hat{\mathbf{A}}^E(\omega)\, e^{i\omega\tau}. \quad (4.15)$$

On the other hand, the field that is reflected from the end mirror, which has reflectivity equal to one, is

$$\mathcal{F}_2^E(t) = \mathcal{E}_2^E\left(t + \frac{x_E}{c}\right) \Rightarrow \hat{\mathbf{F}}_2^E(\omega) = \hat{\mathbf{E}}_2^E(\omega) + \frac{2i\omega_p}{c}\,\mathrm{E}_2^E x_E(\omega), \quad (4.16)$$

where in this case the propagation factor takes into account the phase shift due to the mirror motion x_E. Then the field that hits the beamsplitter is

$$\mathcal{B}^E(t) = \mathcal{F}_2^E\left(t + \frac{L}{c}\right) \Rightarrow \hat{\mathbf{A}}^E(\omega) = \hat{\mathbf{F}}_2^E(\omega)\, e^{i\omega\tau}. \quad (4.17)$$

Now it is useful to split the field in a classical amplitude term, that is the part that is the constant part, and a fluctuation term. In this way the fields that reach the ETM can be written as[2]

$$\hat{\mathbf{e}}_2^E(\omega) = \left(i\sqrt{T_{BS}}\,\hat{\mathbf{p}}(\omega) + \sqrt{R_{BS}}\,\hat{\mathbf{i}}(\omega)\right) e^{i\omega\tau} \quad (4.18)$$

and

$$\mathrm{E}_2^E = i\sqrt{T_{BS}}\,\mathrm{P} + \sqrt{R_{BS}}\,\mathrm{I} \quad (4.19)$$

for the East cavity and

$$\hat{\mathbf{e}}_2^N(\omega) = \left(i\sqrt{T_{BS}}\,\hat{\mathbf{i}}(\omega) + \sqrt{R_{BS}}\,\hat{\mathbf{p}}(\omega)\right) e^{i\omega\tau} \quad (4.20)$$

and

$$\mathrm{E}_2^N = i\sqrt{T_{BS}}\,\mathrm{I} + \sqrt{R_{BS}}\,\mathrm{P} \quad (4.21)$$

for the North cavity.

[2]We are considering as reference phase (set to zero) the phase of the field incident on the beamsplitter.

So the fluctuation of the beams incident on the beamsplitter will be

$$\begin{aligned}\hat{\mathbf{b}}^{E}(\omega) &= \left(\hat{\mathbf{e}}_2^E(\omega) + \frac{2i\omega_p}{c}\,\mathrm{E}_2^E\,x_E(\omega)\right)\,e^{i\omega\tau} \\ &= \left(i\sqrt{T_{BS}}\,\hat{\mathbf{p}}(\omega) + \sqrt{R_{BS}}\,\hat{\mathbf{i}}(\omega)\right)e^{2i\omega\tau} + \frac{2i\omega_p}{c}\,\mathrm{E}_2^E\,x_E(\omega)\,e^{i\omega\tau}\end{aligned} \tag{4.22}$$

for the East cavity and

$$\hat{\mathbf{b}}^{N}(\omega) = \left(i\sqrt{T_{BS}}\,\hat{\mathbf{i}}(\omega) + \sqrt{R_{BS}}\,\hat{\mathbf{p}}(\omega)\right)e^{2i\omega\tau} + \frac{2i\omega_p}{c}\,\mathrm{E}_2^N\,x_N(\omega)\,e^{i\omega\tau} \tag{4.23}$$

for the North cavity.

Finally, inserting equations 4.22 and 4.23 in equation 4.11, we are able to write the quantum fluctuation part of the output of the full interferometer as

$$\begin{aligned}\hat{\mathbf{o}}(\omega) =& i\sqrt{T_{BS}}\left(i\sqrt{T_{BS}}\,e^{2i\omega\tau}\,\hat{\mathbf{i}}(\omega) + \sqrt{R_{BS}}\,e^{2i\omega\tau}\,\hat{\mathbf{p}}(\omega) + \frac{2i\omega_p}{c}\,e^{i\omega\tau}\,\mathrm{E}_2^N\,x_N(\omega)\right) \\ &+ \sqrt{R_{BS}}\left(i\sqrt{T_{BS}}\,e^{2i\omega\tau}\,\hat{\mathbf{p}}(\omega) + \sqrt{R_{BS}}\,e^{2i\omega\tau}\,\hat{\mathbf{i}}(\omega) + \frac{2i\omega_p}{c}\,e^{i\omega\tau}\,\mathrm{E}_2^E\,x_E(\omega)\right) \\ =& \left(-T_{BS} + R_{BS}\right)\,e^{2i\omega\tau}\,\hat{\mathbf{i}}(\omega) + 2i\sqrt{R_{BS}}\sqrt{T_{BS}}\,e^{2i\omega\tau}\,\hat{\mathbf{p}}(\omega) \\ &+ \frac{2i\omega_p}{c}\,\left(i\sqrt{T_{BS}}\,\mathrm{E}_2^N\,x_N(\omega) + \sqrt{R_{BS}}\,\mathrm{E}_2^E\,x_E(\omega)\right)\,e^{i\omega\tau}.\end{aligned} \tag{4.24}$$

For the quantum noise calculation we need to transform the equations 4.18, 4.19, 4.20, 4.21 and 4.24 in the two-photon quadrature notation, according to the rules described in equation 2.11 and then we have

$$\boldsymbol{E}_2^E = \sqrt{T_{BS}}\,\hat{\sigma}\,\boldsymbol{P} + \sqrt{R_{BS}}\,\mathbb{I}\,\boldsymbol{I}, \tag{4.25}$$

$$\boldsymbol{E}_2^N = \sqrt{T_{BS}}\,\hat{\sigma}\,\boldsymbol{I} + \sqrt{R_{BS}}\,\mathbb{I}\,\boldsymbol{P}, \tag{4.26}$$

$$\hat{\boldsymbol{e}}_2^E(\Omega) = \underbrace{\sqrt{T_{BS}}\,\hat{\sigma}\,e^{i\Omega\tau}}_{\mathbb{L}_E^p(\Omega)}\,\hat{\boldsymbol{p}}(\Omega) + \underbrace{\sqrt{R_{BS}}\,\mathbb{I}\,e^{i\Omega\tau}}_{\mathbb{L}_E^i(\Omega)}\,\hat{\boldsymbol{i}}(\Omega) = \mathbb{L}_E^p(\Omega)\,\hat{\boldsymbol{p}}(\Omega) + \mathbb{L}_E^i(\Omega)\,\hat{\boldsymbol{i}}(\Omega), \tag{4.27}$$

$$\hat{\boldsymbol{e}}_2^N(\Omega) = \underbrace{\sqrt{T_{BS}}\,\hat{\sigma}\,e^{i\Omega\tau}}_{\mathbb{L}_N^i(\Omega)}\,\hat{\boldsymbol{i}}(\Omega) + \underbrace{\sqrt{R_{BS}}\,\mathbb{I}\,e^{i\Omega\tau}}_{\mathbb{L}_N^p(\Omega)}\,\hat{\boldsymbol{p}}(\Omega) = \mathbb{L}_N^p(\Omega)\,\hat{\boldsymbol{p}}(\Omega) + \mathbb{L}_N^i(\Omega)\,\hat{\boldsymbol{i}}(\Omega), \tag{4.28}$$

and

$$\hat{\boldsymbol{o}}(\Omega) = \underbrace{\left(-T_{BS} + R_{BS}\right)\, e^{2i\omega\tau}\, \mathbb{I}}_{\mathbb{T}^{io}_{s.n.}(\Omega)}\, \hat{\boldsymbol{i}}(\Omega) + \underbrace{2\sqrt{R_{BS}}\sqrt{T_{BS}}\, e^{2i\omega\tau}\, \hat{\sigma}}_{\mathbb{T}^{po}_{s.n.}(\Omega)}\, \hat{\boldsymbol{p}}(\Omega)$$

$$\underbrace{-\frac{2\omega_p}{c}\sqrt{T_{BS}}\, \mathbb{I}\, \boldsymbol{E}_2^N\, e^{i\omega\tau}}_{\mathbf{R}^{No}(\Omega)}\, x_N(\Omega) + \underbrace{\frac{2\omega_p}{c}\sqrt{R_{BS}}\, \hat{\sigma}\, \boldsymbol{E}_2^E\, e^{i\omega\tau}}_{\mathbf{R}^{Eo}(\Omega)}\, x_E(\Omega) \tag{4.29}$$

$$= \mathbb{T}^{io}_{s.n.}(\Omega)\, \hat{\boldsymbol{i}}(\Omega) + \mathbb{T}^{po}_{s.n.}(\Omega)\, \hat{\boldsymbol{p}}(\Omega) + \mathbf{R}^{Eo}(\Omega)\, x_E(\Omega) + \mathbf{R}^{No}(\Omega)\, x_N(\Omega).$$

Here the transfer matrix $\mathbb{T}^{oi}_{s.n.}(\Omega)$ represents the shot noise in the output $\hat{\boldsymbol{o}}(\Omega)$ correspondent to the field $\hat{\boldsymbol{i}}(\Omega)$ and $\mathbb{T}^{op}_{s.n.}(\Omega)$ that one correspondent to the field $\hat{\boldsymbol{p}}(\Omega)$ and the vectors $\mathbf{R}^E_o$ and $\mathbf{R}^N_o$ are the response functions of the interferometer to the motion of the mirrors of the East and North arm respectively.

In order to include the radiation pressure noise contribution in the transfer matrix we insert equations 4.6, 4.27 and 4.28 in equation 4.29 and we obtain

$$\begin{aligned}
\hat{\boldsymbol{o}}(\Omega) &= \mathbb{T}^{io}_{s.n.}(\Omega)\, \hat{\boldsymbol{i}}(\Omega) + \mathbb{T}^{po}_{s.n.}(\Omega)\, \hat{\boldsymbol{p}}(\Omega) + \mathbf{R}^{Eo}(\Omega)\, x^{GW}_E(\Omega) + \mathbf{R}^{No}(\Omega)\, x^{GW}_N(\Omega) \\
&+ \mathbf{R}^{Eo}(\Omega)\chi_E(\Omega)\frac{2\hbar\omega_p}{c}\left(\boldsymbol{E}_2^E\right)^\dagger\left(\mathbb{L}^p_E(\Omega)\, \hat{\boldsymbol{p}}(\Omega) + \mathbb{L}^i_E(\Omega)\, \hat{\boldsymbol{i}}(\Omega)\right) \\
&+ \mathbf{R}^{No}(\Omega)\chi_N(\Omega)\frac{2\hbar\omega_p}{c}\left(\boldsymbol{E}_2^N\right)^\dagger\left(\mathbb{L}^p_N(\Omega)\, \hat{\boldsymbol{p}}(\Omega) + \mathbb{L}^i_N(\Omega)\, \hat{\boldsymbol{i}}(\Omega)\right) \\
&= \mathbb{T}^{io}_{s.n.}(\Omega)\, \hat{\boldsymbol{i}}(\Omega) + \mathbb{T}^{po}_{s.n.}(\Omega)\, \hat{\boldsymbol{p}}(\Omega) + \mathbf{R}^{Eo}(\Omega)\, x^{GW}_E(\Omega) + \mathbf{R}^{No}(\Omega)\, x^{GW}_N(\Omega) \\
&\underbrace{+\frac{2\hbar\omega_p}{c}\left(\mathbf{R}^{Eo}(\Omega)\chi_E(\Omega)\left(\boldsymbol{E}_2^E\right)^\dagger\mathbb{L}^p_E(\Omega) + \mathbf{R}^{No}(\Omega)\chi_N(\Omega)\left(\boldsymbol{E}_2^N\right)^\dagger\mathbb{L}^p_N(\Omega)\right)}_{\mathbb{T}^{po}_{r.p.}(\Omega)}\, \hat{\boldsymbol{p}}(\Omega) \\
&\underbrace{+\frac{2\hbar\omega_p}{c}\left(\mathbf{R}^{Eo}(\Omega)\chi_E(\Omega)\left(\boldsymbol{E}_2^E\right)^\dagger\mathbb{L}^i_E(\Omega) + \mathbf{R}^{No}(\Omega)\chi_N(\Omega)\left(\boldsymbol{E}_2^N\right)^\dagger\mathbb{L}^i_N(\Omega)\right)}_{\mathbb{T}^{io}_{r.p.}(\Omega)}\, \hat{\boldsymbol{i}}(\Omega) \\
&= \left(\mathbb{T}^{po}_{s.n.}(\Omega) + \mathbb{T}^{po}_{r.p.}(\Omega)\right)\hat{\boldsymbol{p}}(\Omega) + \left(\mathbb{T}^{io}_{s.n.}(\Omega) + \mathbb{T}^{io}_{r.p.}(\Omega)\right)\hat{\boldsymbol{i}}(\Omega) \\
&+ \mathbf{R}^{Eo}(\Omega)\, x^{GW}_E(\Omega) + \mathbf{R}^{No}(\Omega)\, x^{GW}_N(\Omega)
\end{aligned} \tag{4.30}$$

and similarly, the other output of the interferometer is found to be

$$
\begin{aligned}
\hat{\boldsymbol{q}}(\Omega) = & \underbrace{\left(-T_{BS} + R_{BS}\right)\, e^{2i\Omega\tau}\, \mathbb{I}}_{\mathbb{T}^{pq}_{s.n.}(\Omega)}\, \hat{\boldsymbol{p}}(\Omega) + \underbrace{2\sqrt{R_{BS}}\sqrt{T_{BS}}\, e^{2i\Omega\tau}\, \hat{\sigma}}_{\mathbb{T}^{iq}_{s.n.}(\Omega)}\, \hat{\boldsymbol{i}}(\Omega) \\
& \underbrace{+\frac{2\omega_p}{c}\sqrt{R_{BS}}\, \hat{\sigma}\, \boldsymbol{E}_2^N\, e^{i\Omega\tau}}_{\mathbf{R}^{Nq}(\Omega)}\, x_N(\Omega) \underbrace{-\frac{2\omega_p}{c}\sqrt{T_{BS}}\, \mathbb{I}\, \boldsymbol{E}_2^E\, e^{i\Omega\tau}}_{\mathbf{R}^{Eq}(\Omega)}\, x_E(\Omega) \\
= & \mathbb{T}^{pq}_{s.n.}(\Omega)\, \hat{\boldsymbol{p}}(\Omega) + \mathbb{T}^{iq}_{s.n.}(\Omega)\, \hat{\boldsymbol{i}}(\Omega) + \mathbf{R}^{Eq}(\Omega)\, x_E^{GW}(\Omega) + \mathbf{R}^{Nq}(\Omega)\, x_N^{GW}(\Omega) \\
& + \mathbf{R}^{Eq}(\Omega)\chi_E(\Omega)\frac{2\hbar\omega_p}{c}\left(\boldsymbol{E}_2^E\right)^\dagger \left(\mathbb{L}_E^p(\Omega)\, \hat{\boldsymbol{p}}(\Omega) + \mathbb{L}_E^i(\Omega)\, \hat{\boldsymbol{i}}(\Omega)\right) \\
& + \mathbf{R}^{Nq}(\Omega)\chi_N(\Omega)\frac{2\hbar\omega_p}{c}\left(\boldsymbol{E}_2^N\right)^\dagger \left(\mathbb{L}_N^p(\Omega)\, \hat{\boldsymbol{p}}(\Omega) + \mathbb{L}_N^i(\Omega)\, \hat{\boldsymbol{i}}(\Omega)\right) \\
= & \mathbb{T}^{pq}_{s.n.}(\Omega)\, \hat{\boldsymbol{p}}(\Omega) + \mathbb{T}^{iq}_{s.n.}(\Omega)\, \hat{\boldsymbol{i}}(\Omega) + \mathbf{R}^{Eq}(\Omega)\, x_E^{GW}(\Omega) + \mathbf{R}^{Nq}(\Omega)\, x_N^{GW}(\Omega) \\
& \underbrace{+\frac{2\hbar\omega_p}{c}\left(\mathbf{R}^{Eq}(\Omega)\chi_E(\Omega)\left(\boldsymbol{E}_2^E\right)^\dagger \mathbb{L}_E^p(\Omega) + \mathbf{R}^{Nq}(\Omega)\chi_N(\Omega)\left(\boldsymbol{E}_2^N\right)^\dagger \mathbb{L}_N^p(\Omega)\right)}_{\mathbb{T}^{po}_{r.p.}(\Omega)}\, \hat{\boldsymbol{p}}(\Omega) \\
& \underbrace{+\frac{2\hbar\omega_p}{c}\left(\mathbf{R}^{Eo}(\Omega)\chi_E(\Omega)\left(\boldsymbol{E}_2^E\right)^\dagger \mathbb{L}_E^i(\Omega) + \mathbf{R}^{No}(\Omega)\chi_N(\Omega)\left(\boldsymbol{E}_2^N\right)^\dagger \mathbb{L}_N^i(\Omega)\right)}_{\mathbb{T}^{io}_{r.p.}(\Omega)}\, \hat{\boldsymbol{i}}(\Omega) \\
= & \left(\mathbb{T}^{iq}_{s.n.}(\Omega) + \mathbb{T}^{iq}_{r.p.}(\Omega)\right)\hat{\boldsymbol{i}}(\Omega) + \left(\mathbb{T}^{pq}_{s.n.}(\Omega) + \mathbb{T}^{pq}_{r.p.}(\Omega)\right)\hat{\boldsymbol{p}}(\Omega) \\
& + \mathbf{R}^{Eq}(\Omega)\, x_E^{GW}(\Omega) + \mathbf{R}^{Nq}(\Omega)\, x_N^{GW}(\Omega).
\end{aligned}
\tag{4.31}
$$

These are the I/O relations of a Michelson interferometer. We can notice that if we have only the input from the laser, i.e. $\hat{\boldsymbol{i}}(\Omega) = 0$, and a perfect 50:50 beamsplitter, then $\mathbb{T}^{pq}_{s.n.}(\Omega) = 0$ and all the light will exit from the port $\hat{\boldsymbol{o}}(\Omega)$, which is the bright port. The port $\hat{\boldsymbol{q}}(\Omega)$, on the other side is dark port.

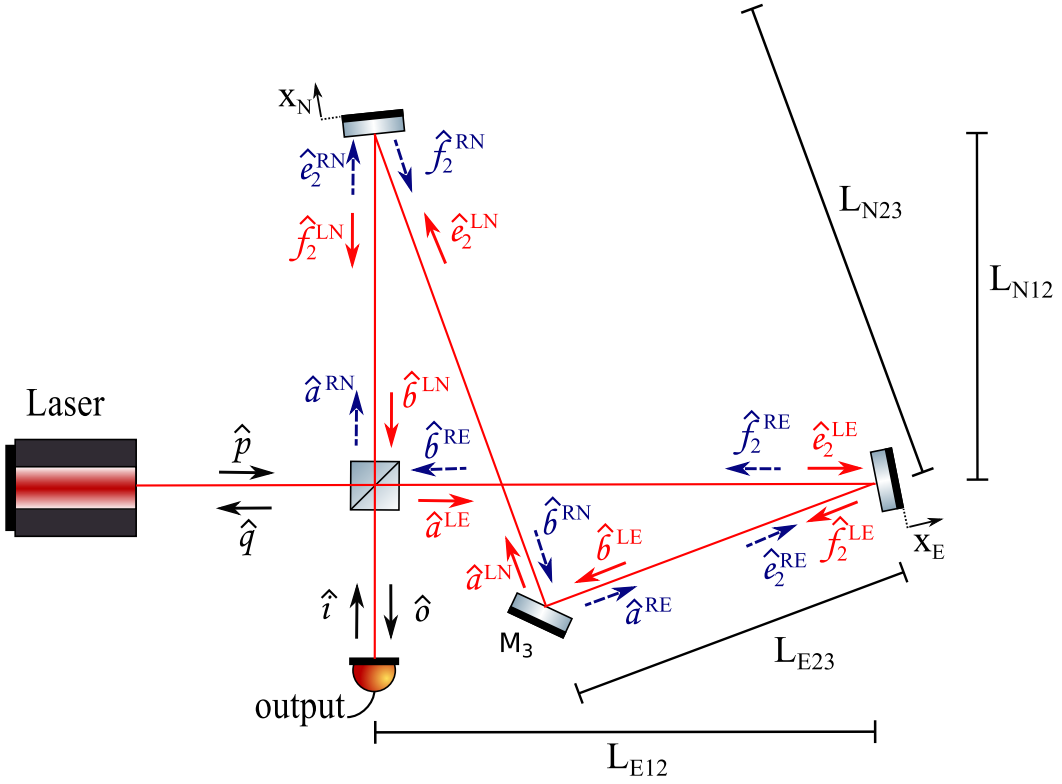

Figure 4.2: Simple Sagnac interferometer.

4.2.2 Simple Sagnac

In this section we will show how the I/O relation of a Sagnac interferometer are obtained. A Sagnac interferometer was introduced by George Sagnac in 1913 with the aim to prove the existence of the aether and its main peculiarity is that the two beams will travel through both arms but in opposite directions [88].

The layout of a *zero-area* Sagnac interferometer and the fields nomenclature that we will use for this calculation are shown in figure 4.2. In this case each beam will hit both end mirrors before coming back at the beamsplitter. That path is possible introducing the steering mirror M_3 (cf. figure 4.2), which will reflect the beam coming from one ETM towards the other.

The transfer matrix in time domain that describe the beamsplitter is the same as described in equation 4.10:

$$\begin{bmatrix} \mathcal{O}(t) \\ \mathcal{Q}(t) \\ \mathcal{A}^{LE}(t) \\ \mathcal{A}^{RN}(t) \end{bmatrix} = \begin{bmatrix} i\sqrt{T_{BS}} & \sqrt{R_{BS}} & 0 & 0 \\ \sqrt{R_{BS}} & i\sqrt{T_{BS}} & 0 & 0 \\ 0 & 0 & i\sqrt{T_{BS}} & \sqrt{R_{BS}} \\ 0 & 0 & \sqrt{R_{BS}} & i\sqrt{T_{BS}} \end{bmatrix} \times \begin{bmatrix} \mathcal{B}^{LN}(t) \\ \mathcal{B}^{RE}(t) \\ \mathcal{P}(t) \\ \mathcal{I}(t) \end{bmatrix}, \tag{4.32}$$

but in this case the beam will have a different path. For example for the clockwise beam, which will be indicate with the superscript L (left), it can be outlined with the following steps:

- the beam arrives at the first ETM with a phase shift $\frac{L_{E12}}{c}$:

$$\mathcal{E}_2^{LE}(t) = \mathcal{A}^{LE}\left(t + \frac{L_{E12}}{c}\right) \Rightarrow \hat{\mathbf{E}}_2^{LE}(\omega) = \hat{\mathbf{A}}^{LE}(\omega)\, e^{i\omega\tau_{E12}}; \tag{4.33}$$

- it is reflected from the ETM:

$$\mathcal{F}_2^{LE}(t) = \sqrt{R_2}\,\mathcal{E}_2^{LE}(t) \Rightarrow \sqrt{R_2}\,\hat{\mathbf{F}}_2^{LE}(\omega) = \hat{\mathbf{E}}_2^{LE}(\omega), \tag{4.34}$$

  where R_2 is the power reflectivity of ETM;

- it has a further phase shift due to the travel towards M_3:

$$\mathcal{B}^{LE}(t) = \mathcal{F}_2^{LE}\left(t + \frac{L_{E23}}{c}\right) \Rightarrow \hat{\mathbf{B}}^{LE}(\omega) = \hat{\mathbf{F}}_2^{LE}(\omega)\, e^{i\omega\tau_{E23}}; \tag{4.35}$$

- it is reflected by M_3 with power reflectivity R_3:

$$\mathcal{A}^{LN}(t) = \sqrt{R_3}\,\mathcal{B}^{LE}(t) \Rightarrow \hat{\mathbf{A}}^{LN}(\omega) = \hat{\mathbf{B}}^{LE}(\omega), \tag{4.36}$$

- it travels to the second ETM at a distance L_{N23}:

$$\mathcal{E}_2^{LN}(t) = \mathcal{A}^{LN}\left(t + \frac{L_{N23}}{c}\right) \Rightarrow \hat{\mathbf{E}}_2^{LN}(\omega) = \hat{\mathbf{A}}^{LN}(\omega)\, e^{i\omega\tau_{N23}}; \tag{4.37}$$

- it is reflected by the second ETM:

$$\mathcal{F}_2^{LN}(t) = \sqrt{R_2}\,\mathcal{E}_2^{LN}(t) \Rightarrow \sqrt{R_2}\,\hat{\mathbf{F}}_2^{LN}(\omega) = \hat{\mathbf{E}}_2^{LN}(\omega); \tag{4.38}$$

- finally it comes back to the beamsplitter

$$\mathcal{B}^{LN}(t) = \mathcal{F}_2^{LN}\left(t + \frac{L_{N12}}{c}\right) \Rightarrow \hat{\mathbf{B}}^{LN}(\omega) = \hat{\mathbf{F}}_2^{LN}(\omega)\, e^{i\omega\tau_{N12}}. \tag{4.39}$$

Here we have indicated with L the distance between two optical elements specified by the subscripts: 1,2 and 3 states for the beamsplitter, the ETM and M_3 respectively and E and N state for East and North cavity. In the same way we have defined τ as the time travel between two optical elements specified in the subscript. Then, in order to simplify the

calculation, we assume that

$$L_{N12} + L_{N23} = L_{E12} + L_{E23} = 2L, \tag{4.40}$$

$$\tau_{N12} + \tau_{N23} = \tau_{E12} + \tau_{E23} = 2\tau \tag{4.41}$$

Furthermore, for sake of simplicity, we will consider that all the mirrors have a power reflectivity equal to one, because the introduction of a transmissivity will entail the presence of loss and then we should also consider the additional noise related to it, as described in section 2.1.4.

Following the same method used for the Michelson interferometer, we obtain all the fields in the two-photon quadrature notation:

$$\begin{aligned}\hat{\boldsymbol{b}}^{LN}(\Omega) = &\left(\left(\sqrt{T_{BS}}\,\hat{\sigma}\,\hat{\boldsymbol{p}}(\Omega) + \sqrt{R_{BS}}\,\hat{\boldsymbol{i}}(\Omega)\,\mathbb{I}\,x_E(\Omega)\right)e^{2i\Omega\tau} + \frac{2\omega_p}{c}\,\hat{\sigma}\,\boldsymbol{E}_2^{LE}\,e^{i\Omega\tau_{E23}}\right)e^{2i\Omega\tau} \\ &+ \frac{2\omega_p}{c}\,\hat{\sigma}\,\boldsymbol{E}_2^{LN}\,e^{i\Omega\tau_{N12}}\,x_N(\Omega)\end{aligned} \tag{4.42}$$

$$\begin{aligned}\hat{\boldsymbol{e}}_2^{LN}(\Omega) &= \left(\left(\sqrt{T_{BS}}\,\hat{\sigma}\,\hat{\boldsymbol{p}}(\Omega) + \sqrt{R_{BS}}\,\mathbb{I}\,\hat{\boldsymbol{i}}(\Omega)\right)e^{2i\Omega\tau} + \frac{2\omega_p}{c}\,\hat{\sigma}\,\boldsymbol{E}_2^{LE}\,e^{i\Omega\tau_{E23}}\,x_E(\Omega)\right)e^{i\Omega\tau_{N23}} \\ &= \mathbb{L}_{LN}^{p}(\Omega)\,\hat{\boldsymbol{p}}(\Omega) + \mathbb{L}_{LN}^{i}(\Omega)\,\hat{\boldsymbol{i}}(\Omega) + \mathbf{X}_{LN}^{E}(\Omega)\,x_E(\Omega)\end{aligned} \tag{4.43}$$

$$\hat{\boldsymbol{e}}_2^{LE}(\Omega) = \left(\sqrt{T_{BS}}\,\hat{\sigma}\,\hat{\boldsymbol{p}}(\Omega) + \sqrt{R_{BS}}\,\mathbb{I}\,\hat{\boldsymbol{i}}(\Omega)\right)e^{i\Omega\tau_{E12}} = \mathbb{L}_{LE}^{p}(\Omega)\,\hat{\boldsymbol{p}}(\Omega) + \mathbb{L}_{LE}^{i}(\Omega)\,\hat{\boldsymbol{i}}(\Omega) \tag{4.44}$$

and because of the symmetry of the system we have

$$\begin{aligned}\hat{\boldsymbol{b}}^{RE}(\Omega) = &\left(\left(\sqrt{T_{BS}}\,\hat{\sigma}\,\hat{\boldsymbol{i}}(\Omega) + \sqrt{R_{BS}}\,\mathbb{I}\,\hat{\boldsymbol{p}}(\Omega)\right)e^{2i\Omega\tau} + \frac{2\omega_p}{c}\,\hat{\sigma}\,\boldsymbol{E}_2^{RN}\,e^{i\Omega\tau_{N23}}\,x_N(\Omega)\right)e^{2i\Omega\tau} \\ &+ \frac{2\omega_p}{c}\,\hat{\sigma}\,\boldsymbol{E}_2^{RE}\,e^{i\Omega\tau_{E12}}\,x_E(\Omega)\end{aligned} \tag{4.45}$$

$$\begin{aligned}\hat{\boldsymbol{e}}_2^{RE}(\Omega) &= \left(\left(\sqrt{T_{BS}}\,\hat{\sigma}\,\hat{\boldsymbol{i}}(\Omega) + \sqrt{R_{BS}}\,\mathbb{I}\,\hat{\boldsymbol{p}}(\Omega)\right) e^{2i\Omega\tau} + \frac{2\omega_p}{c}\,\hat{\sigma}\,\boldsymbol{E}_2^{RN}\, e^{i\Omega\tau_{N23}}\, x_N(\Omega)\right) e^{i\Omega\tau_{E23}} \\ &= \mathbb{L}_{RE}^{p}(\Omega)\,\hat{\boldsymbol{p}}(\Omega) + \mathbb{L}_{RE}^{i}(\Omega)\,\hat{\boldsymbol{i}}(\Omega) + \mathbf{X}_{RE}^{N}(\Omega)\, x_N(\Omega)\end{aligned} \tag{4.46}$$

$$\hat{\boldsymbol{e}}_2^{RN}(\Omega) = \left(\sqrt{T_{BS}}\,\hat{\sigma}\,\hat{\boldsymbol{i}}(\Omega) + \sqrt{R_{BS}}\,\mathbb{I}\,\hat{\boldsymbol{p}}(\Omega)\right) e^{i\Omega\tau_{N12}} = \mathbb{L}_{RN}^{p}(\Omega)\,\hat{\boldsymbol{p}}(\Omega) + \mathbb{L}_{RN}^{i}(\Omega)\,\hat{\boldsymbol{i}}(\Omega). \tag{4.47}$$

So the I/O relation of the full interferometer will be

$$\begin{aligned}\hat{\boldsymbol{o}}(\Omega) = &\underbrace{\left(-T_{BS} + R_{BS}\right) e^{2i\Omega\tau}\,\mathbb{I}}_{\mathbb{T}_{s.n.}^{po}(\Omega)}\,\hat{\boldsymbol{p}}(\Omega) + \underbrace{2\sqrt{R_{BS}T_{BS}}\, e^{2i\Omega\tau}\,\hat{\sigma}}_{\mathbb{T}_{s.n.}^{io}(\Omega)}\,\hat{\boldsymbol{i}}(\Omega) \\ &\underbrace{+\frac{2\omega_p}{c}\left(-\sqrt{T_{BS}}\,\mathbb{I}\,\boldsymbol{E}_2^{LE} e^{i\Omega\tau_{E23}} e^{2i\Omega\tau} + \sqrt{R_{BS}}\,\hat{\sigma}\,\boldsymbol{E}_2^{RE} e^{i\Omega\tau_{E12}}\right)}_{\mathbf{R}_{arm}^{Eo}(\Omega)}\, x_E(\Omega) \\ &\underbrace{+\frac{2\omega_p}{c}\left(\sqrt{R_{BS}}\,\hat{\sigma}\,\boldsymbol{E}_2^{RN} e^{i\Omega\tau_{N23}} e^{2i\Omega\tau} - \sqrt{T_{BS}}\,\mathbb{I}\,\boldsymbol{E}_2^{LN} e^{i\Omega\tau_{N12}}\right)}_{\mathbf{R}_{arm}^{No}(\Omega)}\, x_N(\Omega) \\ = &\,\mathbb{T}_{s.n.}^{po}(\Omega)\,\hat{\boldsymbol{p}}(\Omega) + \mathbb{T}_{s.n.}^{io}(\Omega)\,\hat{\boldsymbol{i}}(\Omega) + \mathbf{R}_{arm}^{Eo}(\Omega)\, x_E(\Omega) + \mathbf{R}_{arm}^{No}(\Omega)\, x_N(\Omega)\end{aligned} \tag{4.48}$$

We have now to include the radiation pressure contribution. In this case we have two beams incident on the same mirror and the total radiation pressure force will be the sum of the

two forces created by each beam:

$$
\begin{aligned}
\hat{\boldsymbol{o}}(\Omega) =& \mathbb{T}^{po}_{s.n.}(\Omega)\,\hat{\boldsymbol{p}}(\Omega) + \mathbb{T}^{io}_{s.n.}(\Omega)\,\hat{\boldsymbol{i}}(\Omega) + \mathbf{R}^{E}_{arm}(\Omega)\,x^{GW}_{E}(\Omega) + \mathbf{R}^{N}_{arm}(\Omega)\,x^{GW}_{N}(\Omega) \\
&+ \mathbf{R}^{Eo}_{arm}(\Omega)\chi_E(\Omega)\frac{\hbar\omega_p}{c}\left(\boldsymbol{E}^{LE}_{2}\right)^{\dagger}\left(\mathbb{L}^{p}_{LE}(\Omega)\,\hat{\boldsymbol{p}}(\Omega) + \mathbb{L}^{i}_{LE}(\Omega)\,\hat{\boldsymbol{i}}(\Omega)\right) \\
&+ \mathbf{R}^{Eo}_{arm}(\Omega)\chi_E(\Omega)\frac{\hbar\omega_p}{c}\left(\boldsymbol{E}^{RE}_{2}\right)^{\dagger}\left(\mathbb{L}^{p}_{RE}(\Omega)\,\hat{\boldsymbol{p}}(\Omega) + \mathbb{L}^{i}_{RE}(\Omega)\,\hat{\boldsymbol{i}}(\Omega) + \mathbf{X}^{N}_{RE}(\Omega)\,x_N(\Omega)\right) \\
&+ \mathbf{R}^{No}_{arm}(\Omega)\chi_N(\Omega)\frac{\hbar\omega_p}{c}\left(\boldsymbol{E}^{LN}_{2}\right)^{\dagger}\left(\mathbb{L}^{p}_{LN}(\Omega)\,\hat{\boldsymbol{p}}(\Omega) + \mathbb{L}^{i}_{LN}(\Omega)\,\hat{\boldsymbol{i}}(\Omega) + \mathbf{X}^{E}_{LN}(\Omega)\,x_E(\Omega)\right) \\
&+ \mathbf{R}^{No}_{arm}(\Omega)\chi_N(\Omega)\frac{\hbar\omega_p}{c}\left(\boldsymbol{E}^{RN}_{2}\right)^{\dagger}\left(\mathbb{L}^{p}_{RN}(\Omega)\,\hat{\boldsymbol{p}}(\Omega) + \mathbb{L}^{i}_{RN}(\Omega)\,\hat{\boldsymbol{i}}(\Omega)\right) \\
=& \mathbb{T}^{po}_{sn}(\Omega)\,\hat{\boldsymbol{p}}(\Omega) + \mathbb{T}^{io}_{sn}(\Omega)\,\hat{\boldsymbol{i}}(\Omega) + \mathbf{R}^{oE}_{arm}(\Omega)\,x^{GW}_{E}(\Omega) + \mathbf{R}^{oN}_{arm}(\Omega)\,x^{GW}_{N}(\Omega) \\
&\overbrace{\underbrace{+\frac{\hbar\omega_p}{c}\left[\mathbf{R}^{Eo}_{arm}(\Omega)\chi_E(\Omega)\left(\left(\boldsymbol{E}^{LE}_{2}\right)^{\dagger}\mathbb{L}^{p}_{LE}(\Omega) + \left(\boldsymbol{E}^{RE}_{2}\right)^{\dagger}\mathbb{L}^{p}_{RE}(\Omega)\right)\right.}^{\mathbb{T}^{po}_{r.p.}(\Omega)}}^{} \\
&\left.+ \mathbf{R}^{No}_{arm}(\Omega)\chi_N(\Omega)\left(\left(\boldsymbol{E}^{LN}_{2}\right)^{\dagger}\mathbb{L}^{p}_{LN}(\Omega) + \left(\boldsymbol{E}^{RN}_{2}\right)^{\dagger}\mathbb{L}^{p}_{RN}(\Omega)\right)\right]\hat{\boldsymbol{p}}(\Omega) \\
&\overbrace{\underbrace{+\frac{\hbar\omega_p}{c}\left[\mathbf{R}^{Eo}_{arm}(\Omega)\chi_E(\Omega)\left(\left(\boldsymbol{E}^{LE}_{2}\right)^{\dagger}\mathbb{L}^{i}_{LE}(\Omega) + \left(\boldsymbol{E}^{RE}_{2}\right)^{\dagger}\mathbb{L}^{i}_{RE}(\Omega)\right)\right.}^{\mathbb{T}^{io}_{r.p.}(\Omega)}}^{} \\
&\left.+ \mathbf{R}^{No}_{arm}(\Omega)\chi_N(\Omega)\left(\left(\boldsymbol{E}^{LN}_{2}\right)^{\dagger}\mathbb{L}^{i}_{LN}(\Omega) + \left(\boldsymbol{E}^{RN}_{2}\right)^{\dagger}\mathbb{L}^{i}_{RN}(\Omega)\right)\right]\hat{\boldsymbol{i}}(\Omega) \\
=& \left(\mathbb{T}^{po}_{s.n.}(\Omega) + \mathbb{T}^{po}_{r.p.}(\Omega)\right)\hat{\boldsymbol{p}}(\Omega) + \left(\mathbb{T}^{io}_{s.n.}(\Omega) + \mathbb{T}^{io}_{r.p.}(\Omega)\right)\hat{\boldsymbol{i}}(\Omega) \\
&+ \mathbf{R}^{Eo}_{arm}(\Omega)\,x^{GW}_{E}(\Omega) + \mathbf{R}^{No}_{arm}(\Omega)\,x^{GW}_{N}(\Omega),
\end{aligned}
\tag{4.49}
$$

where we have considered that in this case the new terms in x are zero because

$$
\left(\boldsymbol{E}^{IJ}_{2}\right)^{\dagger}\mathbf{X}^{J}_{IJ} \propto \begin{bmatrix}1 & 0\end{bmatrix}\cdot\begin{bmatrix}0 & 1\\ -1 & 0\end{bmatrix}\cdot\begin{bmatrix}1\\ 0\end{bmatrix} = 0, \tag{4.50}
$$

since we chose the phase of the intracavity field as reference (i.e. equal to 0).

The details of this calculation and what happens when the cavity is detuned will be shown

in section 4.3.

For the output $\hat{\boldsymbol{q}}(\Omega)$, the solution is quite similar. In fact, from equation 4.32 we have

$$\begin{aligned}\hat{\boldsymbol{q}}(\Omega) = &\underbrace{\left(R_{BS} - T_{BS}\right) e^{2i\Omega\tau}}_{\mathbb{T}^{iq}_{s.n.}(\Omega)}\, \hat{\boldsymbol{i}}(\Omega) + \underbrace{2\sqrt{R_{BS}T_{BS}}\, e^{2i\Omega\tau}\, \hat{\sigma}}_{\mathbb{T}^{pq}_{s.n.}(\Omega)}\, \hat{\boldsymbol{p}}(\Omega) \\ &\underbrace{+\frac{2\omega_p}{c}\left(-\sqrt{T_{BS}}\, \boldsymbol{E}_2^{RE} e^{i\Omega\tau_{E12}} e^{2i\Omega\tau} + \sqrt{R_{BS}}\, \hat{\sigma}\, \boldsymbol{E}_2^{LE} e^{i\Omega\tau_{E23}}\right)}_{\mathbf{R}^{Eq}_{arm}(\Omega)}\, x_E^{GW}(\Omega) \\ &\underbrace{+\frac{2\omega_p}{c}\left(\sqrt{R_{BS}}\, \hat{\sigma}\, \boldsymbol{E}_2^{LN} e^{i\Omega\tau_{N12}} e^{2i\Omega\tau} - \sqrt{T_{BS}}\, \boldsymbol{E}_2^{RN} e^{i\Omega\tau_{N23}}\right)}_{\mathbf{R}^{Nq}_{arm}(\Omega)}\, x_N^{GW}(\Omega) \\ = &\mathbb{T}^{iq}_{s.n.}(\Omega)\, \hat{\boldsymbol{i}}(\Omega) + \mathbb{T}^{qp}_{s.n.}(\Omega)\, \hat{\boldsymbol{p}}(\Omega) + \mathbf{R}^{Eq}_{arm}(\Omega)\, x_E(\Omega) + \mathbf{R}^{Nq}_{arm}\, x_N(\Omega).\end{aligned} \tag{4.51}$$

And replacing the motion of the mirrors x with the sum of the two contributions described

in equation 4.6, we have

$$
\begin{aligned}
\hat{\boldsymbol{q}}(\Omega) =& \mathbb{T}^{iq}_{s.n.}(\Omega)\,\hat{\boldsymbol{i}}(\Omega) + \mathbb{T}^{pq}_{s.n.}(\Omega)\,\hat{\boldsymbol{p}}(\Omega) + \mathbf{R}^{E}_{arm}(\Omega)\,x^{GW}_{E}(\Omega) + \mathbf{R}^{N}_{arm}(\Omega)\,x^{GW}_{N}(\Omega) \\
&+ \mathbf{R}^{Eq}_{arm}(\Omega)\chi_E(\Omega)\frac{\hbar\omega_p}{c}\left(\boldsymbol{E}^{LE}_{2}\right)^{\dagger}\left(\mathbb{L}^{p}_{LE}(\Omega)\,\hat{\boldsymbol{p}}(\Omega) + \mathbb{L}^{i}_{LE}(\Omega)\,\hat{\boldsymbol{i}}(\Omega)\right) \\
&+ \mathbf{R}^{Eq}_{arm}(\Omega)\chi_E(\Omega)\frac{\hbar\omega_p}{c}\left(\boldsymbol{E}^{RE}_{2}\right)^{\dagger}\left(\mathbb{L}^{p}_{RE}(\Omega)\,\hat{\boldsymbol{p}}(\Omega) + \mathbb{L}^{i}_{RE}(\Omega)\,\hat{\boldsymbol{i}}(\Omega) + \mathbf{X}^{N}_{RE}(\Omega)\,x_N(\Omega)\right) \\
&+ \mathbf{R}^{Nq}_{arm}(\Omega)\chi_N(\Omega)\frac{\hbar\omega_p}{c}\left(\boldsymbol{E}^{LN}_{2}\right)^{\dagger}\left(\mathbb{L}^{p}_{LN}(\Omega)\,\hat{\boldsymbol{p}}(\Omega) + \mathbb{L}^{i}_{LN}(\Omega)\,\hat{\boldsymbol{i}}(\Omega) + \mathbf{X}^{E}_{LN}(\Omega)\,x_E(\Omega)\right) \\
&+ \mathbf{R}^{Nq}_{arm}(\Omega)\chi_N(\Omega)\frac{\hbar\omega_p}{c}\left(\boldsymbol{E}^{RN}_{2}\right)^{\dagger}\left(\mathbb{L}^{p}_{RN}(\Omega)\,\hat{\boldsymbol{p}}(\Omega) + \mathbb{L}^{i}_{RN}(\Omega)\,\hat{\boldsymbol{i}}(\Omega)\right) \\
=& \mathbb{T}^{iq}_{s.n.}(\Omega)\,\hat{\boldsymbol{i}}(\Omega) + \mathbb{T}^{pq}_{s.n.}(\Omega)\,\hat{\boldsymbol{p}}(\Omega) + \mathbf{R}^{E}_{arm}(\Omega)\,x^{GW}_{E}(\Omega) + \mathbf{R}^{N}_{arm}(\Omega)\,x^{GW}_{N}(\Omega) \\
&\overbrace{\underbrace{+\frac{\hbar\omega_p}{c}\left[\mathbf{R}^{Eq}_{arm}(\Omega)\chi_E(\Omega)\left(\left(\boldsymbol{E}^{LE}_{2}\right)^{\dagger}\mathbb{L}^{p}_{LE}(\Omega) + \left(\boldsymbol{E}^{RE}_{2}\right)^{\dagger}\mathbb{L}^{p}_{RE}(\Omega)\right)\right.}^{\mathbb{T}^{pq}_{r.p.}(\Omega)}}^{} \\
&\left.+ \mathbf{R}^{Nq}_{arm}(\Omega)\chi_N(\Omega)\left(\left(\boldsymbol{E}^{LN}_{2}\right)^{\dagger}\mathbb{L}^{p}_{LN}(\Omega) + \left(\boldsymbol{E}^{RN}_{2}\right)^{\dagger}\mathbb{L}^{p}_{RN}(\Omega)\right)\right]\hat{\boldsymbol{p}}(\Omega) \\
&\overbrace{\underbrace{+\frac{\hbar\omega_p}{c}\left[\mathbf{R}^{Eq}_{arm}(\Omega)\chi_E(\Omega)\left(\left(\boldsymbol{E}^{LE}_{2}\right)^{\dagger}\mathbb{L}^{i}_{LE}(\Omega) + \left(\boldsymbol{E}^{RE}_{2}\right)^{\dagger}\mathbb{L}^{i}_{RE}(\Omega)\right)\right.}^{\mathbb{T}^{iq}_{r.p.}(\Omega)}}^{} \\
&\left.+ \mathbf{R}^{Nq}_{arm}(\Omega)\chi_N(\Omega)\left(\left(\boldsymbol{E}^{LN}_{2}\right)^{\dagger}\mathbb{L}^{i}_{LN}(\Omega) + \left(\boldsymbol{E}^{RN}_{2}\right)^{\dagger}\mathbb{L}^{i}_{RN}(\Omega)\right)\right]\hat{\boldsymbol{i}}(\Omega) \\
=& \left(\mathbb{T}^{iq}_{s.n.}(\Omega) + \mathbb{T}^{iq}_{r.p.}(\Omega)\right)\hat{\boldsymbol{i}}(\Omega) + \left(\mathbb{T}^{pq}_{s.n.}(\Omega) + \mathbb{T}^{pq}_{r.p.}(\Omega)\right)\hat{\boldsymbol{p}}(\Omega) \\
&+ \mathbf{R}^{Eq}_{arm}(\Omega)\,x^{GW}_{E}(\Omega) + \mathbf{R}^{Nq}_{arm}(\Omega)\,x^{GW}_{N}(\Omega).
\end{aligned}
\tag{4.52}
$$

We can notice that in this interferometric configuration the situation is the opposite of the Michelson interferometer. In fact in this case the dark port is towards the photodiode and the bright port towards the laser.

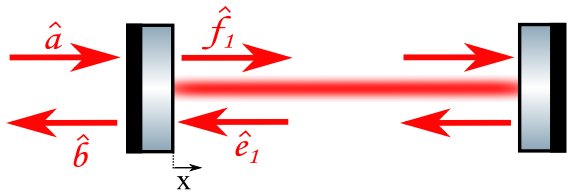

Figure 4.3: Linear cavity with massive perfectly reflective ETM.

4.2.3 Single cavity

All current interferometric gravitational wave detectors have a Michelson configuration, but, in order to increase the sensitivity, optical cavities are introduced in the arms.

When we introduce the cavity in the interferometer arms the calculation of the I/O relations is a bit different, since we have to include in the calculation another mirror between the beamsplitter and the ETM. First of all, apart from solving the transfer matrix for the beamsplitter, we have to write and solve it also for the ITM. So referring to the cavity shown in figure 4.3, the relations between the input $\mathcal{A}(t)$, the output $\mathcal{B}(t)$ and the intra-cavity fields $\mathcal{E}_1(t)$ and $\mathcal{F}_1(t)$ are

$$\mathcal{B}(t) = \sqrt{R_{ITM}}\,\mathcal{A}(t - 2x/c) + i\sqrt{T_{ITM}}\,\mathcal{E}_1(t)\,, \tag{4.53a}$$

$$\mathcal{F}_1(t) = \sqrt{R_{ITM}}\,\mathcal{E}_1(t + 2x/c) + i\sqrt{T_{ITM}}\,\mathcal{A}(t)\,, \tag{4.53b}$$

$$\mathcal{E}_1(t) = \mathcal{F}_1(t + 2L/c)\,. \tag{4.53c}$$

In the first terms of the first two equations we take into account the phase shift due to the mirror motion and in the last equation we considered that the field $\mathcal{E}_1(t)$ is simply equal to the field $\mathcal{F}_1(t)$ after a roundtrip, since we are assuming massive (so the radiation pressure can be neglected) and perfectly reflective ETM.

The solution of this system is found following the same method used in the previous sections. So after having transformed the equations into frequency domain and in the two-photon quadrature, we find that the intra-cavity and the output modes are

$$\begin{aligned}\hat{\boldsymbol{e}}_1(\Omega) &= \frac{\sqrt{T_{ITM}}\,e^{2i\Omega\tau}}{1-\sqrt{R_{ITM}}\,e^{2i\Omega\tau}}\,\hat{\sigma}\,\hat{\boldsymbol{a}}(\Omega) + \frac{2\omega_p}{c}\frac{\sqrt{R_{ITM}}\,e^{2i\Omega\tau}}{1-\sqrt{R_{ITM}}\,e^{2i\Omega\tau}}\,\hat{\sigma}\,\boldsymbol{E}_1\,x(\Omega)\\ &= \mathbb{L}(\Omega)\,\hat{\boldsymbol{a}}(\Omega) + \boldsymbol{X}(\Omega)\,x(\Omega),\end{aligned} \tag{4.54}$$

$$\begin{aligned}\hat{\boldsymbol{b}}(\Omega) &= \left(\sqrt{R_{ITM}}\,\mathbb{I} + \sqrt{T_{ITM}}\,\hat{\sigma}\,\mathbb{L}(\Omega)\right)\hat{\boldsymbol{a}}(\Omega) + \frac{2\omega_p}{c}\sqrt{R_{ITM}}\,\hat{\sigma}\left(\mathbb{L}(\Omega)\,\boldsymbol{E}_1 - \boldsymbol{A}\right)x(\Omega)\\ &= \mathbb{T}_{s.n}(\Omega)\,\hat{\boldsymbol{a}}(\Omega) + \mathbf{R}_{arm}(\Omega)\,x(\Omega).\end{aligned} \tag{4.55}$$

Now we have to include the radiation pressure effects on the mirror motion, replacing equation 4.6 in 4.55. Notice that in this case there are two beams that contribute to the radiation pressure: $\boldsymbol{E}_1$ and $\boldsymbol{A}$ and that we set as convention that the radiation pressure force due to intra-cavity field is positive and that one due to inout field is negative. Then we have

$$\begin{aligned}\hat{\boldsymbol{b}}(\Omega) =& \mathbb{T}_{s.n}(\Omega)\,\hat{\boldsymbol{a}}(\Omega) + \mathbf{R}_{arm}(\Omega)\,x^{GW}(\Omega) \\ &+ \frac{2\omega_p\hbar}{c}\,\mathbf{R}_{arm}(\Omega)\chi(\Omega)\left(\boldsymbol{E}\right)^{\dagger}\left(\mathbb{L}(\Omega)\,\hat{\boldsymbol{a}}(\Omega) + \mathbf{X}(\Omega)\,x(\Omega)\right) \\ =& \left(\mathbb{T}_{s.n.}(\Omega) + \mathbb{T}_{r.p.}(\Omega)\right)\,\hat{\boldsymbol{a}}(\Omega) + \mathbf{R}^{J}_{arm}(\Omega)\,x^{GW}(\Omega) \\ =& \mathbb{T}_{arm}(\Omega)\,\hat{\boldsymbol{a}}(\Omega) + \mathbf{R}^{J}_{arm}(\Omega)\,x^{GW}(\Omega).\end{aligned} \tag{4.56}$$

Here again we have that the additional terms in x are zero because 4.50 is still verified.

Usually at this point a Taylor expansion in τ is made in order to write the I/O relations in a clearer way. So using equations 4.9 and keeping only the first non vanishing terms we obtain

$$\mathbb{L}(\Omega) \approx \frac{1}{\gamma - i\Omega}\sqrt{\frac{\gamma}{\tau}}\,\hat{\sigma} \tag{4.57}$$

$$\mathbb{T}_{s.n.}(\Omega) \approx \left(1 - \frac{2\gamma}{\gamma - i\Omega}\right)\mathbb{I} \tag{4.58}$$

$$\mathbf{R}_{arm}(\Omega) \approx \frac{1}{(\gamma - i\Omega)}\sqrt{\frac{8\gamma P_c\omega_p}{c^2\tau^2\hbar\Omega^2}}\begin{bmatrix}0\\1\end{bmatrix} \tag{4.59}$$

$$\mathbb{T}_{r.p.}(\Omega) \approx \frac{8\omega_p\gamma P_c}{c^2\tau(\gamma - i\Omega)^2}\,\chi\begin{bmatrix}0 & 0\\-1 & 0\end{bmatrix}. \tag{4.60}$$

$$\tag{4.61}$$

Here we have used as phase reference the phase of the intra-cavity field reflected on the ITM, which has been supposed to be equal to zero. Furthermore the I/O relations are often written with the displacement x^{GW} normalised to the SQL displacement $x_{SQL} = \sqrt{\frac{2\hbar}{\mu\Omega^2}}$ and in this way the response function and the radiation pressure transfer matrix become

$$\mathbf{R}_{arm}(\Omega) \approx \frac{1}{(\gamma - i\Omega)}\sqrt{\frac{4\,\Theta\gamma}{\Omega^2}}\begin{bmatrix}0\\1\end{bmatrix}\,\frac{1}{x_{SQL}}, \tag{4.62}$$

$$\mathbb{T}_{r.p.}(\Omega) \approx \frac{2\,\Theta\gamma\,\mu}{(\gamma - i\Omega)^2}\,\chi \begin{bmatrix} 0 & 0 \\ -1 & 0 \end{bmatrix}, \tag{4.63}$$

where we have defined the normalised circulating power Θ and effective mass μ of the cavity as

$$\Theta = \frac{4\omega_p P_c}{\mu c L}, \tag{4.64}$$

$$\mu = \frac{m_{ITM} m_{ETM}}{m_{ITM} + m_{ETM}}. \tag{4.65}$$

The I/O relation finally becomes

$$\begin{aligned} \hat{\boldsymbol{b}}(\Omega) = &\left(\left(1 - \frac{1}{\gamma - i\Omega} \sqrt{\frac{\gamma}{\tau}} \right) \mathbb{I} + \frac{2\,\Theta\gamma\,\mu}{(\gamma - i\Omega)^2}\,\chi \begin{bmatrix} 0 & 0 \\ -1 & 0 \end{bmatrix} \right) \hat{\boldsymbol{a}}(\Omega) \\ &+ \frac{1}{(\gamma - i\Omega)} \sqrt{\frac{4\,\Theta\gamma}{\Omega^2}} \begin{bmatrix} 0 \\ 1 \end{bmatrix} \frac{x^{GW}}{x_{SQL}}. \end{aligned} \tag{4.66}$$

This calculation has been made considering a linear cavity, but it can be easily extended to any cavity geometry. In particular as far as we assume that all the end mirrors have reflectivity equal to 1, that they are massive test masses, so that they are not affected by radiation pressure and that there is no loss, then the solution will be same. Under these assumptions in fact, as far as it concerns this calculation, any cavity is equivalent to a linear cavity with a length equal to the total length of the path traveled by the beam to reach all the mirrors and a effective mass properly modified in order to include all mirrors.

4.2.4 Michelson with linear arm cavities

In this section we want to see how the I/O relations for a Michelson interferometer with linear arm cavities (shown in figure 4.4) can be written. Once we have the solution for a single cavity, we are able to write the full interferometer I/O relations just recombining the

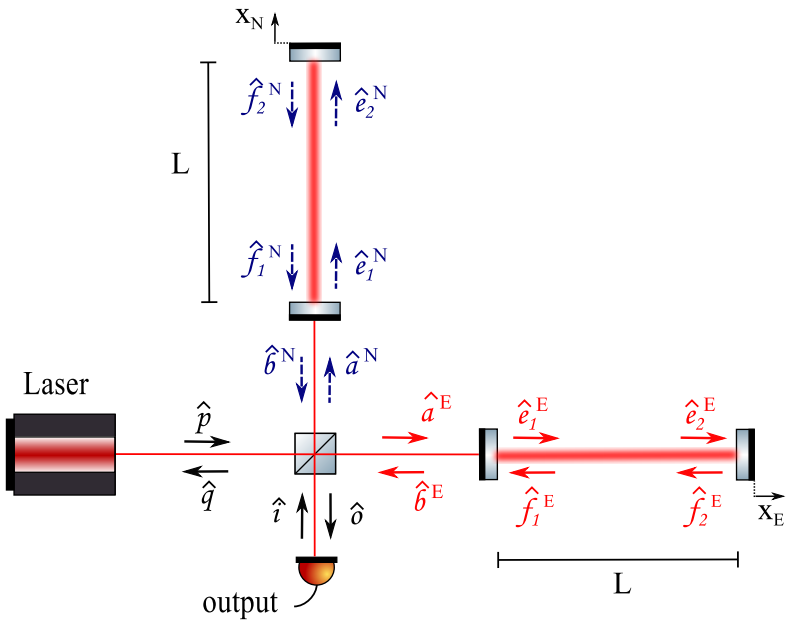

Figure 4.4: Michelson interferometer with linear arm cavities.

outputs of the two cavities at the beamsplitter[3]

$$\begin{aligned}\hat{\boldsymbol{o}}(\Omega) =& \sqrt{R_{BS}}\,\hat{\boldsymbol{b}}^{E}(\Omega) + \hat{\sigma}\,\sqrt{T_{BS}}\,\hat{\boldsymbol{b}}^{N}(\Omega) \\ =& \sqrt{R_{BS}}\left(\mathbb{T}^{E}_{arm}(\Omega)\,\hat{\boldsymbol{a}}^{E}(\Omega) + \mathbf{R}^{E}_{arm}(\Omega)\,x^{GW}_{E}(\Omega)\right) \\ &+ \hat{\sigma}\,\sqrt{T_{BS}}\left(\mathbb{T}^{N}_{arm}(\Omega)\,\hat{\boldsymbol{a}}^{N}(\Omega) + \mathbf{R}^{N}_{arm}(\Omega)\,x^{GW}_{N}(\Omega)\right)\end{aligned} \tag{4.67}$$

Then if we consider that

$$\hat{\boldsymbol{a}}^{E}(\Omega) = \hat{\sigma}\,\sqrt{T_{BS}}\,\hat{\boldsymbol{p}}(\Omega) + \sqrt{R_{BS}}\,\hat{\boldsymbol{i}}(\Omega), \tag{4.68}$$

$$\hat{\boldsymbol{a}}^{N}(\Omega) = \hat{\sigma}\,\sqrt{T_{BS}}\,\hat{\boldsymbol{i}}(\Omega) + \sqrt{R_{BS}}\,\hat{\boldsymbol{p}}(\Omega), \tag{4.69}$$

[3]Here, since we are using the two-photon formalism, the phases of the transmitted beams are included in $\hat{\sigma}$.

we can replace them in order to have the output written as a function of the inputs $\hat{\boldsymbol{p}}(\Omega)$ and $\hat{\boldsymbol{i}}(\Omega)$:

$$\begin{aligned}
\hat{\boldsymbol{o}}(\Omega) =& \sqrt{R_{BS}}\,\mathbb{T}^{E}_{arm}(\Omega)\left(\hat{\sigma}\,\sqrt{T_{BS}}\,\hat{\boldsymbol{p}}(\Omega)+\sqrt{R_{BS}}\,\hat{\boldsymbol{i}}(\Omega)\right)\\
&+\hat{\sigma}\,\sqrt{T_{BS}}\,\mathbb{T}^{N}_{arm}(\Omega)\left(\hat{\sigma}\,\sqrt{T_{BS}}\,\hat{\boldsymbol{i}}(\Omega)+\sqrt{R_{BS}}\,\hat{\boldsymbol{p}}(\Omega)\right)\\
&+\sqrt{R_{BS}}\,\mathbf{R}^{E}_{arm}(\Omega)\,x^{GW}_{E}(\Omega)+\hat{\sigma}\,\sqrt{T_{BS}}\,\mathbf{R}^{N}_{arm}(\Omega)\,x^{GW}_{N}(\Omega)\\
=&\underbrace{\left(R_{BS}\,\mathbb{T}^{E}_{arm}(\Omega)+T_{BS}\,\mathbb{T}^{N}_{arm}(\Omega)\right)}_{\mathbb{T}^{io}_{mic}(\Omega)}\hat{\boldsymbol{i}}(\Omega)\\
&\underbrace{+\hat{\sigma}\,\sqrt{R_{BS}T_{BS}}\left(\mathbb{T}^{E}_{arm}(\Omega)+\mathbb{T}^{N}_{arm}(\Omega)\right)}_{\mathbb{T}^{po}_{mic}(\Omega)}\hat{\boldsymbol{p}}(\Omega)\\
&\underbrace{+\sqrt{R_{BS}}\,\mathbf{R}^{E}_{arm}(\Omega)}_{\mathbf{R}^{Eo}_{mic}(\Omega)}\,x^{GW}_{E}(\Omega)+\underbrace{\hat{\sigma}\,\sqrt{T_{BS}}\,\mathbf{R}^{N}_{arm}(\Omega)}_{\mathbf{R}^{No}_{mic}(\Omega)}\,x^{GW}_{N}(\Omega)\\
=&\,\mathbb{T}^{io}_{mic}(\Omega)\,\hat{\boldsymbol{i}}(\Omega)+\mathbb{T}^{po}_{mic}(\Omega)\,\hat{\boldsymbol{p}}(\Omega)+\mathbf{R}^{Eo}_{mic}(\Omega)\,x^{GW}_{E}(\Omega)+\mathbf{R}^{No}_{mic}(\Omega)\,x^{GW}_{N}(\Omega)
\end{aligned}\tag{4.70}$$

and

$$\begin{aligned}
\hat{\boldsymbol{q}}(\Omega) =& \sqrt{R_{BS}}\,\mathbb{T}^{E}_{arm}(\Omega)\left(\hat{\sigma}\,\sqrt{T_{BS}}\,\hat{\boldsymbol{i}}(\Omega)+\sqrt{R_{BS}}\,\hat{\boldsymbol{p}}(\Omega)\right)\\
&+\hat{\sigma}\,\sqrt{T_{BS}}\,\mathbb{T}^{N}_{arm}(\Omega)\left(\hat{\sigma}\,\sqrt{T_{BS}}\,\hat{\boldsymbol{p}}(\Omega)+\sqrt{R_{BS}}\,\hat{\boldsymbol{i}}(\Omega)\right)\\
&+\sqrt{R_{BS}}\,\mathbf{R}^{Eq}_{arm}(\Omega)\,x^{GW}_{E}(\Omega)+\hat{\sigma}\,\sqrt{T_{BS}}\,\mathbf{R}^{Nq}_{arm}(\Omega)\,x^{GW}_{N}(\Omega)\\
=&\underbrace{\left(R_{BS}\,\mathbb{T}^{E}_{arm}(\Omega)-T_{BS}\,\mathbb{T}^{N}_{arm}(\Omega)\right)}_{\mathbb{T}^{pq}_{mic}(\Omega)}\hat{\boldsymbol{p}}(\Omega)+\underbrace{\hat{\sigma}\,\sqrt{R_{BS}T_{BS}}\left(\mathbb{T}^{E}_{arm}(\Omega)+\mathbb{T}^{N}_{arm}(\Omega)\right)}_{\mathbb{T}^{iq}_{mic}(\Omega)}\hat{\boldsymbol{i}}(\Omega)\\
&+\underbrace{\sqrt{R_{BS}}\,\mathbf{R}^{Eq}_{arm}(\Omega)}_{\mathbf{R}^{Eq}_{mic}(\Omega)}\,x^{GW}_{E}(\Omega)+\underbrace{\hat{\sigma}\,\sqrt{T_{BS}}\,\mathbf{R}^{Nq}_{arm}(\Omega)}_{\mathbf{R}^{Nq}_{mic}(\Omega)}\,x^{GW}_{N}(\Omega)\\
=&\,\mathbb{T}^{iq}_{mic}(\Omega)\,\hat{\boldsymbol{i}}(\Omega)+\mathbb{T}^{pq}_{mic}(\Omega)\,\hat{\boldsymbol{p}}(\Omega)+\mathbf{R}^{Eq}_{mic}(\Omega)\,x^{GW}_{E}(\Omega)+\mathbf{R}^{Nq}_{mic}(\Omega)\,x^{GW}_{N}(\Omega).
\end{aligned}\tag{4.71}$$

From the previous equations we can see that, as before, for a Michelson interferometer, in

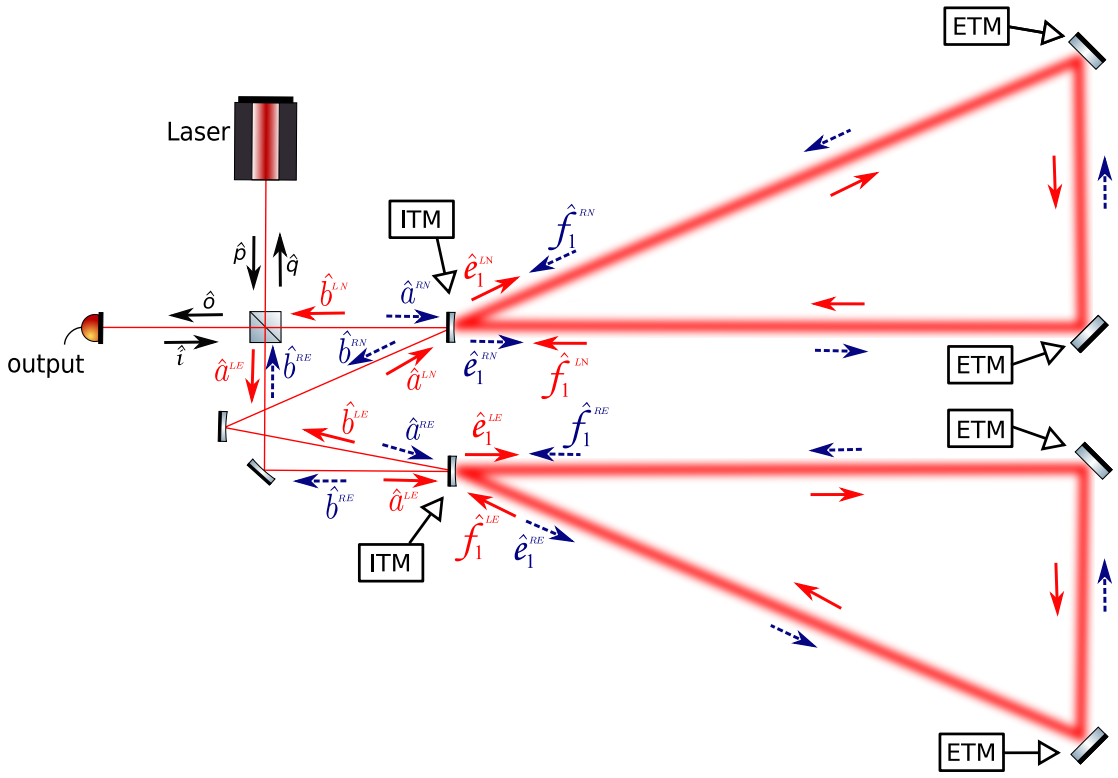

Figure 4.5: Sagnac interferometer with triangular arm cavities.

case we have identical cavities and a perfect 50:50 beamsplitter, the dark port corresponds input port (where the laser is placed) and the bright corresponds to the readout port (where the photodiode is placed).

4.2.5 Sagnac with triangular arm cavities

We want now to obtain the I/O relation for a Sagnac interferometer with triangular arm cavities. This configuration is similar to that one used for the Glasgow SSM proof-of-concept experiment described in chapter 3. As done before, we consider that the two ETM have a reflectivity equal to one and no loss. In this way the shape of the cavity does not affect the results because it will behave exactly the same as a linear cavity (or any other geometry) with the same length.

The main difference between a Michelson and a Sagnac interferometer is the fact that in the latter there are two beams circulating in the cavity and one of them is the output of the other cavity. This means that the results for a single cavity is the same as the Michelson, but we have then to replace one of the inputs with the output of the other cavity.

So first we need the I/O relations for a single cavity calculated in section 4.2.3, but in this case we have two beams circulating in each cavity and then we have to consider the solution

for each of them. However, since the two beams do not couple, the solution will be the same. So we can rewrite equations 4.54 and 4.55 in the general form

$$\begin{aligned}\hat{\boldsymbol{e}}_1^{IJ}(\Omega) &= \frac{\sqrt{T_{ITM}}\, e^{2i\Omega\tau}}{1-\sqrt{R_{ITM}}\, e^{2i\Omega\tau}}\,\hat{\sigma}\,\hat{\boldsymbol{a}}^{IJ}(\Omega) + \frac{2\omega_p}{c}\frac{\sqrt{R_{ITM}}\, e^{2i\Omega\tau}}{1-\sqrt{R_{ITM}}\, e^{2i\Omega\tau}}\,\hat{\sigma}\,\boldsymbol{E}_{IJ}\, x_J(\Omega) \\ &= \mathbb{L}_J(\Omega)\,\hat{\boldsymbol{a}}^{IJ}(\Omega) + \frac{2\omega_p}{c}\sqrt{\frac{R_{ITM}}{T_{ITM}}}\,\mathbb{L}_J(\Omega)\,\boldsymbol{E}_{IJ}\, x_J(\Omega),\end{aligned} \tag{4.72}$$

$$\begin{aligned}\hat{\boldsymbol{b}}^{IJ}(\Omega) &= \underbrace{\left(\sqrt{R_{ITM}}\,\mathbb{I} + \sqrt{T_{ITM}}\,\mathbb{L}_J(\Omega)\right)}_{\mathbb{T}_{s.n}^{IJ}(\Omega)}\hat{\boldsymbol{a}}_{IJ}(\Omega) \\ &\quad \underbrace{+\frac{2\omega_p}{c}\sqrt{R_{ITM}}\,\hat{\sigma}\,\mathbb{L}_J(\Omega)\boldsymbol{E}_{IJ}}_{\mathbf{R}_{arm}^{IJ}(\Omega)}\, x_J(\Omega) \\ &= \mathbb{T}_{s.n.}^{IJ}(\Omega)\,\hat{\boldsymbol{a}}^{IJ}(\Omega) + \mathbf{R}_{arm}^{IJ}(\Omega)\, x_J(\Omega),\end{aligned} \tag{4.73}$$

where $I = R, L$ (right and left) stands for the beam's direction of propagation and $J = N, E$ (North and East) stands for the cavity[4] .

At this point we need to split x_J into the motion due to radiation pressure and the motion due to the signal as done in section 4.1. but in this case we have four beams that contribute to the radiation pressure force, two intra-cavity and two input beams. However usually the contributions of the input beams are neglected, because of the much smaller value of the

[4]The justification of the choice of the notations is probably not immediate and needs an explanation. The direction of propagation of the beam can be clockwise (the beam goes first in the North cavity and then in the East cavity) or counterclockwise, but for shortness we will refer to them as R and L respectively. For the cavities, instead, we will use the notation of North and East cavity, commonly used to indicate the cavities of GW detectors, even if in our layout the arms are not perpendicular to each other.

power.

$$\begin{aligned}
\hat{\boldsymbol{b}}^{IJ}(\Omega) =& \mathbb{T}^{IJ}_{s.n.}(\Omega)\,\hat{\boldsymbol{a}}^{IJ}(\Omega) + \mathbf{R}^{IJ}_{arm}(\Omega)\,x^{GW}_{J}(\Omega) \\
&+ \mathbf{R}^{IJ}_{arm}(\Omega)\,\chi_J(\Omega)\frac{\hbar\omega_p}{c}\left(\boldsymbol{A}^{IJ}\right)^{\dagger}\hat{\boldsymbol{a}}^{IJ}(\Omega) + \mathbf{R}^{IJ}_{arm}(\Omega)\,\chi_J(\Omega)\frac{\hbar\omega_p}{c}\left(\boldsymbol{A}^{\bar{I}J}\right)^{\dagger}\hat{\boldsymbol{a}}^{\bar{I}J}(\Omega) \\
&+ \mathbf{R}^{IJ}_{arm}(\Omega)\,\chi_J(\Omega)\frac{\hbar\omega_p}{c}\left(\boldsymbol{E}^{IJ}\right)^{\dagger}\left(\mathbb{L}_J(\Omega)\,\hat{\boldsymbol{a}}^{IJ}(\Omega) + \frac{1}{\sqrt{T_{ITM}}}\mathbf{R}^{IJ}_{arm}(\Omega)\,x_J(\Omega)\right) \\
&+ \mathbf{R}^{IJ}_{arm}(\Omega)\,\chi_J(\Omega)\frac{\hbar\omega_p}{c}\left(\boldsymbol{E}^{\bar{I}J}\right)^{\dagger}\left(\mathbb{L}_J(\Omega)\,\hat{\boldsymbol{a}}^{\bar{I}J}(\Omega) + \frac{1}{\sqrt{T_{ITM}}}\mathbf{R}^{\bar{I}J}_{arm}(\Omega)\,x_J(\Omega)\right) \\
=& \left(\mathbb{T}^{IJ}_{s.n.}(\Omega) + \mathbb{T}^{IJ}_{r.p.}(\Omega)\right)\hat{\boldsymbol{a}}^{IJ}(\Omega) + \mathbb{T}^{\bar{I}J}_{arm,r.p.}(\Omega)\,\hat{\boldsymbol{a}}^{\bar{I}J}(\Omega) + \mathbf{R}^{IJ}_{arm}(\Omega)\,x^{GW}_{J}(\Omega) \\
=& \mathbb{T}^{IJ}_{arm}(\Omega)\,\hat{\boldsymbol{a}}^{IJ}(\Omega) + \mathbb{T}^{\bar{I}J}_{arm,r.p.}(\Omega)\,\hat{\boldsymbol{a}}^{\bar{I}J}(\Omega) + \mathbf{R}^{IJ}_{arm}(\Omega)\,x^{GW}_{J}(\Omega).
\end{aligned} \tag{4.74}$$

Here again we have that the additional terms in x_J are zero because 4.50 is still verified.

In order to find the full interferometer I/O relations, we have now to consider that one of the input beams of one cavity is the output of the other and vice versa. So, using the notation shown in figure 4.5 for the beams nomenclature, we have to replace in the previous equation

$$\hat{\boldsymbol{a}}^{LN}(\Omega) = \hat{\boldsymbol{b}}^{LE}(\Omega), \qquad \hat{\boldsymbol{a}}^{RE}(\Omega) = \hat{\boldsymbol{b}}^{RN}(\Omega). \tag{4.75}$$

In this way we found that the two beams that leave the cavity and go back to the beam-

splitter are [89]

$$
\begin{aligned}
\hat{\boldsymbol{b}}^{LN}(\Omega) = & \underbrace{\mathbb{T}^{LN}_{arm}(\Omega)\,\mathbb{Q}_{L}(\Omega)\,\mathbb{T}^{LE}_{arm}(\Omega)}_{\mathbb{T}^{LE}_{LN}(\Omega)}\,\hat{\boldsymbol{a}}^{LE}(\Omega) \\
& + \underbrace{\left(\mathbb{T}^{RN}_{arm,r.p.}(\Omega) + \mathbb{T}^{LN}_{arm}(\Omega)\,\mathbb{Q}_{L}(\Omega)\,\mathbb{T}^{RE}_{arm,r.p.}(\Omega)\,\mathbb{T}^{RN}_{arm}(\Omega)\right)}_{\mathbb{T}^{RN}_{LN}(\Omega)}\hat{\boldsymbol{a}}^{RN}(\Omega) \\
& + \underbrace{\left(\mathbf{R}^{LN}_{arm}(\Omega) + \mathbb{T}^{LN}_{arm}(\Omega)\,\mathbb{Q}_{L}(\Omega)\,\mathbb{T}^{RE}_{arm,r.p.}(\Omega)\,\mathbf{R}^{RN}_{arm}(\Omega)\right)}_{\mathbf{R}^{N}_{LN}(\Omega)}\,x_{N}(\Omega) \\
& + \underbrace{\mathbb{T}^{LN}_{arm}(\Omega)\,\mathbb{Q}_{L}(\Omega)\,\mathbf{R}^{LE}_{arm}(\Omega)}_{\mathbf{R}^{E}_{LN}(\Omega)}\,x_{E}(\Omega) \\
= & \mathbb{T}^{LE}_{LN}(\Omega)\,\hat{\boldsymbol{a}}^{LE}(\Omega) + \mathbb{T}^{RN}_{LN}(\Omega)\,\hat{\boldsymbol{a}}^{RN}(\Omega) + \mathbf{R}^{N}_{LN}(\Omega)\,x_{N}(\Omega) + \mathbf{R}^{E}_{LN}(\Omega)\,x_{E}(\Omega);
\end{aligned}
\tag{4.76}
$$

and

$$
\begin{aligned}
\hat{\boldsymbol{b}}^{RE}(\Omega) = & \underbrace{\mathbb{T}^{RE}_{arm}(\Omega)\,\mathbb{Q}_{R}(\Omega)\,\mathbb{T}^{RN}_{arm}(\Omega)}_{\mathbb{T}^{RN}_{RE}(\Omega)}\,\hat{\boldsymbol{a}}^{RN}(\Omega) \\
& + \underbrace{\left(\mathbb{T}^{LE}_{arm,r.p.}(\Omega) + \mathbb{T}^{RE}_{arm}(\Omega)\,\mathbb{Q}^{R}(\Omega)\,\mathbb{T}^{LN}_{arm,r.p.}(\Omega)\,\mathbb{T}^{LE}_{arm}(\Omega)\right)}_{\mathbb{T}^{LE}_{RE}(\Omega)}\hat{\boldsymbol{a}}^{LE}(\Omega) \\
& + \underbrace{\left(\mathbf{R}^{RE}_{arm}(\Omega) + \mathbb{T}^{RE}_{arm}(\Omega)\,\mathbb{Q}_{R}(\Omega)\,\mathbb{T}^{LN}_{arm,r.p.}(\Omega)\,\mathbf{R}^{LE}_{arm}(\Omega)\right)}_{\mathbf{R}^{E}_{RE}(\Omega)}\,x_{E}(\Omega) \\
& + \underbrace{\mathbb{T}^{RE}_{arm}(\Omega)\,\mathbb{Q}_{R}(\Omega)\,\mathbf{R}^{RN}_{arm}(\Omega)}_{\mathbf{R}^{N}_{RE}(\Omega)}\,x_{N}(\Omega) \\
= & \mathbb{T}^{RN}_{RE}(\Omega)\,\hat{\boldsymbol{a}}^{RN}(\Omega) + \mathbb{T}^{LE}_{RE}(\Omega)\,\hat{\boldsymbol{a}}^{LE}(\Omega) + \mathbf{R}^{N}_{RE}(\Omega)\,x_{N}(\Omega) + \mathbf{R}^{E}_{RE}(\Omega)\,x_{E}(\Omega);
\end{aligned}
\tag{4.77}
$$

with

$$
\mathbb{Q}_{L} = \left(\mathbb{I} - \mathbb{T}^{RE}_{arm,r.p}\,\mathbb{T}^{LN}_{arm,r.p.}\right)^{-1}, \tag{4.78}
$$

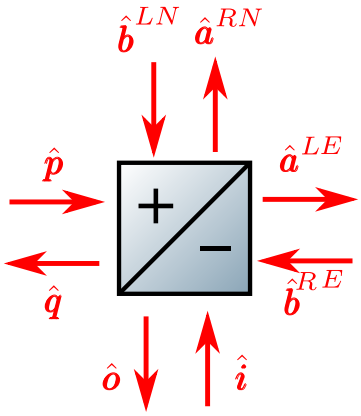

Figure 4.6: Input and output beams at the beamsplitter. The beams in reflection on the upper side are supposed to have a phase shift equal to zero and that one ones on the lower side have a phase shift equal to π.

$$\mathbb{Q}_R = \left(\mathbb{I} - \mathbb{T}^{LN}_{arm,r.p} \mathbb{T}^{RE}_{arm,r.p.} \right)^{-1}. \tag{4.79}$$

Finally, the full interferometers I/O relations are found using the beamsplitter transfer matrix. However in this case is more convenient to use a different convention for the phases, in order that the two cavity input beams have the same phase. So we define the phase in transmission equal to zero and the phase in reflection equal to π on one side and zero on the other side, as shown in figure 4.6.

So the beamsplitter transfer matrix can be written as

$$\begin{bmatrix} \hat{\boldsymbol{a}}^{RN}(\Omega) \\ \hat{\boldsymbol{a}}^{LE}(\Omega) \\ \hat{\boldsymbol{q}}(\Omega) \\ \hat{\boldsymbol{o}}(\Omega) \end{bmatrix} = \begin{bmatrix} \sqrt{R_{BS}} & \sqrt{T_{BS}} & 0 & 0 \\ \sqrt{T_{BS}} & -\sqrt{R_{BS}} & 0 & 0 \\ 0 & 0 & \sqrt{R_{BS}} & \sqrt{T_{BS}} \\ 0 & 0 & \sqrt{T_{BS}} & -\sqrt{R_{BS}} \end{bmatrix} \times \begin{bmatrix} \hat{\boldsymbol{p}}(\Omega) \\ \hat{\boldsymbol{i}}(\Omega) \\ \hat{\boldsymbol{b}}^{LN}(\Omega) \\ \hat{\boldsymbol{b}}^{RE}(\Omega) \end{bmatrix}, \tag{4.80}$$

and the output $\hat{\boldsymbol{o}}(\Omega)$ is then

$$\begin{aligned}
\hat{\boldsymbol{o}}(\Omega) &= -\sqrt{R_{BS}}\,\hat{\boldsymbol{b}}^{RE}(\Omega) + \sqrt{T_{BS}}\,\hat{\boldsymbol{b}}^{LN}(\Omega) \\
&= -\sqrt{R_{BS}}\left(\mathbb{T}_{RE}^{RN}(\Omega)\,\hat{\boldsymbol{a}}^{RN}(\Omega) + \mathbb{T}_{RE}^{LE}(\Omega)\,\hat{\boldsymbol{a}}^{LE}(\Omega) + \mathbf{R}_{RE}^{N}(\Omega)\,x_N(\Omega) + \mathbf{R}_{RE}^{E}(\Omega)\,x_E(\Omega)\right) \\
&\quad + \sqrt{T_{BS}}\left(\mathbb{T}_{LN}^{RN}(\Omega)\,\hat{\boldsymbol{a}}^{RN}(\Omega) + \mathbb{T}_{LN}^{LE}(\Omega)\,\hat{\boldsymbol{a}}^{LE}(\Omega) + \mathbf{R}_{LN}^{N}(\Omega)\,x_N(\Omega) + \mathbf{R}_{LN}^{E}(\Omega)\,x_E(\Omega)\right) \\
&= \left(-\sqrt{R_{BS}}\,\mathbb{T}_{RE}^{RN}(\Omega) + \sqrt{T_{BS}}\,\mathbb{T}_{LN}^{RN}(\Omega)\right)\hat{\boldsymbol{a}}^{RN}(\Omega) \\
&\quad + \left(\sqrt{R_{BS}}\,\mathbb{T}_{RE}^{LE}(\Omega) + \sqrt{T_{BS}}\,\mathbb{T}_{LN}^{LE}(\Omega)\right)\hat{\boldsymbol{a}}^{LE}(\Omega) \\
&\quad + \underbrace{\left(-\sqrt{R_{BS}}\,\mathbf{R}_{RE}^{E}(\Omega) + \sqrt{T_{BS}}\,\mathbf{R}_{LN}^{E}(\Omega)\right)}_{\mathbf{R}_{sag}^{Eo}} x_E(\Omega) \\
&\quad + \underbrace{\left(-\sqrt{R_{BS}}\,\mathbf{R}_{RE}^{N}(\Omega) + \sqrt{T_{BS}}\,\mathbf{R}_{LN}^{N}(\Omega)\right)}_{\mathbf{R}_{sag}^{No}} x_N(\Omega)
\end{aligned} \tag{4.81}$$

We can now replace the cavity input beams $\hat{\boldsymbol{a}}^{RN}(\Omega)$ and $\hat{\boldsymbol{a}}^{LE}(\Omega)$ with the interferometer input beams $\hat{\boldsymbol{p}}(\Omega)$ and $\hat{\boldsymbol{i}}(\Omega)$ using equations that come from the beamsplitter transfer matrix.

Finally we have

$$
\begin{aligned}
\hat{\boldsymbol{o}}(\Omega) = &\left(-\sqrt{R_{BS}}\,\mathbb{T}_{RE}^{RN}(\Omega) + \sqrt{T_{BS}}\,\mathbb{T}_{LN}^{RN}(\Omega)\right)\left(\sqrt{R_{BS}}\,\hat{\boldsymbol{p}}(\Omega) + \sqrt{T_{BS}}\,\hat{\boldsymbol{i}}(\Omega)\right) \\
&+ \left(-\sqrt{R_{BS}}\,\mathbb{T}_{RE}^{LE}(\Omega) + \sqrt{T_{BS}}\,\mathbb{T}_{LN}^{LE}(\Omega)\right)\left(-\sqrt{R_{BS}}\,\hat{\boldsymbol{i}}(\Omega) + \sqrt{T_{BS}}\,\hat{\boldsymbol{p}}(\Omega)\right) \\
&+ \mathbf{R}_{sag}^{No}(\Omega)\,x_N(\Omega) + \mathbf{R}_{sag}^{Eo}(\Omega)\,x_E(\Omega) \\
= &\underbrace{\left(-R_{BS}\,\mathbb{T}_{RE}^{RN}(\Omega) + \sqrt{R_{BS}T_{BS}}\,\mathbb{T}_{LN}^{RN}(\Omega) - \sqrt{R_{BS}T_{BS}}\,\mathbb{T}_{RE}^{LE}(\Omega) + T_{BS}\,\mathbb{T}_{LN}^{LE}(\Omega)\right)}_{\mathbb{T}_{sag}^{po}(\Omega)}\hat{\boldsymbol{p}}(\Omega) \\
&+ \underbrace{\left(R_{BS}\,\mathbb{T}_{RE}^{LE}(\Omega) - \sqrt{R_{BS}T_{BS}}\,\mathbb{T}_{LN}^{LE}(\Omega) - \sqrt{R_{BS}T_{BS}}\,\mathbb{T}_{RE}^{RN}(\Omega) + T_{BS}\,\mathbb{T}_{LN}^{RN}(\Omega)\right)}_{\mathbb{T}_{sag}^{io}(\Omega)}\hat{\boldsymbol{i}}(\Omega) \\
&+ \mathbf{R}_{sag}^{No}(\Omega)\,x_N(\Omega) + \mathbf{R}_{sag}^{Eo}(\Omega)\,x_E(\Omega) \\
= &\mathbb{T}_{sag}^{po}(\Omega)\,\hat{\boldsymbol{p}}(\Omega) + \mathbb{T}_{sag}^{io}(\Omega)\,\hat{\boldsymbol{i}}(\Omega) + \mathbf{R}_{sag}^{No}(\Omega)\,x_N(\Omega) + \mathbf{R}_{sag}^{Eo}(\Omega)\,x_E(\Omega).
\end{aligned}
\tag{4.82}
$$

And, following the same steps, the other output is found to be

$$
\begin{aligned}
\hat{\boldsymbol{q}}(\Omega) =& \sqrt{R_{BS}}\,\hat{\boldsymbol{b}}^{LN}(\Omega) + \sqrt{T_{BS}}\,\hat{\boldsymbol{b}}^{RE}(\Omega) \\
=& \underbrace{\left(R_{BS}\,\mathbb{T}_{LN}^{RN}(\Omega) + \sqrt{R_{BS}T_{BS}}\,\mathbb{T}_{RE}^{RN}(\Omega) + \sqrt{R_{BS}T_{BS}}\,\mathbb{T}_{LN}^{LE}(\Omega) + T_{BS}\mathbb{T}_{RE}^{LE}(\Omega) \right)}_{\mathbb{T}_{pq}^{sag}(\Omega)} \hat{\boldsymbol{p}}(\Omega) \\
&+ \underbrace{\left(-R_{BS}\,\mathbb{T}_{LN}^{LE}(\Omega) + \sqrt{R_{BS}T_{BS}}\,\mathbb{T}_{LN}^{RN}(\Omega) - \sqrt{R_{BS}T_{BS}}\,\mathbb{T}_{RE}^{LE}(\Omega) + T_{BS}\mathbb{T}_{RE}^{RN}(\Omega) \right)}_{\mathbb{T}_{iq}^{sag}(\Omega)} \hat{\boldsymbol{i}}(\Omega) \\
&+ \underbrace{\left(\sqrt{R_{BS}}\,\mathbf{R}_{LN}^{N}(\Omega) + \sqrt{T_{BS}}\,\mathbf{R}_{RE}^{N}(\Omega) \right)}_{\mathbf{R}_{sag}^{Nq}(\Omega)} x_N(\Omega) \\
&+ \underbrace{\left(\sqrt{R_{BS}}\,\mathbf{R}_{LN}^{E}(\Omega) + \sqrt{T_{BS}}\,\mathbf{R}_{RE}^{E}(\Omega) \right)}_{\mathbf{R}_{sag}^{Eq}(\Omega)} x_E(\Omega) \\
=& \mathbb{T}_{pq}^{sag}(\Omega)\,\hat{\boldsymbol{p}}(\Omega) + \mathbb{T}_{iq}^{sag}(\Omega)\,\hat{\boldsymbol{i}}(\Omega) + \mathbf{R}_{sag}^{Nq}(\Omega)\,x_N(\Omega) + \mathbf{R}_{sag}^{Eq}(\Omega)x_E(\Omega).
\end{aligned}
\tag{4.83}
$$

From equations 4.82 and 4.83 we can see that in case of two identical cavities, a perfect beamsplitter ratio of 50:50 and the laser providing the only input field, we have again that the port toward the laser is the bright port and the port towards the photodiode is the dark port. In this case it is probably not as immediate as before to see that because, in order to make the equations less cumbersome, we introduced the transfer matrices $\mathbb{T}(\Omega)$. However, it becomes more clear if we notice that because of the symmetry of the system we have $\mathbb{T}_{RE}^{LN}(\Omega) = \mathbb{T}_{LN}^{LE}(\Omega)$ and $\mathbb{T}_{RN}^{LN}(\Omega) = \mathbb{T}_{RE}^{LE}(\Omega)$, which makes the term in $\hat{\boldsymbol{p}}(\Omega)$ in equation 4.82 vanish.

4.3 Detuned cavities and optical rigidity

A cavity is said to be detuned when it is slightly off from its resonance condition, i.e. when $\omega_0\tau = n\pi + \theta$, with n an integer and $\theta \neq 0$. This fact will induce a phase shift θ of the field propagating inside the cavity and a rotation of the quadratures of the field. In fact, the intra-cavity field in a detuned cavity will have a non-zero component in both sine and

cosine quadrature, since equation 4.57 becomes [89]

$$\mathbb{L}_J(\Omega) = \frac{1}{(\gamma - i\Omega)^2 + \delta^2} \sqrt{\frac{\gamma}{\tau}} \left((\gamma - i\Omega)\, \hat{\sigma} + \delta\, \mathbb{I} \right), \tag{4.84}$$

where $\delta \equiv \theta/\tau$ is the detuning from the cavity resonance frequency. This means that the equation 4.50 is not valid anymore and then the additional terms in x_J in equation 4.74 are not zero anymore.

In order to understand the physical meaning of this additional term, we have to understand first what happens in a detuned cavity. The mirror displacement changes the resonance frequency of the cavity and then the intra-cavity power will change according to the equation [51]

$$P_c = \frac{\gamma^2}{\gamma^2 + \left(\delta + \omega_0 \frac{x}{L}\right)^2} P_c^{max}, \tag{4.85}$$

where P_c^{max} is the intra-cavity power without detuning. This means that the radiation pressure force, that is equal to P_c/c, depends on the position of the mirror and the derivative of the force is defined as the *rigidity* of the cavity:

$$K(\Omega) = -\frac{1}{c}\frac{dP_c}{dx} = -\frac{2P_c\omega_0}{Lc} \frac{\delta}{(\Omega - \delta + i\gamma)(\Omega + \delta + i\gamma)}. \tag{4.86}$$

For sideband frequencies $\Omega < \delta$ and $\Omega < \gamma$, the previous equation can be approximated performing the Taylor expansion, that gives

$$K(\Omega) \approx \frac{2P_c\omega_0}{Lc} \left(\frac{\delta}{\gamma^2 + \delta^2} + \frac{2i\gamma\delta}{(\gamma^2 + \delta^2)^2} \Omega \right) \equiv K_{opt} - i\gamma_{opt}\Omega. \tag{4.87}$$

In this way we are able to split the real part that correspond to the rigidity and an imaginary part that represents a damping term. To have an idea of the meaning of these two terms we can think of them as a restoring force (like a spring with a spring constant equal to K_{opt} attached to the mirror) and a viscous damping force, which will always go against the other. We can notice, indeed, that the two terms will always have opposite sign, so when one is positive the other one is negative and vice versa. This means that the system will always be unstable.

The plot of the intra-cavity power, the rigidity and the damping terms are shown in figure 4.7.

So the additional term in x is the rigidity and the force described in equation 4.4 will have two terms: the radiation pressure force and the optical rigidity, i.e.

$$\tilde{F}(\Omega) = F_{r.p.}(\Omega) - K(\Omega)x. \tag{4.88}$$

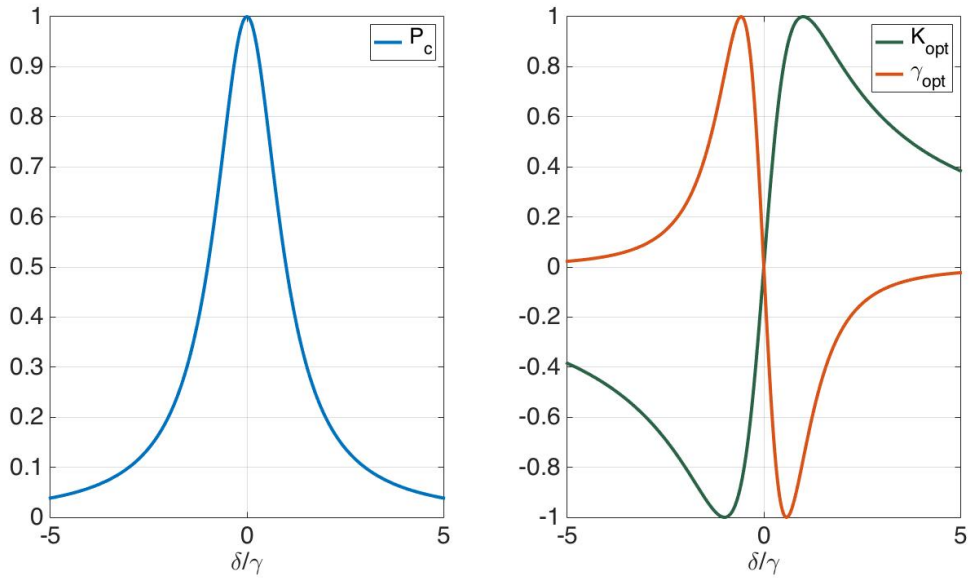

Figure 4.7: *Left*: intra-cavity power as a function of the cavity detuning relative to the half-bandwidth. *Right*: real (rigidity) and imaginary (damping) terms of the optical spring constant $K(\Omega)$. All plots are normalised to their respective maxima, which corresponds to $\delta = 1$ for K_{opt} and $\delta = -1/\sqrt{3}$ for γ_{opt}.

When the rigidity is non-zero we have to redefine the mechanical susceptibility defined in equation 4.7 as

$$\chi_J^{new}(\Omega) = \frac{\chi_J(\Omega)}{1 + \chi_J(\Omega)K(\Omega)} \tag{4.89}$$

and the I/O relation of the cavity can be written simply replacing $\chi_J(\Omega)$ with $\chi_J^{new}(\Omega)$.

4.4 Quantum noise

We have already introduced the quantum noise in chapter 3, where we explained its origin and physical meaning. However in this section we will give details on how the quantum noise can be calculated practically in the framework of the two-photon formalism and we will show the results for the configurations described in the previous section.

Once we have the contribution of shot noise and radiation pressure noise in the I/O relations, the quantum noise power spectral density (PSD) and the quantum noise limited sensitivity of the interferometer can be calculated. The PSD of the quantum noise is calculated summing the contribution of the optical response of each field relative to the output. So if the I/O relations are written in the general form

$$\hat{\boldsymbol{o}}(\Omega) = \sum_i \mathbb{T}_i(\Omega)\,\hat{\boldsymbol{i}}_i(\Omega), \tag{4.90}$$

with $\hat{\boldsymbol{i}}_i(\Omega)$ the input fields, then the PSD of the quantum noise is simply given by the sum of the PSD of the contribution of each field, i.e. [50]

$$S_{qn}(\Omega) = \sum_i \mathbb{T}_i^\dagger(\Omega) \cdot \mathbb{S}_i^{in}(\Omega) \cdot \mathbb{T}_i(\Omega), \tag{4.91}$$

where $\mathbb{S}_i^{in}(\Omega)$ is the spectral density matrix of the input field as defined in 2.18.

There are different methods to read the output signal of the interferometer. However if we want to be able to take into account both quadratures of the output field, we can use for example a balanced homodyne detector, described in section 3.4.3 and used also as readout method for the Glasgow SSM. In this way we can define the homodyne vector $\mathbf{H}_\zeta$ as

$$\mathbf{H}_\zeta = \begin{bmatrix} \cos\zeta \\ \sin\zeta \end{bmatrix}, \tag{4.92}$$

where ζ is the homodyne angle, and the PSD of the quantum noise becomes

$$S_{qn}(\Omega) = \sum_i \mathbf{H}_\zeta^\dagger \cdot \mathbb{T}_i^\dagger(\Omega) \cdot \mathbb{S}_i^{in}(\Omega) \cdot \mathbb{T}_i(\Omega) \cdot \mathbf{H}_\zeta. \tag{4.93}$$

In order to estimate the quantum noise limited sensitivity we have to normalise the PSD in the appropriate way in order to have the sensitivity referred to the chosen variable. In GW detectors the sensitivity is often expressed in terms of the strain or simply in terms of displacement x_- of the mirrors differential motion, defined as

$$x_- = x_N - x_E. \tag{4.94}$$

The PSD of the quantum noise limited sensitivity in terms of the displacement can then be written as

$$S_x(\Omega) = x_{SQL}^2(\Omega)\, \frac{\sum_i \mathbf{H}_\zeta^\dagger \cdot \mathbb{T}_i^\dagger(\Omega) \cdot \mathbb{S}_i^{in}(\Omega) \cdot \mathbb{T}_i(\Omega) \cdot \mathbf{H}_\zeta}{\left|\mathbf{H}_\zeta^\dagger \cdot \mathbf{R}^-(\Omega)\right|^2}, \tag{4.95}$$

where $\mathbf{R}^-(\Omega)$ is the response function of the interferometer to the differential motion of the mirrors

$$\mathbf{R}^-(\Omega) = \frac{\mathbf{R}^N(\Omega) - \mathbf{R}^E(\Omega)}{2}. \tag{4.96}$$

In figure 4.8 the plots of the quantum noise are shown for interferometers with and without cavities, as described in the previous section. In both figures the big plot on the left shows the quantum noise limited sensitivity and the two small plots on the right show the quantum noise amplitude spectral density and the response function of the interferometer

to the differential mirror motion[5]. As we can see, in both case the quantum noise limited sensitivity of the Sagnac interferometer is better than the equivalent Michelson, especially at low frequencies. The reason why this happens is clear if we look at the behaviour of the quantum noise and the response function for the two topologies of interferometer. At low frequencies, in fact, we have that:

- the quantum noise amplitude spectral density of the Michelson interferometer goes like $1/f^2$, while in the Sagnac it is constant;
- the response function is constant in the Michelson and goes like f in the Sagnac.

The quantum noise limited sensitivity according to equation 4.95 is given by the ratio of the these two functions. So at low frequencies, i.e. before the point of minimum, it is proportional to $1/f^2$ in the Michelson and proportional to $1/f$ in the Sagnac. This means that the quantum noise limited sensitivity of a Sagnac interferometer at low frequencies will always be higher than an equivalent Michelson.

4.5 Conclusions

In this chapter we showed how the calculation of the quantum noise can be done for a few different interferometer configurations. Specifically we focused our analysis on the Michelson configuration and the Sagnac configuration. At the beginning of the chapter we showed how the radiation pressure noise can be calculated starting from the equation of motion of the mirror. In the second section, then, we calculated the I/O relations for each of these configurations, considering both cases with and without cavities. The particular situation of a detuned cavity is explained in section 3, where we introduced also the concept of optical rigidity and optical spring. In the last section, finally, we showed how the quantum noise limited sensitivity can be calculated.

The results, shown in figure 4.95, demostrate that, using exactly the same parameters for a Michelson and a Sagnac, the latter will always have a lower radiation pressure noise.

[5]The bounces at high frequencies represent the free spectral range, defined as $FSR = c/2L$ [54].

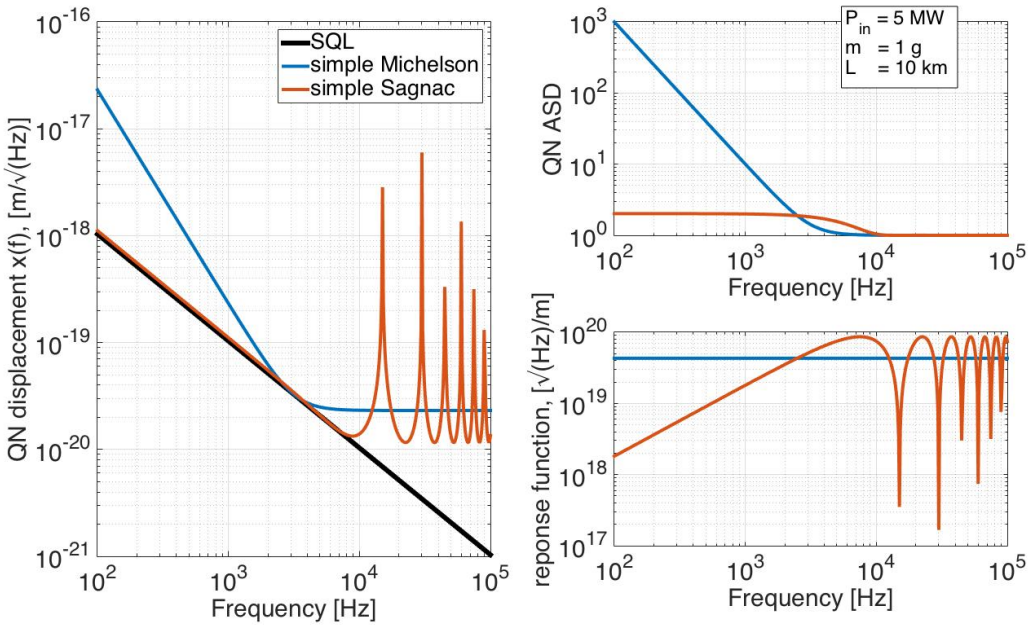

(a) Plot of the quantum noise limited sensitivity(left), quantum noise amplitude spectral density (top right) and response function (bottom right) for a Michelson (blue line) and a Sagnac (red line) without cavities.

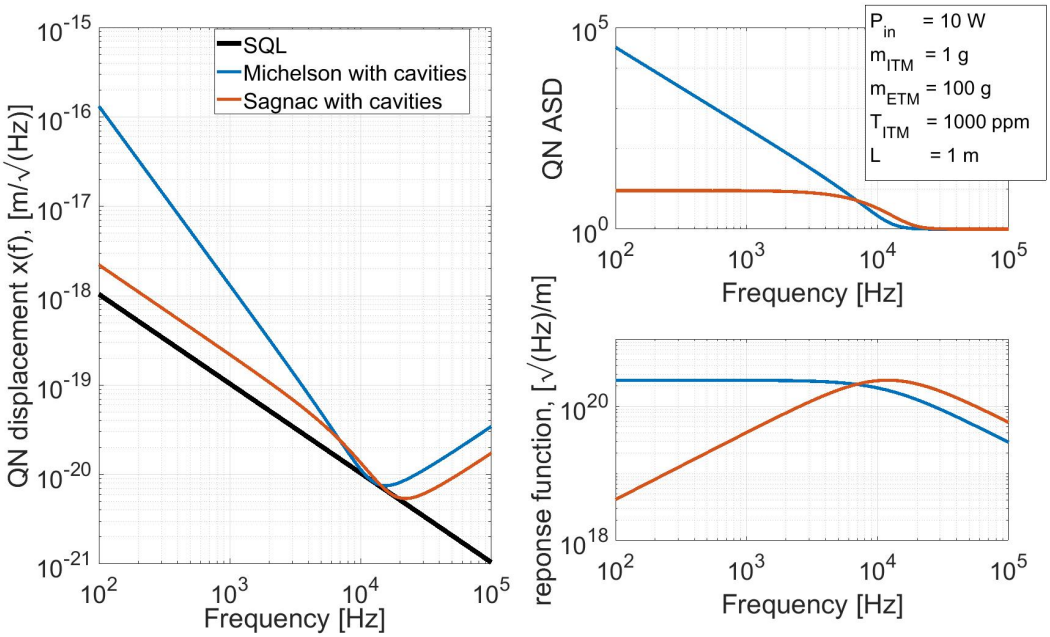

(b) Plot of the quantum noise limited sensitivity(left), quantum noise amplitude spectral density (top right) and response function (bottom right) for a Michelson (blue line) and a Sagnac (red line) with cavities.

Figure 4.8: Plots of the quantum noise for interferometers with (bottom) and without (top) cavities. The plots are made considering only the sine quadrature and in all cases the output signal is taken at the dark port. Notice that in order to have comparable results between the interferometers with and without cavities, in the first case we had to use some uncommon parameters, like extremely high power and very long arms.

Chapter 5

Requirements of the arm cavity mirrors of the SSM experiment

In section 4.2.5 we showed the results of the quantum noise calculation for a lossless Sagnac interferometer with a configuration similar to that one used for the Glasgow SSM experiment. However, because of the high cavity finesse the quantum noise is very sensitive to the loss. Some of the most important sources of loss in the cavity, like scattering or creation of higher order modes, are due to mirror surface imperfections and this is the reason why we need very restrictive requirements for the arm cavity mirrors of the SSM experiment. The specifications documents that have been sent to the vendors can be found in appendix C.

In this chapter we will show how the requirements of the arm cavity mirrors are determined. In the first section we will show the relation between loss and quantum noise. We will show then in the second section the first simulations run made with OSCAR using real maps of a sample mirror and in the third section we explain how the simulations for the derivation of the requirements through synthetic maps specifically created to represent each surface imperfection were made. Finally in the last section the outcome of the analysis is shown, describing how the real mirrors match the requirements requested.

5.1 Loss influence on quantum noise in a Sagnac speed meter

In SSM interferometers the loss has a role much more important than in the Michelson. This is because the presence of loss in the arm cavity creates two important effects. The first one is the fact that when the beam leaves the first cavity it will be affected by the loss, hence its power in the second cavity will be reduced. This means that the subtraction of

the radiation pressure force is not perfect anymore. The second effect is the fact that the vacuum fields associated to the loss that must be added (as we showed in section 2.1.4) create a further radiation pressure force that is not compensated by any other field.

When we have to include the loss in the calculation equation 4.90 becomes

$$\hat{\boldsymbol{o}}(\Omega) = \sum_i \mathbb{T}_i(\Omega)\,\hat{\boldsymbol{i}}_i(\Omega) + \sum_n \mathbb{N}_n(\Omega)\,\hat{\boldsymbol{n}}_n(\Omega), \tag{5.1}$$

with $\hat{\boldsymbol{i}}_i(\Omega)$ the input fields and $\hat{\boldsymbol{n}}_n(\Omega)$ any vacuum field that should be added in case of loss, as explained in section 2.1.4. Then the power spectral density of the quantum noise limited sensitivity is [50]

$$S_x(\Omega) = x^2_{SQL}(\Omega)\,\frac{\sum_i \mathbf{H}^\dagger_\zeta \cdot \mathbb{T}^\dagger_i(\Omega) \cdot \mathbb{S}^{in}_i(\Omega) \cdot \mathbb{T}_i(\Omega) \cdot \mathbf{H}_\zeta + \sum_n \mathbf{H}^\dagger_\zeta \cdot \mathbb{N}^\dagger_n(\Omega) \cdot \mathbb{N}_n(\Omega) \cdot \mathbf{H}_\zeta}{\left|\mathbf{H}^\dagger_\zeta \cdot \mathbf{R}^{-}(\Omega)\right|^2}, \tag{5.2}$$

where now the optical transfer matrices and the response function defined in equations 4.57-4.60 must be modified as

$$\mathbb{L}(\Omega) = \frac{1}{\gamma + \gamma_{loss} - i\Omega}\sqrt{\frac{\gamma}{\tau}}\;\hat{\sigma}, \tag{5.3}$$

$$\mathbb{T}_{s.n.}(\Omega) \approx \left(1 - \frac{2\gamma}{\gamma + \gamma_{loss} - i\Omega}\right)\mathbb{I}, \tag{5.4}$$

$$\mathbf{R}_{arm}(\Omega) \approx \frac{1}{(\gamma + \gamma_{loss} - i\Omega)}\sqrt{\frac{8\gamma P_c \omega_p}{c^2\tau^2\hbar\Omega^2}}\begin{bmatrix}0\\1\end{bmatrix}, \tag{5.5}$$

$$\mathbb{T}_{r.p.}(\Omega) \approx \frac{8\omega_p \gamma P_c}{c^2\tau(\gamma + \gamma_{loss} - i\Omega)^2}\,\chi\begin{bmatrix}0 & 0\\-1 & 0\end{bmatrix}, \tag{5.6}$$

$$\tag{5.7}$$

and the optical transfer matrices of the vacuum fields are defined as

$$\mathbb{N}(\Omega) = \mathbb{N}_{s.n.}(\Omega) + \mathbb{N}_{r.p.}(\Omega) = -\frac{2\sqrt{\gamma\gamma_{loss}}}{\gamma + \gamma_{loss} - i\Omega}\,\mathbb{I} + \frac{8\omega_p\sqrt{\gamma\gamma_{loss}}P_c}{c^2\tau(\gamma + \gamma_{loss} - i\Omega)^2}\,\chi\begin{bmatrix}0 & 0\\-1 & 0\end{bmatrix}. \tag{5.8}$$

In these equations we have defined the cavity half bandwidth due to the loss T_{loss} as $\gamma_{loss} = T_{loss}/4\tau$.

Figure 5.1 shows the behaviour of the quantum noise limited sensitivity with the loss for the Glasgow SSM and for ET-LF [43]. We can see that for the first configuration the loss is a crucial factor that affects the sensitivity of the instrument. The situation is much less critical

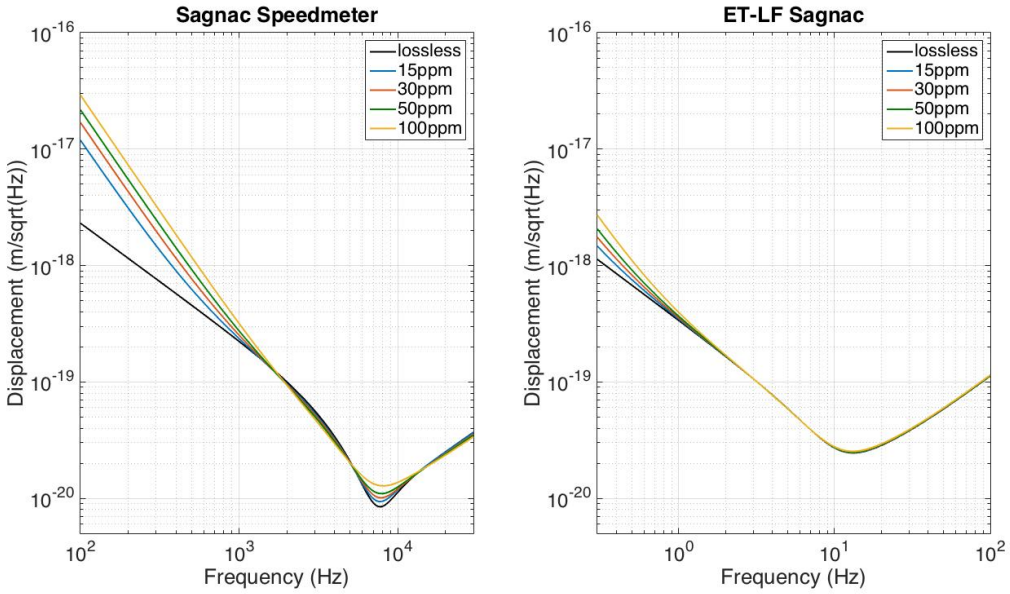

Figure 5.1: Reproduction of the results from Danilishin *et al.* [89]. Quantum noise limited sensitivity for different values of the round trip loss for Glasgow Sagnac speed meter (left) and ET-LF (right). The roundtrip loss is considered symmetric in both cavities. The parameters used for ET-LF are listed in table 1.1 and we used an ITM power transmissivity of 10 000 ppm. Furthermore we increased the input power to 45.73 W in order to compesate the absence of the power recycling mirror.

for large scale interferometers, where the influence of the loss on the quantum noise is not so strong. This can be explained by the fact that the finesse of the cavity in the Glasgow SSM is about 20 times larger than in ET-LF and hence the effective loss will also be 20 times larger. This behaviour forced us to require very restrictive specifications for the arm cavity mirrors of the SSM experiment.

5.2 Test simulations run

The requirements of the mirrors are found creating synthetic maps that represents the surface errors and simulating what is the cavity behaviour and the loss that they cause. However before doing that, we make an initial analysis of the simulations considering perfect arm cavity mirrors first and real mirrors then. These first analyses are made with the aim to have a first estimation of the loss associated to a real mirror.

For this purpose the surface profile of a sample mirror is measured and the maps obtained from these measurements are used for a first analysis of the loss.

parameter	**value**
laser input power	1.7 W
laser wavelength	1064 nm
ITM-ETM distance	1.3153 m
ETM-ETM distance	0.2 m
ITM power transmissivity	700 ppm
ITM diameter	1 cm
ITM radius of curvature	7.91 m (concave)
ETM power transmissivity	2 ppm
ETM diameter	5 cm
ETM radius of curvature	∞
beam radius on ITM	1.112 mm
angle of incidence on ITM	4.3987 °
angle of incidence on ETM	42.8 °

Table 5.1: List of the parameters of the Glasgow SSM.

5.2.1 OSCAR results for a perfect cavity

Before starting with the simulations with a real mirror surface, we want to check what are OSCAR's results for a perfect cavity, in order to better understand its behaviour. In this first tests we will use the parameters of the cavities of the Glasgow SSM listed in table 5.1.

Defining the cavity

First of all we have to define the cavity. We want to simulate a triangular cavity where the distances between the mirrors are: 0.2 m between M2 and M3 and 1.3153 m between M1 and M2 and between M1 and M3 (for the mirrors nomenclature refer to figure 3.6).

To do that we define the three interfaces that form the cavity: M1 has a diameter of 10 mm, a radius of curvature 7.91 m (concave) and a transmission in power of 700ppm and M2 and M3 are flat, have a diameter of 50 mm and a transmission in power of 2 ppm. The laser beam has a wavelength of 1064 nm, a radius of 1.12 mm on the input mirror[1], an input power on each cavity of 0.85 W (assuming that the beam is perfectly 50% transmitted and 50% reflected by the beam splitter) and an angle of incidence of 4.3987 degree on M1 and

[1]This is not the beam waist, because the waist is between the two M_2 and M_3.

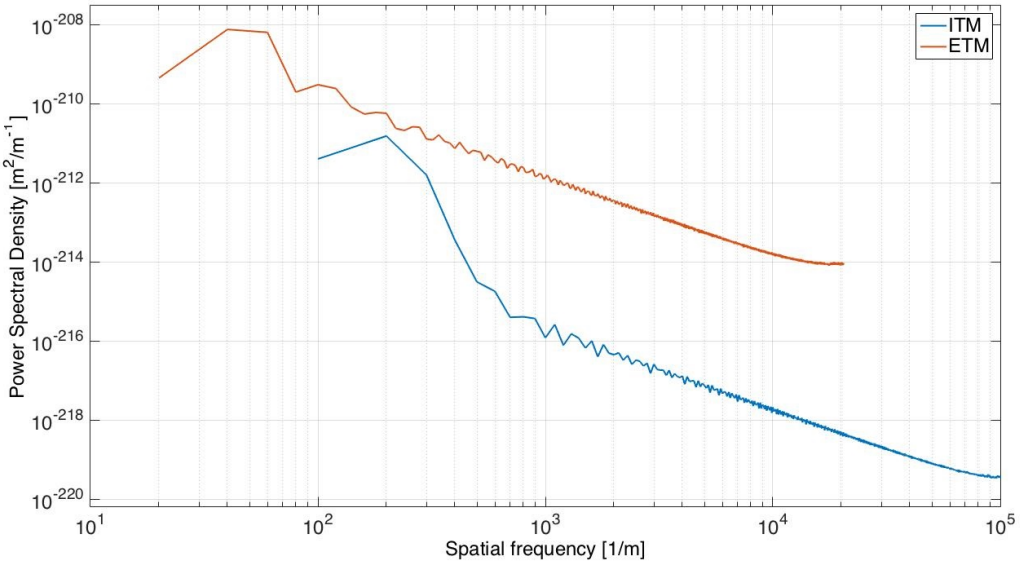

Figure 5.2: Power spectral density of the surface of the input and the end mirrors. For the ITM the curvature has been removed, otherwise it will dominate the PSD values. Since the surface is supposed to be perfect, the values of the PSD represent rounding errors.

42.8 degree on M2 and M3. The cavity is defined through the OSCAR function `CavityN` described in section 2.3.4.

Through the function `Plot_PSD` it is possible to calculate and plot the power spectral density of the surfaces flatness shown in figure 5.2. This function calculates the 2D PSD of the surface and then it transforms it in 1D. To do it first a Hanning window[2] is applied to the data, then the 2D PSD is calculated and finally it is transformed in 1D PSD summing all the spatial frequencies along one direction (in this case along the radial direction). As we can see, since the surface of the mirrors are defined perfect, the PSD is practically zero at all frequencies, i.e. dominated by numerical errors.

Then running the function `Check_stability`, we have as output all the values needed in order to have a stable cavity and the finesse of the cavity:

```
----------------- For the surface 1  -----------------
RofC fitted (m): 7.90997
Center of the map, horizontal (mm): -6.2242e-09
Center of the map, vertical (mm): -7.30011e-09
Tilt horizontal (nrad): 0.00078688
```

[2]A Hanning window is a window defined through the Hann function:

$$w(n) = \begin{cases} \frac{1}{2}\left(1 - \cos\frac{2\pi n}{N}\right) & \text{for } 0 \le n \le N \\ 0 & \text{otherwise} \end{cases},$$

with N the length of the window [90].

```
Tilt vertical (nrad): 0.0009229
Flatness RMS (nm): 1.98829,

----------------- For the surface 2  -----------------
RofC fitted (m): -4.07628e+98
Center of the map, horizontal (mm): 0
Center of the map, vertical (mm): 0
Tilt horizontal (nrad): 0
Tilt vertical (nrad): 0
Flatness RMS (nm): 1.85268e-95,

----------------- For the surface 3  -----------------
RofC fitted (m): -4.07628e+98
Center of the map, horizontal (mm): 0
Center of the map, vertical (mm): 0
Tilt horizontal (nrad): 0
Tilt vertical (nrad): 0
Flatness RMS (nm): 1.85268e-95,

  Beam radius on the first mirror: 0.00111829
  Beam radius on mirror 2 [m]: 0.00101387
  Beam radius on mirror 3 [m]: 0.00101387
  Cavity finesse: 8921.87
  Cavity gain: 5647.59
  Mode matched input beam parameters:
  Beam radius [m]: 0.00111837      Wavefront curvature [m]: -5.45515
```

The most important parameters in this output are the values of the beam radii and the wavefront curvature in the last lines. They are required in order to have a stable cavity and so all the following simulations will be carried out using these values. It must also be noticed that the large value of the flatness for the surface 1, i.e. the ITM, is due to the mirror curvature.

Circulating power

With the function `Calculate_field_AC` it is possible to calculate the circulating power inside the cavity and with the function `Display_results` we can display the profile of the input, circulating, reflected and transmitted beams. The output is:

```
 Power in the input beam 0.85 [W]
```

```
 Circulating power 4800.43 [W]
 Total transmitted power 0.0192017 [W]
 Reflected power 0.830798 [W]

Round trip losses [ppm]: 1.38235e-05
```

As expected, the roundtrip loss is very low, since it is only due to clipping loss of the beam, which have radii much smaller than the mirror respective dimensions. This simulation is done using a grid with a size of 512 points and a physical size of 0.011 m (so we consider only clipping loss on the ITM).

Cavity eigen modes

The next simulation performed with OSCAR is the analysis of the eigenmodes created by a macroscopic roundtrip length detuning. When we have a detuned cavity in fact, the input beam, which is of the fundamental order HG(0,0), does not fit the surface of the mirror anymore, because the change in the length of the cavity will change the curvature of the beam on the surface of the mirror. This fact causes the generation of higher order modes which in turn increases the roundtrip loss, because of the different power distribution on the surface.

To find the cavity eigenmodes the OSCAR function `Display_cavity_modes` is used. In this case we use a grid with the same number of points as before (512) but a smaller physical size (5 mm), since we only need to check the profile of the beam (which has a radius of 1.12 mm) and the mirror size does not affect the results significantly. The output of this function is a plot of the roundtrip loss as a function of the detuning and the profile of the corresponding Hermite-Gaussian modes that create it. The output is shown in figure 5.3 (for the first 10 modes).

5.2.2 Surface measurements

After having performed the simulations for a perfect cavity, we can start the second phase of the analysis, namely adding a surface map on the mirrors to investigate what happens in a more realistic situation.

To do that a *Laseroptik Garbsen* flat mirror with a diameter of 50 mm, a thickness of 9 mm and a flatness of $\sim$ 60 nm rms is used. The measurements of the surface flatness of this mirror are done with the Zygo interferometer, described in section 2.2.2. Since there are many factors that can affect the measurements (like thermal effects due to the laser heating up the mirror or ground vibrations), the mirror is left in the set up for about 30 hours and

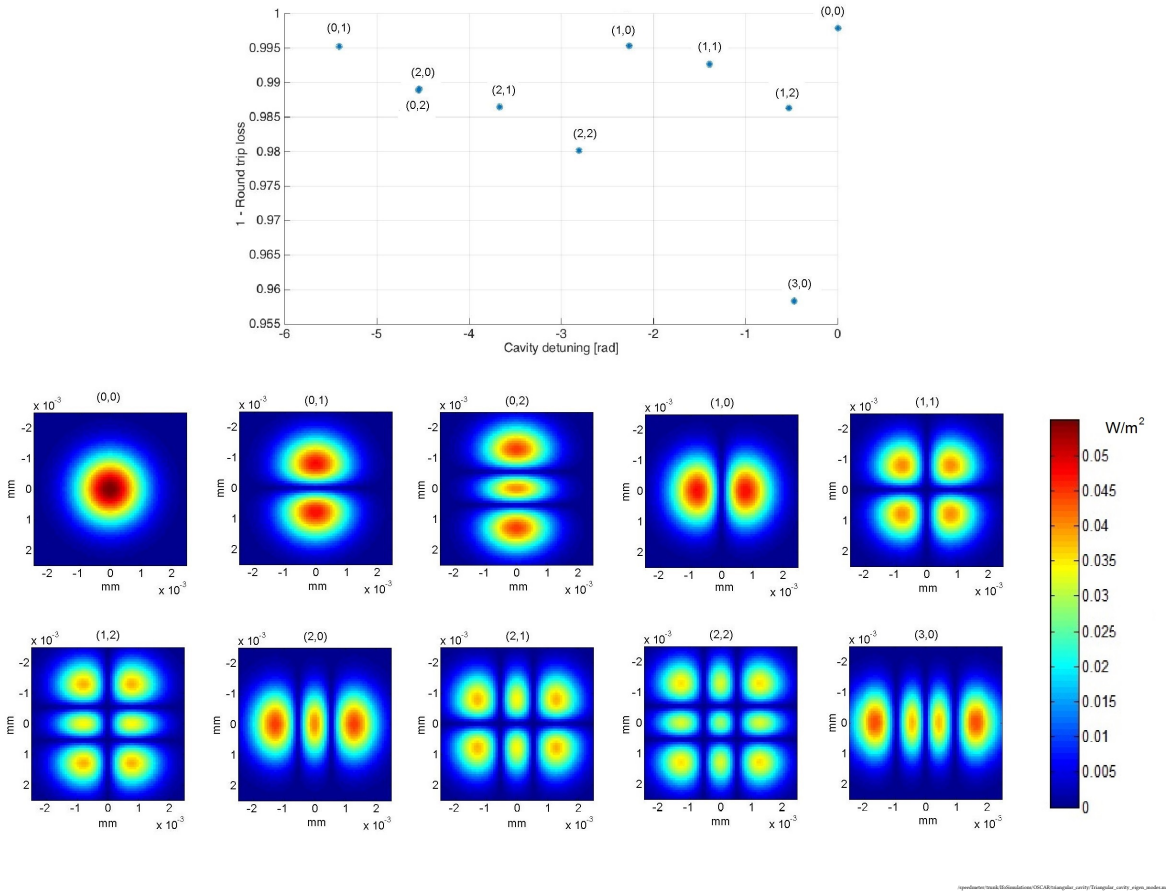

Figure 5.3: *Top*: round trip loss as a function of the detuning. Each of the point corresponds to an eigenmode created by the detuning. The order of the eigenmode is written near the correspondent point. *Bottom*: surface profile of the mode corresponding to the eigenmodes showed in the plot on the top.

different measurements are taken during this period. The results of these investigations will be described and discussed in the following.

The analysis of the mirror maps are made through *SimTools*: first of all we centre the map in the grid and then we remove the offset, so the mirror centre is set to zero, and the piston is corrected. These corrections are made using the proper functions described in section 2.2.3. After this corrections, the flatness is calculated using the *SimTools* function `FT_map_rms.m`, which calculates the rms according to the definition in equation 2.38. Figure 5.4 shows the flatness of the surface after each correction respect to the time that the mirror was in the set up.

Through this analysis it is possible to understand how the measurements of the flatness of the mirror changes from one measurement to another. We take a total of 8 measurements and we compare them making the difference between each map and its consecutive and between each with the last one taken. The rms of the resulting maps are also calculated and plotted (see figure 5.5). We obtain that the difference between the measurements are

all below 8.5 nm and the flatness of the residual maps are below 25.5 nm rms.

The surface profiles of all the measurements can be found in Appendix B.

In addition we can estimate the radius of curvature. Since the mirror is supposed to be flat, the theoretical value of the radius of curvature is infinite and then the real value will give its error. The radius of curvature is calculated using the *SimTools* function `FT_map_remove_curvature_from_mirror_map.m`. It must be noted that an edge of 5 mm has been cut out from the map before this calculation, because the values are affected by a measurement artifact (it can be seen in the mirror surface profiles shown in figure B.2). The results for all maps are shown in figure 5.6 and they give a mean value for the radius of curvature of 80.7 km.

A description of the mirror surface profile can be obtained calculating the power spectral density (PSD) of the surface, which gives the level of the imperfections as a function of the spatial frequency as explained in section 2.2.1. In figure 5.7 the PSD of the ITM and the ETM after adding the same map (number 8, i.e. the last one taken) is shown[3]. For the ITM we have to remove the curvature of the mirror before calculating the PSD, because the curvature has a dominant effect on the PSD.

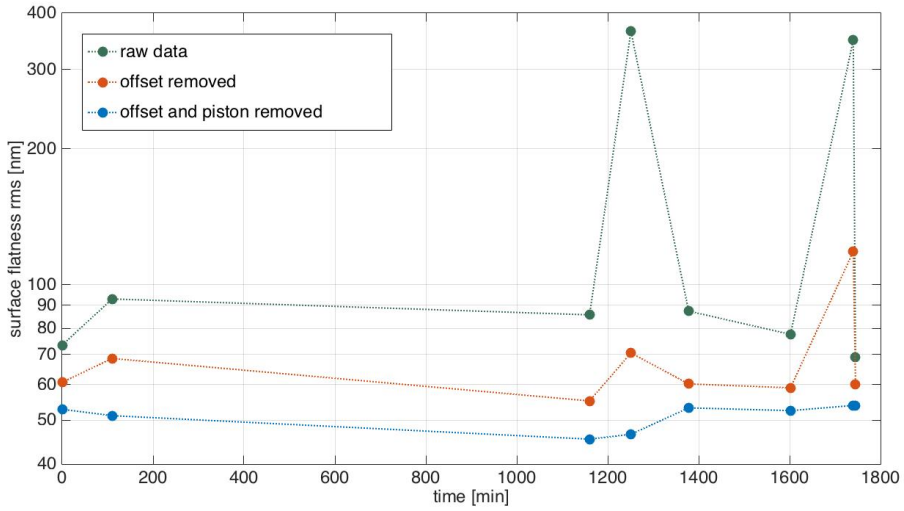

Figure 5.4: The plot shows how the mirror surface flatness changed with the passing of time. The flatness is calculated after each adjustment made with *SimTools*.

5.2.3 Roundtrip loss simulations

In order to find a threshold value of the mirror flatness we can afford, we make a simulation of the cavity after having added a map to the ITM. So, using one of the map measured

[3]With OSCAR it is possible to add the same map on mirrors with different sizes because an interpolation is done internally when the map is added.

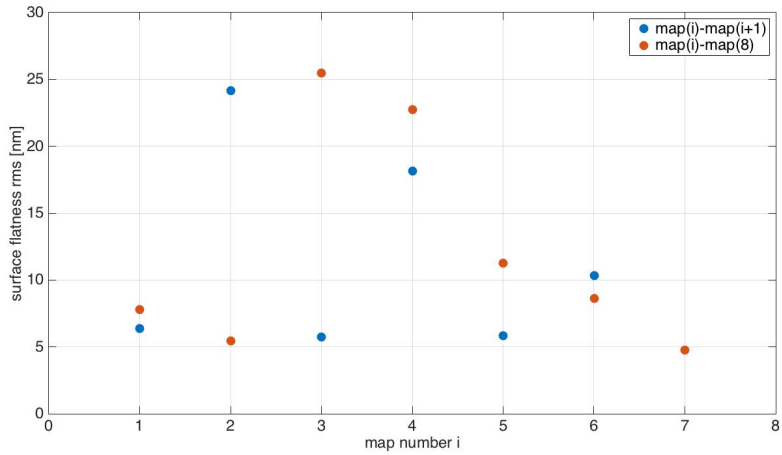

Figure 5.5: Flatnesses of the surfaces obtained by the differences between two maps.

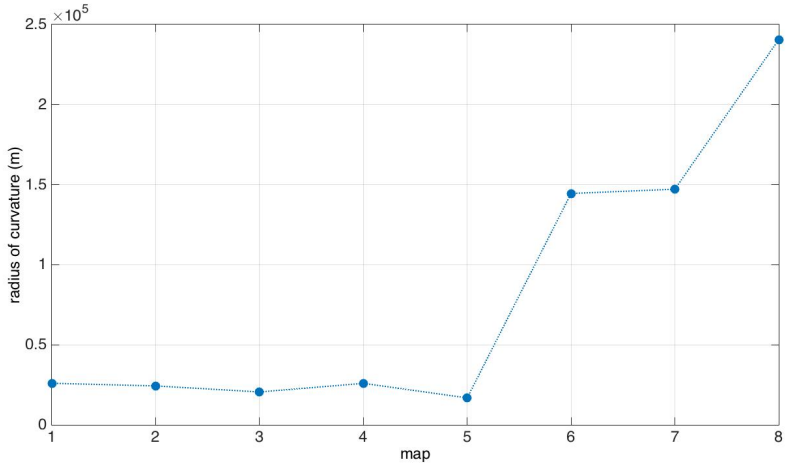

Figure 5.6: Values of the radius of curvature for each measurements obtained with *SimTools*.

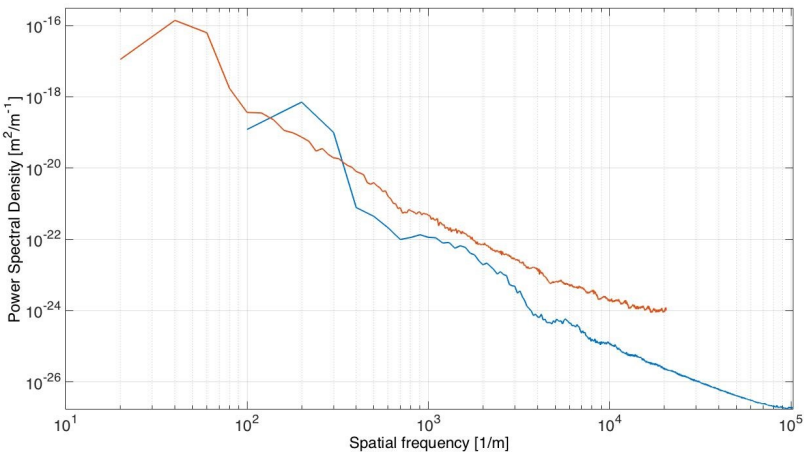

Figure 5.7: PSD of the ITM (with curvature removed) and ETM with the map number 8 added on the surface.

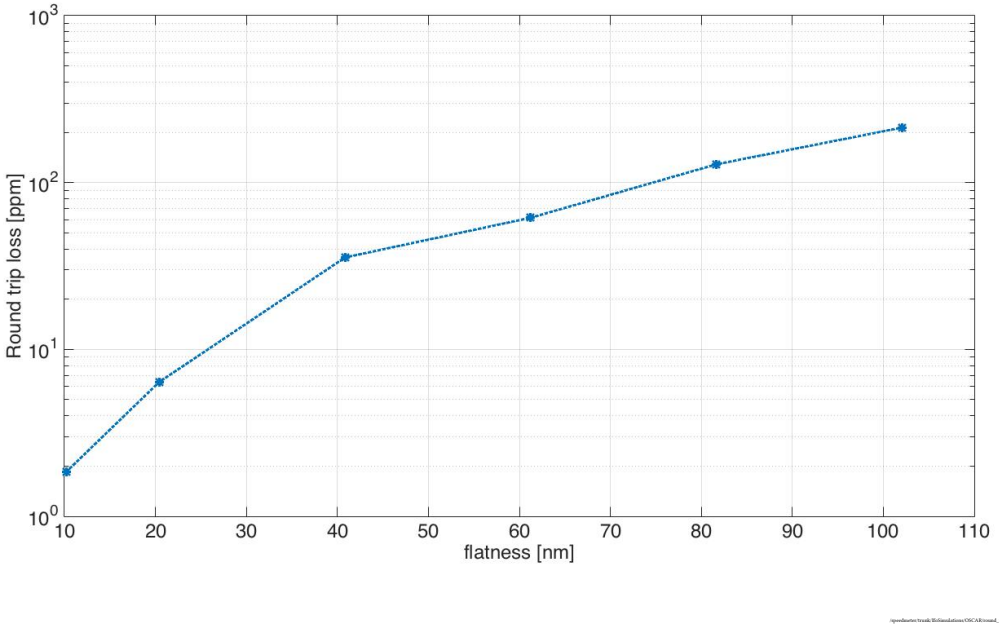

Figure 5.8: Round trip loss trend as a function of the flatness of the mirror.

with Zygo (the map number 8) described in the previous section, a simulation of the cavity is performed. The map is added to the ITM, scaling its values by different factors. The roundtrip loss as a function of the flatness is calculated (see figure 5.8).

This analysis allows us to evaluate the loss versus the flatness of the ITM. Furthermore we deduce that for a scale factor of 1 (corresponding to a flatness of $\sim 10\,\text{nm}$), so considering the real mirror map, the round trip loss is estimated to be $\sim 2\,\text{ppm}$.

5.3 Mirrors surface requirements

The analyses made so far give us a first estimate of a real mirror surface specifications and the associated loss. However, it would be too expensive to set requirements for all of mirror. It is more economic to divide the mirror surface in zones and to set the requirements for each different surface imperfections. So we need a more rigorous way to describe the different surface errors and define the requirements for each different type of error. With the analysis made in the previous section, in fact, we are not able to distinguish the surface errors and then the effects of each of them. So in this section we will show how the analysis of the effects of each surface errors is made and how we define the requirements of the arm cavity mirrors of the Glasgow SSM experiment.

First of all we consider that the central zone of the surface affects much more the loss, because it will be hit by the beam area with most of the power in it. So we divide the mirror surface in zones. The size and the number of the zones will be different for the ITM and

the ETM, because of their different dimensions. Specifically, the choice of the size of the central zone is made simply calculating the power outside the zone through the equation

$$P_{out} = e^{-\frac{2r^2}{w^2}}, \tag{5.9}$$

where r is the radius of the central zone and w is the beam radius on the mirror surface.

ITM

As said we need to divide the mirror in zones. For the ITM, considering that it has a radius of 5 mm and the beam radius on its surface is 1.12 mm (as obtained from the OSCAR output described in section 5.2.1), we choose:

- Zone A: inside a radius of 3mm (0.58 ppm of power outside this area according to equation 5.9);
- Zone B: outside a radius of 3mm.

So we can make the analysis for the two zones in order to set requirements more restrictive in the central zone.

ETM

Since the ETM is much larger than the ITM we decide to define three zones instead of two. At first we define the central area with a radius of 4 mm, which will give about the same value of the power as for the ITM (0.58 ppm outside of it). However, the larger dimensions of the mirror give us much more large range of choice and we increase it to 5 mm, which gives a power outside the central zone of $\sim 10^{-16}$ ppm. So the zones are defined as:

- zone A: the surface inside a radius of 5mm;
- zone B: ring 5 mm from centre to 15 mm from centre;
- zone C: the surface outside a radius of 15mm.

5.3.1 Point defects

We gave a first overview of the point defects behaviour in section 2.2.1. Here we we will see how we simulated in MATLAB® their effect on the roundtrip loss of the cavity.

In the mirror surface requirements we want to specify the size and the total area of defects over the whole surface, so for a full analysis of this effect done using the equation 2.35,

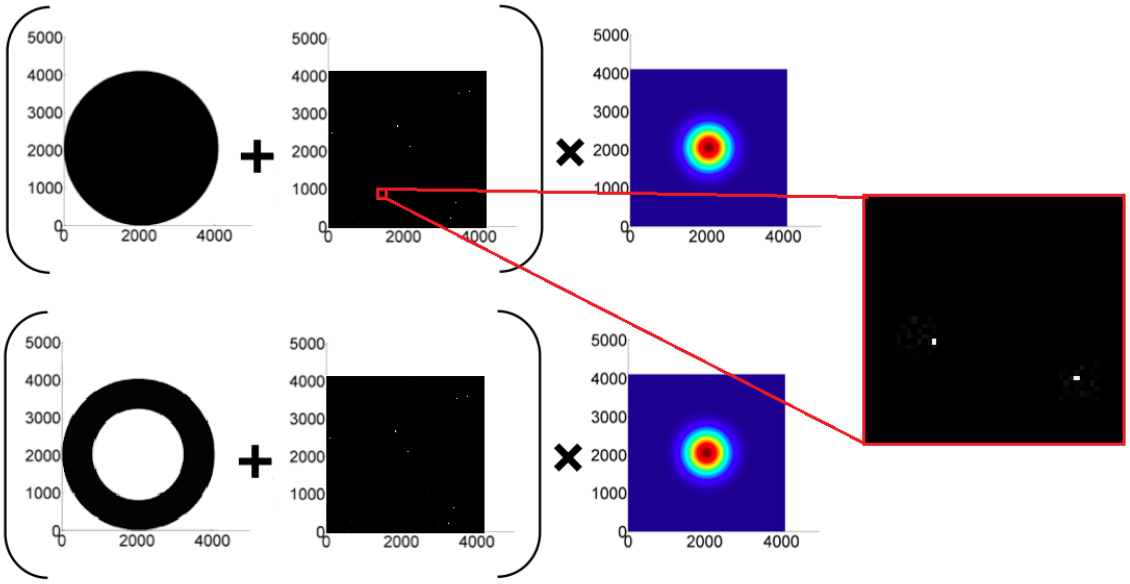

Figure 5.9: Procedure used to calculate the loss due to point defects for the zone A (top) and B or C (bottom). On the right there is a zoom of the matrix that represents the point defects, in order to be able to see them.

we need to have an estimation of the height of the point defects. Then the simulations are performed using the following procedure (a schematic description of this procedure is shown in figure 5.9):

- first we make an initial guess for the dimension of the defects (1 μm), which will also be the resolution of the grid, since we will consider each defect equal to one pixel;
- we define the mirror through a matrix with the value 0 inside a circle with radius equal to the mirror radius and NaN outside;
- we define the defects as a matrix with the same size of the previous one with all 0 elements and some elements equal to 1 randomly placed in the matrix: each of these elements represent a point defect;
- we sum these two matrix: in this way we have a matrix of the same size of the surface of the mirror with the point defects on it;
- we define a matrix that describe the beam profile (a gaussian beam) and we multiply it for the matrix that describes the mirror surface with the point defects;
- finally the power inside the pixels corresponding to the point defects is calculated and all these values are summed in order to have the total power loss.

We should note that this calculation is an upper limit of the power loss because we are considering that all the light that hits the point defects will be lost and this is not necessarily true. However this method gives us an approximation of the order of magnitude of the loss.

We can estimate the height of the point defects comparing these results with equation 2.35. The value of the a height of the point defects at which the two results agrees can be considered a good estimation of the height of the point defects. In particular this comparison is done changing the numerical density of the point defects and calculating the respective loss due to these defects.

ITM

For the ITM the value of the height for which this result matches with equation 2.35 is found to be $\sim$ 85 nm for both zone A and B. As we can see in figure 5.10, in fact, the value of the loss obtained through the simulations changing the density of point defects on the surface (circles in the plot) and the trend of the equation 2.35 using the value of 85 nm (line) match.

Once we found this value, we use again equation 2.35 for a plot of the loss as a function of the size of the point defects, changing the number of points. For the zone B the calculation is the same, but we also consider the beam shifted from the central position of the mirror of 2 mm, in order to see how much it affects the loss (see figure 5.11). This simulation is made with a grid size of 4096 and a pixel size (which corresponds to the size of the point defects) of 1.5 μm for the zone A and 2.4 μm for the zone B.

In this way, once set the maximum loss due to this imperfections that we can afford, we have the chance to choose the number and the maximum size of points defects. In this case we decide to set no point defects with size > 1 μm and a total area $< 100\mu m^2$ for zone A and no point defects with size > 1 μm and a total area $< 2000\mu m^2$ for the zone B, which should result in a loss <5 ppm.

ETM

For the ETM we have that for the zone A results are similar to that one obtained for the ITM. In fact we have a difference of the loss of about a factor 2 and the equation 2.35 agrees with the results of the simulation considering a height of the point defects of $\sim$ 110 nm. For the zone B instead we have that the two results agrees for an height of the point defects of ~ 6 μm. Finally for the zone C, since the total power that hits that area of the mirror is negligible, no simulations are performed.

The simulations are made with 8192 points and a pixel size 1.2 μm for the zone A and 3.7 μm for the zone B. The results are shown in figures 5.12 and 5.13. The requirements chosen are no point defects with size > 1 μm and a total area $< 600\mu m^2$ for zone A and no point defects with size > 1 μm and a total area $< 3000\mu m^2$ for the zone B, and also in this case this should result a loss of <5 ppm.

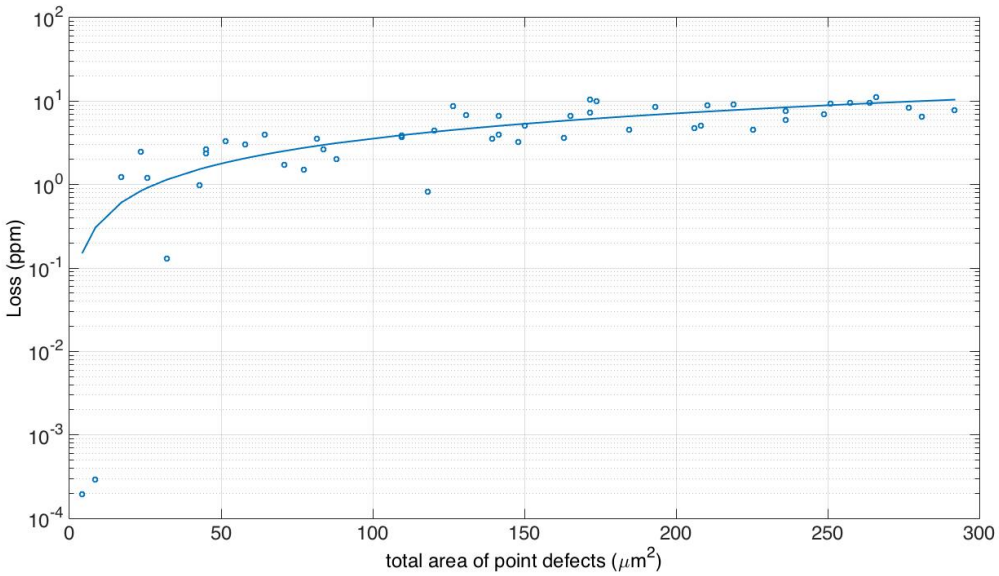

(a)

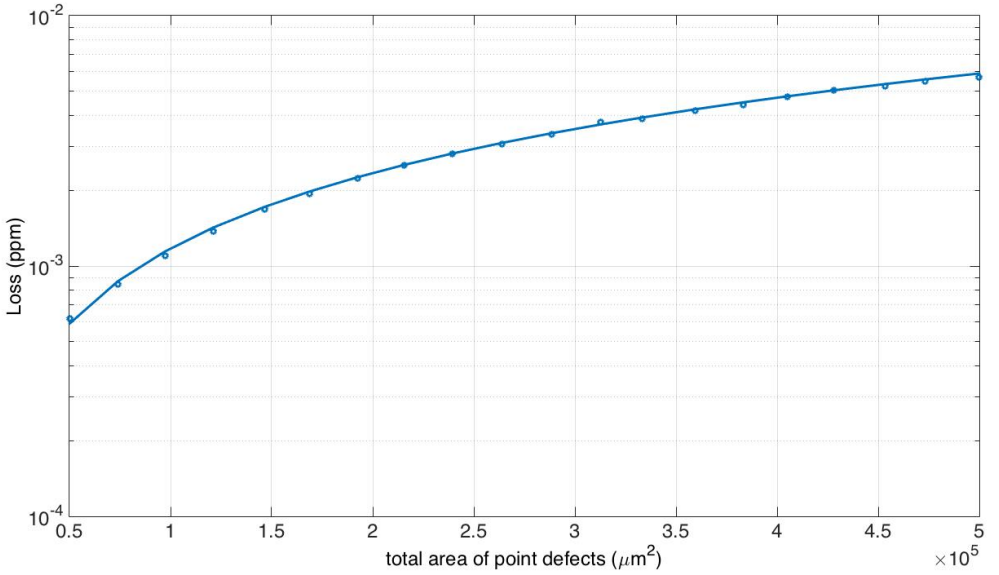

(b)

Figure 5.10: Loss as a function of the size of the point defects, considering different number of points for the zone A (a) and B(b) for the ITM. The circles represent the values of the loss obtained with a fixed size of 1 μm changing the numerical density of point defects (i.e. their total area). The line represents equation 2.35 for $h = 85$ nm.

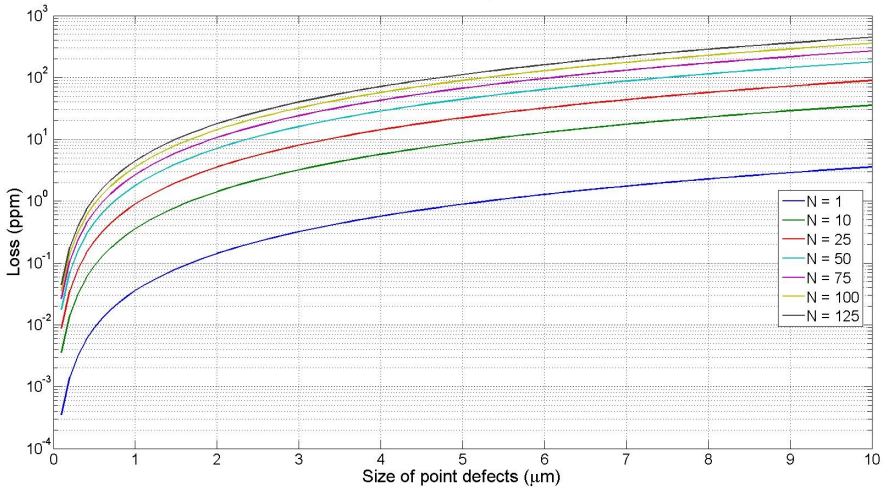

(a)

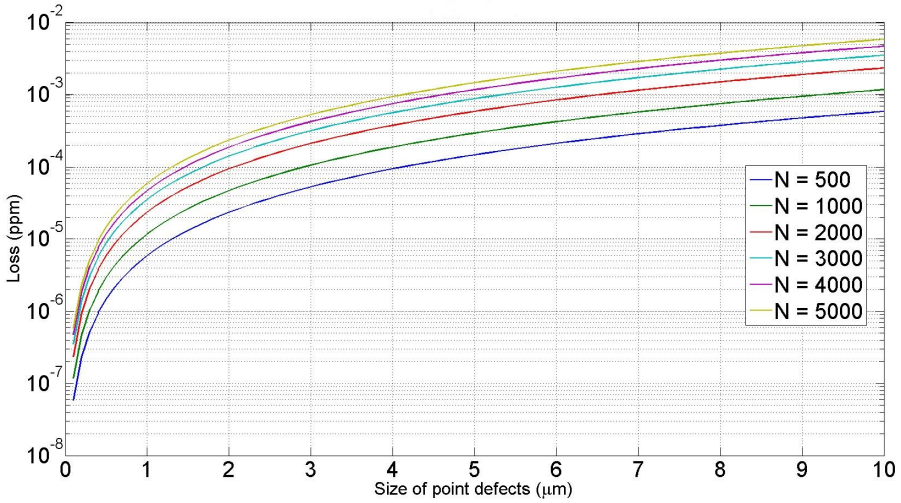

(b)

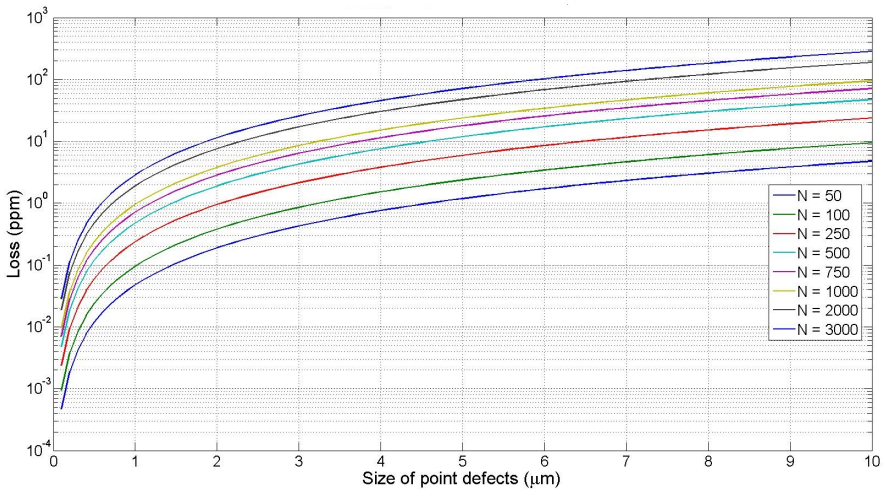

(c)

Figure 5.11: Loss as a function of the size and the number of the point defects on the ITM for the zone A (a), B (b) and for the zone B with the beam shifted of 2 mm from the centre of the mirror.

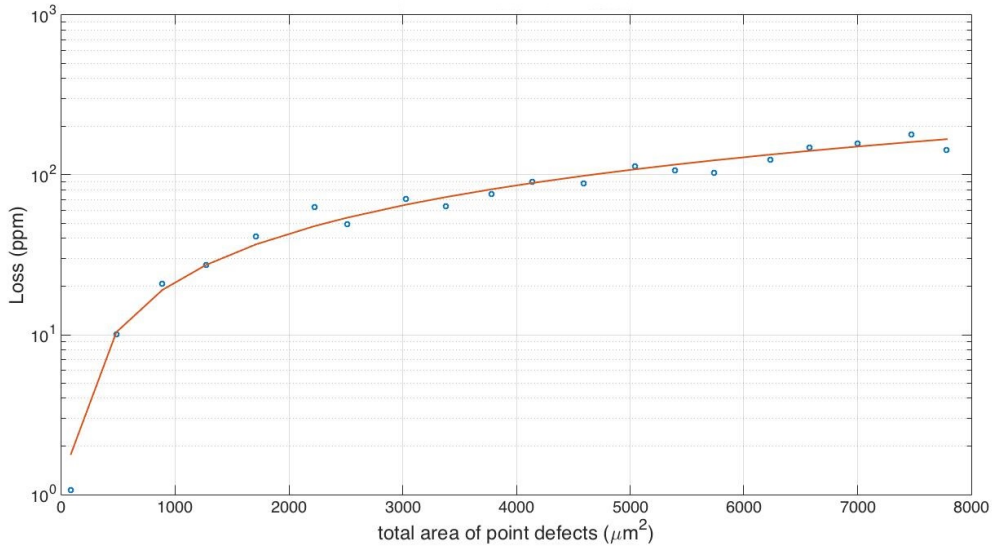

(a)

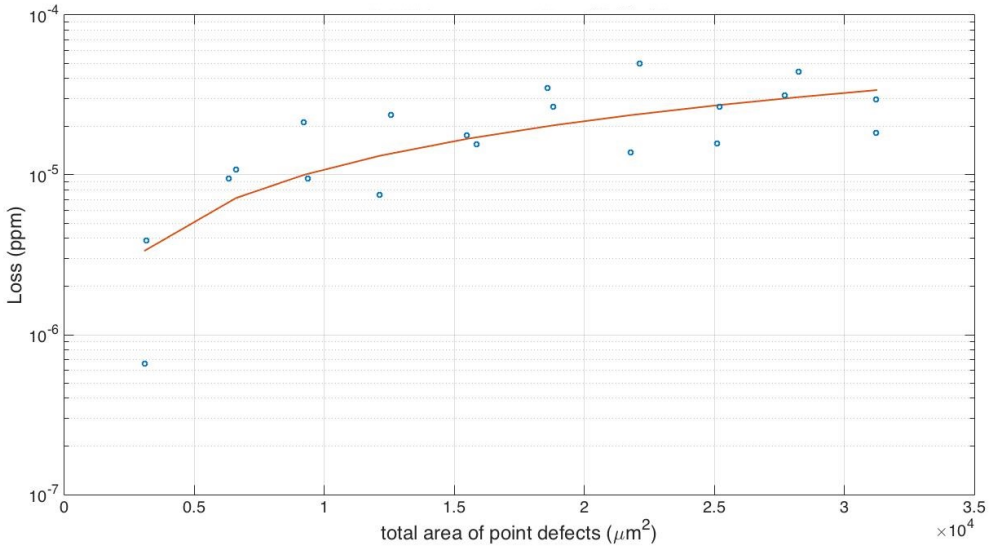

(b)

Figure 5.12: Loss as a function of the size of the point defects, considering different number of points for the zone A (a) and B(b) for the ETM. The circles represent the values of the loss obtained with a fixed size of 1 μm changing the numerical density of point defects (i.e. their total area). The line represents equation 2.35 for $h = 110$ nm for the zone A (a) and $h = 6\,\mu$m for the zone B (b).

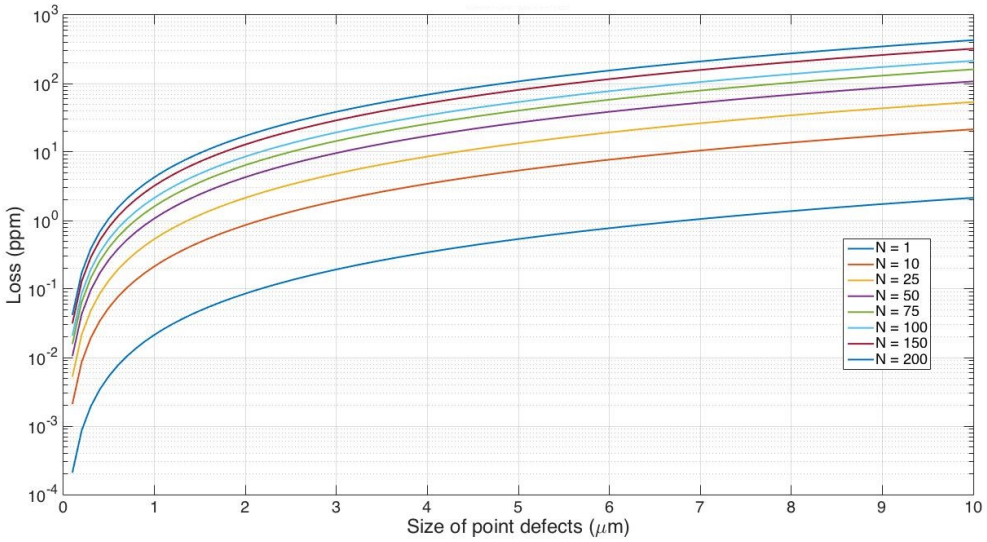

(a)

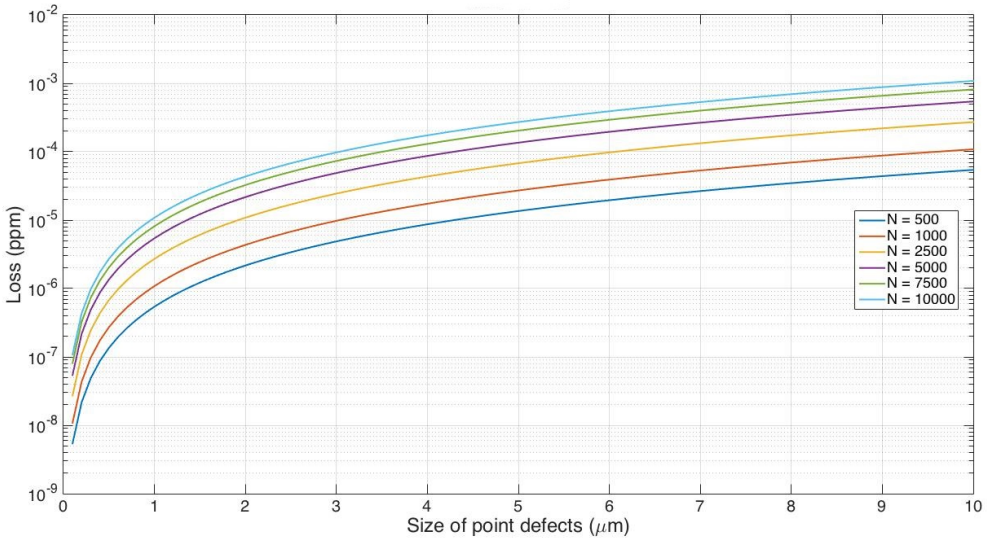

(b)

Figure 5.13: Loss as a function of the size and the number of the point defects for the zone A (a), B (b) of the ETM.

5.3.2 Radius of curvature and astigmatism

ITM

According to the design paper the radius of curvature of the ITM must be 7.91m. The reason why we chose this particular value is clear from figure 3.7. In fact the radius of curvature of the input mirror and the length of the cavity are the critical factors that determine the resonance of the higher order modes in the cavity, which can affect the performance of the instrument. So we need to check what is the maximum error in the radius of curvature in order to avoid this effect.

To have an estimation of the error of the radius of curvature, we change the radius of curvature in the x direction in one cavity and in the y direction in the other one with equal values ΔR, but opposite sign (see figure 5.14). The difference between these two beams can be considered the loss due to destructive interference. Some examples of the beam profile obtained by the difference of these two beams are shown in figure 5.15 and the roundtrip loss as a function of ΔR is shown in figure 5.16. This calculation is made using the OSCAR function `minus`, which allows to calculate the difference between two fields.

For the requirements of the ITM we choose an error on the radius of curvature < 0.02 m, which corresponds to a loss of 10^{-6} W, i.e. 2×10^{-4} ppm.

A similar approach is used to find the power loss as a function of the astigmatism. In order to find the power loss due to this kind of deformation, we add an error to the radii of curvature of the two ITM with equal values and opposite sign and we calculate the difference between the reflected beams obtained. As before, the power of this difference between the beams corresponds to the loss.

Finally the amplitude of the Zernike 2,2 polynomial that corresponds to the error of the radius of curvature is calculated (through *SimTools*) and so we are able to plot the power loss as a function of the astigmatism (see figure 5.17).

The requirements for the astigmatism of the ITM has been set to be < 8 nm, which should give a loss $< 10^{-6}$ W, that corresponds to 2×10^{-3} ppm.

ETM

For the error of the radius of curvature of the ETM we follow the same method as described above, but this time, since the mirror must be flat and then with a radius of curvature infinite, we need to set a minimum value as requirement. Figure 5.18 shows the amount of power lost when the error ΔR is added to the two directions x and y with equal value and opposite sign on both ETM. We set as requirement a minimum value of the radius of curvature of 10 km, which corresponds to a loss of $< 10^{-6}$ W.

For the astigmatism the method used for the ETM is a little different from that one used for the ITM. In this case we simply add two maps that represents the astigmatism with opposite signs and then we calculate the difference of the intra-cavity beams obtained adding these maps. We do this with different combinations of the maps on the four ETM in order to consider any possibility. The results are shown in figure 5.19. We choose a value of the astigmatism for the ETM < 16 nm, which should result in a loss $< 10^{-7}$ W ($2{\times}10^{-4}$ ppm) in the worst case scenario.

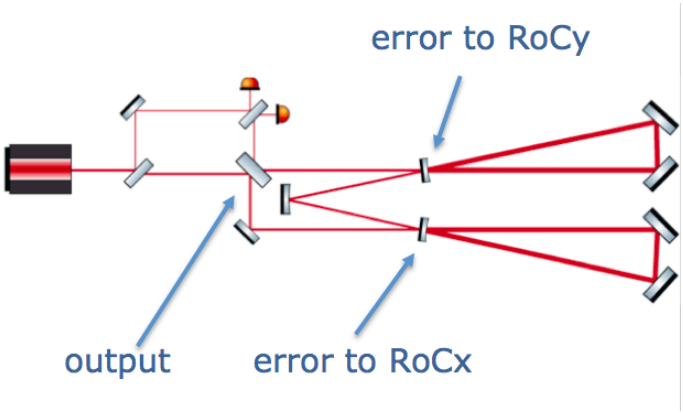

Figure 5.14: (a) Representation of the method used to calculate the loss due to the error of the ITM radius of curvature: and error in the x-direction is added to the radius of curvature of one of the ITM and along the y-direction to the other and the difference between the two two output beams was calculated.

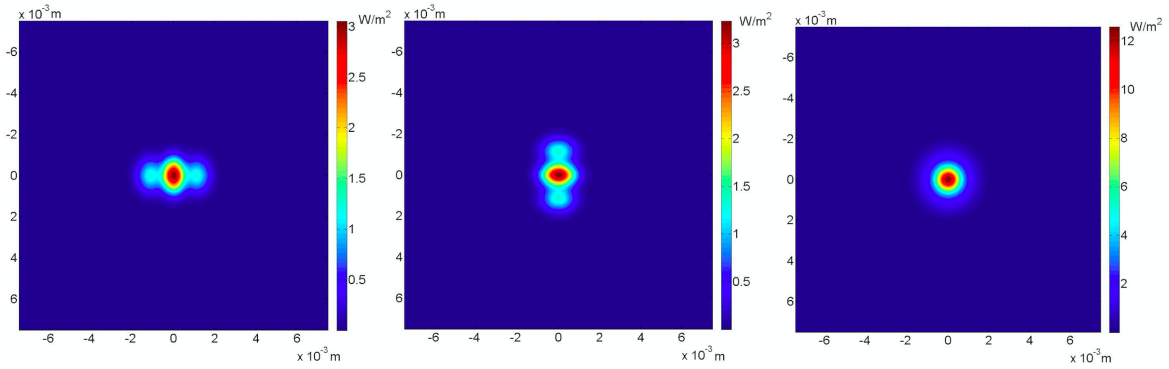

(a) (b) (c)

Figure 5.15: Intensity profile of the difference between: (a) the beam of the first cavity with ITM's radius of 7.91 m and no error added and the beam of the second cavity with the ITM's radius of curvature in the x direction $r_x = 8.01$ m and no error in the y-direction, so $r_y = 7.91$ m; (b) the beam of the first cavity with ITM's radius of 7.91 m and no error added and the beam of the second cavity with $r_x = 7.91$ m (no error added) and $r_y = 7.81$ m; (c) the beam of the first cavity with ITM's radius $r_x = 8.01$ m and the beam of the second cavity with $r_y = 7.81$ m.

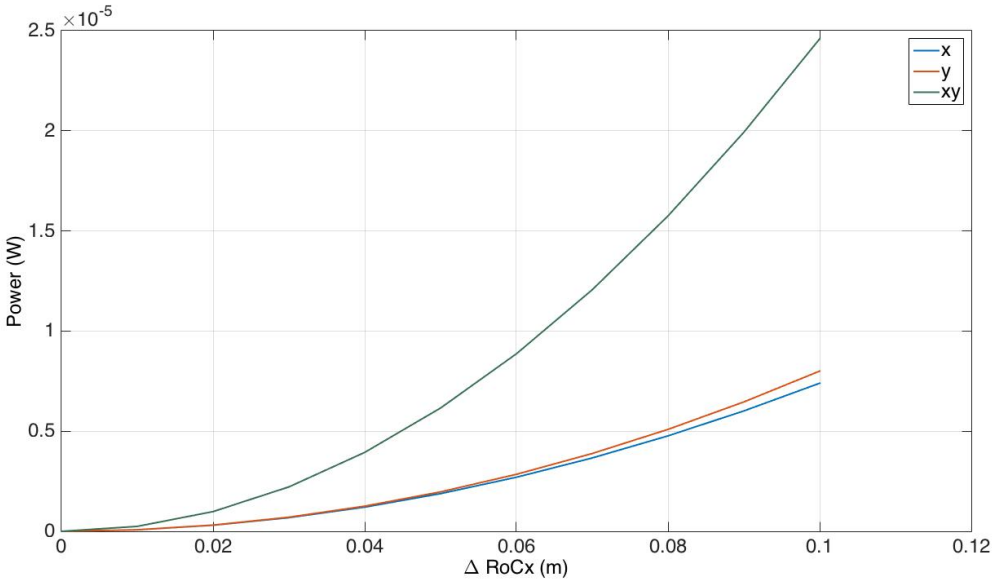

Figure 5.16: Power loss (referred to the input power) due to the overlap of the beams obtained when an error ΔR is added on one of the two ITM only along the x-direction (blue line), only along the y-direction (red line) and on both ITM with opposite value in the two directions (green line).

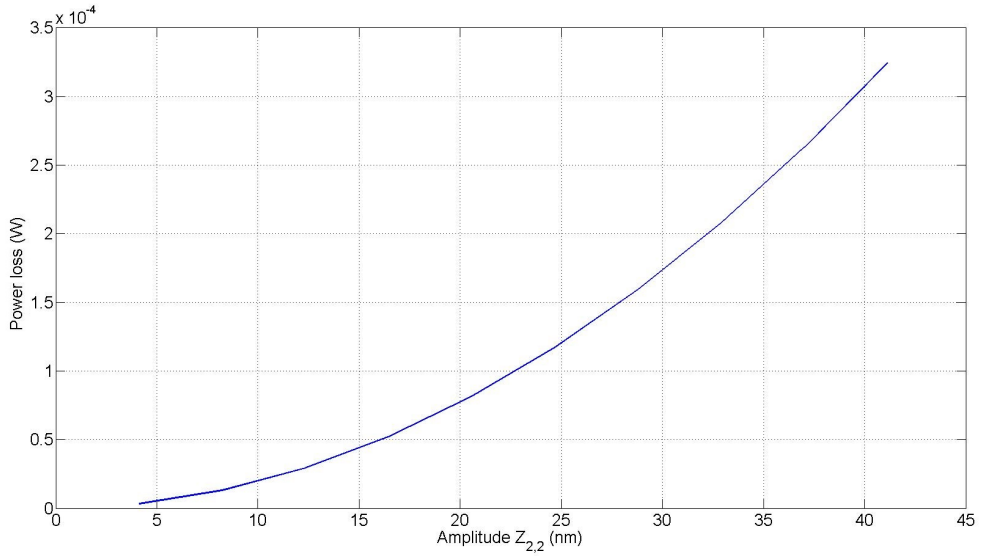

Figure 5.17: Power loss (referred to the input power) due to the overlap of the beams obtained when an error ΔR is added on both ITM with opposite value in the two directions (same as the green line in figure 5.16). On the x-axis we have the correspondent values of the radius of curvature in terms of amplitude of the Zernike polynomial (2,2), which represents the astigmatism

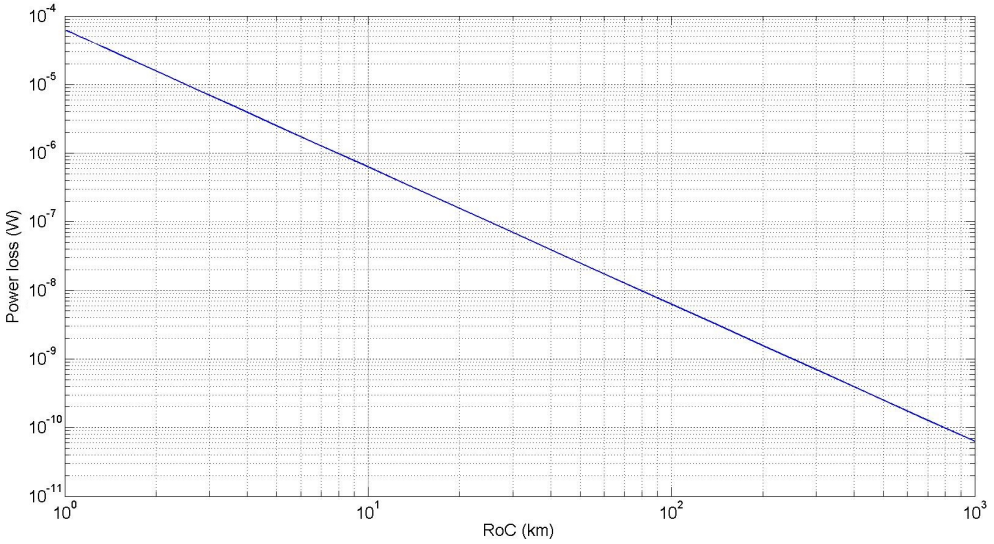

Figure 5.18: Power loss (referred to the input power) due to the error in the radius of curvature of the ETM.

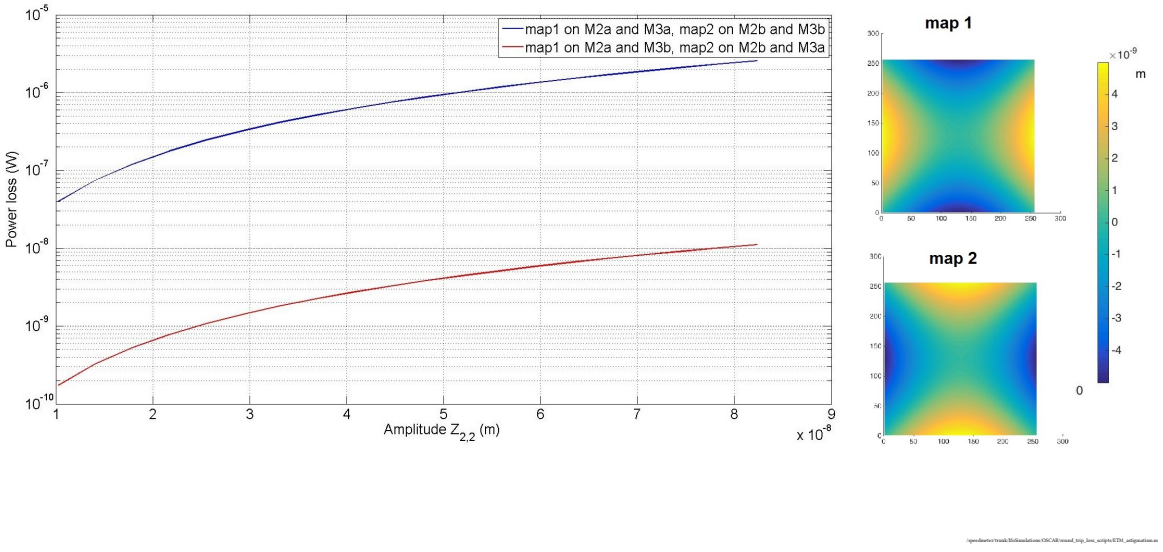

Figure 5.19: Power loss (referred to the input power) obtained adding two different maps that represent the astigmatism (the two figures on the right) on the four ETM as a function of the of amplitude of the Zernike polynomial (2,2).

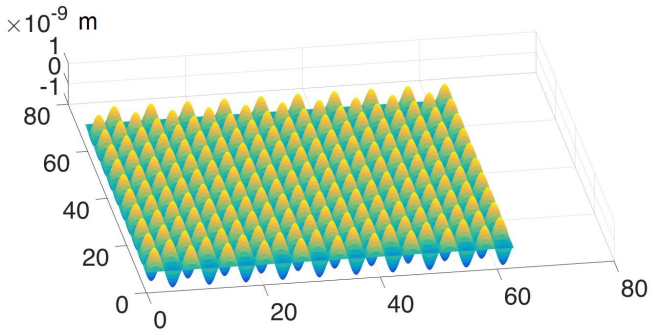

Figure 5.20: Sinusoidal map used to simulate errors at different spatial frequencies.

5.3.3 Errors at discrete spatial frequencies

We want now to define the requirements of the surface error based on their spatial frequencies. The analysis is made using a perfect sinusoidal map as that one shown in figure 5.20. This map is added to the mirror and the simulations for the calculation of the round trip loss are performed with OSCAR. The analysis made can be divided in two main parts. First the simulations are performed with a constant amplitude of 1 nm and the round trip loss is calculated changing the spatial frequencies from $0.3\,\mathrm{mm}^{-1}$ to $2\,\mathrm{mm}^{-1}$. In this way it is possible to see the dependance of the loss from the spatial frequencies and to select some crucial values and then define the requirements for each range of spatial frequencies as described below. The second part of the analysis is the calculation of the round trip loss as a function of the amplitude. To do that we fix the spatial frequencies at the two selected values, which define the limits of two ranges of frequencies. We make then the same calculation as before changing the amplitude. So, it is possible to give the requirements for the peak to peak value of the error in each range of frequencies.

Note that this analysis represents the upper limit of the loss. The requirement defines the maximum amplitude peak to peak that a surface error can have, but this calculation considers that all the peaks have the maximum value and this is not true for real mirrors.

In this case the method used is exactly the same for ITM and ETM. The results are shown in figures 5.21 and 5.22. In figure 5.21 we have the plot of the loss as a function of the spatial frequencies for both ITM and ETM. The simulations for the ITM are made using a grid with 256 points and a physical size of 0.015 (to evaluate the clipping loss we need that the physical size must be a little larger than the size of the mirror) and we define a map with an amplitude of 1 nm, and a size of 256 points. So since the ITM size is 1 cm, the resolution of the map is $\sim 40\,\mu$m. When we make the same simulations for the ETM, we have to consider its larger dimension. So we define a grid with 256 points and a physical size of 5.5 cm and a map with 1 nm amplitude and 2048 points[4], which gives a resolution

[4]The map does not need to have the same size of the grid, since an interpolation is done internally by OSCAR when the map is added.

close to the previous one, i.e. $\sim 24\ \mu$m. The fluctuation of the values that we can see for the ETM is probably due to the fact that in this case the angle of incident is $\sim \pi/4$. The peak and the valley at each cycle in fact differ of half the wavelength of the sinusoidal map, so the beam will be reflected in opposite directions in the two cases. From these results, we decide to set as limits for the description of the spatial frequencies $0.3\ \text{mm}^{-1}$ and $1\ \text{mm}^{-1}$. Notice that $1\ \text{mm}^{-1}$ corresponds to the size of the beam and we can see in fact that at this value the trend of the curve changes.

In figure 5.22 the plot of the loss for a fixed spatial frequency at these two values and changing the amplitude is shown. We set as requirements for the ITM 0.3 nm P-V for high spatial frequencies and 2 nm P-V for low spatial frequencies and for the ETM 0.25 nm P-V for high spatial frequencies and 1 nm P-V for low spatial frequencies, which should give about the same loss for both, i.e. $4\times \sim 10^{-7}$ ppm for low spatial frequencies and 3 ppm for high spatial frequencies.

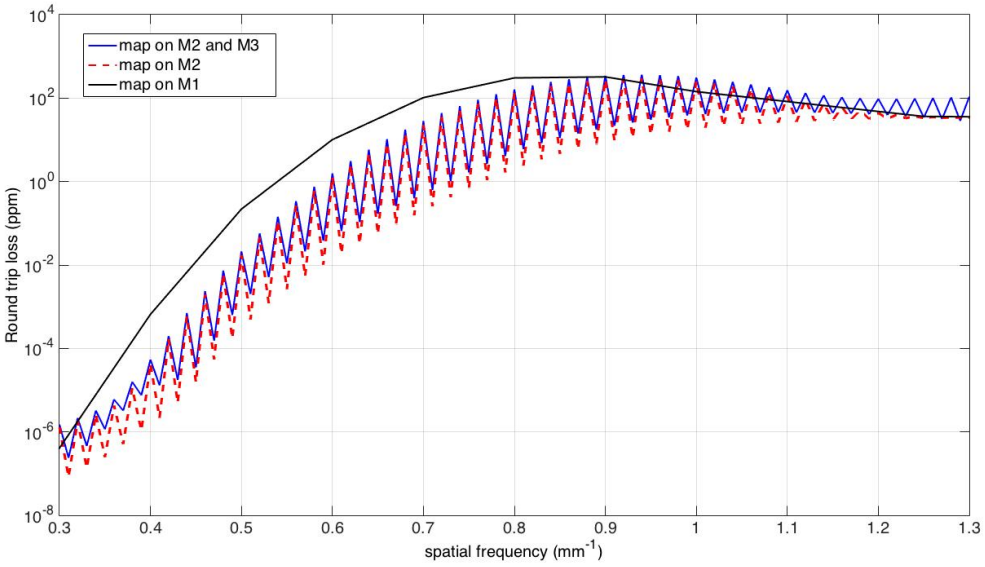

Figure 5.21: Dependence of the power loss from the spatial frequency of the periodic surface errors with a fixed amplitude of 1 nm when the map is added only on the ITM (black line), only on one ETM (red line) and on both ETM (blue line). Notice that, because of the larger dimensions of the ETM, we needed a map with a greater number of points in order to have a similar resolution.

5.3.4 Microroughness

An analysis of the loss due to the microroughness is very difficult to do. This kind of errors, in fact, has typical spatial frequencies of the order of the microns and high resolution maps are then required. For this reason we decide to set as requirements 0.1 nm rms, which is a standard value for microroughness of high quality optics.

5.3.5 Flat edge of the ITM

Since for the SSM experiment we use monolithic suspensions for the arm cavity mirrors, the test masses have to feature a flat edge, where the ears can be bonded. However, because of the small dimensions of the ITM, even a very small flat edge could cause a significant increase of the clipping loss.

So we make a calculation of the loss as a function of the dimensions of the flat edge. To do that, we modify the mask of the `Interface` function in OSCAR, changing the value of the flat edge thickness from 0.5 mm to 2 mm. This simulation is made with one of the map provided in the OSCAR package (with flatness of 96.61 nm rms) added to the input mirror and a plot of the round trip loss as a function of the flat edge thickness is made (figure 5.23). We decide to set the thickness of the flat edge to 2 mm.

5.4 Outcome and conclusions

According to the manufacturer, the required radius of curvature value for ITM of 7.91 ± 0.02 m was overly difficult and expensive to achieve, so they suggested to change it to 8.0 ± 0.2 m. In order to be sure that this change was not critical for our experiments, we analysed how it affects the behaviour of our cavity. As explained before, the resonance of the high order modes in the cavity depends on the radius of curvature of the ITM and the length of the cavity. So we made a plot similar to that one shown in figure 3.7, but this time we kept the radius of curvature constant and changed the length of the cavity. We can see from figure 5.24 that in order to avoid the resonance of the 11th order mode, we had to slightly change the length of the cavity by about 10 cm.

Once the mirrors arrived we had the chance to make some tests to check if the requirements were satisfied. The company provided the measurements of the maps of the surfaces (shown in appendix B), and so it was possible to re-run the simulations with the real surface profiles. We calculated the round trip loss with these maps added to the mirrors.

In the case of the ETM we have two possible orientations, since the substrates have two flat edges on opposite sides. So we calculated the round trip loss with the two possible positions. The results are shown in table 5.2: as we can see all values are below 5 ppm.

Then choosing the two worst and the two best cases (highlighted in red and green in table) we calculated the round trip loss in these cases when also the map on the ITM is added. The results are shown in table 5.3.

Thanks to the surface measurements provided by the company we were also able to calculate the PSD of the mirrors surfaces. The plots are shown in figure 5.25. As we can see, for the ETM the PSD is about one order of magnitude better than that one of the sample

mirror used for the first simulations and shown in figure 5.7. The peaks that appear at different frequencies for each map are due to the fact that the measurements were taken when the substrates did not have the coating yet and hence there were interference fringes from reflection off the back surface, as it is clear from the surface profile shown in figure B.6.

On the other side, for the ITM it could look like they are worse than the sample mirror, since the PSD is about three orders of magnitude higher. However, we have to consider that in this case the curvature has not been removed and then it dominates in the spectrum.

In this chapter the derivation of the requirements for the arm cavity mirrors of the Glasgow SSM experiments has been shown. We have described how the different surface errors are simulated and the results obtained for the round trip loss that each of them causes (a summary of the requirements can be found in appendix C where the specifications documents are reported). The total loss estimated by the simulations were of the order of 19 ppm, while the values obtained with the real mirrors maps is between 8.64 and 13.30 ppm.

The substrates were then coated in order to have the required transmissivity and after the coating the scattering of ETM were measured again by the company and a value between 2.2 and 9 ppm were found (the complete set of measurements is listed in table 5.4).

After these procedures, the mirrors were ready to be bonded in order to be assembled in the monolithic suspensions. A picture of the mirror is shown in figure 5.26. A brief overview of the bonding procedure can be found in appendix D, while a detailed description of this procedure and in general on the Glasgow SSM mirrors suspensions can be found in [83].

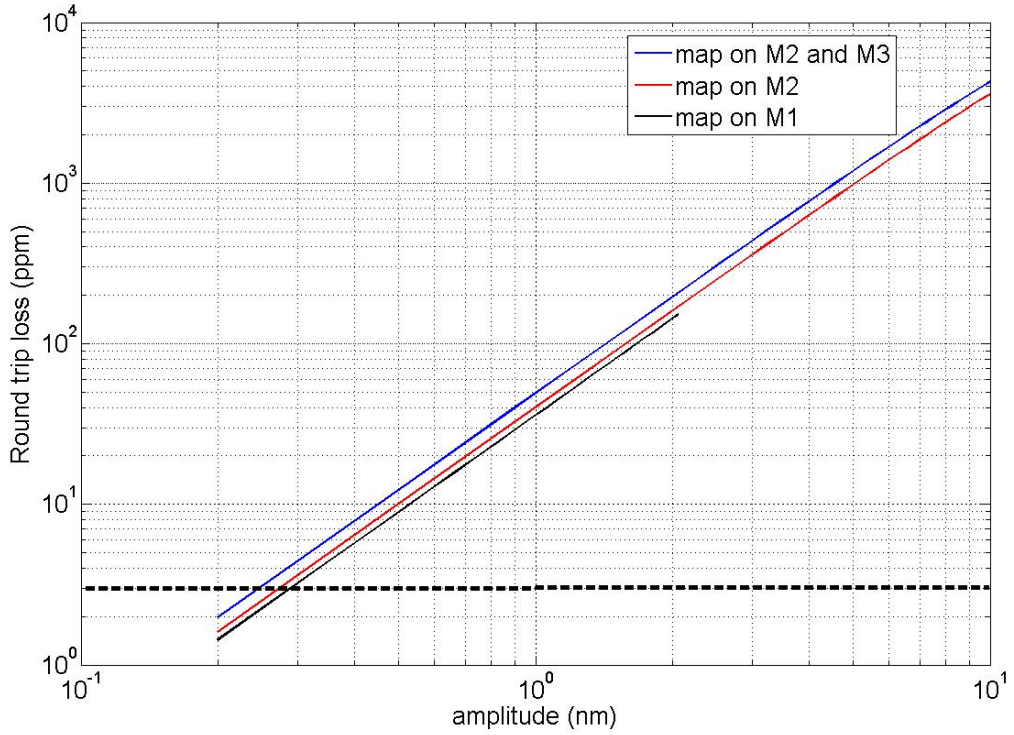

(a)

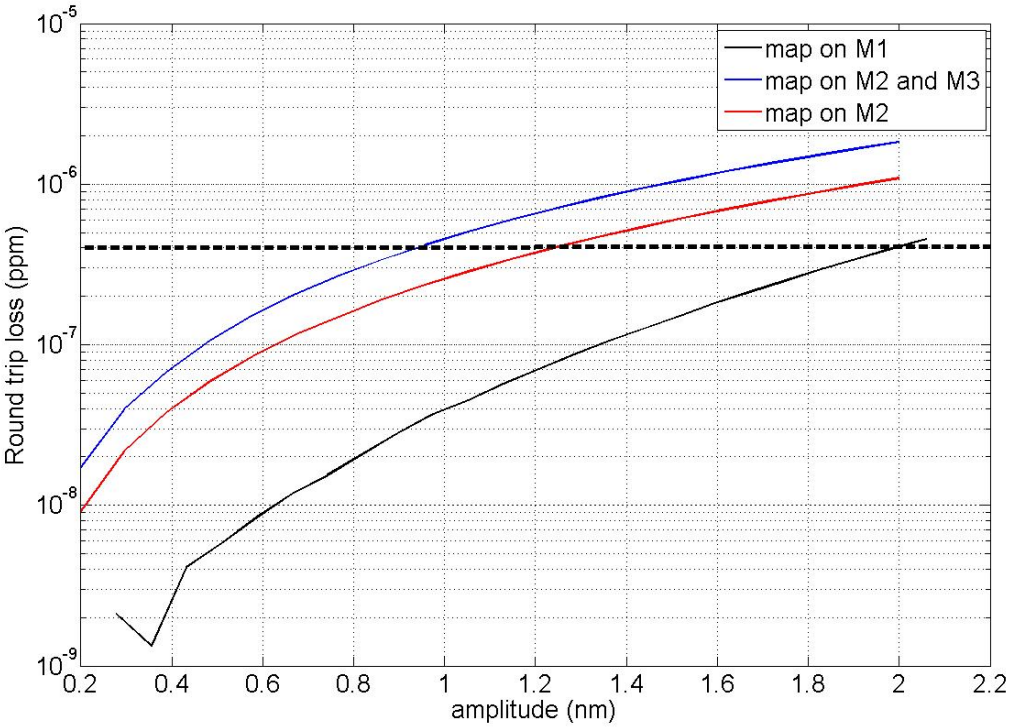

(b)

Figure 5.22: Dependence of the power loss from the amplitude of the periodic surface errors with a fixed spatial frequency of $1\,\mathrm{mm}^{-1}$ (a) and $0.3\,\mathrm{mm}^{-1}$ (b). In both plots the dashed line shows the chosen requirements.

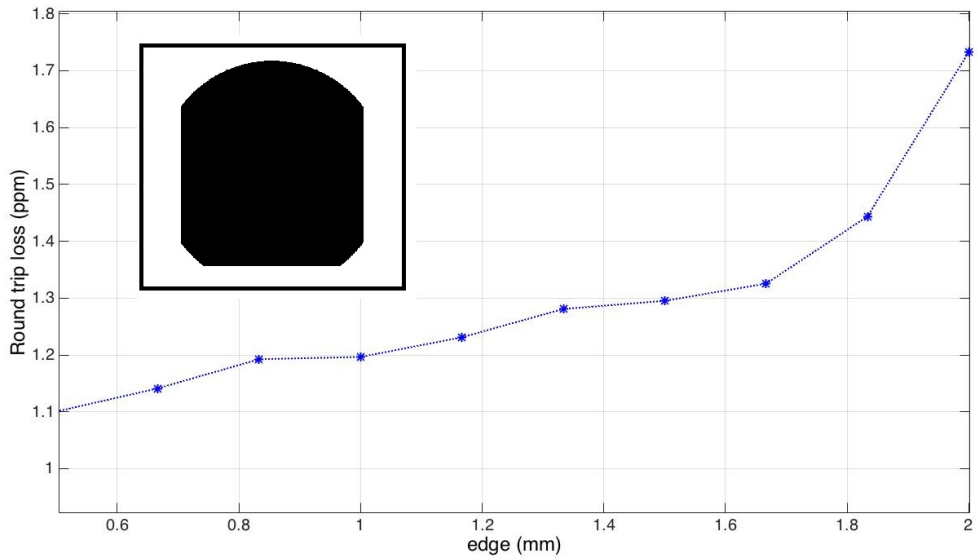

Figure 5.23: Roundtrip loss as a function of the flat edge thickness of the ITM. In the box the shape of the mirror is shown (seen from the front).

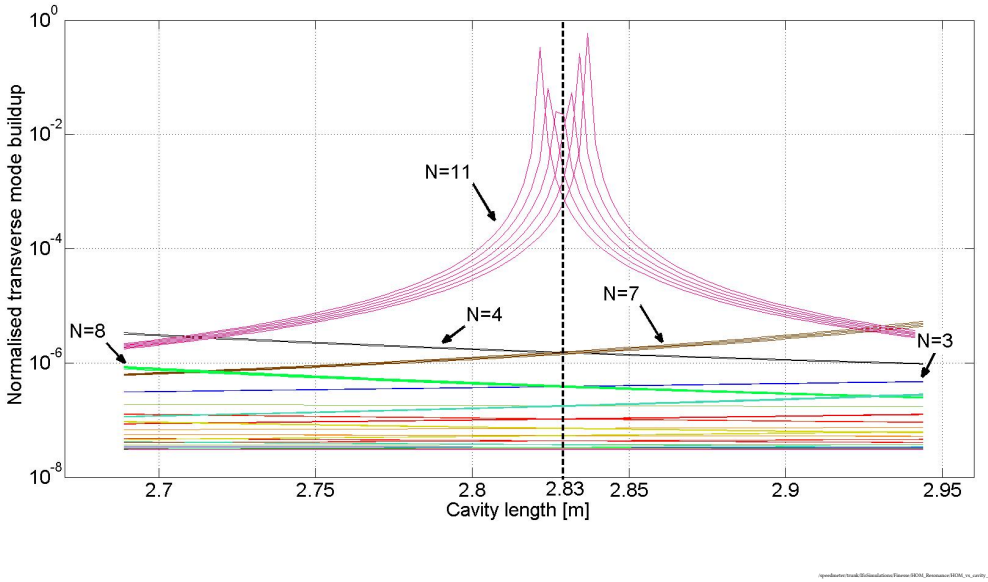

Figure 5.24: Build up of the higher order modes as a function of the cavity length considering the radius of curvature of the ITM equal to 8.2 m.

Map rotated by 90°

	ETM#3	ETM#6	ETM#7	ETM#8	ETM#10
ETM#2	1.92	4.42	2.14	3.16	2.91
ETM#3	-	2.87	1.76	2.43	2.60
ETM#6	-	-	3.27	3.79	4.12
ETM#7	-	-	-	3.25	2.77
ETM#8	-	-	-	-	4.13

Map rotated by 270°

	ETM#3	ETM#6	ETM#7	ETM#8	ETM#10
ETM#2	1.92	4.91	2.14	3.16	2.91
ETM#3	-	3.21	1.76	2.43	2.60
ETM#6	-	-	3.49	4.46	4.67
ETM#7	-	-	-	3.25	2.77
ETM#8	-	-	-	-	4.13

Table 5.2: Round trip loss with the real maps added to the ETM with the two possible orientations. The two best and worst values are highlighted in green and red respectively. All values are in ppm.

No map on ITM	1.76	1.92	4.67	4.91
ITM#1	8.68	8.64	11.24	10.84
ITM#2	11.03	11.33	13.15	13.30
ITM#3	9.29	9.14	12.19	11.59

Table 5.3: Round trip loss with the real maps added to both ETM and ITM. In the first line we reported as comparison also the loss when only the ETM the map is added. All values are in ppm.

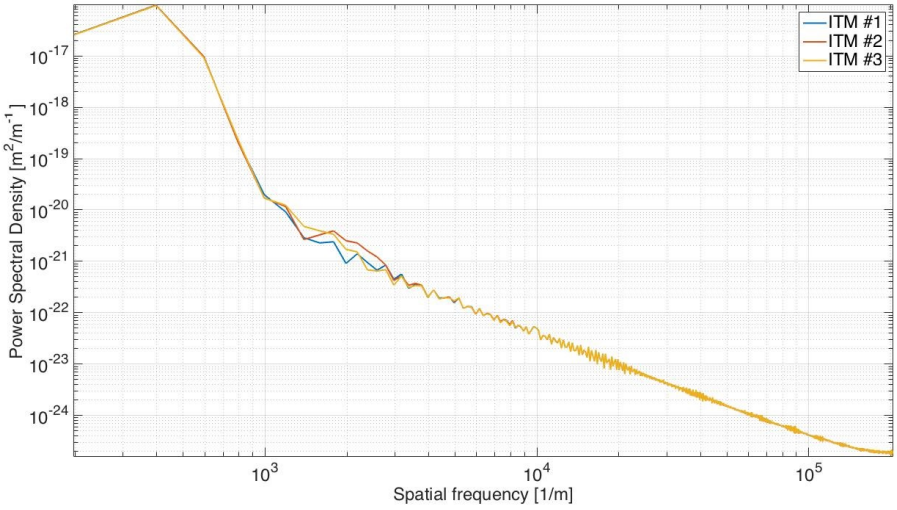

(a) ITM back side.

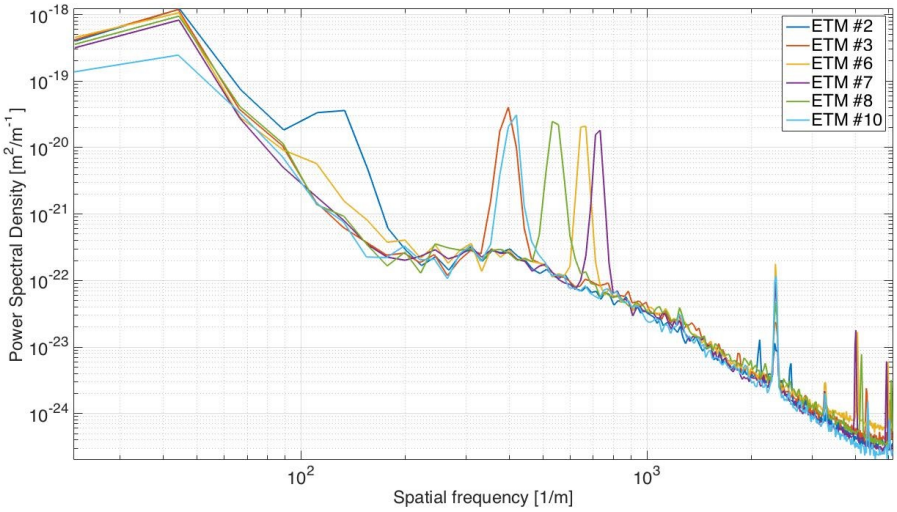

(b) ETM front side.

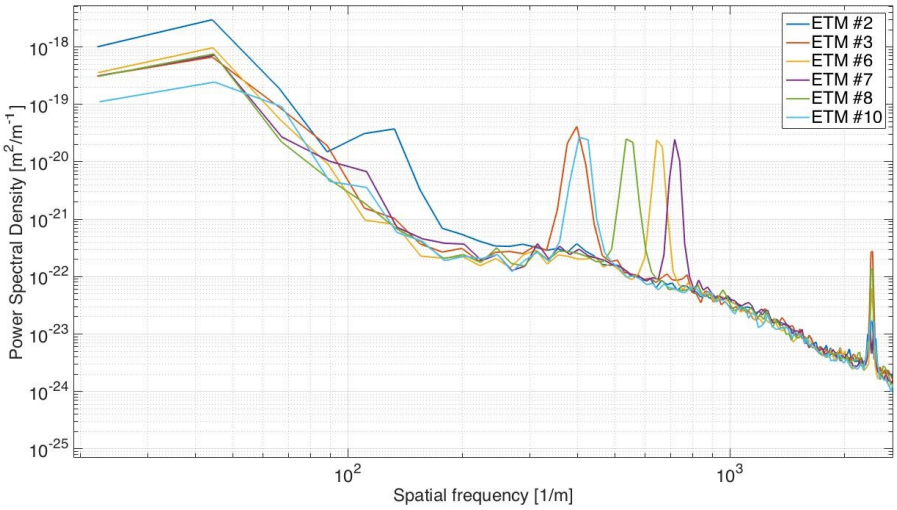

(c) ETM back side.

Figure 5.25: PSD of the surfaces of the SSM substrates.

test mass	scattering
ITM	5 (average)
ETM#2	2.8
ETM#3	4.5
ETM#6	9.0
ETM#7	4.0
ETM#8	7.7
ETM#10	2.2

Table 5.4: Measurements of the scattering of the arm cavity mirrors after coating. All values are in ppm.

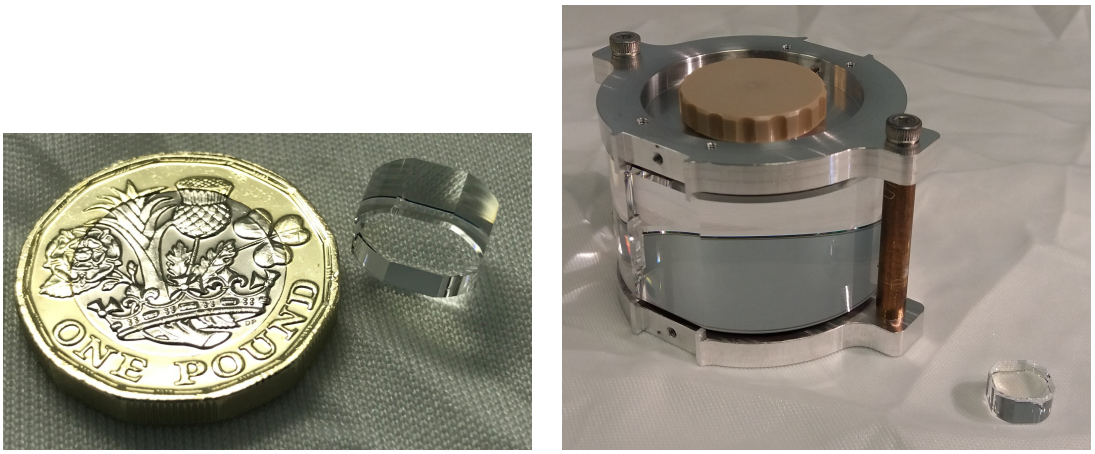

(a) (b)

Figure 5.26: Pictures of the ITM compared to a 1 pound coin (a) and of the ITM and ETM (b).

Chapter 6

Backscattering effects in triangular cavities

In this chapter we will analyse the influence of backscattering inside the arm cavities of the speed meter. After a short introduction on the optical scattering, given in the first section, we will explain the backscattering effects and their properties in terms of amplitude and phase of the scattering beams in the second section. In the third section we will derive the optical transfer matrix of a mirror taking into account all the first orders (plus and minus) scattering beams in both reflection and transmission. Finally, in the fourth section we will show the calculation of the I/O relations of a triangular cavity with an ITM with the optical transfer matrix described in the third section. The numerical solutions obtained applying this results to real interferometers parameters will be shown in the next chapter.

6.1 Introduction to optical scattering

With optical scattering we mean the effects of the interaction between radiation and matter on the propagation path of the light. The scattering can be due to the interaction of the photons with other individual particles or due to the interaction of light beams with a surface. In this analysis we will only study the second case.

A sketch of optical scattering is shown in figure 6.1, where the deflection of the radiation due to some imperfections on the mirror surface is shown.

In the case of coherent scattering, the relation between the incident light and the scattered light are easier to deduce since the only effect of the scattering surface is the modification of the direction of propagation, without changing the intrinsic properties of the radiation (like the wavelength). Specifically, we have that the angle of the m^{th} order scattering beam θ_m is related with the incidence angle θ_i and the spatial frequency of the mirror surface

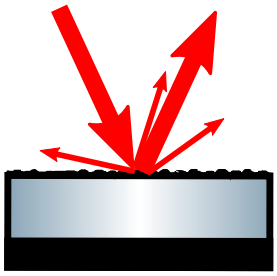

Figure 6.1: Light beams scattered by the roughness of a reflective surface.

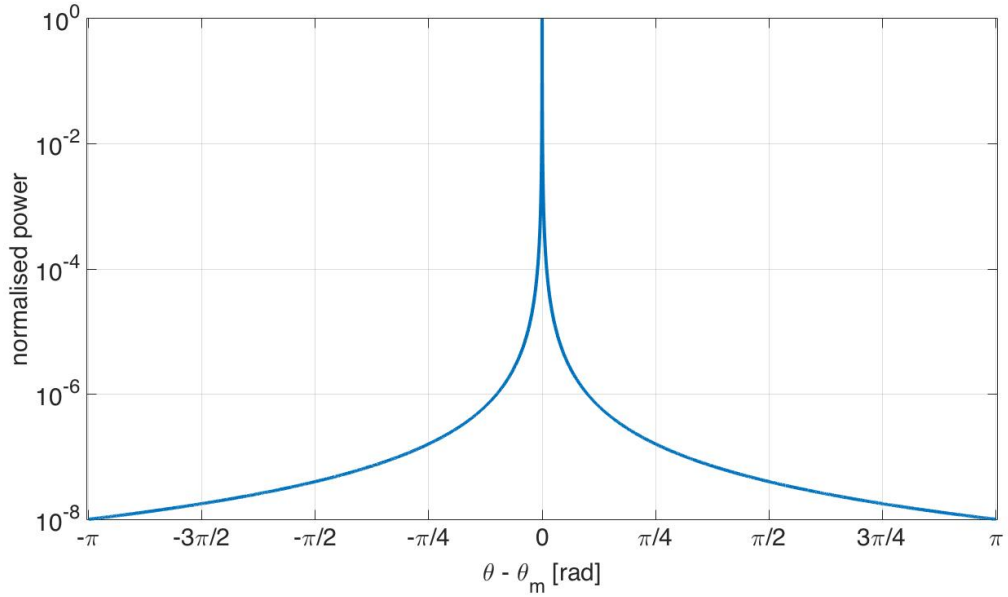

Figure 6.2: Normalised power distribution of the scattered beam ($\propto \theta_m^{-2}$).

imperfections f_g through the equation [91]

$$\sin\theta_m = \sin\theta_i + m f_g \lambda. \tag{6.1}$$

From this equation it is clear that mirror surface imperfections with high spatial frequencies, like microroughness, create scattering at large angle, whereas surface imperfections with low spatial frequencies, like flatness, creates scattering at small angle.

Furthermore, we have that the power distribution function of the scattered light can be approximated (for small angles) to be proportional to θ_m^{-2} [92]. This means that the power of the scattered beam is not concentrated in one direction, but it is distributed in a broad function around θ_m, as shown in figure 6.2.

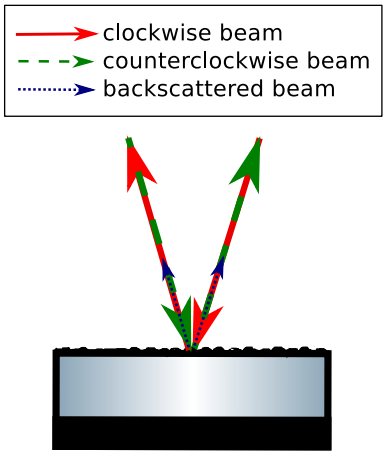

Figure 6.3: Mirror with incident clockwise (in red) and counterclockwise (in green) beams and the surface roughness that creates a backscattering beam (in blue).

6.2 Backscattering effect

For the Glasgow SSM experiment the scattering could have an important effect on the performance of the cavity. In this case, in fact, the beam can be scattered back in the same direction of the incident beam. As we explained in the previous section, the scattered beam has a broad power distribution function and this mean that part of it will couple with the counter-propagating mode (see figure 6.3).

This effect is called backscattering and, as we will see in the next sections, it can affect significantly the quantum noise of the SSM.

6.2.1 Amplitude of the backscattered radiation

A first estimation of the amplitude of the backscattering beam as a function of the mirror microroughness was made for the Virgo input mode cleaner[1] [93][94]. In this analysis the mirror surface is described by the function

$$f(x,y) = \frac{x^2+y^2}{2R} + \epsilon(x,y), \tag{6.2}$$

where the first terms represents the curvature of the mirror with radius of curvature R and the second term is a function that describes the microroughness. A clockwise beam is

[1]The input mode cleaner in Virgo is a triangular cavity placed before the power recycling mirror with the aim to select only the fundamental mode before being injected in the interferometer. The mode cleaner cavity, in fact is tuned to the resonance frequency of the fundamental mode, that is different from that ones of the higher order order modes, which will be then suppressed.

present in the cavity and it is supposed to be gaussian, so it is described by the equation

$$\psi_0(x,y) = \sqrt{\frac{2}{\pi w^2}}\,\exp\left[-\frac{x^2+y^2}{w^2} - ik\frac{x^2+y^2}{2\rho} + ik\theta\,(x\cos\phi + y\sin\phi)\right], \tag{6.3}$$

where w is the beam width on the mirror surface, ρ is its curvature, supposed to be equal to the mirror curvature R, $k = \frac{2\pi}{\lambda}$ is the wave number and (θ,ϕ) are the incidence angles measured respect to the mirror axis. Furthermore, in the cavity there is also a counter-propagating mode that is the same as the clockwise mode, but with opposite phase. So its equation will be

$$\psi_c(x,y) = \sqrt{\frac{2}{\pi w^2}}\,\exp\left[-\frac{x^2+y^2}{w^2} + ik\frac{x^2+y^2}{2\rho} - ik\theta\,(x\cos\phi + y\sin\phi)\right]. \tag{6.4}$$

The equation of the beam reflected by the curved mirror is

$$\psi_R(x,y) = \psi_0(x,y)\,\exp\left[2ikf(x,y)\right], \tag{6.5}$$

and the coupling between the counter-clockwise and the reflected beam is given by the hermitian scalar product between the two fields, i.e.

$$\begin{aligned}
\gamma(\theta,\phi) &= \langle\psi_c,\psi_R\rangle \\
&= \int_{\mathbb{R}^2}\frac{2}{\pi w^2}\,\exp\left[-2\frac{x^2+y^2}{w^2}\right]\exp\left[2ik\left(f(x,y) - \frac{x^2+y^2}{2\rho}\right)\right] \\
&\quad\cdot\exp\left[-2ik\theta(x\cos\phi + y\sin\phi)\right]dx\,dy \\
&= \int_{\mathbb{R}^2} I(x,y)\exp\left[2ik\epsilon(x,y)\right]\exp\left[-2ik\theta(x\cos\phi + y\sin\phi)\right]dx\,dy,
\end{aligned} \tag{6.6}$$

where we have defined the normalised intensity distribution of the incident beam as

$$I(x,y) = \frac{2}{\pi w^2}\exp\left[-2\frac{x^2+y^2}{w^2}\right]. \tag{6.7}$$

The square modulus of γ is called coupling factor Γ and it represents the relative intensity coupled by backscattering in the counter-propagating mode. If the microroughness is small compared to the wavelength, then the coupling factor can be written as

$$\Gamma(\theta,\phi) = \left|\int_{\mathbb{R}^2} I(x,y)\left(1 + 2ik\epsilon(x,y) - 2k^2\epsilon(x,y)^2\right)\exp\left[2ik\theta(x\cos\phi + y\sin\phi)\right]\right|^2 dx\,dy. \tag{6.8}$$

Then since

$$\int_{\mathbb{R}^2} I(x,y)\exp\left[2ik\theta(x\cos\phi + y\sin\phi)\right]dx\,dy = \exp\left[-\frac{\theta^2k^2w^2}{2}\right], \tag{6.9}$$

we have

$$\begin{aligned}\Gamma(\theta,\phi) &= \left|\int_{\mathbb{R}^2} I(x,y)\left(1+2ik\epsilon(x,y)-2k^2\epsilon(x,y)^2\right)\exp\left[2ik\theta(x\cos\phi+y\sin\phi)\right]\right|^2\\ &= \left|\exp\left[-\frac{2\theta^2\pi^2w^2}{\lambda^2}\right] + 2ik\int_{\mathbb{R}^2} I(x,y)\,\epsilon(x,y)\exp\left[2ik\theta(x\cos\phi+y\sin\phi)\right]dx\,dy\right.\\ &\left.-2k^2\int_{\mathbb{R}^2} I(x,y)\,\epsilon(x,y)^2\exp\left[2ik\theta(x\cos\phi+y\sin\phi)\right]\right|^2 dx\,dy.\end{aligned} \tag{6.10}$$

If we define the natural overlap between the two beams as the overlap that we have when the microroughness is zero, i.e.

$$\Gamma_0(\theta) = \exp\left[-\frac{2\,\theta^2\pi^2w^2}{\lambda^2}\right] = \exp\left[-\frac{2\,\theta^2}{\theta_g^2}\right], \tag{6.11}$$

we can notice that for $\theta \gg \theta_g$ (as happens for both the Virgo input mode cleaner and the arm cavity of the Glasgow SSM experiment) then we can neglect the natural overlap term and the coupling factor becomes

$$\begin{aligned}\Gamma(\theta,\phi) = 4k^2\left|\int_{\mathbb{R}^2} I(x,y)\,\epsilon(x,y)\exp\left[2ik\theta(x\cos\phi+y\sin\phi)\right]\right.\\ \left.+ik\int_{\mathbb{R}^2} I(x,y)\,\epsilon(x,y)^2\exp\left[2ik\theta(x\cos\phi+y\sin\phi)\right]\right|^2,\end{aligned} \tag{6.12}$$

that is the Fourier transform of the microroughness function weighted by the intensity of the beam. A numerical solution obtained using a real mirror map with a microroughness of 1.3 nm rms is shown in figure 6.4.

Unfortunately we do not have a mirror map of the microroughness of the arm cavity mirror of the Glasgow SSM, so we cannot apply this analysis at our case. However these results are useful, because they provide an idea of the order of magnitude that we can expected for the power of the backscattered beam. We have in fact that for mirrors with microroughness of 1.3 nm rms the power of the backscattered beam is below 0.1 ppm (see figure 6.4). Considering that for the SSM's ITM the microroughness is 0.1 nm rms, we can expect that in this case the backscattered power will be even smaller.

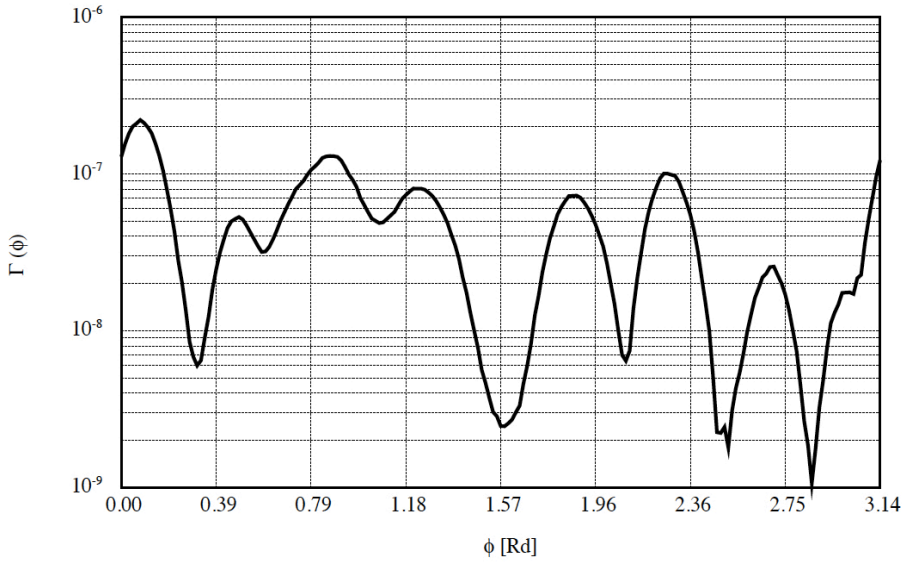

Figure 6.4: Coupling factor for backscattering as a function of the angle of rotation of the mirror ϕ for the Virgo input mode cleaner. Figure taken from [93].

6.3 Relations between plus and minus first order scattering beams

Since the amplitude of the electromagnetic fields involved in the backscattering are very small, we need to take into account all first order scattering terms (see figure 6.5). So, we need to know the amplitudes and the phases of the scattering beams. To that end some simulations were performed[2], considering a binary grating with amplitude 0.5 nm, a grating period of 6.9 μm, an angle of incidence of 4.4° and a radiation wavelength of 1064 nm. Furthermore, in order to have a transmissivity $\sim$ 700 ppm, a coating composed by 12 pairs of silica and tantala is considered.

Amplitude

As a general rule the amplitude of plus and minus scattering terms are the same for the reflection and the transmission, but the ratios between the first order and the zero order beams for the reflected and the transmitted beams are not the same. This can be easily explained considering the grating equation (see equation 6.1). Through this equation, in fact, we can calculate the maximum scattering order allowed $m^{(max)}$, considering that the maximum angle must be $< \pi/2$. Combining the grating equation with the Snell's law we have

$$\sin\theta_m^{(max)} = m_{max}\, n\lambda f_g < 1. \tag{6.13}$$

[2]The simulations were performed by Dr Stefanie Kroker from the Friedrich Schiller University Jena, using a software based on the RCWA (Rigorous Coupled-Wave Analysis) method.

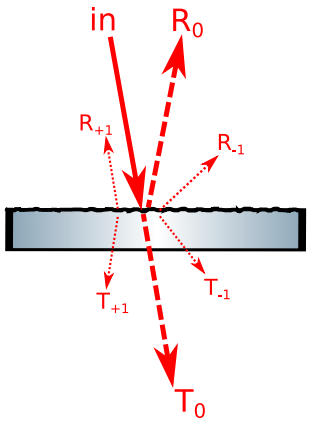

Figure 6.5: Mirror with all first order scattering beams. The point of incidence/reflection should be the same for all beams, but for practical reason the beams have been slightly shifted from their real position in order to be be able to distinguish them.

In our case the refractive index of the medium where the beam is reflected (air, with n=1) and where it is transmitted (silica, with n=1.45) are different, and specifically it is larger for the latter. This means that we will have the transmitted power split in a larger number of beams.

However we have also to consider that in our case because of the low transmissivity the amount of power in the higher order beams can be neglected and then the efficiency in reflection and transmission can be considered equal. From the simulations we have indeed that he intensities of each order are (in %)

T+5	T+4	T+3	T+2	T+1	T0	T-1	T-2	T-3	T-4	T-5
4e-8	2e-14	1e-8	1e-14	1e-7	0.1	1e-7	1e-14	1e-8	1e-14	7e-9

for the transmissivity and

R+5	R+4	R+3	R+2	R+1	R0	R-1	R-2	R-3	R-4	R-5
6e-6	4e-11	5e-5	5e-11	4e-4	99.9	4e-4	5e-11	5e-5	5e-11	1e-5

for the reflectivity. Then the ratios between the first and the zero orders are

$$\frac{T_{+1}}{T_0} \approx 1\times10^{-6}, \quad \frac{T_{-1}}{T_0} \approx 1\times10^{-6}, \quad \frac{R_{+1}}{R_0} \approx 4\times10^{-6}, \quad \frac{R_{-1}}{R_0} \approx 4\times10^{-6}.$$

So in our analysis we will consider that all these four are the same.

Phases

In order to be able to write the transfer matrix of the mirror considering all the scattering beams, we also need to have some information about the phases. The relations between the phases of the beams can be obtained from the same simulations performed for the amplitudes, which gives (in rad)

T+5	T+4	T+3	T+2	T+1	T0	T-1	T-2	T-3	T-4	T-5
1.61	-0.72	2.57	0.49	3.05	5e-3	8e-3	0.89	-0.28	0.11	-0.98

for the transmissivity and

R+5	R+4	R+3	R+2	R+1	R0	R-1	R-2	R-3	R-4	R-5
2.05	-0.45	2.73	0.58	3.08	9e-3	9e-3	0.92	-0.20	0.27	-0.71

for the reflectivity. From these results we can notice that the difference between the phase of the "plus" mode and the respective "minus" is always $\sim \pi$.

6.4 Transfer matrix of a mirror with all first order scattering beams

We have now all the means to derive the optical transfer matrix of a mirror considering all the first order scattering beams. Figure 6.6a shows the ITM that we want to study with the microroughness that creates backscattering and all the other first order beams in both transmission and reflection. As we can see the +1st order terms have the same direction as the counter-propagating beams and hence they will couple with them. On the other hand, the -1st order terms can be considered as loss since they create four additional ports that do not couple to the cavity. As we explained in section 2.1.4, in case of loss, a mirror is equivalent to an optical system composed by the mirror without loss and one beamsplitter with reflectivity equal to the loss. In our case, since there are four input beams, in the calculation we need the four beamsplitters shown in figure 6.6b.

However in this case we have to be more careful, since we have four input beams and the loss in each port is the coupling of the T_{-1} term and R_{-1} term of two different input beams. Then we can describe the optical system dividing the process in three parts:

- the first part describes the coupling between the -1st order terms, described by the matrix $\mathbb{C}$;

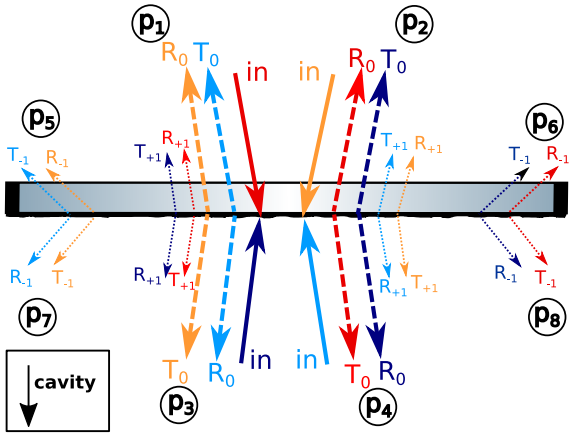

(a)

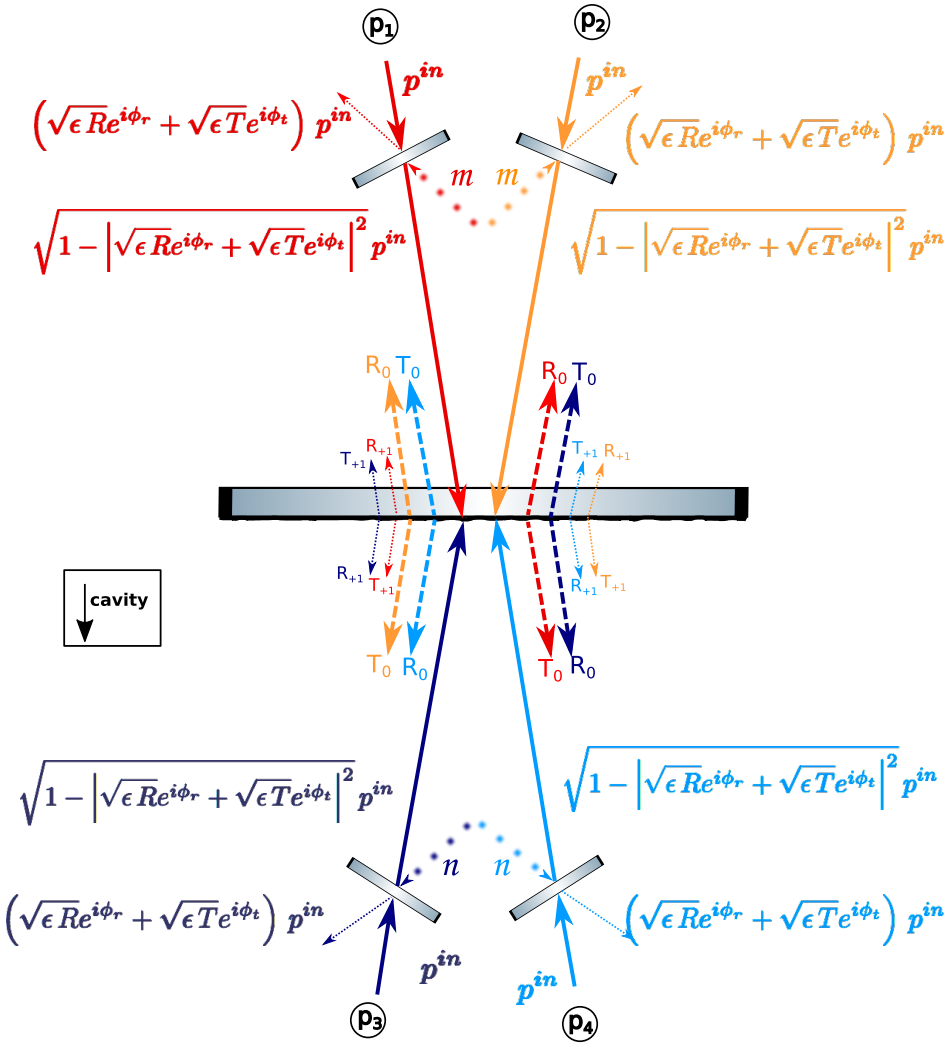

(b)

Figure 6.6: (a) Mirror with 4 input beams and all the first order scattering beams in reflection and transmission. (b) Equivalent system of the mirror in (a) composed by the lossless mirror and four beamsplitters.
Also in this case all the beams in each port are supposed to be overlapped but we have drawn them here slightly shifted in order to be able to distinguish them.

- the second part is the transfer matrix of the mirror with 0 and +1 order terms, described by the matrix $\mathbb{T}$;
- the third and last part is the second passage through the beamsplitter that gives the output beams, described by the matrix $\mathbb{B}$.

In this way the optical system is described by the following equations

$$\begin{bmatrix} \hat{\mathbf{P}}_1^{out}(\omega) \\ \hat{\mathbf{P}}_2^{out}(\omega) \\ \hat{\mathbf{P}}_3^{out}(\omega) \\ \hat{\mathbf{P}}_4^{out}(\omega) \\ \hat{\mathbf{P}}_5^{out}(\omega) \\ \hat{\mathbf{P}}_6^{out}(\omega) \\ \hat{\mathbf{P}}_7^{out}(\omega) \\ \hat{\mathbf{P}}_8^{out}(\omega) \end{bmatrix} = \begin{bmatrix} \mathbb{B}_1 & \mathbb{B}_2 \\ \mathbb{B}_3 & \mathbb{B}_4 \end{bmatrix} \begin{bmatrix} \mathbb{T}_1 & \mathbb{T}_2 \\ \mathbb{T}_3 & \mathbb{T}_4 \end{bmatrix} \begin{bmatrix} \mathbb{C}_1 & \mathbb{C}_2 \\ \mathbb{C}_3 & \mathbb{C}_4 \end{bmatrix} \begin{bmatrix} \hat{\mathbf{P}}_1^{in}(\omega) \\ \hat{\mathbf{P}}_2^{in}(\omega) \\ \hat{\mathbf{P}}_3^{in}(\omega) \\ \hat{\mathbf{P}}_4^{in}(\omega) \\ \hat{\mathbf{P}}_5^{in}(\omega) \\ \hat{\mathbf{P}}_6^{in}(\omega) \\ \hat{\mathbf{P}}_7^{in}(\omega) \\ \hat{\mathbf{P}}_8^{in}(\omega) \end{bmatrix}, \tag{6.14}$$

with

$$\mathbb{T}_1 = \begin{bmatrix} \sqrt{\epsilon R}\, e^{i\phi_{r+}} & \sqrt{R}\, e^{i\phi_{r0}} & \sqrt{\epsilon T}\, e^{i\phi_{t+}} & \sqrt{T}\, e^{i\phi_{t0}} \\ \sqrt{R}\, e^{i\phi_{r0}} & \sqrt{\epsilon R}\, e^{i\phi_{r+}} & \sqrt{T}\, e^{i\phi_{t0}} & \sqrt{\epsilon T}\, e^{i\phi_{t+}} \\ \sqrt{\epsilon T}\, e^{i\phi_{t+}} & \sqrt{T}\, e^{i\phi_{t0}} & \sqrt{\epsilon R}\, e^{i\phi_{r+}} & \sqrt{R}\, e^{i\phi_{r0}} \\ \sqrt{T}\, e^{i\phi_{t0}} & \sqrt{\epsilon T}\, e^{i\phi_{t+}} & \sqrt{R}\, e^{i\phi_{r0}} & \sqrt{\epsilon R}\, e^{i\phi_{r+}} \end{bmatrix} \tag{6.15}$$

$$\mathbb{T}_2 = \mathbb{T}_3 = \mathbb{O}, \quad \mathbb{T}_4 = \mathbb{I}, \tag{6.16}$$

$$\mathbb{C}_1 = \mathbb{C}_4 = e^{i\Phi}\sqrt{1 - |\epsilon R e^{i\phi_{r-}} + \epsilon T e^{i\phi_{t-}}|^2}\,\mathbb{I}, \tag{6.17}$$

$$\mathbb{C}_3 = \begin{bmatrix} 0 & \sqrt{\epsilon R}\, e^{i\phi_{r-}} & 0 & \sqrt{\epsilon T}\, e^{i\phi_{t-}} \\ \sqrt{\epsilon R}\, e^{i\phi_{r-}} & 0 & \sqrt{\epsilon T}\, e^{i\phi_{t-}} & 0 \\ 0 & \sqrt{\epsilon T}\, e^{i\phi_{t-}} & 0 & \sqrt{\epsilon R}\, e^{i\phi_{r-}} \\ \sqrt{\epsilon T}\, e^{i\phi_{t-}} & 0 & \sqrt{\epsilon R}\, e^{i\phi_{r-}} & 0 \end{bmatrix}, \tag{6.18}$$

$$\mathbb{C}_2 = \mathbb{C}_3^{\dagger}, \tag{6.19}$$

$$\mathbb{B}_1 = \mathbb{C}_1, \quad \mathbb{B}_2 = \mathbb{O}, \quad \mathbb{B}_3 = \mathbb{C}_3, \quad \mathbb{B}_4 = \mathbb{I} \tag{6.20}$$

and we have defined as $\hat{\mathbf{P}}_n^{in}(\omega)$ and $\hat{\mathbf{P}}_n^{out}(\omega)$ the input and output of the port n respectively. Using the phase convention described in section 2.1.3, the results of the simulations showed in the previous section and considering that the matrices must be unitary[3], we obtain

$$\phi_{t0} = \frac{\pi}{2}, \quad \phi_{r0} = 0, \quad \phi_{t-1} = -\pi, \quad \phi_{t+1} = 0, \quad \phi_{r-1} = \frac{\pi}{2}, \quad \phi_{r+1} = -\frac{\pi}{2}. \tag{6.21}$$

In this way the transfer matrix becomes

$$\mathbb{T}_1 = \begin{bmatrix} -i\sqrt{\epsilon R} & \sqrt{R} & \sqrt{\epsilon T} & i\sqrt{T} \\ \sqrt{R} & -i\sqrt{\epsilon R} & i\sqrt{T} & \sqrt{\epsilon T} \\ \sqrt{\epsilon T} & i\sqrt{T} & -i\sqrt{\epsilon R} & \sqrt{R} \\ i\sqrt{T} & \sqrt{\epsilon T} & \sqrt{R} & -i\sqrt{\epsilon R} \end{bmatrix}, \tag{6.22}$$

$$\mathbb{C}_3 = \begin{bmatrix} 0 & i\sqrt{\epsilon R} & 0 & -\sqrt{\epsilon T} \\ i\sqrt{\epsilon R} & 0 & -\sqrt{\epsilon T} & 0 \\ 0 & -\sqrt{\epsilon T} & 0 & i\sqrt{\epsilon R} \\ -\sqrt{\epsilon T} & 0 & i\sqrt{\epsilon R} & 0 \end{bmatrix}, \tag{6.23}$$

$$\mathbb{C}_1 = \mathbb{C}_4 = e^{i\Phi}\sqrt{1-\epsilon(R+T)}\,\mathbb{I}, \tag{6.24}$$

with the condition

$$R + T + \epsilon R + \epsilon T = 1. \tag{6.25}$$

In the end the I/O relations of the mirror can be written as

$$\begin{bmatrix} \hat{\mathbf{P}}_1^{out}(\omega) \\ \hat{\mathbf{P}}_2^{out}(\omega) \\ \hat{\mathbf{P}}_3^{out}(\omega) \\ \hat{\mathbf{P}}_4^{out}(\omega) \\ \hat{\mathbf{P}}_5^{out}(\omega) \\ \hat{\mathbf{P}}_6^{out}(\omega) \\ \hat{\mathbf{P}}_7^{out}(\omega) \\ \hat{\mathbf{P}}_8^{out}(\omega) \end{bmatrix} = \begin{bmatrix} \mathbb{C}_1\mathbb{T}_1\mathbb{C}_1 & \mathbb{C}_1\mathbb{T}_1\mathbb{C}_2 \\ \mathbb{C}_3\mathbb{T}_1\mathbb{C}_1 + \mathbb{C}_3 & \mathbb{C}_3\mathbb{T}_1\mathbb{C}_2 + \mathbb{C}_4 \end{bmatrix} \begin{bmatrix} \hat{\mathbf{P}}_1^{in}(\omega) \\ \hat{\mathbf{P}}_2^{in}(\omega) \\ \hat{\mathbf{P}}_3^{in}(\omega) \\ \hat{\mathbf{P}}_4^{in}(\omega) \\ \hat{\mathbf{P}}_5^{in}(\omega) \\ \hat{\mathbf{P}}_6^{in}(\omega) \\ \hat{\mathbf{P}}_7^{in}(\omega) \\ \hat{\mathbf{P}}_8^{in}(\omega) \end{bmatrix}. \tag{6.26}$$

In the next section we will see how, starting from these equations it is possible to obtain the I/O relations of one cavity and the full Sagnac interferometer, from which it is possible to calculate the quantum noise.

[3] A matrix $\mathbb{M}$ is unitary if $\mathbb{M}^\dagger \cdot \mathbb{M} = \mathbb{I}$

6.5 I/O relations with scattering beams

In equation 6.26 we are only interested in the output of the first four ports, since the other four represent the loss. So we can ignore the last four terms in the output column and the second row in the transfer matrix. On the other hand for the input beams we need to consider all the 8 ports, since we have to take into account the contributions of the vacuum fields. Then we have

$$\begin{bmatrix} \hat{\mathbf{P}}_1^{out}(\omega) \\ \hat{\mathbf{P}}_2^{out}(\omega) \\ \hat{\mathbf{P}}_3^{out}(\omega) \\ \hat{\mathbf{P}}_4^{out}(\omega) \end{bmatrix} = \left(e^{i\Phi}\sqrt{1-\mathscr{L}}\right)^2 \begin{bmatrix} -i\sqrt{\epsilon R} & \sqrt{R} & \sqrt{\epsilon T} & i\sqrt{T} \\ \sqrt{R} & -i\sqrt{\epsilon R} & i\sqrt{T} & \sqrt{\epsilon T} \\ \sqrt{\epsilon T} & i\sqrt{T} & -i\sqrt{\epsilon R} & \sqrt{R} \\ i\sqrt{T} & \sqrt{\epsilon T} & \sqrt{R} & -i\sqrt{\epsilon R} \end{bmatrix} \begin{bmatrix} \hat{\mathbf{P}}_1^{in}(\omega) \\ \hat{\mathbf{P}}_2^{in}(\omega) \\ \hat{\mathbf{P}}_3^{in}(\omega) \\ \hat{\mathbf{P}}_4^{in}(\omega) \end{bmatrix} \tag{6.27}$$
$$+e^{i\Phi}\sqrt{1-\mathscr{L}}\,\sqrt{\epsilon}(R+T) \begin{bmatrix} -i & -\sqrt{\epsilon} & 0 & 0 \\ -\sqrt{\epsilon} & -i & 0 & 0 \\ 0 & 0 & -i & -\sqrt{\epsilon} \\ 0 & 0 & -\sqrt{\epsilon} & -i \end{bmatrix} \begin{bmatrix} \hat{\mathbf{P}}_5^{in}(\omega) \\ \hat{\mathbf{P}}_6^{in}(\omega) \\ \hat{\mathbf{P}}_7^{in}(\omega) \\ \hat{\mathbf{P}}_8^{in}(\omega) \end{bmatrix}$$

In order to make the calculation more clear and consistent with the ones shown in chapter 4, we rename the fields as

$$\hat{\mathbf{P}}_1^{out}(\omega) \to \hat{\mathbf{B}}^{\bar{I}J}(\omega), \quad \hat{\mathbf{P}}_2^{out}(\omega) \to \hat{\mathbf{B}}^{IJ}(\omega), \quad \hat{\mathbf{P}}_3^{out}(\omega) \to \hat{\mathbf{F}}^{\bar{I}J}(\omega), \quad \hat{\mathbf{P}}_4^{out}(\omega) \to \hat{\mathbf{F}}^{IJ}(\omega),$$

$$\hat{\mathbf{P}}_1^{in}(\omega) \to \hat{\mathbf{A}}^{IJ}(\omega), \quad \hat{\boldsymbol{p}}_2^{in}(\Omega) \to \hat{\mathbf{A}}^{\bar{I}J}(\omega), \quad \hat{\mathbf{P}}_3^{in}(\omega) \to \hat{\mathbf{E}}^{IJ}(\omega), \quad \hat{\mathbf{P}}_4^{in}(\omega) \to \hat{\mathbf{E}}^{\bar{I}J}(\omega),$$

where the fields $\hat{\mathbf{B}}^{IJ}(\omega)$ and $\hat{\mathbf{A}}^{IJ}(\omega)$ are the cavity output and input fields respectively and $\hat{\mathbf{F}}^{IJ}(\omega)$ and $\hat{\mathbf{E}}^{IJ}(\omega)$ are the intra-cavity fields (see figure 4.5). Furthermore, we will rename the other four input fields, which are vacuum fields due to the loss, as

$$\hat{\mathbf{P}}_5^{in}(\omega) \to \hat{\boldsymbol{m}}^{\bar{I}J}(\Omega), \quad \hat{\mathbf{P}}_6^{in}(\omega) \to \hat{\boldsymbol{m}}^{IJ}(\Omega), \quad \hat{\mathbf{P}}_7^{in}(\omega) \to \hat{\boldsymbol{n}}^{\bar{I}J}(\Omega), \quad \hat{\mathbf{P}}_8^{in}(\omega) \to \hat{\boldsymbol{n}}^{IJ}(\Omega),$$

where we have considered that the classical amplitude of the vacuum fields is zero (therefore the lowercase).

6.5.1 Intra-cavity fields

In order to find the I/O relations of one cavity, we can solve the equations 6.27 and find the intra-cavity fields following the same method shown in section 4.2.5. We will do this calculation only for the quantum fluctuation part, since the classical part is easy to deduce

from it just replacing the quantum fields with the classical fields and setting the frequency equal to zero. The intra-cavity fields reflected from the ITM is then

$$\begin{aligned}\hat{\mathbf{f}}^{IJ}(\omega) = (1-\mathscr{L})\Big[&i\sqrt{T_{ITM}}\,\hat{\mathbf{a}}^{IJ}(\omega) + \sqrt{\epsilon T}\,\hat{\mathbf{a}}^{\bar{I}J}(\omega)\\ &+\sqrt{R_{ITM}}\,\hat{\mathbf{e}}^{IJ}(\omega) - i\sqrt{\epsilon R_{ITM}}\,\hat{\mathbf{e}}^{IJ}(\omega)\\ &+\left(\sqrt{R_{ITM}}\,2ik_p\mathrm{E}^{IJ} + \sqrt{\epsilon R_{ITM}}\,2k_p\mathrm{E}^{\bar{I}J}\right)x_J\Big]\\ &-\sqrt{1-\mathscr{L}}\,\sqrt{\epsilon}\,\left(R_{ITM}+T_{ITM}\right)\left(i\,\hat{\mathbf{n}}^{IJ}(\omega) + \sqrt{\epsilon}\,\hat{\mathbf{n}}^{\bar{I}J}(\omega)\right).\end{aligned} \tag{6.28}$$

Since we are considering massive ETM with reflectivity equal to 1, the intra-cavity field incident on the ITM is just the field reflected from the ITM with the phase shift due to the round trip and then

$$\begin{aligned}\hat{\mathbf{e}}^{IJ}(\omega) &= \hat{\mathbf{f}}^{IJ}(\omega)\,e^{2i\omega\tau}\\ &= (1-\mathscr{L})\,e^{2i\omega\tau}\Big[i\sqrt{T_{ITM}}\,\hat{\mathbf{a}}^{IJ}(\omega) + \sqrt{\epsilon T}\,\hat{\mathbf{a}}^{\bar{I}J}(\omega)\\ &\quad+\sqrt{R_{ITM}}\,\hat{\mathbf{e}}^{IJ}(\omega) - i\sqrt{\epsilon R_{ITM}}\,\hat{\mathbf{e}}^{IJ}(\omega)\\ &\quad+\left(\sqrt{R_{ITM}}\,2ik_p\mathrm{E}^{IJ} + \sqrt{\epsilon R_{ITM}}\,2k_p\mathrm{E}^{\bar{I}J}\right)x_J\Big]\\ &\quad-\sqrt{1-\mathscr{L}}\,\sqrt{\epsilon}\,\left(R_{ITM}+T_{ITM}\right)\left(i\,\hat{\mathbf{n}}^{IJ}(\omega) + \sqrt{\epsilon}\,\hat{\mathbf{n}}^{\bar{I}J}(\omega)\right).\end{aligned} \tag{6.29}$$

Moving all the terms in $\hat{\mathbf{e}}^{IJ}(\omega)$ on the left side of the equation, we have

$$\begin{aligned}\hat{\mathbf{e}}^{IJ}(\omega)\left(1-(1-\mathscr{L})\,e^{2i\omega\tau}\sqrt{R_{ITM}}\right) &= (1-\mathscr{L})\,e^{2i\omega\tau}\Big[i\sqrt{T_{ITM}}\,\hat{\mathbf{a}}^{IJ}(\omega) + \sqrt{\epsilon T}\,\hat{\mathbf{a}}^{\bar{I}J}(\omega)\\ &\quad-i\sqrt{\epsilon R_{ITM}}\,\hat{\mathbf{e}}^{\bar{I}J}(\omega) + \left(\sqrt{R_{ITM}}\,2ik_p\mathrm{E}^{IJ} + \sqrt{\epsilon R_{ITM}}\,2k_p\mathrm{E}^{\bar{I}J}\right)x_J\Big]\\ &\quad-\sqrt{1-\mathscr{L}}\,\sqrt{\epsilon}\,\left(R_{ITM}+T_{ITM}\right)\left(i\,\hat{\mathbf{n}}^{IJ}(\omega) + \sqrt{\epsilon}\,\hat{\mathbf{n}}^{\bar{I}J}(\omega)\right).\end{aligned} \tag{6.30}$$

Because of the symmetry of the system, the counter-propagating field can be written as

$$\begin{aligned}\hat{\mathbf{e}}^{\bar{I}J}(\omega) = \frac{(1-\mathscr{L})\ e^{2i\omega\tau}}{1-(1-\mathscr{L})\ e^{2i\omega\tau}\sqrt{R_{ITM}}}\Big[&i\sqrt{T_{ITM}}\,\hat{\mathbf{a}}^{\bar{I}J}(\omega)+\sqrt{\epsilon T}\,\hat{\mathbf{a}}^{IJ}(\omega)\\ &-i\sqrt{\epsilon R_{ITM}}\,\hat{\mathbf{e}}^{IJ}(\omega)+\left(\sqrt{R_{ITM}}\,2ik_p\mathrm{E}^{\bar{I}J}+\sqrt{\epsilon R_{ITM}}\,2k_p\mathrm{E}^{IJ}\right)x_J\Big]\\ &-\frac{\sqrt{1-\mathscr{L}}\,\sqrt{\epsilon}\,\left(R_{ITM}+T_{ITM}\right)}{1-(1-\mathscr{L})\ e^{2i\omega\tau}\sqrt{R_{ITM}}}\left(i\,\hat{\mathbf{n}}^{IJ}(\omega)+\sqrt{\epsilon}\,\hat{\mathbf{n}}^{\bar{I}J}(\omega)\right).\end{aligned} \tag{6.31}$$

Now, in order to have the intra-cavity field as a function of the input field, we have to substitute equation 6.31 in equation 6.30, which gives

$$\begin{aligned}\hat{\mathbf{e}}^{IJ}(\omega)\left(1-(1-\mathscr{L})\ e^{2i\omega\tau}\sqrt{R_{ITM}}\right) &= (1-\mathscr{L})\ e^{2i\omega\tau}\Big[i\sqrt{T_{ITM}}\,\hat{\mathbf{a}}^{IJ}(\omega)+\sqrt{\epsilon T}\,\hat{\mathbf{a}}^{\bar{I}J}(\omega)\\ &+\left(\sqrt{R_{ITM}}\,2ik_p\mathrm{E}^{IJ}+\sqrt{\epsilon R_{ITM}}\,2k_p\mathrm{E}^{\bar{I}J}\right)x_J\Big]\\ &-\sqrt{1-\mathscr{L}}\,\sqrt{\epsilon}\,\left(R_{ITM}+T_{ITM}\right)\left(i\,\hat{\mathbf{n}}^{IJ}(\omega)+\sqrt{\epsilon}\,\hat{\mathbf{n}}^{\bar{I}J}(\omega)\right)\\ &-i\sqrt{\epsilon R_{ITM}}\,\frac{(1-\mathscr{L})\ e^{2i\omega\tau}}{1-(1-\mathscr{L})\ e^{2i\omega\tau}\sqrt{R_{ITM}}}\Big[i\sqrt{T_{ITM}}\,\hat{\mathbf{a}}^{\bar{I}J}(\omega)+\sqrt{\epsilon T}\,\hat{\mathbf{a}}^{IJ}(\omega)\\ &-i\sqrt{\epsilon R_{ITM}}\,\hat{\mathbf{e}}^{IJ}(\omega)+\left(\sqrt{R_{ITM}}\,2ik_p\mathrm{E}^{\bar{I}J}+\sqrt{\epsilon R_{ITM}}\,2k_p\mathrm{E}^{IJ}\right)x_J\Big]\\ &+i\sqrt{\epsilon R_{ITM}}\,\frac{\sqrt{1-\mathscr{L}}\,\sqrt{\epsilon}\,\left(R_{ITM}+T_{ITM}\right)}{1-(1-\mathscr{L})\ e^{2i\omega\tau}\sqrt{R_{ITM}}}\left(i\,\hat{\mathbf{n}}^{IJ}(\omega)+\sqrt{\epsilon}\,\hat{\mathbf{n}}^{\bar{I}J}(\omega)\right).\end{aligned} \tag{6.32}$$

In this way we have an additional term in $\hat{\mathbf{e}}^{IJ}(\omega)$ on the right side of the equation, that can

be moved on the left and then we obtain

$$
\begin{aligned}
&\hat{\mathbf{e}}^{IJ}(\omega)\left(1-(1-\mathscr{L})\,e^{2i\omega\tau}\,\sqrt{R_{ITM}}+\epsilon R_{ITM}\,\frac{(1-\mathscr{L})^2\,e^{4i\omega\tau}}{1-(1-\mathscr{L})\,e^{2i\omega\tau}\,\sqrt{R_{ITM}}}\right)\\
&\quad=(1-\mathscr{L})\,e^{2i\omega\tau}\left[i\sqrt{T_{ITM}}\,\hat{\mathbf{a}}^{IJ}(\omega)+\sqrt{\epsilon T}\,\hat{\mathbf{a}}^{\bar{I}J}(\omega)\right.\\
&\quad\left.+\left(\sqrt{R_{ITM}}\,2ik_p\mathrm{E}^{IJ}+\sqrt{\epsilon R_{ITM}}\,2k_p\mathrm{E}^{\bar{I}J}\right)x_J\right]\\
&\quad-\sqrt{1-\mathscr{L}}\,\sqrt{\epsilon}\,\left(R_{ITM}+T_{ITM}\right)\left(i\,\hat{\mathbf{n}}^{IJ}(\omega)+\sqrt{\epsilon}\,\hat{\mathbf{n}}^{\bar{I}J}(\omega)\right)\\
&\quad-i\sqrt{\epsilon R_{ITM}}\,\frac{(1-\mathscr{L})\,e^{2i\omega\tau}}{1-(1-\mathscr{L})\,e^{2i\omega\tau}\,\sqrt{R_{ITM}}}\left[i\sqrt{T_{ITM}}\,\hat{\mathbf{a}}^{\bar{I}J}(\omega)+\sqrt{\epsilon T}\,\hat{\mathbf{a}}^{IJ}(\omega)\right.\\
&\quad\left.+\left(\sqrt{R_{ITM}}\,2ik_p\mathrm{E}^{\bar{I}J}+\sqrt{\epsilon R_{ITM}}\,2k_p\mathrm{E}^{IJ}\right)x_J\right]\\
&\quad+i\sqrt{\epsilon R_{ITM}}\,\frac{\sqrt{1-\mathscr{L}}\,\sqrt{\epsilon}\,\left(R_{ITM}+T_{ITM}\right)}{1-(1-\mathscr{L})\,e^{2i\omega\tau}\,\sqrt{R_{ITM}}}\left(i\,\hat{\mathbf{n}}^{IJ}(\omega)+\sqrt{\epsilon}\,\hat{\mathbf{n}}^{\bar{I}J}(\omega)\right).
\end{aligned}
\tag{6.33}
$$

We have obtained the equation for the intra-cavity field, which can be rewritten in a clearer

way gathering all the terms corresponding to each field

$$
\begin{aligned}
&\hat{\mathbf{e}}^{IJ}(\omega)\left(1-(1-\mathscr{L})\,e^{2i\omega\tau}\,\sqrt{R_{ITM}}+\frac{(1-\mathscr{L})^2\,e^{4i\omega\tau}\epsilon R_{ITM}}{1-(1-\mathscr{L})\,e^{2i\omega\tau}\,\sqrt{R_{ITM}}}\right)\\
&\quad=i\,(1-\mathscr{L})\,e^{2i\omega\tau}\,\sqrt{T_{ITM}}\left(1-\frac{(1-\mathscr{L})\,e^{2i\omega\tau}\,\epsilon\sqrt{R_{ITM}}}{1-(1-\mathscr{L})\,e^{2i\omega\tau}\,\sqrt{R_{ITM}}}\right)\hat{\mathbf{a}}^{IJ}(\omega)\\
&\quad+(1-\mathscr{L})\,e^{2i\omega\tau}\,\sqrt{\epsilon T_{ITM}}\left(1+\frac{(1-\mathscr{L})\,e^{2i\omega\tau}\,\sqrt{R_{ITM}}}{1-(1-\mathscr{L})\,e^{2i\omega\tau}\,\sqrt{R_{ITM}}}\right)\hat{\mathbf{a}}^{\bar{I}J}(\omega)\\
&\quad-\sqrt{1-\mathscr{L}}\sqrt{\epsilon}\,(R+T)\,e^{2i\omega\tau}\left(1-\frac{(1-\mathscr{L})\,e^{2i\omega\tau}\,\epsilon\sqrt{R_{ITM}}}{1-(1-\mathscr{L})\,e^{2i\omega\tau}\,\sqrt{R_{ITM}}}\right)\hat{\mathbf{n}}^{IJ}(\omega)\\
&\quad-\sqrt{1-\mathscr{L}}\sqrt{\epsilon}\,(R+T)\,e^{2i\omega\tau}\left(\sqrt{\epsilon}+\frac{(1-\mathscr{L})\,e^{2i\omega\tau}\,\epsilon\sqrt{R_{ITM}}}{1-(1-\mathscr{L})\,e^{2i\omega\tau}\,\sqrt{R_{ITM}}}\right)\hat{\mathbf{n}}^{\bar{I}J}(\omega)\\
&\quad+(1-\mathscr{L})\,e^{2i\omega\tau}\,2ik_p\sqrt{R_{ITM}}\left(1-\frac{(1-\mathscr{L})\,e^{2i\omega\tau}\,\epsilon\sqrt{R_{ITM}}}{1-(1-\mathscr{L})\,e^{2i\omega\tau}\,\sqrt{R_{ITM}}}\right)\mathrm{E}^{IJ}\,x_J\\
&\quad+(1-\mathscr{L})\,e^{2i\omega\tau}\,2ik_p\sqrt{\epsilon R_{ITM}}\left(1+\frac{(1-\mathscr{L})\,e^{2i\omega\tau}\,\epsilon\sqrt{R_{ITM}}}{1-(1-\mathscr{L})\,e^{2i\omega\tau}\,\sqrt{R_{ITM}}}\right)\mathrm{E}^{\bar{I}J}\,x_J
\end{aligned}
\tag{6.34}
$$

and multiplying all terms by $\left(1-(1-\mathscr{L})\,e^{2i\omega\tau}\,\sqrt{R_{ITM}}\right)$ we have

$$
\begin{aligned}
&\hat{\mathbf{e}}^{IJ}(\omega)\left(\left(1-(1-\mathscr{L})\,e^{2i\omega\tau}\,\sqrt{R_{ITM}}\right)^2+(1-\mathscr{L})^2\,e^{4i\omega\tau}\epsilon R_{ITM}\right)\\
&\quad=i\,(1-\mathscr{L})\,e^{2i\omega\tau}\,\sqrt{T_{ITM}}\left(1-(1-\mathscr{L})\,e^{2i\omega\tau}\,(\epsilon+1)\sqrt{R_{ITM}}\right)\hat{\mathbf{a}}^{IJ}(\omega)\\
&\quad+(1-\mathscr{L})\,e^{2i\omega\tau}\,\sqrt{\epsilon T_{ITM}}\,\hat{\mathbf{a}}^{\bar{I}J}(\omega)\\
&\quad-\sqrt{1-\mathscr{L}}\sqrt{\epsilon}\,(R+T)\,e^{2i\omega\tau}\left(1-(1-\mathscr{L})\,e^{2i\omega\tau}\,(\epsilon+1)\sqrt{R_{ITM}}\right)\hat{\mathbf{n}}^{IJ}(\omega)\\
&\quad-\sqrt{1-\mathscr{L}}\,\epsilon\,(R+T)\,e^{2i\omega\tau}\,\hat{\mathbf{n}}^{\bar{I}J}(\omega)\\
&\quad+2ik_p\,(1-\mathscr{L})\,e^{2i\omega\tau}\,\sqrt{R_{ITM}}\left(1-(1-\mathscr{L})\,e^{2i\omega\tau}\,(\epsilon+1)\sqrt{R_{ITM}}\right)\mathrm{E}^{IJ}\,x_J\\
&\quad+2k_p\,(1-\mathscr{L})\,e^{2i\omega\tau}\,\sqrt{\epsilon R_{ITM}}\,\mathrm{E}^{\bar{I}J}\,x_J.
\end{aligned}
\tag{6.35}
$$

Now, transforming in two-photon quadrature formalism and defining the following transfer matrices

$$\mathbb{L}_J(\Omega) = (1-\mathscr{L})\ e^{2i\omega\tau}\ \sqrt{T_{ITM}}\ \frac{1-(1-\mathscr{L})\ e^{2i\omega\tau}\ (\epsilon+1)\sqrt{R_{ITM}}}{D_J(\Omega)}\ \hat{\sigma} \tag{6.36}$$

$$\mathbb{L}_J^{(cp)}(\Omega) = (1-\mathscr{L})\ e^{2i\omega\tau}\ \sqrt{T_{ITM}}\ \frac{\sqrt{\epsilon}}{D_J(\Omega)}\ \mathbb{I} \tag{6.37}$$

$$\mathbb{L}_{Jvac}(\Omega) = -\sqrt{1-\mathscr{L}}\ e^{2i\omega\tau}\ \frac{\mathscr{L}}{D_J(\Omega)}\ \mathbb{I} \tag{6.38}$$

$$\mathbb{L}_{Jvac}^{(cp)}(\Omega) = -\sqrt{1-\mathscr{L}}\ e^{2i\omega\tau}\ \sqrt{\epsilon}\ \left(R_{ITM}+T_{ITM}\right)\ \frac{1-(1-\mathscr{L})\ e^{2i\omega\tau}\ (\epsilon+1)\sqrt{R_{ITM}}}{D_J(\Omega)}\ \hat{\sigma}, \tag{6.39}$$

with

$$D_J(\Omega) = \left(1-(1-\mathscr{L})\ e^{2i\omega\tau}\ \sqrt{R_{ITM}}\right)^2 + (1-\mathscr{L})^2\ e^{4i\omega\tau}\epsilon R_{ITM}, \tag{6.40}$$

and the following vectors

$$\mathbf{X}^{IJ}(\Omega) = 2k_p\sqrt{\frac{R_{ITM}}{T_{ITM}}}\ \mathbb{L}_J(\Omega)\boldsymbol{E}^{IJ}, \tag{6.41}$$

$$\mathbf{X}_{cp}^{IJ}(\Omega) = 2k_p\sqrt{\frac{R_{ITM}}{T_{ITM}}}\ \mathbb{L}_J^{(cp)}(\Omega)\boldsymbol{E}^{\bar{I}J}, \tag{6.42}$$

then the intra-cavity fields can simply be written as

$$\begin{aligned}\hat{\boldsymbol{e}}^{IJ}(\Omega) = {} & \mathbb{L}_J(\Omega)\,\hat{\boldsymbol{a}}^{IJ}(\Omega) + \mathbb{L}_J^{(cp)}(\Omega)\,\hat{\boldsymbol{a}}^{\bar{I}J}(\Omega) + \mathbb{L}_{Jvac}(\Omega)\,\hat{\boldsymbol{n}}^{IJ}(\Omega) + \mathbb{L}_{Jvac}^{(cp)}(\Omega)\,\hat{\boldsymbol{n}}^{\bar{I}J}(\Omega) \\ & + \left(\mathbf{X}^{IJ}(\Omega) + \mathbf{X}_{cp}^{IJ}(\Omega)\right) x_J(\Omega)\end{aligned} \tag{6.43}$$

As we can see, since we have an anti-diagonal transfer matrix relative to one input field ($\mathbb{L}_J(\Omega)$) and a diagonal transfer matrix relative to the other ($\mathbb{L}_J^{(cp)}(\Omega)$), the classical part of the intra-cavity fields will have a non-zero component in both quadratures and then equation 4.50 is not verified. We will see in the next chapter that from this fact it follows that optical springs will be created in the cavity.

6.5.2 Cavity output fields

Once we have the intra-cavity fields, the calculation of the cavity output fields is straightforward. From equation 6.27 in fact we have

$$\begin{aligned}\hat{\mathbf{b}}^{IJ}(\omega) &= (1-\mathscr{L})\sqrt{R_{ITM}}\,\hat{\mathbf{a}}^{IJ}(\omega) - i\,(1-\mathscr{L})\sqrt{\epsilon R_{ITM}}\,\hat{\mathbf{a}}^{\bar{I}J}(\omega)\\ &+ i\,(1-\mathscr{L})\sqrt{T_{ITM}}\,\hat{\mathbf{e}}^{IJ}(\omega) + (1-\mathscr{L})\sqrt{\epsilon T_{ITM}}\,\hat{\mathbf{e}}^{\bar{I}J}(\omega)\\ &- i\sqrt{1-\mathscr{L}}\,\frac{\mathscr{L}}{\sqrt{\epsilon}}\,\hat{\mathbf{m}}^{IJ}(\omega) - \sqrt{1-\mathscr{L}}\,\mathscr{L}\,\hat{\mathbf{m}}^{\bar{I}J}(\omega)\\ &- 2ik_p(1-\mathscr{L})\sqrt{R_{ITM}}\left(\mathrm{A}^{IJ} - i\sqrt{\epsilon}\,\mathrm{A}^{\bar{I}J}\right)x_J(\omega),\end{aligned} \tag{6.44}$$

which in two-photon quadrature can be written as

$$\begin{aligned}\hat{\boldsymbol{b}}^{IJ}(\Omega) &= (1-\mathscr{L})\sqrt{R_{ITM}}\,\hat{\boldsymbol{a}}^{IJ}(\Omega) - \hat{\sigma}\,(1-\mathscr{L})\sqrt{\epsilon R_{ITM}}\,\hat{\boldsymbol{a}}^{\bar{I}J}(\Omega)\\ &+ \hat{\sigma}\,(1-\mathscr{L})\sqrt{T_{ITM}}\,\hat{\boldsymbol{e}}^{IJ}(\Omega) + (1-\mathscr{L})\sqrt{\epsilon T_{ITM}}\,\hat{\boldsymbol{e}}^{\bar{I}J}(\Omega)\\ &- \hat{\sigma}\sqrt{1-\mathscr{L}}\,\frac{\mathscr{L}}{\sqrt{\epsilon}}\,\hat{\boldsymbol{m}}^{IJ}(\Omega) - \sqrt{1-\mathscr{L}}\,\mathscr{L}\,\hat{\boldsymbol{m}}^{\bar{I}J}(\Omega)\\ &- 2\hat{\sigma}k_p(1-\mathscr{L})\sqrt{R_{ITM}}\left(\boldsymbol{A}^{IJ} - \hat{\sigma}\sqrt{\epsilon}\,\boldsymbol{A}^{\bar{I}J}\right)x_J(\Omega).\end{aligned} \tag{6.45}$$

Now we can substitute in the previous equation the intra-cavity fields in equation 6.43 and we get

$$\begin{aligned}
\hat{\boldsymbol{b}}^{IJ}(\Omega) &= (1-\mathscr{L})\sqrt{R_{ITM}}\,\hat{\boldsymbol{a}}^{IJ}(\Omega) - \hat{\sigma}\,(1-\mathscr{L})\sqrt{\epsilon R_{ITM}}\,\hat{\boldsymbol{a}}^{\bar{I}J}(\Omega) \\
&+ \hat{\sigma}\,(1-\mathscr{L})\sqrt{T_{ITM}}\,\Big(\mathbb{L}_J(\Omega)\,\hat{\boldsymbol{a}}^{IJ}(\Omega) + \mathbb{L}_J^{(cp)}(\Omega)\,\hat{\boldsymbol{a}}^{\bar{I}J}(\Omega) \\
&+ \mathbb{L}_{Jvac}(\Omega)\,\hat{\boldsymbol{n}}^{IJ}(\Omega) + \mathbb{L}_{Jvac}^{(cp)}(\Omega)\,\hat{\boldsymbol{n}}^{\bar{I}J}(\Omega) \\
&+ 2k_p\sqrt{\frac{R_{ITM}}{T_{ITM}}}\mathbb{L}_J(\Omega)\boldsymbol{E}^{IJ}\,x_J(\Omega) + 2k_p\sqrt{\frac{R_{ITM}}{T_{ITM}}}\mathbb{L}_J^{(cp)}(\Omega)\boldsymbol{E}^{\bar{I}J}\,x_J(\Omega)\Big) \\
&+ (1-\mathscr{L})\sqrt{\epsilon T_{ITM}}\,\Big(\mathbb{L}_J(\Omega)\,\hat{\boldsymbol{a}}^{\bar{I}J}(\Omega) + \mathbb{L}_J^{(cp)}(\Omega)\,\hat{\boldsymbol{a}}^{IJ}(\Omega) \\
&+ \mathbb{L}_{Jvac}(\Omega)\,\hat{\boldsymbol{n}}^{\bar{I}J}(\Omega) + \mathbb{L}_{Jvac}^{(cp)}(\Omega)\,\hat{\boldsymbol{n}}^{IJ}(\Omega) \\
&+ 2k_p\sqrt{\frac{R_{ITM}}{T_{ITM}}}\mathbb{L}_J(\Omega)\boldsymbol{E}^{\bar{I}J}\,x_J(\Omega) + 2k_p\sqrt{\frac{R_{ITM}}{T_{ITM}}}\mathbb{L}_J^{(cp)}(\Omega)\boldsymbol{E}^{IJ}\,x_J(\Omega)\Big) \\
&- \hat{\sigma}\sqrt{1-\mathscr{L}}\,\frac{\mathscr{L}}{\sqrt{\epsilon}}\,\hat{\boldsymbol{m}}^{IJ}(\Omega) - \sqrt{1-\mathscr{L}}\,\mathscr{L}\,\hat{\boldsymbol{m}}^{\bar{I}J}(\Omega) \\
&- 2\hat{\sigma}k_p\,(1-\mathscr{L})\sqrt{R_{ITM}}\,\Big(\boldsymbol{A}^{IJ} - \hat{\sigma}\sqrt{\epsilon}\,\boldsymbol{A}^{\bar{I}J}\Big)\,x_J(\Omega).
\end{aligned} \tag{6.46}$$

Finally, defining the following transfer matrices which represents the shot noise contributions of the respective fields

$$\mathbb{T}_{s.n.}^{IJ}(\Omega) = (1-\mathscr{L})\left(\sqrt{R_{ITM}}\,\mathbb{I} + \sqrt{T_{ITM}}\,\hat{\sigma}\mathbb{L}_J(\Omega) + \sqrt{\epsilon T_{ITM}}\,\mathbb{L}_{Jvac}(\Omega)\right), \tag{6.47}$$

$$\mathbb{T}_{s.n.,cp}^{IJ}(\Omega) = (1-\mathscr{L})\left(-\hat{\sigma}\sqrt{\epsilon R_{ITM}} + \sqrt{T_{ITM}}\,\hat{\sigma}\mathbb{L}_{Jvac}(\Omega) + \sqrt{\epsilon T_{ITM}}\,\mathbb{L}_J(\Omega)\right), \tag{6.48}$$

$$\mathbb{M}^{IJ}(\Omega) = -\hat{\sigma}\sqrt{1-\mathscr{L}}\,\frac{\mathscr{L}}{\sqrt{\epsilon}}, \tag{6.49}$$

$$\mathbb{M}_{cp}^{IJ}(\Omega) = -\sqrt{1-\mathscr{L}}\,\mathscr{L}, \tag{6.50}$$

$$\mathbb{N}_{s.n.}^{IJ}(\Omega) = (1-\mathscr{L})\sqrt{T_{ITM}}\left(\hat{\sigma}\mathbb{L}_{Jvac}(\Omega) + \sqrt{\epsilon}\mathbb{L}_{Jvac}^{(cp)}(\Omega)\right), \tag{6.51}$$

$$\mathbb{N}_{s.n.,cp}^{IJ}(\Omega) = (1-\mathscr{L})\sqrt{T_{ITM}}\left(\hat{\sigma}\mathbb{L}_{Jvac}^{(cp)}(\Omega) + \sqrt{\epsilon}\mathbb{L}_{Jvac}(\Omega)\right), \tag{6.52}$$

and the response vector

$$\begin{aligned}\mathbf{R}^{IJ}_{arm}(\Omega) = 2k_p\,(1-\mathscr{L})\,\sqrt{R_{ITM}}\,\Big[&\Big(\hat{\sigma}\mathbb{L}_J(\Omega) + \sqrt{\epsilon}\mathbb{L}^{(cp)}_J(\Omega)\Big)\,\boldsymbol{E}^{IJ} \\ &+ \Big(\hat{\sigma}\mathbb{L}^{(cp)}_{Jvac}(\Omega) + \sqrt{\epsilon}\mathbb{L}_{Jvac}(\Omega)\Big)\,\boldsymbol{E}^{\bar{I}J} - \hat{\sigma}\boldsymbol{A}^{IJ} - \sqrt{\epsilon}\boldsymbol{A}^{\bar{I}J}\Big],\end{aligned} \tag{6.53}$$

then the output fields of the cavity $\boldsymbol{J}$ can be written as

$$\begin{aligned}\hat{\boldsymbol{b}}^{IJ}(\Omega) = {}& \mathbb{T}^{IJ}_{s.n.}(\Omega)\,\hat{\boldsymbol{a}}^{IJ}(\Omega) + \mathbb{T}^{IJ}_{s.n.,cp}(\Omega)\,\hat{\boldsymbol{a}}^{\bar{I}J}(\Omega) + \mathbb{M}^{IJ}(\Omega)\,\hat{\boldsymbol{n}}^{J}_1(\Omega) + \mathbb{M}^{IJ}_{cp}(\Omega)\,\hat{\boldsymbol{n}}^{J}_2(\Omega) \\ &+ \mathbb{N}^{IJ}_{s.n.}(\Omega)\,\hat{\boldsymbol{n}}^{J}_3(\Omega) + \mathbb{N}^{IJ}_{s.n.,cp}(\Omega)\,\hat{\boldsymbol{n}}^{J}_4(\Omega) + \mathbf{R}^{IJ}_{arm}(\Omega)\,x_J(\Omega).\end{aligned} \tag{6.54}$$

In order to include the radiation pressure contribution, we have now to substitute equation 4.6 in 6.54 and then we get and equation similar to equation 4.74:

$$\begin{aligned}\hat{\boldsymbol{b}}^{IJ}(\Omega) = {}& \mathbb{T}^{IJ}_{s.n}(\Omega)\,\hat{\boldsymbol{a}}^{IJ}(\Omega) + \mathbb{T}^{IJ}_{s.n.,cp}(\Omega)\,\hat{\boldsymbol{a}}^{\bar{I}J}(\Omega) + \mathbb{M}^{IJ}(\Omega)\,\hat{\boldsymbol{m}}^{IJ}(\Omega) + \mathbb{M}^{IJ}_{cp}(\Omega)\,\hat{\boldsymbol{m}}^{\bar{I}J}(\Omega) \\ &+ \mathbb{N}^{IJ}_{s.n.}(\Omega)\,\hat{\boldsymbol{n}}^{IJ}(\Omega) + \mathbb{N}^{IJ}_{s.n.,cp}(\Omega)\,\hat{\boldsymbol{n}}^{\bar{I}J}(\Omega) + \mathbf{R}^{IJ}_{arm}(\Omega)\,x^{GW}_J(\Omega) \\ &+ \mathbf{R}^{IJ}_{arm}(\Omega)\,\chi_J(\Omega)\frac{2\hbar\omega_p}{c}\left(\boldsymbol{A}^{IJ}\right)^{\dagger}\,\hat{\boldsymbol{a}}^{IJ}(\Omega) + \mathbf{R}^{IJ}_{arm}\,\chi_J\frac{\hbar\omega_p}{c}\left(\boldsymbol{A}^{\bar{I}J}\right)^{\dagger}\,\hat{\boldsymbol{a}}^{\bar{I}J}(\Omega) \\ &+ \mathbf{R}^{IJ}_{arm}(\Omega)\,\chi_J(\Omega)\frac{2\hbar\omega_p}{c}\left(\boldsymbol{E}^{IJ}\right)^{\dagger}\Big[\mathbb{L}_J(\Omega)\,\hat{\boldsymbol{a}}^{IJ}(\Omega) + \mathbb{L}^{(cp)}_J(\Omega)\,\hat{\boldsymbol{a}}^{\bar{I}J}(\Omega) \\ &+ \mathbb{L}_{Jvac}(\Omega)\,\hat{\boldsymbol{n}}^{IJ}(\Omega) + \mathbb{L}^{(cp)}_{Jvac}(\Omega)\,\hat{\boldsymbol{n}}^{\bar{I}J}(\Omega) + \Big(\mathbf{X}^{IJ}(\Omega) + \mathbf{X}^{IJ}_{cp}(\Omega)\Big)\,x_J(\Omega)\Big] \\ &+ \mathbf{R}^{IJ}_{arm}(\Omega)\,\chi_J(\Omega)\frac{2\hbar\omega_p}{c}\left(\boldsymbol{E}^{\bar{I}J}\right)^{\dagger}\Big[\mathbb{L}_J(\Omega)\,\hat{\boldsymbol{a}}^{\bar{I}J}(\Omega) + \mathbb{L}^{(cp)}_J(\Omega)\,\hat{\boldsymbol{a}}^{IJ}(\Omega) \\ &+ \mathbb{L}_{Jvac}(\Omega)\,\hat{\boldsymbol{n}}^{\bar{I}J}(\Omega) + \mathbb{L}^{(cp)}_{Jvac}(\Omega)\,\hat{\boldsymbol{n}}^{IJ}(\Omega) + \Big(\mathbf{X}^{\bar{I}J}(\Omega) + \mathbf{X}^{\bar{I}J}_{cp}(\Omega)\Big)\,x_J(\Omega)\Big].\end{aligned}$$

However in this case the additional terms in x_J are not zero, because of the presence of $\mathbf{X}^{IJ}_{cp}(\Omega)$ for which equation 4.50 is not true. Here in fact we find that the intra-cavity field has components in both quadratures and then the optical rigidity is not zero. So we have to use the modified mechanical susceptibility, as described in section 4.3, but since here we have two beams that gives two different contributions to the rigidity, equation 4.89 must be written as

$$\chi^{new}_J(\Omega) = \frac{\chi_J(\Omega)}{1 + \chi_J(\Omega)\left(K^{IJ}_{arm}(\Omega) + K^{\bar{I}J}_{arm}(\Omega)\right)}, \tag{6.55}$$

where

$$K_{arm}^{IJ}(\Omega) = -\frac{4\hbar\omega_p^2}{c^2}\left(\boldsymbol{E}^{IJ}\right)^{\dagger}\mathbb{L}_J^{(cp)}(\Omega)\boldsymbol{E}^{\bar{I}J}. \tag{6.56}$$

We can write then the transfer matrices of the radiation pressure contribution as

$$\mathbb{T}_{r.p.}^{IJ}(\Omega) = \mathbf{R}_{arm}^{IJ}\,\chi_J^{new}\frac{2\hbar\omega_p}{c}\left[\left(\boldsymbol{E}^{IJ}\right)^{\dagger}\mathbb{L}_J(\Omega) + \left(\boldsymbol{E}^{\bar{I}J}\right)^{\dagger}\mathbb{L}_J^{(cp)}(\Omega)\right] \tag{6.57}$$

$$\mathbb{T}_{r.p.,cp}^{IJ}(\Omega) = \mathbf{R}_{arm}^{IJ}\,\chi_J^{new}\frac{2\hbar\omega_p}{c}\left[\left(\boldsymbol{E}^{IJ}\right)^{\dagger}\mathbb{L}_J^{(cp)}(\Omega) + \left(\boldsymbol{E}^{\bar{I}J}\right)^{\dagger}\mathbb{L}_J(\Omega)\right] \tag{6.58}$$

$$\mathbb{N}_{r.p.}^{IJ}(\Omega) = \mathbf{R}_{arm}^{IJ}\,\chi_J^{new}\frac{2\hbar\omega_p}{c}\left[\left(\boldsymbol{E}^{IJ}\right)^{\dagger}\mathbb{L}_{Jvac}(\Omega) + \left(\boldsymbol{E}^{\bar{I}J}\right)^{\dagger}\mathbb{L}_{Jvac}^{(cp)}(\Omega)\right] \tag{6.59}$$

$$\mathbb{N}_{r.p.,cp}^{IJ}(\Omega) = \mathbf{R}_{arm}^{IJ}\,\chi_J^{new}\frac{2\hbar\omega_p}{c}\left[\left(\boldsymbol{E}^{IJ}\right)^{\dagger}\mathbb{L}_{Jvac}^{(cp)}(\Omega) + \left(\boldsymbol{E}^{\bar{I}J}\right)^{\dagger}\mathbb{L}_{Jvac}(\Omega)\right] \tag{6.60}$$

and the output mode becomes

$$\begin{aligned}
\hat{\boldsymbol{b}}^{IJ}(\Omega) = {} & \underbrace{\left(\mathbb{T}_{s.n.}^{IJ}(\Omega) + \mathbb{T}_{r.p.}^{IJ}(\Omega)\right)}_{\mathbb{T}_{arm}^{IJ}(\Omega)}\hat{\boldsymbol{a}}^{IJ}(\Omega) + \underbrace{\left(\mathbb{T}_{s.n.,cp}^{IJ}(\Omega) + \mathbb{T}_{r.p.,cp}^{IJ}(\Omega)\right)}_{\mathbb{T}_{arm,cp}^{IJ}(\Omega)}\hat{\boldsymbol{a}}^{\bar{I}J}(\Omega) \\
& + \underbrace{\left(\mathbb{N}_{s.n.}^{IJ}(\Omega) + \mathbb{N}_{r.p.}^{IJ}(\Omega)\right)}_{\mathbb{N}_{arm}^{IJ}(\Omega)}\hat{\boldsymbol{n}}^{IJ}(\Omega) + \underbrace{\left(\mathbb{N}_{s.n.,cp}^{IJ}(\Omega) + \mathbb{N}_{r.p.,cp}^{IJ}(\Omega)\right)}_{\mathbb{N}_{arm,cp}^{IJ}(\Omega)}\hat{\boldsymbol{n}}^{\bar{I}J}(\Omega) \\
& + \mathbb{M}^{IJ}(\Omega)\,\hat{\boldsymbol{m}}^{IJ}(\Omega) + \mathbb{M}_{cp}^{IJ}(\Omega)\,\hat{\boldsymbol{m}}^{\bar{I}J}(\Omega) + \mathbf{R}_{arm}^{IJ}\,x_J^{GW} \\
= {} & \mathbb{T}_{arm}^{IJ}(\Omega)\,\hat{\boldsymbol{a}}^{IJ}(\Omega) + \mathbb{T}_{arm,cp}^{IJ}(\Omega)\,\hat{\boldsymbol{a}}^{\bar{I}J}(\Omega) + \mathbb{N}_{arm}^{IJ}(\Omega)\,\hat{\boldsymbol{n}}^{IJ}(\Omega) + \mathbb{N}_{arm,cp}^{IJ}(\Omega)\,\hat{\boldsymbol{n}}^{\bar{I}J}(\Omega) \\
& + \mathbb{M}^{IJ}(\Omega)\,\hat{\boldsymbol{m}}^{IJ}(\Omega) + \mathbb{M}_{cp}^{IJ}(\Omega)\,\hat{\boldsymbol{m}}^{\bar{I}J}(\Omega) + \mathbf{R}_{arm}^{IJ}\,x_J^{GW}.
\end{aligned} \tag{6.61}$$

6.5.3 Full Sagnac solution and quantum noise calculation

Once we got the I/O relations for one cavity, the solution for the full Sagnac is straightforward. As done in section 4.2.5 in fact, we have now to consider that one of the output beams of one cavity is the input of the other and the vice versa. So using equation 4.75, we obtain the two output beams that arrive to the beamsplitter, which can be written as

$$\hat{\boldsymbol{b}}^{LN}(\Omega) = \mathbb{T}^{RN}_{LN}(\Omega)\,\hat{\boldsymbol{a}}^{RN}(\Omega) + \mathbb{T}^{LE}_{LN}(\Omega)\,\hat{\boldsymbol{a}}^{LE}(\Omega) + \mathbf{R}^{N}_{LN}(\Omega)\,x_N(\Omega) + \mathbf{R}^{E}_{LN}(\Omega)\,x_E(\Omega)$$
$$+ \mathbb{N}^{RE}_{LN}(\Omega)\,\hat{\boldsymbol{n}}^{RE}(\Omega) + \mathbb{N}^{LE}_{LN}(\Omega)\,\hat{\boldsymbol{n}}^{LE}(\Omega) + \mathbb{N}^{RN}_{LN}(\Omega)\,\hat{\boldsymbol{n}}^{RN}(\Omega) + \mathbb{N}^{LN}_{LN}(\Omega)\,\hat{\boldsymbol{n}}^{LN}(\Omega)$$
$$+ \mathbb{M}^{RE}_{LN}(\Omega)\,\hat{\boldsymbol{m}}^{RE}(\Omega) + \mathbb{M}^{LE}_{LN}(\Omega)\,\hat{\boldsymbol{m}}^{LE}(\Omega) + \mathbb{M}^{RN}_{LN}(\Omega)\,\hat{\boldsymbol{m}}^{RN}(\Omega) + \mathbb{M}^{LN}_{LN}(\Omega)\,\hat{\boldsymbol{m}}^{LN}(\Omega) \tag{6.62}$$

and

$$\hat{\boldsymbol{b}}^{RE}(\Omega) = \mathbb{T}^{RN}_{RE}(\Omega)\,\hat{\boldsymbol{a}}^{RN}(\Omega) + \mathbb{T}^{LE}_{RE}(\Omega)\,\hat{\boldsymbol{a}}^{LE}(\Omega) + \mathbf{R}^{N}_{RE}(\Omega)\,x_N(\Omega) + \mathbf{R}^{E}_{RE}(\Omega)\,x_E(\Omega)$$
$$+ \mathbb{N}^{RE}_{RE}(\Omega)\,\hat{\boldsymbol{n}}^{RE}(\Omega) + \mathbb{N}^{LE}_{RE}(\Omega)\,\hat{\boldsymbol{n}}^{LE}(\Omega) + \mathbb{N}^{RN}_{RE}(\Omega)\,\hat{\boldsymbol{n}}^{RN}(\Omega) + \mathbb{N}^{LN}_{RE}(\Omega)\,\hat{\boldsymbol{n}}^{LN}(\Omega)$$
$$+ \mathbb{M}^{RE}_{RE}(\Omega)\,\hat{\boldsymbol{m}}^{RE}(\Omega) + \mathbb{M}^{LE}_{RE}(\Omega)\,\hat{\boldsymbol{m}}^{LE}(\Omega) + \mathbb{M}^{RN}_{RE}(\Omega)\,\hat{\boldsymbol{m}}^{RN}(\Omega) + \mathbb{M}^{LN}_{RE}(\Omega)\,\hat{\boldsymbol{m}}^{LN}(\Omega); \tag{6.63}$$

where we have for the North cavity

$$\mathbb{T}^{RN}_{LN}(\Omega) = \mathbb{T}^{LN}_{arm}(\Omega)\,\mathbb{Q}_L(\Omega)\,\mathbb{T}^{LE}_{arm,cp}(\Omega)\,\mathbb{T}^{RN}_{arm}(\Omega) + \mathbb{T}^{LN}_{arm,cp}(\Omega), \tag{6.64}$$

$$\mathbb{T}^{LE}_{LN}(\Omega) = \mathbb{T}^{LN}_{arm}(\Omega)\,\mathbb{Q}_L(\Omega)\,\mathbb{T}^{LE}_{arm}(\Omega), \tag{6.65}$$

$$\mathbb{N}^{RE}_{LN}(\Omega) = \mathbb{T}^{LN}_{arm}(\Omega)\,\mathbb{Q}_L(\Omega)\,\mathbb{N}^{LE}_{arm,cp}(\Omega), \tag{6.66}$$

$$\mathbb{N}^{LE}_{LN}(\Omega) = \mathbb{T}^{LN}_{arm}(\Omega)\,\mathbb{Q}_L(\Omega)\,\mathbb{N}^{LE}_{arm}(\Omega), \tag{6.67}$$

$$\mathbb{N}^{RN}_{LN}(\Omega) = \mathbb{T}^{LN}_{arm}(\Omega)\,\mathbb{Q}_L(\Omega)\,\mathbb{T}^{LE}_{arm,cp}(\Omega)\,\mathbb{N}^{RN}_{arm}(\Omega) + \mathbb{N}^{LN}_{arm,cp}(\Omega), \tag{6.68}$$

$$\mathbb{N}^{LN}_{LN}(\Omega) = \mathbb{T}^{LN}_{arm}(\Omega)\,\mathbb{Q}_L(\Omega)\,\mathbb{T}^{LE}_{arm,cp}(\Omega)\,\mathbb{N}^{RN}_{arm,cp}(\Omega) + \mathbb{N}^{LN}_{arm}(\Omega), \tag{6.69}$$

$$\mathbb{M}^{RE}_{LN}(\Omega) = \mathbb{T}^{LN}_{arm}(\Omega)\,\mathbb{Q}_L(\Omega)\,\mathbb{M}^{LE}_{arm,cp}(\Omega), \tag{6.70}$$

$$\mathbb{M}^{LE}_{LN}(\Omega) = \mathbb{T}^{LN}_{arm}(\Omega)\,\mathbb{Q}_L(\Omega)\,\mathbb{M}^{LE}_{arm}(\Omega), \tag{6.71}$$

$$\mathbb{M}^{RN}_{LN}(\Omega) = \mathbb{T}^{LN}_{arm}(\Omega)\,\mathbb{Q}_L(\Omega)\,\mathbb{T}^{LE}_{arm,cp}(\Omega)\,\mathbb{M}^{RN}_{arm}(\Omega) + \mathbb{M}^{LN}_{arm,cp}(\Omega), \tag{6.72}$$

$$\mathbb{M}^{LN}_{LN}(\Omega) = \mathbb{T}^{LN}_{arm}(\Omega)\,\mathbb{Q}_L(\Omega)\,\mathbb{T}^{LE}_{arm,cp}(\Omega)\,\mathbb{M}^{RN}_{arm,cp}(\Omega) + \mathbb{M}^{LN}_{arm}(\Omega), \tag{6.73}$$

$$\mathbf{R}^{N}_{LN}(\Omega) = \mathbb{T}^{LN}_{arm}(\Omega)\,\mathbb{Q}_L(\Omega)\,\mathbb{T}^{LE}_{arm,cp}(\Omega)\,\mathbf{R}^{RN}_{arm}(\Omega) + \mathbf{R}^{LN}_{arm}(\Omega), \tag{6.74}$$

$$\mathbf{R}^{E}_{LN}(\Omega) = \mathbb{T}^{LN}_{arm}(\Omega)\,\mathbb{Q}_{L}(\Omega)\,\mathbf{R}^{LE}_{arm}(\Omega), \tag{6.75}$$

and for the East cavity

$$\mathbb{T}^{RN}_{RE}(\Omega) = \mathbb{T}^{RE}_{arm}(\Omega)\,\mathbb{Q}_{R}(\Omega)\,\mathbb{T}^{RN}_{arm}(\Omega), \tag{6.76}$$

$$\mathbb{T}^{LE}_{RE}(\Omega) = \mathbb{T}^{RE}_{arm}(\Omega)\,\mathbb{Q}_{R}(\Omega)\,\mathbb{T}^{RN}_{arm,cp}(\Omega)\,\mathbb{T}^{LE}_{arm}(\Omega) + \mathbb{T}^{RE}_{arm,cp}(\Omega), \tag{6.77}$$

$$\mathbb{N}^{RE}_{RE}(\Omega) = \mathbb{T}^{RE}_{arm}(\Omega)\,\mathbb{Q}_{R}(\Omega)\,\mathbb{T}^{RN}_{arm,cp}(\Omega)\,\mathbb{N}^{LE}_{arm,cp}(\Omega) + \mathbb{N}^{RE}_{arm}(\Omega), \tag{6.78}$$

$$\mathbb{N}^{LE}_{RE}(\Omega) = \mathbb{T}^{RE}_{arm}(\Omega)\,\mathbb{Q}_{R}(\Omega)\,\mathbb{T}^{RN}_{arm,cp}(\Omega)\,\mathbb{N}^{LE}_{arm}(\Omega) + \mathbb{N}^{RE}_{arm,cp}(\Omega), \tag{6.79}$$

$$\mathbb{N}^{RN}_{RE}(\Omega) = \mathbb{T}^{RE}_{arm}(\Omega)\,\mathbb{Q}_{R}(\Omega)\,\mathbb{N}^{RN}_{arm}(\Omega), \tag{6.80}$$

$$\mathbb{N}^{LN}_{RE}(\Omega) = \mathbb{T}^{RE}_{arm}(\Omega)\,\mathbb{Q}_{R}(\Omega)\,\mathbb{N}^{RN}_{arm,cp}(\Omega), \tag{6.81}$$

$$\mathbb{M}^{RE}_{RE}(\Omega) = \mathbb{T}^{RE}_{arm}(\Omega)\,\mathbb{Q}_{R}(\Omega)\,\mathbb{T}^{RN}_{arm,cp}(\Omega)\,\mathbb{M}^{LE}_{arm,cp}(\Omega) + \mathbb{M}^{RE}_{arm}(\Omega), \tag{6.82}$$

$$\mathbb{M}^{LE}_{RE}(\Omega) = \mathbb{T}^{RE}_{arm}(\Omega)\,\mathbb{Q}_{R}(\Omega)\,\mathbb{T}^{RN}_{arm,cp}(\Omega)\,\mathbb{M}^{LE}_{arm}(\Omega) + \mathbb{M}^{RE}_{arm,cp}(\Omega), \tag{6.83}$$

$$\mathbb{M}^{RN}_{RE}(\Omega) = \mathbb{T}^{RE}_{arm}(\Omega)\,\mathbb{Q}_{R}(\Omega)\,\mathbb{M}^{RN}_{arm}(\Omega), \tag{6.84}$$

$$\mathbb{M}^{LN}_{RE}(\Omega) = \mathbb{T}^{RE}_{arm}(\Omega)\,\mathbb{Q}_{R}(\Omega)\,\mathbb{M}^{RN}_{arm,cp}(\Omega), \tag{6.85}$$

$$\mathbf{R}^{N}_{RE}(\Omega) = \mathbb{T}^{LN}_{arm}(\Omega)\,\mathbb{Q}_{L}(\Omega)\mathbf{R}^{RN}_{arm}(\Omega), \tag{6.86}$$

$$\mathbf{R}^{E}_{RE}(\Omega) = \mathbb{T}^{LN}_{arm}(\Omega)\,\mathbb{Q}_{L}(\Omega)\,\mathbb{T}^{RN}_{arm,cp}(\Omega)\,\mathbf{R}^{LE}_{arm}(\Omega) + \mathbf{R}^{RE}_{arm}(\Omega), \tag{6.87}$$

with

$$\mathbb{Q}_{L} = \left(\mathbb{I} - \mathbb{T}^{RE}_{arm,cp}\,\mathbb{T}^{LN}_{arm,cp}\right)^{-1}, \tag{6.88}$$

$$\mathbb{Q}_{R} = \left(\mathbb{I} - \mathbb{T}^{LN}_{arm,cp}\,\mathbb{T}^{RE}_{arm,cp}\right)^{-1}. \tag{6.89}$$

In this way the I/O relations for the full Sagnac correspond to equations 4.82 and 4.83 plus the additional terms relative to the vacuum fields, i.e.

$$\hat{\boldsymbol{o}}(\Omega) = \mathbb{T}^{p}_{o}(\Omega)\,\hat{\boldsymbol{p}}(\Omega) + \mathbb{T}^{i}_{o}(\Omega)\,\hat{\boldsymbol{i}}(\Omega) + \mathbb{N}^{RE}_{o}(\Omega)\,\hat{\boldsymbol{n}}^{RE}(\Omega) + \mathbb{N}^{LE}_{o}(\Omega)\,\hat{\boldsymbol{n}}^{LE}(\Omega)$$

$$+ \mathbb{N}_o^{RN}(\Omega)\,\hat{\boldsymbol{n}}^{RN}(\Omega) + \mathbb{N}_o^{LN}(\Omega)\,\hat{\boldsymbol{n}}^{LN}(\Omega) + \mathbb{M}_o^{RE}(\Omega)\,\hat{\boldsymbol{m}}^{RE}(\Omega) + \mathbb{M}_o^{LE}(\Omega)\,\hat{\boldsymbol{m}}^{LE}(\Omega)$$

$$+ \mathbb{M}_o^{RN}(\Omega)\,\hat{\boldsymbol{m}}^{RN}(\Omega) + \mathbb{M}_o^{LN}(\Omega)\,\hat{\boldsymbol{m}}^{LN}(\Omega) + \mathbf{R}_o^{N}(\Omega)\,x_N(\Omega) + \mathbf{R}_o^{E}(\Omega)\,x_E(\Omega) \tag{6.90}$$

$$\hat{\boldsymbol{q}}(\Omega) = \mathbb{T}_q^{p}(\Omega)\,\hat{\boldsymbol{p}}(\Omega) + \mathbb{T}_q^{i}(\Omega)\,\hat{\boldsymbol{i}}(\Omega) + \mathbb{N}_q^{RE}(\Omega)\,\hat{\boldsymbol{n}}^{RE}(\Omega) + \mathbb{N}_q^{LE}(\Omega)\,\hat{\boldsymbol{n}}^{LE}(\Omega)$$

$$+ \mathbb{N}_q^{RN}(\Omega)\,\hat{\boldsymbol{n}}^{RN}(\Omega) + \mathbb{N}_q^{LN}(\Omega)\,\hat{\boldsymbol{n}}^{LN}(\Omega) + \mathbb{M}_q^{RE}(\Omega)\,\hat{\boldsymbol{m}}^{RE}(\Omega) + \mathbb{M}_q^{LE}(\Omega)\,\hat{\boldsymbol{m}}^{LE}(\Omega)$$

$$+ \mathbb{M}_q^{RN}(\Omega)\,\hat{\boldsymbol{m}}^{RN}(\Omega) + \mathbb{M}_q^{LN}(\Omega)\,\hat{\boldsymbol{m}}^{LN}(\Omega) + \mathbf{R}_q^{N}(\Omega)\,x_N(\Omega) + \mathbf{R}_q^{E}(\Omega)\,x_E(\Omega), \tag{6.91}$$

where for the output $\hat{\boldsymbol{o}}(\Omega)$

$$\mathbb{T}_o^{i}(\Omega) = R_{BS}\,\mathbb{T}_{RE}^{LE}(\Omega) + T_{BS}\,\mathbb{T}_{LN}^{RN}(\Omega) - \sqrt{R_{BS}T_{BS}}\left(\mathbb{T}_{LN}^{LE}(\Omega) + \mathbb{T}_{RE}^{RN}(\Omega)\right), \tag{6.92}$$

$$\mathbb{T}_o^{p}(\Omega) = -R_{BS}\,\mathbb{T}_{RE}^{RN}(\Omega) + T_{BS}\,\mathbb{T}_{LN}^{LE}(\Omega) + \sqrt{R_{BS}T_{BS}}\left(\mathbb{T}_{LN}^{RN}(\Omega) + \mathbb{T}_{RE}^{LE}(\Omega)\right), \tag{6.93}$$

$$\mathbb{N}_o^{IJ}(\Omega) = -\sqrt{R_{BS}}\,\mathbb{N}_{RE}^{IJ}(\Omega) + \sqrt{T_{BS}}\,\mathbb{N}_{LN}^{IJ}(\Omega), \tag{6.94}$$

$$\mathbb{M}_o^{IJ}(\Omega) = -\sqrt{R_{BS}}\,\mathbb{M}_{RE}^{IJ}(\Omega) + \sqrt{T_{BS}}\,\mathbb{M}_{LN}^{IJ}(\Omega), \tag{6.95}$$

$$\mathbf{R}_o^{N}(\Omega) = -\sqrt{R_{BS}}\,\mathbf{R}_{RE}^{N}(\Omega) + \sqrt{T_{BS}}\,\mathbf{R}_{LN}^{N}(\Omega), \tag{6.96}$$

$$\mathbf{R}_o^{E}(\Omega) = -\sqrt{R_{BS}}\,\mathbf{R}_{RE}^{E}(\Omega) + \sqrt{T_{BS}}\,\mathbf{R}_{LN}^{E}(\Omega), \tag{6.97}$$

and, similarly, for the output $\hat{\boldsymbol{q}}(\Omega)$

$$\mathbb{T}_q^{i}(\Omega) = -R_{BS}\,\mathbb{T}_{LN}^{LE}(\Omega) + T_{BS}\,\mathbb{T}_{RE}^{RN}(\Omega) + \sqrt{R_{BS}T_{BS}}\left(\mathbb{T}_{LN}^{RN}(\Omega) - \mathbb{T}_{RE}^{LE}(\Omega)\right), \tag{6.98}$$

$$\mathbb{T}_q^{p}(\Omega) = R_{BS}\,\mathbb{T}_{LN}^{RN}(\Omega) + T_{BS}\,\mathbb{T}_{RE}^{LE}(\Omega) + \sqrt{R_{BS}T_{BS}}\left(\mathbb{T}_{LN}^{LE}(\Omega) + \mathbb{T}_{RE}^{RN}(\Omega)\right), \tag{6.99}$$

$$\mathbb{N}_q^{IJ}(\Omega) = \sqrt{R_{BS}}\,\mathbb{N}_{LN}^{IJ}(\Omega) + \sqrt{T_{BS}}\,\mathbb{N}_{RE}^{IJ}(\Omega), \tag{6.100}$$

$$\mathbb{M}_q^{IJ}(\Omega) = \sqrt{R_{BS}}\,\mathbb{M}_{LN}^{IJ}(\Omega) + \sqrt{T_{BS}}\,\mathbb{M}_{RE}^{IJ}(\Omega), \tag{6.101}$$

$$\mathbf{R}_q^{N}(\Omega) = \sqrt{R_{BS}}\,\mathbf{R}_{LN}^{N}(\Omega) + \sqrt{T_{BS}}\,\mathbf{R}_{RE}^{N}(\Omega), \tag{6.102}$$

$$\mathbf{R}_q^{E}(\Omega) = \sqrt{R_{BS}}\,\mathbf{R}_{LN}^{E}(\Omega) + \sqrt{T_{BS}}\,\mathbf{R}_{RE}^{E}(\Omega). \tag{6.103}$$

Finally for the quantum noise calculation, since in this case we have loss, the output equation have the form of equation 5.1, then the quantum noise limited sensitivity must be calculated with equation 5.2. The numerical results of this calculation will be shown in the

next chapter.

6.6 Conclusions

In this chapter we have described the backscattering effect and we have shown the calculation of the I/O relations and the quantum noise for a SSM with triangular cavity. With the help of simulations we have been able to derive the optical transfer matrix of a mirror with 4 input beams and 24 output beams, distributed in 8 ports, which represents the ITM of the two cavities. With these results the I/O relations of one cavity first and then the full Sagnac were calculated with a method similar to that one presented in section 4.2.5 for a lossless Sagnac. The calculation has been carried out by hand by the author. Since this fact could entail some errors, in order to verify the correctness of the results, multiple checks have been made by the author (for the whole calculation) and also, independently, by other people (for some part of the calculation).

The calculation described in this chapter refers to the coupling between backscattered and counter-propagating beams in a triangular cavity. However the method is absolutely general and can be applied to any kind of coupling in any kind of cavity. For example, it can also be applied to the class of polarisation speed meter (some examples of polarisation speed meter can be found in [95, 96]). The layout of a polarisation speed meter is shown in figure 6.7. In this case the two beams will pass through a polarising beamsplitter (PBS), which gives to each of them a different polarisation. Then each beam will travel into one cavity with a polarisation, will be reflected by the PBS and it will travel into the other cavity with a different polarisation. Quarter-wave plates between the ITM and the PBS are added in order to transform the polarisation from linear to circular at each passage. In this way we have two beams traveling in the two cavities in sequence, each of them with a different polarisation. The working principle is then compatible to a speed meter interferometer [97]. However, since in this topology the cavity are linear instead of triangular, the backscattering effect is not a mechanism that creates the coupling, but a birefringence effect can be present and give a similar results. The calculation shown in this chapter can be applied also in this case.

Some numerical examples and the interpretation of the results are discussed in the next chapter.

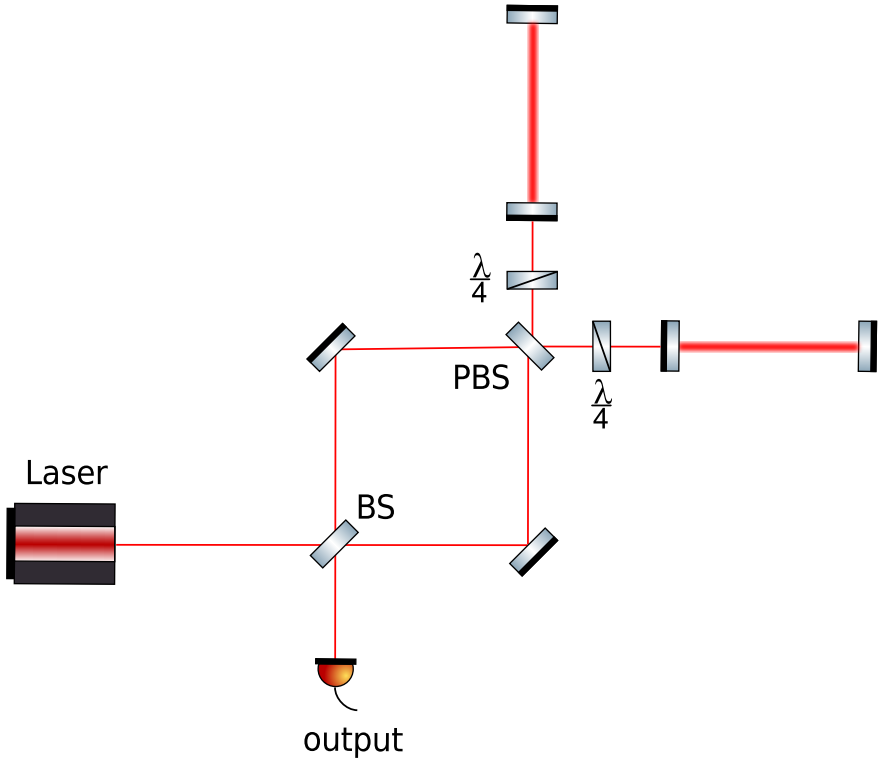

Figure 6.7: Layout of a polarisation speed meter.

Chapter 7

Influence of backscattering on the sensitivity of speed meters

In this chapter we will show the results of the calculation of the quantum noise limited sensitivity including the backscattering effect described in the previous chapter. We will analyse several interferometers configurations spanning length scale from 1 m (SSM) to 40 km (Cosmic Explorer). First of all we show the results for the Glasgow SSM, where, because of the high finesse and the low mass of the ITM, we expect that this effect will be much more relevant. Then we will analyse the results, giving the explanations of the peculiar features that we obtain in the sensitivity plots. We will explain why some particular values of the backscattering coefficient set the limit between what we will call weak and strong coupling. We will then describe how to interpret the results, with a special focus on the presence of the optical spring effect created by the backscattering, which changes the dynamics of the mirrors. Finally, in the last section, we will show the results for three large scale interferometer configurations: Voyager, Cosmic Explorer and the ET-LF, described in chapter 1. We will show that, as expected, in this cases the presence of backscattering affects much less the sensitivity respect to what happens for the Glasgow SSM.

The results presented in this chapter can be found in reference [98].

7.1 Results for the Glasgow SSM experiment

We will see now what are the results of the calculation of the backscattering effect, made in the previous chapter, considering the parameters of the Glasgow SSM interferometer. The summary of the parameters used are listed in table 7.1. Some of them are slightly different from that ones defined in the design paper [79], since here we are using the final values, optimised through the years of the experiment preparation. Furthermore, all calculations

parameter	**value**
laser input power	1.7 W
roundtrip length	2.86 m
laser wavelength	1064 nm
photodetector efficiency	1
homodyne angle	$\pi/2$
power reflectivity of the beamsplitter	0.5
power transmissivity of the beamsplitter	0.5
North cavity ITM power transmissivity	632 ppm
North cavity ITM mass	1 g
North cavity ETM mass	100 g
East cavity ITM power transmissivity	632 ppm
East cavity ITM mass	1 g
East cavity ETM mass	100 g

Table 7.1: List of the SSM parameters used for the results shown in this chapter.

are made considering a perfect 50:50 beamsplitter with no loss and a perfect photodetector with 100% efficiency, because we want to exclude any other source of noise in the analysis.

Figure 7.1 shows the plots of the spectral density of the quantum noise limited sensitivity (left), the quantum noise amplitude spectral density (top right) and the response function of the interferometer to the differential mirrors motion (bottom left) for 5 values of the backscattered coefficient ϵ, compared to the results for an interferometer with perfect mirrors ($\epsilon = 0$). In these plots we can notice three peculiar features:

- for $\epsilon \geq 0.1$ ppm the response function and then the sensitivity curve do not have a regular behaviour anymore, but they are completely off respect to the other curves;
- a peak appears at different frequencies for each backscattering coefficient;
- at low frequencies the sensitivity seems to increase with the increase of backscattering coefficient ϵ and it goes below the SQL.

We will explain now the physical meaning of each of these features.

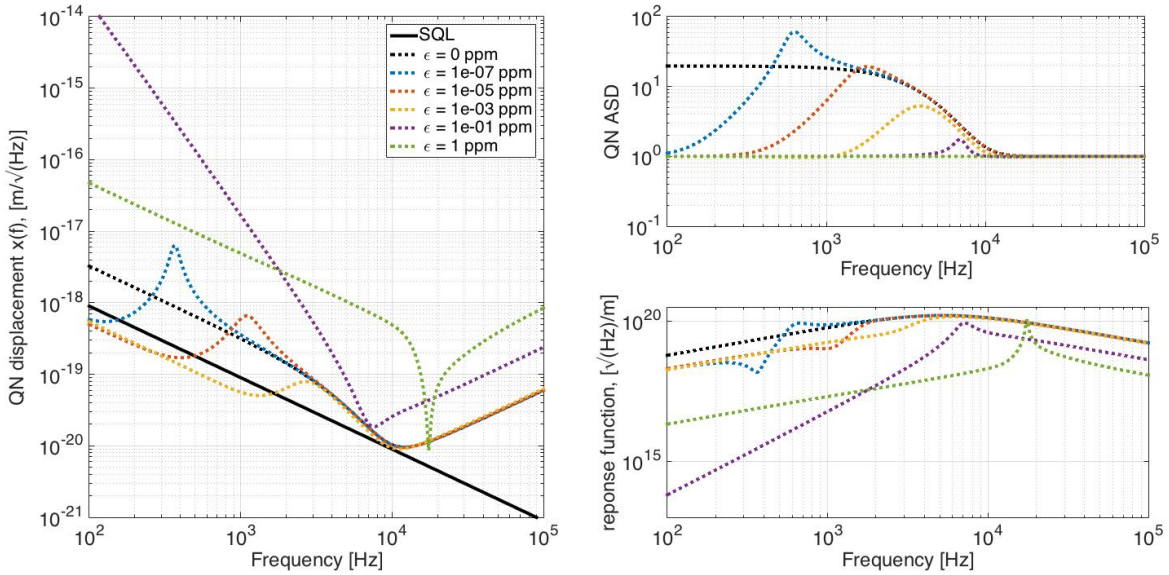

Figure 7.1: Plots of the results of the quantum noise calculation for the Glasgow SSM with different values of the backscattering coefficient ϵ. *On the left*: PSD of the quantum noise limited sensitivity. *On the top right*: Amplitude spectral density of the quantum noise. *On the bottom right*: Response function of the interferometer to the differential displacement of the mirrors of the two cavities. The peculiar features (the presence of peaks and the sensitivity increasing with backscattering) and the meaning of the critical value$\epsilon \geq 0.1$ ppm will be explained later in this chapter.

7.1.1 Critical values

It seems that some value around $\epsilon \sim 0.1$ ppm must have a special physical meaning since for values $\epsilon > 0.1$ ppm the sensitivity stops to have a regular behaviour with the increasing of the backscattering coefficient and a complete different regime scheme to dominate. In order to understand what happens a simple analysis of the DC power of each beam involved in the calculation can help.

We consider first only one cavity with the two input beams of equal power. A schematic drawing of the power of the beams involved is shown in figure 7.2, where we have only considered one beam outside the cavity (the red arrows) and one inside the cavity (the light blue arrows) with the respective scattered beams, because the other two beams will give the same results. So we calculated the power of each beam for three values of backscattering coefficient: 10 ppm, 0.1 ppm and 0.001 ppm. As we can see, for $\epsilon = 0.1$ ppm the power of the scattered beam in reflection inside the cavity and the power of the transmitted input beam are of the same order. Furthermore, if we recall the mirror transfer matrix described in equation 6.22, we can notice that these two beams also have opposite phases. This means that we will have destructive interference in the cavity and so it is like no input power is present.

When we consider both cavities and the fact that one of the input beam is the output of the

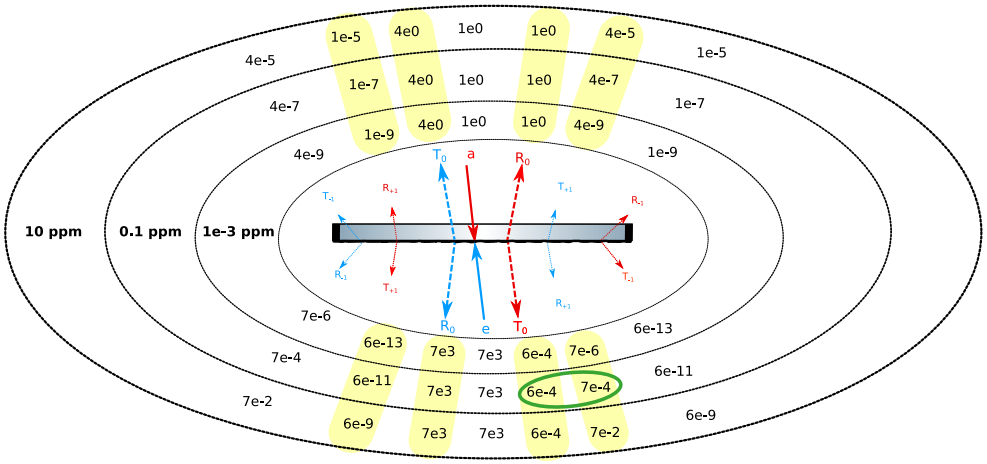

Figure 7.2: Schematic drawing of the power involved in the backscattering calculation. Here we have considered only one cavity and one input beam (red) and one intra-cavity beam (blue). We have highlighted in yellow the beams that we want to compare.

other cavity and it is already affected by the backscattering effect the situation is different. In this case in fact the destructive interference creates a strong asymmetry between the two intra-cavity beams, since one of the input beam is approximately equal to zero. This situation is shown in figure 7.3, where we can see that since the input beam that comes from the other cavity is zero due to the backscattering effect, the input beam for this direction of propagation will be the backscattered beam of the counter-propagating mode, which have the same amplitude as the original input beam but opposite phase. In other words in this case we have a cavity with only one circulating beam and with the backscattered beam that replaces the input beam.

However this particular situation happens only for a specific value of the backscattering coefficient ϵ_c, that can be approximated to

$$T_{ITM}\, P_{in} = \epsilon_c R_{ITM}\, P_{circ} \approx \epsilon_c \frac{4P_{IN}}{T_{ITM}} \Rightarrow \epsilon_c \approx \frac{T_{ITM}^2}{4}, \tag{7.1}$$

which for our value $T_{ITM} = 632\,\text{ppm}$ gives $\epsilon_c = 0.0999\,\text{ppm}$.

7.1.2 Optical springs

The other feature in the sensitivity plot that we need to explain is the presence of the peaks. This can be done considering the fact that the backscattering effect creates a detuning in the cavity. The optical rigidity in fact is not zero anymore since the intra-cavity mode has non-zero components in both quadratures. As described in section 4.3, this fact creates an

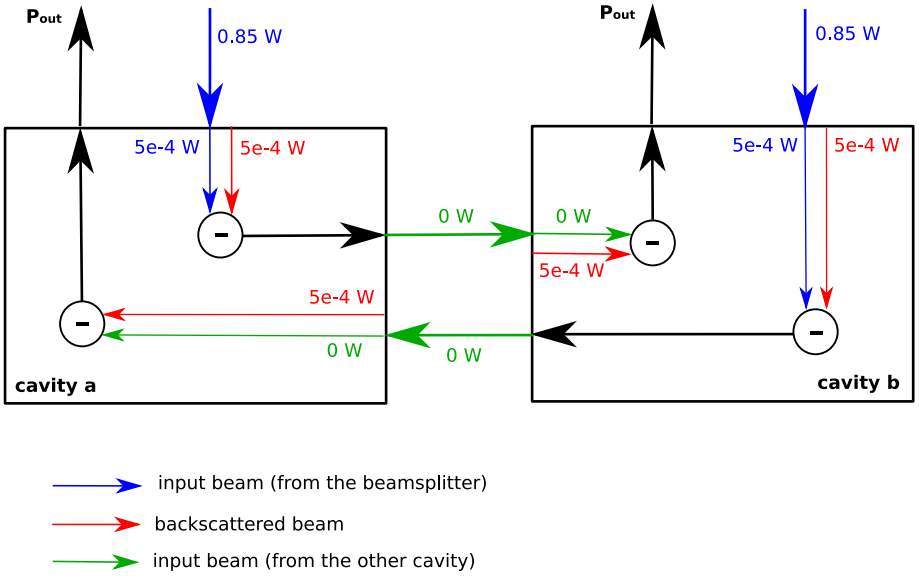

Figure 7.3: Schematic drawing of the power involved in the backscattering calculation for $\epsilon = 0.1$ ppm considering both cavities. Here the only scattered beam considered is R_{+1} of the intra-cavity beam. As we can see, the power of the transmitted input beam (blue arrows) couples with the reflected first order scattered beam R_{+1} of the intra-cavity beam (red arrows) and, since they have opposite phase their sum will be zero. So the output of the first cavity and then the input of the second cavity will be zero (green arrows).

optical spring, i.e. a restoring force acting on the mirrors.

The detuning from resonace can be evaluated from the optical rigidity of the cavity. Making the Taylor expansion in τ until the first non vanishing order and keeping only the first order of ϵ, we have that the rigidity given in equation 6.56 can be rewritten as

$$K_{arm}^{IJ}(\Omega) = -\frac{8P_c\omega_p}{cL}\frac{\frac{\sqrt{\epsilon}}{2\tau}}{(\gamma+\epsilon\gamma-i\Omega)^2+\frac{\epsilon^2}{4\tau^2}}, \tag{7.2}$$

where $P_c = \frac{\hbar\omega_p}{2}\boldsymbol{E}^\dagger\boldsymbol{E}$ is the circulating power, that can be considered equal for both beams. Comparing this equation with the definition of the optical rigidity in equation 4.86, we obtain that the detuning of the cavity due to backscattering is

$$\delta = \frac{\sqrt{\epsilon}}{2\tau}. \tag{7.3}$$

In figure 7.4 the value of the detuning as a function of the backscattering coefficient is shown.

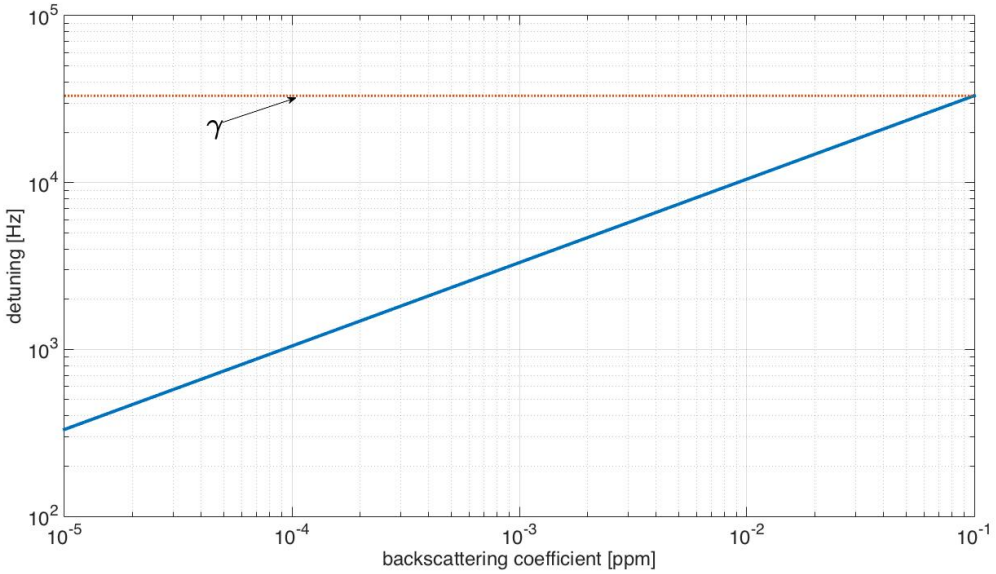

Figure 7.4: Plot of the cavity detuning due to backscattering as a function of the backscattering coefficient (blue line). The dotted red line represents the value of the half bandwidth γ.

7.1.3 Normalisation

Another important aspect of the results that needs to be explained is the fact that the radiation pressure noise seems to disappear at low frequencies, bringing the sensitivity below the SQL level. However this does not mean that the sensitivity is improved, because we did not consider the force created by the optical spring. As explained in the previous section, in fact, the backscattering effect creates an optical spring in the cavity and then another force is involved in the picture. So in order to better understand what is happening, it is useful to analyse the results in terms of forces.

The signal read by interferometric gravitational wave detectors is usually expressed in terms of mirror motion, which causes asymmetry in the length of the two cavities and creates an interference pattern. However with this view the test masses are supposed to be free (as it is thanks to the multistage pendulum suspensions). This assumption is not correct anymore when the optical springs are present. Furthermore when the mirrors cannot be considered free masses anymore the *x-normalisation* used so far can give misleading results.

So the sensitivity must be rewritten in terms of forces to be sure that all the forces acting on the mirror are taken into account. To do that we can normalise the PSD of the sensitivity as done in section 3.2 for the SQL. So we can write the corresponding of equation 3.28 for the sensitivity, which will be

$$S^F(\Omega) = \frac{S^x(\Omega)}{\left|\chi_{xx}(\Omega)\right|^2}, \tag{7.4}$$

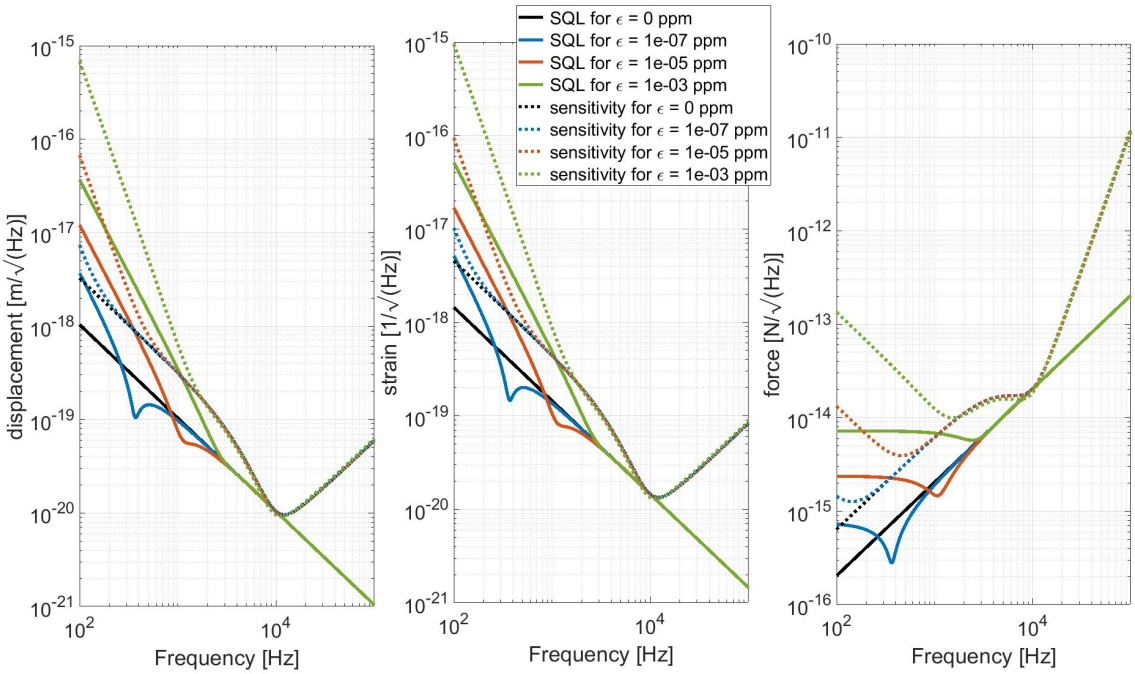

Figure 7.5: Plots of the quantum noise limited sensitivity displacement (left), strain (centre) and force (right) for the Glasgow SSM, with the parameters listed in table 7.1.

or, in terms of the familiar strain h

$$S^h(\Omega) = \frac{4S^x(\Omega)}{M^2L^2\Omega^4\left|\chi_{xx}(\Omega)\right|^2}, \tag{7.5}$$

where $\chi_{xx}(\Omega)$ is now defined by equation 6.55

In figure 7.5 the quantum noise limited sensitivities in terms of force and strain are shown. As explained in section 3.2 when we do not have a free mass the SQL will change too and in our case it is dependent on the backscattering coefficient. In the figure we have the sensitivity and the respective SQL for three values of the backscattering coefficient. As we can see, with this correction the sensitivity does not go below the respective SQL and it gets worst, as one should expect.

7.2 Energy conservation law

In order to prove that the results are right we checked if the energy conservation law is verified. The energy conservation law for one cavity can be determined from the optical transfer matrix defined in equation 6.27. However for the power calculation we do not need the whole transfer matrix, but only the classical part, since it is the only part that gives some

contribution. The equations for the classical part can be written as

$$\begin{aligned}\begin{bmatrix}\boldsymbol{B}^{\bar{I}J}\\ \boldsymbol{B}^{IJ}\\ \boldsymbol{E}^{\bar{I}J}\\ \boldsymbol{E}^{IJ}\end{bmatrix} &= (1-\mathscr{L})\begin{bmatrix}-i\sqrt{\epsilon R} & \sqrt{R} & \sqrt{\epsilon T} & i\sqrt{T}\\ \sqrt{R} & -i\sqrt{\epsilon R} & i\sqrt{T} & \sqrt{\epsilon T}\\ \sqrt{\epsilon T} & i\sqrt{T} & -i\sqrt{\epsilon R} & \sqrt{R}\\ i\sqrt{T} & \sqrt{\epsilon T} & \sqrt{R} & -i\sqrt{\epsilon R}\end{bmatrix}\begin{bmatrix}\boldsymbol{A}^{IJ}\\ \boldsymbol{A}^{\bar{I}J}\\ \boldsymbol{E}^{IJ}\\ \boldsymbol{E}^{\bar{I}J}\end{bmatrix}\\ &= (1-\mathscr{L})\,\mathbb{T}_1\begin{bmatrix}\boldsymbol{A}^{IJ}\\ \boldsymbol{A}^{\bar{I}J}\\ \boldsymbol{E}^{IJ}\\ \boldsymbol{E}^{\bar{I}J}\end{bmatrix}.\end{aligned} \tag{7.6}$$

By definition the power of a generic field $\boldsymbol{E}$ is $P_E = \frac{\hbar\omega_p}{2}\boldsymbol{E}^\dagger\boldsymbol{E}$ and for the energy conservation law the total output power (the term on the left in the previous equation) must be equal to to the total input power minus the loss (the term on the right). So, calculating the power we will have

$$\frac{\hbar\omega_p}{2}\begin{bmatrix}\boldsymbol{B}^{\bar{I}J}\\ \boldsymbol{B}^{IJ}\\ \boldsymbol{E}^{\bar{I}J}\\ \boldsymbol{E}^{IJ}\end{bmatrix}^\dagger\begin{bmatrix}\boldsymbol{B}^{\bar{I}J}\\ \boldsymbol{B}^{IJ}\\ \boldsymbol{E}^{\bar{I}J}\\ \boldsymbol{E}^{IJ}\end{bmatrix} = \frac{\hbar\omega_p}{2}\left((1-\mathscr{L})\,\mathbb{T}_1\begin{bmatrix}\boldsymbol{A}^{IJ}\\ \boldsymbol{A}^{\bar{I}J}\\ \boldsymbol{E}^{IJ}\\ \boldsymbol{E}^{\bar{I}J}\end{bmatrix}\right)^\dagger\left((1-\mathscr{L})\,\mathbb{T}_1\begin{bmatrix}\boldsymbol{A}^{IJ}\\ \boldsymbol{A}^{\bar{I}J}\\ \boldsymbol{E}^{IJ}\\ \boldsymbol{E}^{\bar{I}J}\end{bmatrix}\right), \tag{7.7}$$

which, using the matrix property $(AB)^\dagger = B^\dagger A^\dagger$, becomes

$$\begin{aligned}&\frac{\hbar\omega_p}{2}\begin{bmatrix}(\boldsymbol{B}^{\bar{I}J})^\dagger & \left(\boldsymbol{B}^{IJ}\right)^\dagger & \left(\boldsymbol{E}^{\bar{I}J}\right)^\dagger & \left(\boldsymbol{E}^{IJ}\right)^\dagger\end{bmatrix}\begin{bmatrix}\boldsymbol{B}^{\bar{I}J}\\ \boldsymbol{B}^{IJ}\\ \boldsymbol{E}^{\bar{I}J}\\ \boldsymbol{E}^{IJ}\end{bmatrix} = \frac{\hbar\omega_p}{2}(1-\mathscr{L})^2\begin{bmatrix}\boldsymbol{A}^{IJ}\\ \boldsymbol{A}^{\bar{I}J}\\ \boldsymbol{E}^{IJ}\\ \boldsymbol{E}^{\bar{I}J}\end{bmatrix}^\dagger\mathbb{T}_1^\dagger\mathbb{T}_1\begin{bmatrix}\boldsymbol{A}^{IJ}\\ \boldsymbol{A}^{\bar{I}J}\\ \boldsymbol{E}^{IJ}\\ \boldsymbol{E}^{\bar{I}J}\end{bmatrix}\\ &= \frac{\hbar\omega_p}{2}(1-\mathscr{L})^2\begin{bmatrix}(\boldsymbol{A}^{IJ})^\dagger & (\boldsymbol{A}^{\bar{I}J})^\dagger & \left(\boldsymbol{E}^{IJ}\right)^\dagger & \left(\boldsymbol{E}^{\bar{I}J}\right)^\dagger\end{bmatrix}\mathbb{I}\begin{bmatrix}\boldsymbol{A}^{IJ}\\ \boldsymbol{A}^{\bar{I}J}\\ \boldsymbol{E}^{IJ}\\ \boldsymbol{E}^{\bar{I}J}\end{bmatrix},\end{aligned} \tag{7.8}$$

where we have used the condition that $\mathbb{T}_1$ is unitary. The previous equation can be written

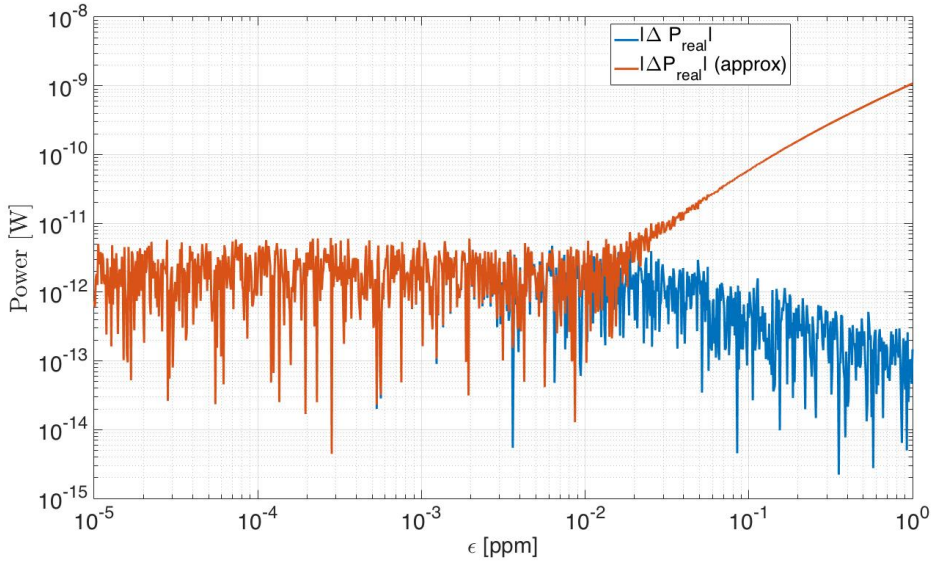

Figure 7.6: *In blue*: Results of the equation 7.10, which should be theoretically zero, but it actually represents the numerical accuracy of the calcualtion. *In red*: The same as before but neglecting the second order terms in $\mathscr{L}$.

in terms of power as

$$P_B^{IJ} + P_B^{\bar{I}J} + P_E^{IJ} + P_E^{\bar{I}J} = (1-\mathscr{L})^2 \left(P_A^{IJ} + P_A^{\bar{I}J} + P_E^{IJ} + P_E^{\bar{I}J} \right). \tag{7.9}$$

So the relation between the input, output and lost power is

$$\underbrace{P_A^{IJ} + P_A^{\bar{I}J}}_{input} - \underbrace{P_B^{IJ} + P_B^{\bar{I}J}}_{output} - \underbrace{\left(2\mathscr{L} - \mathscr{L}^2\right) \left(P_A^{IJ} + P_A^{\bar{I}J} + P_E^{IJ} + P_E^{\bar{I}J} \right)}_{loss} = 0. \tag{7.10}$$

The difference between input, output and loss power described in the previous equation must be, theoretically, equal to zero. However performing the calculation with MATLAB® we have that it is not exactly zero, but some value around 10^{-12} W. The results of this calculation is shown in figure 7.6. However given the small value (compared to an input power of 1.7 W) and the noisy appearance of the plot, we can say that it is the numerical accuracy of the calculation. Furthermore, we evaluated also the results in case we want to neglect the second order terms of the loss and we can see that this approximation is valid only for a backscattering coefficient smaller than the critical value of 0.1 ppm, the meaning of which has been explained in section 7.1.1.

7.3 Analysis of km-scale speed meters with backscattering

The results of the backscattering calculation for the Glasgow SSM show that even for 10^{-5} ppm of backscattered radiation we could have a decrease by one order of magnitude in the strain sensitivity of the interferometer at very low frequencies. However this is true only for this particular case, but the effect is much less influent for large scale interferometers. In order to prove that, we applied the calculation to three configurations of future gravitational wave detectors: Voyager, Cosmic explorer and Einstein Telescope (optimised at low frequencies).

The parameters used for these calculations are listed in table 7.2. In all cases, since in the configurations the presence of the power recycling mirror is planned, the input power has been increased in order to compensate its absence and to provide the same circulating power. It should also be noted that the baseline configurations of Voyager, Cosmic Explorer and ET are not speed meters. Furthermore for Voyager and Cosmic Explorer the presence of a Signal Extraction mirror (which will affect the effective bandwidth) is planned and the value of the ITM transmissivity has not been fixed yet (the actual proposed value is about 1000 ppm). So we choose the value of 7000 ppm for Voyager and 15000 ppm for Cosmic Explorer, in order to compensate these differences and to be able to see the speed meter behaviour (sensitivity parallel to the SQL at low frequencies). We will only analyse the case of weak coupling, for which we have a full understanding of the mechanism. The critical value of backscattering coefficient that defines the transition between weak and strong coupling is obviously different in each case and it has been calculated through equation 7.1 for each of them. Their values are listed in table 7.3. Furthermore, all calculations are made considering a perfect 50:50 beamsplitter with no loss and a perfect photodetector with 100% efficiency, as done for the previous calculation.

In figures 7.7, 7.8 and 7.9 the quantum noise limited sensitivity in terms of strain (on the left) and force (on the right) are shown for Voyager, Cosmic Explorer and ET-LF respectively. For Voyager we have that the backscattering effect is much less significant than in the Glasgow SSM. However it becomes to be significant at frequencies below a few hertz, where the interferometer sensitivity is dominated by seismic noise, so probably it would not affect the total noise. For Cosmic explorer the effects are even less significant, due to the longer arms. In this case in fact the sensitivity becomes to decrease only for frequencies below 0.8 Hz. On the other side, for ET-LF the backscattering effect becomes significant already around 2 Hz. However it must be noted that for all of them, because the backscattering effect would be significant at higher frequencies, we need a high backscattering coefficient, around 0.1 ppm.

parameter	**Voyager**	**CE**	**ET-LF**
laser input power	750 W (140 W)	500 W (220 W)	31.5 W (3 W)
arm power	3 MW	2 MW	18 kW
cavity length	4 km	40 km	10 km
laser wavelength	2 μm	1550 nm	1550 nm
ITM power transmissivity	7000 ppm	15000 ppm	7000 ppm
ITM mass	200 kg	320 kg	211 kg
ETM mass	200 kg	320 kg	211 kg
photodetector efficiency	1	1	1
homodyne angle	$\pi/2$	$\pi/2$	$\pi/2$
power reflectivity of the beamsplitter	0.5	0.5	0.5
power transmissivity of the beamsplitter	0.5	0.5	0.5

Table 7.2: List of the parameters used for the results shown in figure 7.7, 7.8 and 7.9 for Voyager, Cosmic Explorer and ET-LF configurations respectively [39, 99]. The laser input power has been increased in order to compensate the absence of the power recycling mirror (in brackets the real power).

	ϵ_c **[ppm]**	S^h $[1/\sqrt{\text{Hz}}]$		**ratio**	f **[Hz]**
		$\epsilon = 10^{-3}$ **ppm**	$\epsilon = 0$ **ppm**		
Glasgow SSM	~ 0.1	$\sim 1 \times 10^{-15}$	$\sim 5 \times 10^{-18}$	~ 200	100
Voyager	~ 12	$\sim 1 \times 10^{-20}$	$\sim 1 \times 10^{-21}$	~ 10	0.5
Cosmic Explorer	~ 56	$\sim 3 \times 10^{-21}$	$\sim 5 \times 10^{-22}$	~ 6	0.1
ET-LF	~ 12	$\sim 4 \times 10^{-20}$	$\sim 1 \times 10^{-21}$	~ 40	0.1

Table 7.3: List of the critical value of the backscattering coefficient ϵ_c, the value of the quantum noise limited sensitivity at the specified frequency f for a backscattering coefficient $\epsilon = 10^{-3}$ ppm and without backscattering and the ratio between these two values for all the interferometer configurations considered in this chapter. In all cases the value of the frequency at which the sensitivity is taken is chosen in order to be 2 orders of magnitude below the frequency at which the interferometer is most sensitive. Note that we expect that these interferometers do not have a meaningful sensitivity below 1 Hz (due to noises other than quantum noise).

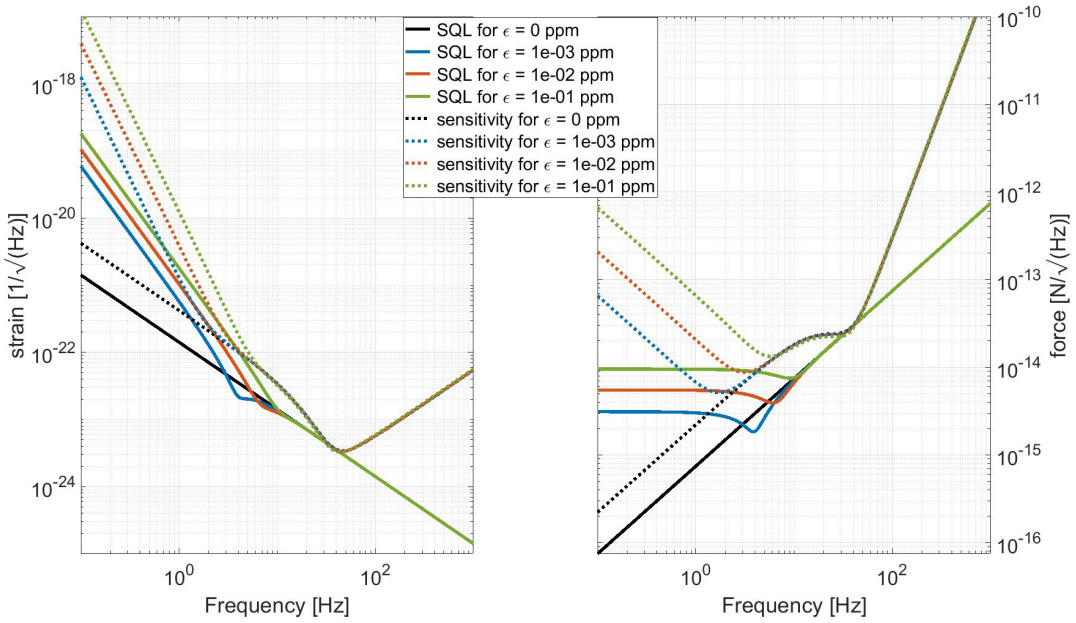

Figure 7.7: Plot of the quantum noise limited sensitivity force for Voyager.

In order to compare these effects between the four interferometers considered in this chapter, we choose a backscattering coefficient of $\epsilon = 10^{-3}$ ppm at which we calculate the strain quantum noise limited sensitivity. The frequency at which this value is taken is chosen to be two order of magnitude below the frequency at which the interferometer has the maximum sensitivity (different from each of them). All the results are listed in table 7.3. As expected the effects of the backscattering on large scale interferometers are smaller than a small scale interferometer like the Glasgow SSM. Furthermore for this comparison we are considering the value of the sensitivity at frequencies smaller than 1 Hz, where the total noise is dominated by seismic noise. So this effect probably will not affect the final sensitivity of the detectors.

7.4 Conclusions and outlook

In this chapter we have shown the results of the quantum noise limited sensitivity when this newly discovered noise coupling, called backscattering effect, is present in the cavities. First of all we made the calculation with the parameters of the Glasgow SSM experiment. The results show some peculiar features, which we have been able to explain. One important fact that we have discovered is the presence of a critical value of the backscattering coefficient, that makes us to divide the mechanism in two cases: weak coupling, that happens below the critical value and strong coupling, that happens above it. While the weak coupling case has been understood in every aspect, the strong coupling is not yet clear. In fact, the critical value of the backscattering coefficient, which corresponds at the situation

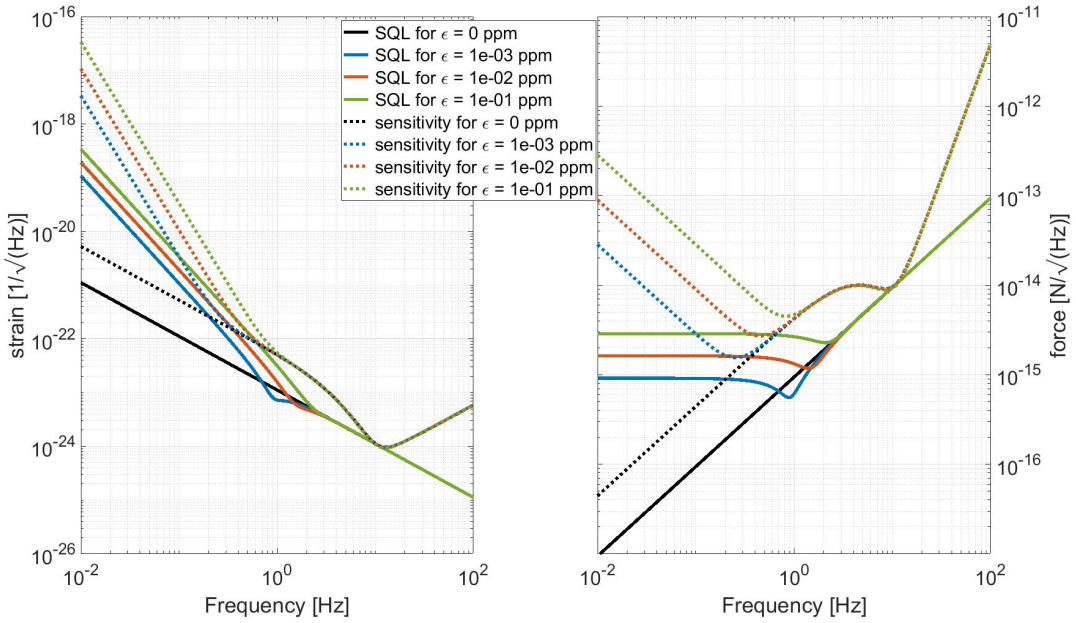

Figure 7.8: Plot of the quantum noise limited sensitivity force for CE.

when the backscattered beam and the transmitted input beam have the same power, activates some mechanism not yet fully understood and that will be analysed in the next future, in order to complete the picture.

However for all future GW detectors we assume that the mirrors quality will be good enough so that we stay in the range of weak coupling, hence this case is more important than the case of strong coupling. The weak coupling situation has been studied and understood for the Glasgow SSM, Voyager, Cosmic Explorer and ET-LF. The results show that while in the first case we could have a significant increment of the quantum noise, that does not happen in the large scale interferometers. For these interferometers in fact we have that the backscattering effect begins to significantly affect the quantum noise at low frequencies ($\sim$ 1 Hz), where the sensitivity is dominated by seismic noise and then it will probably not affect the total noise of the detectors.

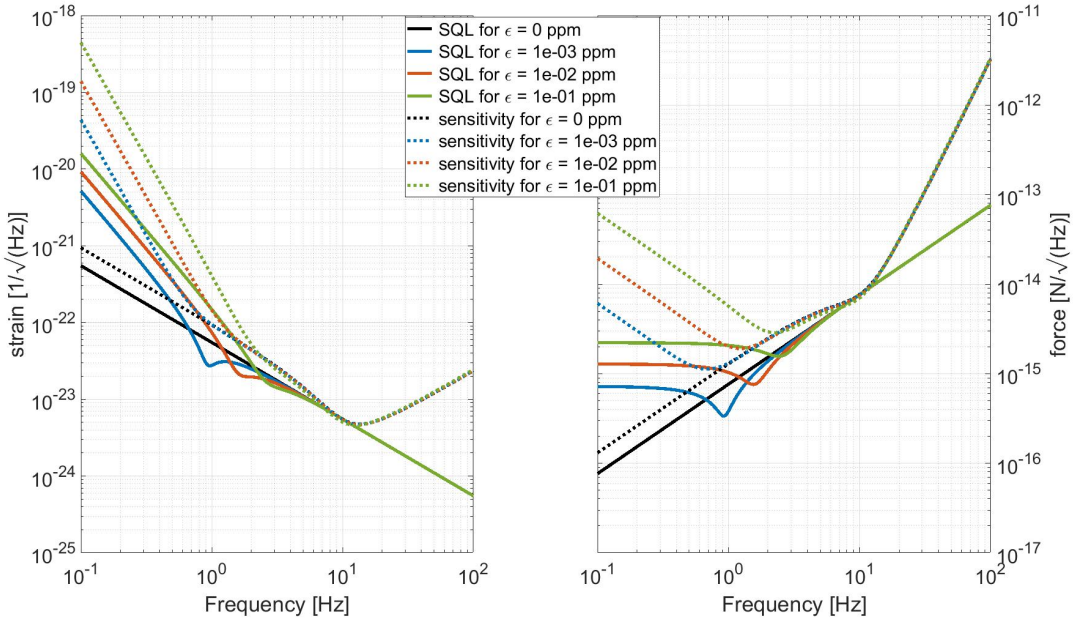

Figure 7.9: Plot of the quantum noise limited sensitivity force for ET-LF.

Chapter 8

Conclusions

Current gravitational wave detectors are based on a Michelson configuration, which is limited in the audio band frequencies mainly by quantum noise. However, it has been proved theoretically that using an interferometer with a different configuration can reduce the radiation pressure noise and even allows measurements below the SQL. This kind of interferometers, called speed meters, perform continuous measurements of the momentum of the mirrors, which is a quantum non-demolition (QND) observable and then it can be measured without being limited by the standard quantum limit (SQL). The simplest speed meter configuration is the Sagnac interferometer, which has been proved theoretically that is a speed meter as it is, without any change at its basic configuration. With the aim to prove that this assumption is right and also that in a Sagnac interferometer the radiation pressure is actually smaller than in an equivalent Michelson interferometer, the Sagnac speed meter proof-of-concept experiment in underway at the University of Glasgow. The theoretical basis of the speed meters and the details of this experiment have been described in chapter 3. However, the features of this particular experiment (small ITM and short cavity length) makes the interferometer very sensitive to optical loss. We have in fact, as shown in section 5.1, that quantum noise increases in a significant way when loss is present.

In chapter 4 I introduced the quantum noise calculation for several interferometer configurations. I showed how the I/O relations can be obtained, from which it is possible to calculate the quantum noise and then the PSD of the quantum noise limited sensitivity. First I discussed the radiation pressure and how the radiation pressure force can be calculated and included in the I/O relations. From these results then it is possible to calculate the quantum noise. However, these results are obtained considering the ideal cases, i.e. without any loss or detuning in the cavities.

Since the Glasgow SSM is very sensitive to optical loss, the cavity mirrors surfaces requirements must be very restrictive. So in chapter 5 the analyses that I made to derive these requirements are shown. The round trip loss in the cavity is estimated performing simu-

lations, most of them using the MATLAB® package OSCAR, which is a code that uses the FFT method to simulate cavities with arbitrary mirror profiles. After the requirements have been defined, I sent the specifications documents for ETM and ITM, that can be found in appendix C, to several companies, in order to obtain the quotes, but also and most important to have an idea of the feasibility of such kind of mirrors. Most companies in fact replied that they cannot achieve such quality and others accepted the work but with some exceptions. Then I analysed these exceptions, before the manufacturing, in order to confirm their compatibility with the experiment target.

In chapter 6 then, I introduced a theoretical analysis that shows how the microroughness can create the backscattering effect and how this mechanism affects the quantum noise. Since in triangular cavities the angle of incidence on the ITM is not zero, in fact, the beam can be scattered back in the same direction of the incident beam. The backscattered beam will then couple with the counter-propagating beam. This effect affects the quantum noise of the interferometer and so there will be a decreasing of the sensitivity. I showed in this chapter how the transfer matrix of a mirror can be written when all first orders scattered beams are taken into account. From this transfer matrix I calculated the I/O relations for one cavity first and for the full Sagnac interferometer are calculated. The equation of the quantum noise and the quantum noise limited sensitivity is then straightforward, since it is obtained following the same steps as the ideal case, including all the additional terms. However, even if I calculated the backscattering effect for the particular case of a triangular cavity with two intra-cavity beams propagating in opposite directions, the calculation is actually absolutely general and can be applied to any case of coupling inside a cavity.

The results of this analysis, described in chapter 7, show that this mechanism creates a detuning in the cavity that will then produce an optical spring effect. Furthermore there is a particular value of the backscattering coefficient (i.e. the amount of power scattered back) that corresponds to the value at which the transmitted input beam and the backscattered beam have the same power. The optical transfer matrix that describes the mirror shows that these two beams have opposite phase and then a destructive interference arises. While for the situation when backscattering coefficients are smaller than this critical value (weak coupling) is fully understood, the case when the backscattered power is of the same order or larger than the transmitted input power (strong coupling) is not yet clear, but this scenario is less likely to occur with state of the art experiments. I analysed the weak coupling situation for the special cases of the Glasgow SSM and for some large scale interferometers planned for the next future. The results show that even if in the first case this effect is very significant, the influence is much less important for the other cases, because of the longer arms and the bigger test masses.

In the end we can say that the speed meter is a possible candidate for the topology of future gravitational wave detectors. However this configuration has some constraints and

in this thesis I described two of them. The first one is the dependence of the quantum noise from optical loss, which is particular significant for the Glasgow SSM, since, because of the purpose of the experiment, its sensitivity must be dominated by quantum noise. So I showed the methods used to define the requirements of the arm cavity mirrors of the Glasgow SSM in order to reduce as much as possible the optical loss inside the cavities. The second constraint showed in the thesis is a newly discovered noise coupling present in speed meter: the backscattering effect. I made the mathematical computation of the quantum noise when this effect is present in the cavities, in order to show that, even if in the Glasgow experiment it could be significative, its importance is much less significant in large scale interferometers.

Appendix A

Symbols and formulae used

$\hat{a}_\omega$, $\hat{a}^\dagger_\omega$		single photon annihilation and creation operators
$\mathcal{A}(t)$		electric fields in time domain
$\hat{\mathbf{A}}(\omega)$	$= \mathrm{A} + \hat{\mathbf{a}}(\omega)$	field $\mathcal{A}(t)$ in frequency domain
A		classical amplitude of field $\hat{\mathbf{A}}(\omega)$
$\hat{\mathbf{a}}(\omega)$		quantum fluctuation of field $\hat{\mathbf{A}}(\omega)$
$\boldsymbol{A}$		classical amplitude in two-photon quadrature notation
$\hat{\boldsymbol{a}}(\Omega)$		quantum fluctuation in two-photon quadrature notation
c	$= 299792458\ \frac{\mathrm{m}}{\mathrm{s}}$	speed of light
$\hbar$	$= 1.055 \times 10^{-34}\ \frac{\mathrm{J \cdot s}}{\mathrm{rad}}$	reduced Planck constant
$\mathbb{I}$		identity matrix
I	= R, L	direction of propagation of the beam
$\bar{I}$		the opposite direction of I
J	= N, E	cavity (North (N) or East (E))
K^{IJ}_{arm}		optical rigidity
L		cavity length
R_{BS}		beamsplitter power reflectivity
R_{ITM}		ITM power reflectivity
T_{BS}		beamsplitter power transmissivity
T_{ITM}		ITM power transmissivity
x_J		arm elongation

x_J^{GW}		arm elongation due to the signal
x_{SQL}	$= \sqrt{\frac{2\hbar}{\mu_{arm}\Omega^2}}$	standard quantum limit
γ	$= \frac{cT}{4L}$	cavity half bandwith
Θ^{IJ}	$= \frac{4\omega_p P_c^{IJ}}{\mu_{arm} c L}$	normalised circulating power
λ		optical wavelength
μ_J	$= \frac{m_{ITM} m_{ETM}}{m_{ITM}+m_{ETM}}$	effective mass of the arm J (for a linear cavity)
μ_J	$= \frac{2m_{ITM} m_{ETM}}{m_{ITM}+2m_{ETM}}$	effective mass of the arm J (for a triangular cavity)
μ	$= \frac{\mu_N \mu_E}{\mu_N+\mu_E}$	effective mass of the full interferometer
$\hat{\sigma}$	$\begin{bmatrix} 0 & 1 \\ -1 & 0 \end{bmatrix}$	Pauli matrix
τ	$= \frac{L}{c}$	half roundtrip time
χ	$= -\frac{1}{\mu\Omega^2}$	mechanical susceptibility function
ω		optical band frequencies
ω_p	$= 2\pi c/\lambda$	laser frequency
Ω	$= \omega - \omega_p$	measured band frequencies
P_c		intra-cavity power

Appendix B

Mirrors surface measurements

In this appendix we show the measurements of the mirrors surface profiles made with Zygo. Figure B.1 show the raw data, without any corrections made. These data were then corrected with *Simtools* and the offset and the pistons were removed as described in section 5.2.2. The profile of the surface after these corrections are shown in figure B.2. The profile of the residual after the subtraction of each map with its consecutive (figure B.3) and with the last one taken are also shown (figure B.4).

Figures B.5 and B.6 at the end show the surface profile of the ITM and ETM substrates of the Glasgow SSM experiment respectively.

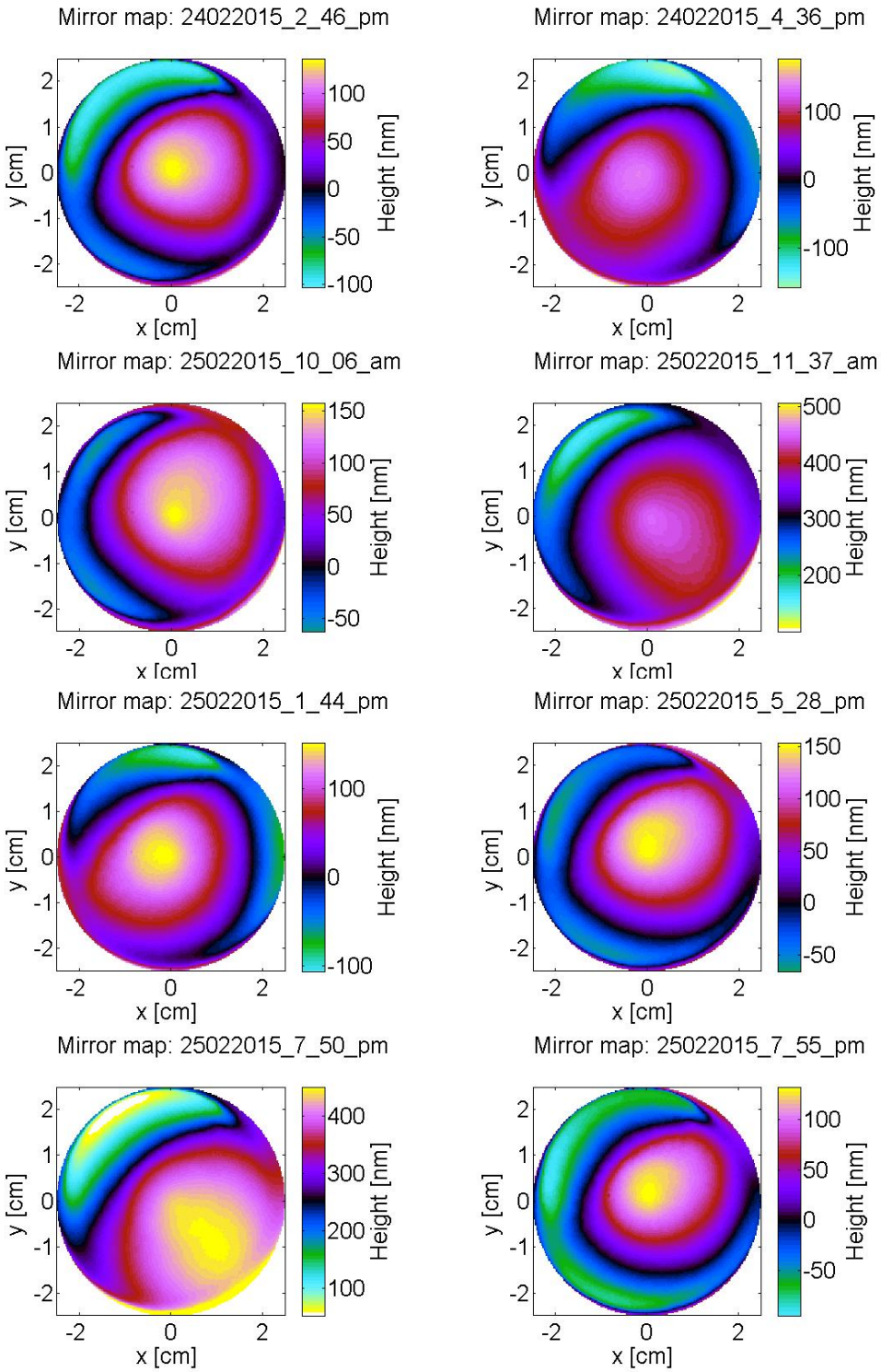

Figure B.1: Maps of the raw data of flatness measurements of the sample mirror.

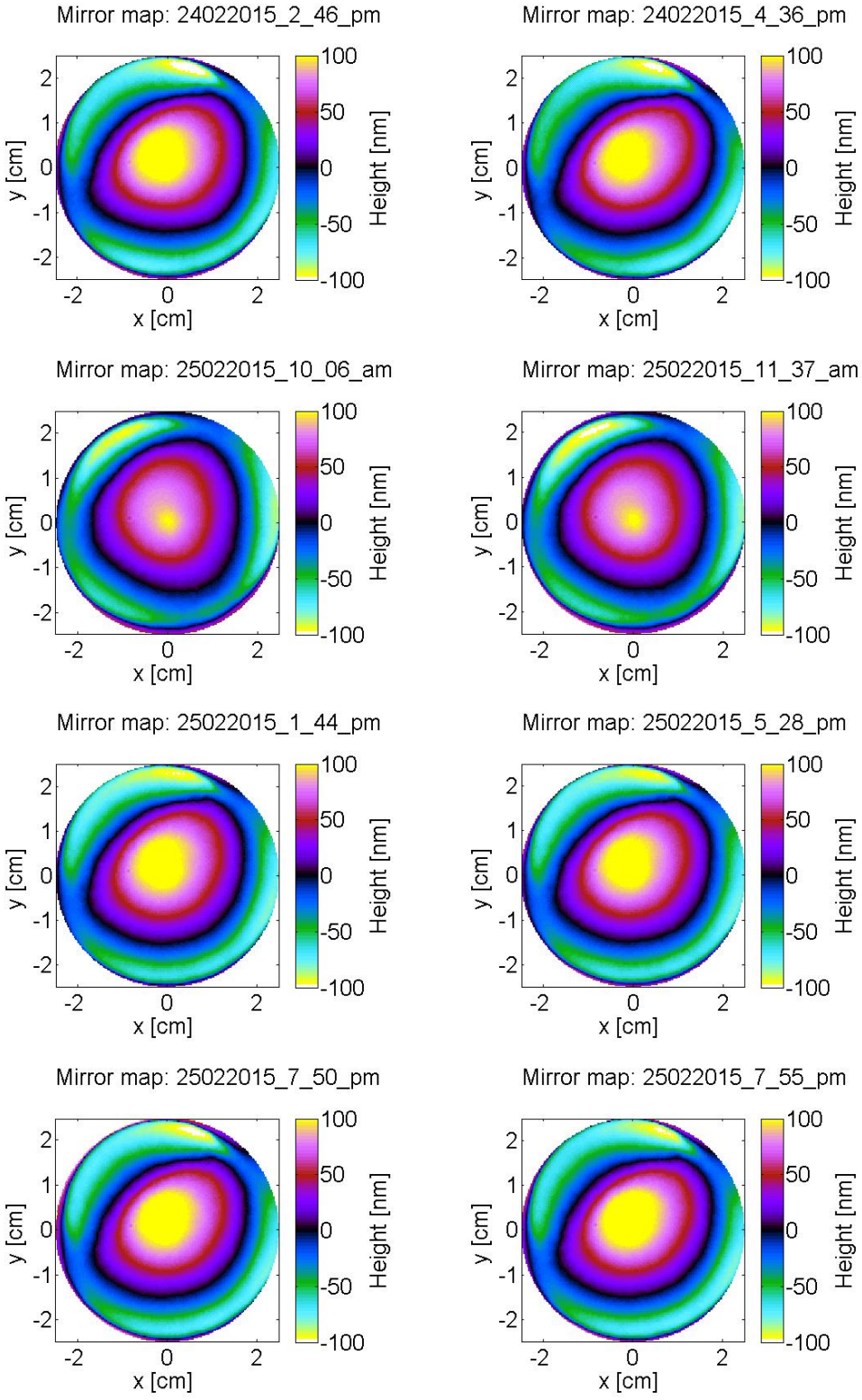

Figure B.2: Maps of the sample mirror with offset and piston removed.

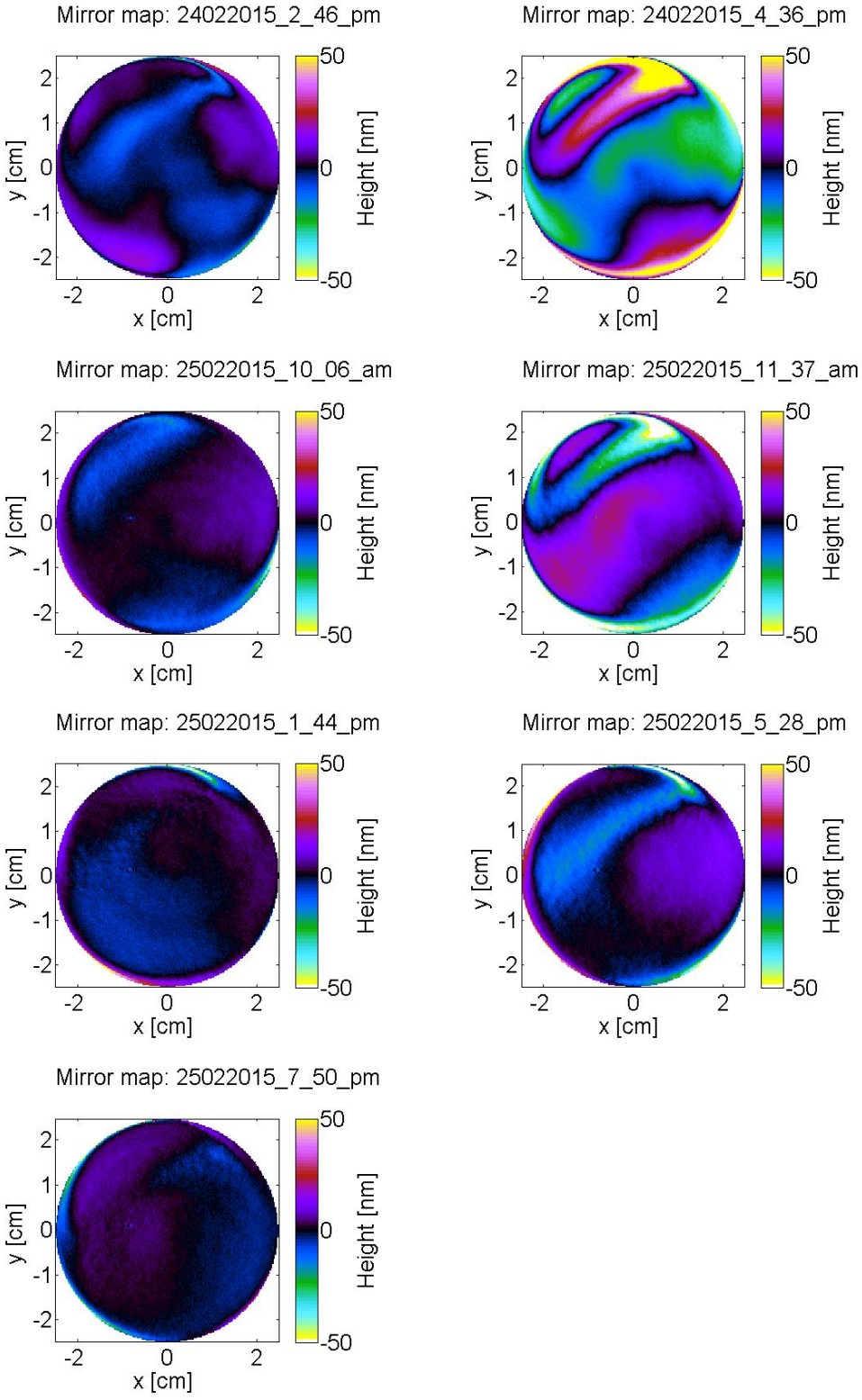

Figure B.3: Maps of the residual data of the difference of each map with its consecutive.

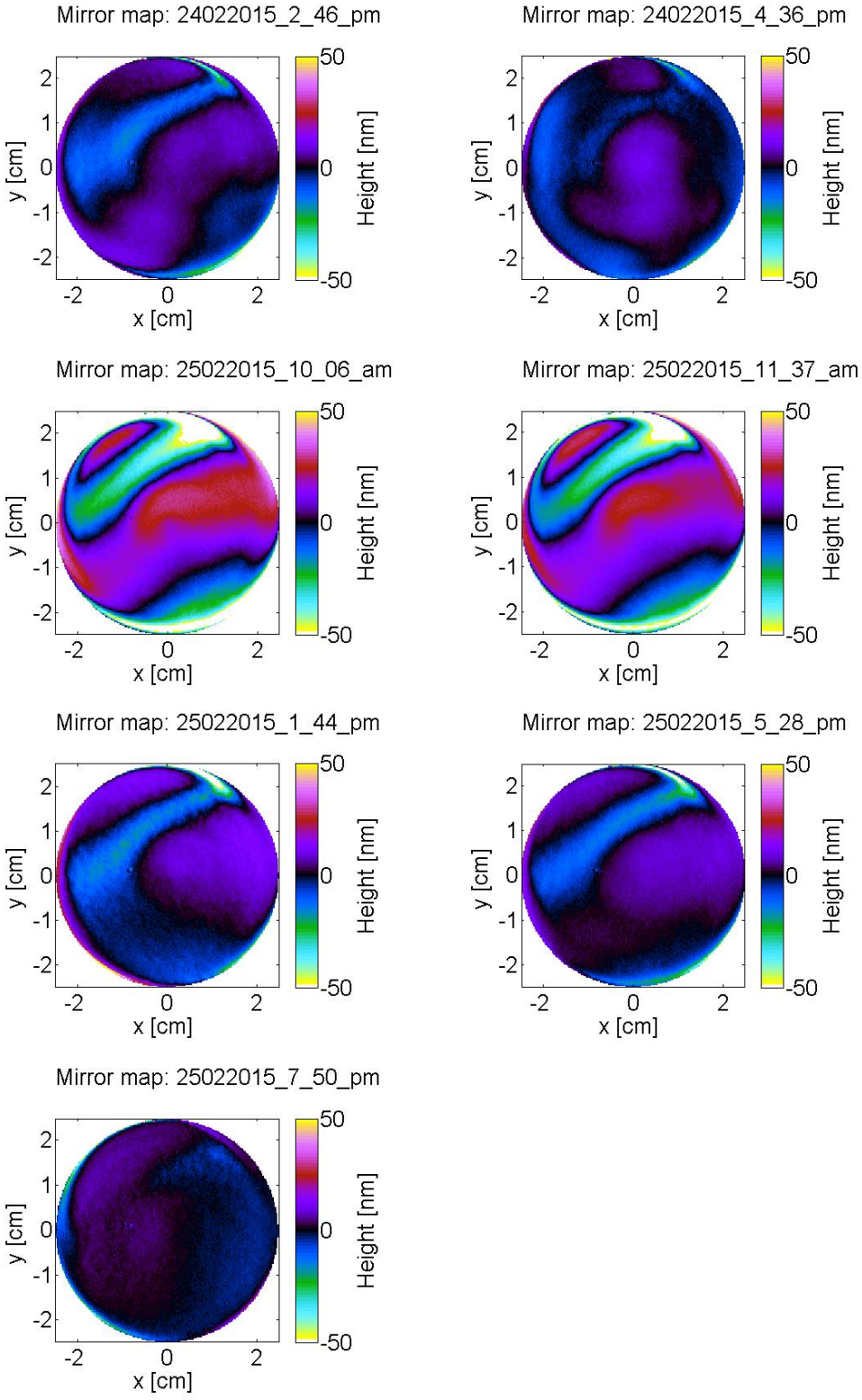

Figure B.4: Maps of the residual data of the difference of each map with the last one taken.

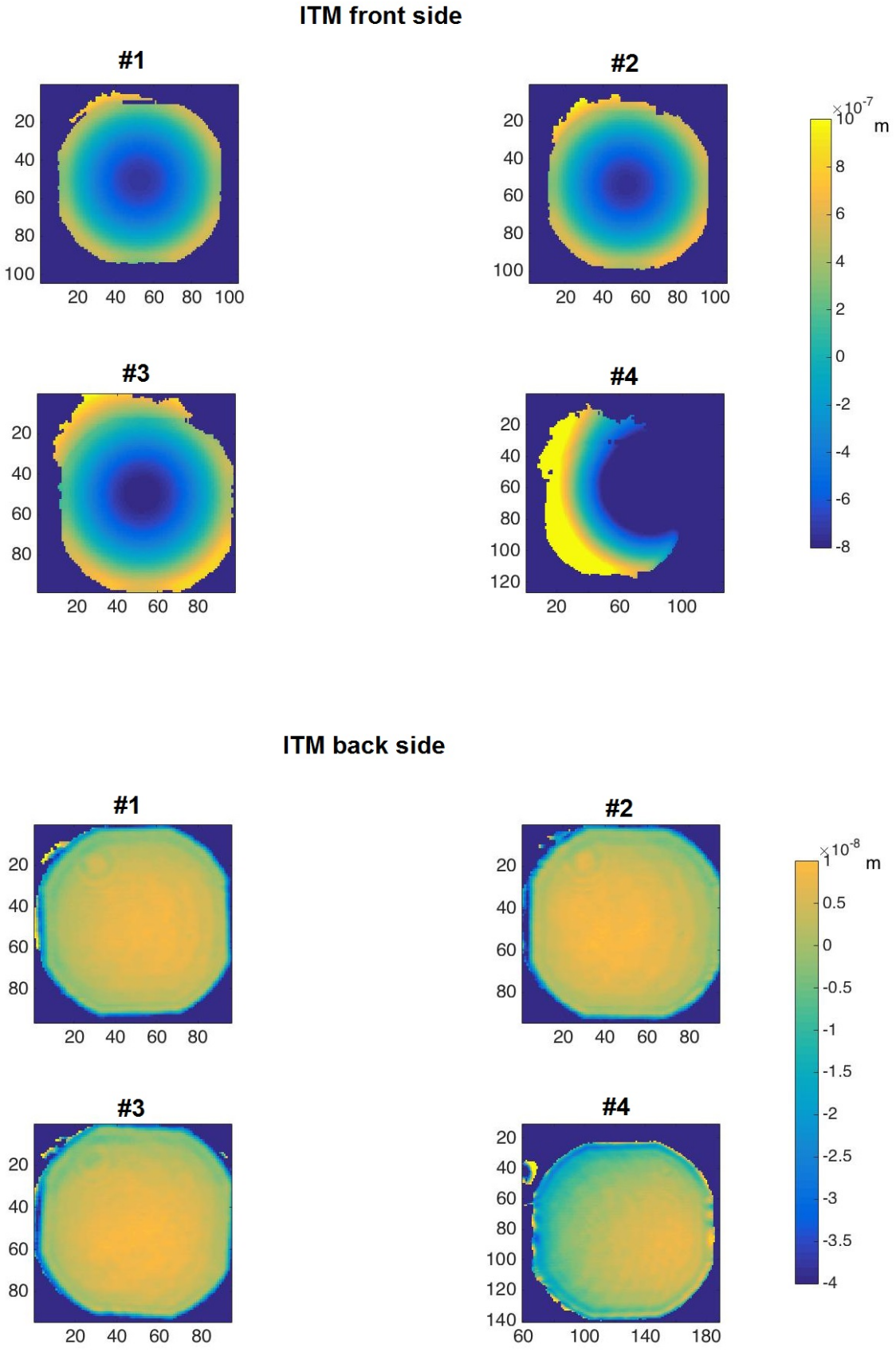

Figure B.5: Maps of the ITM front and back surfaces.

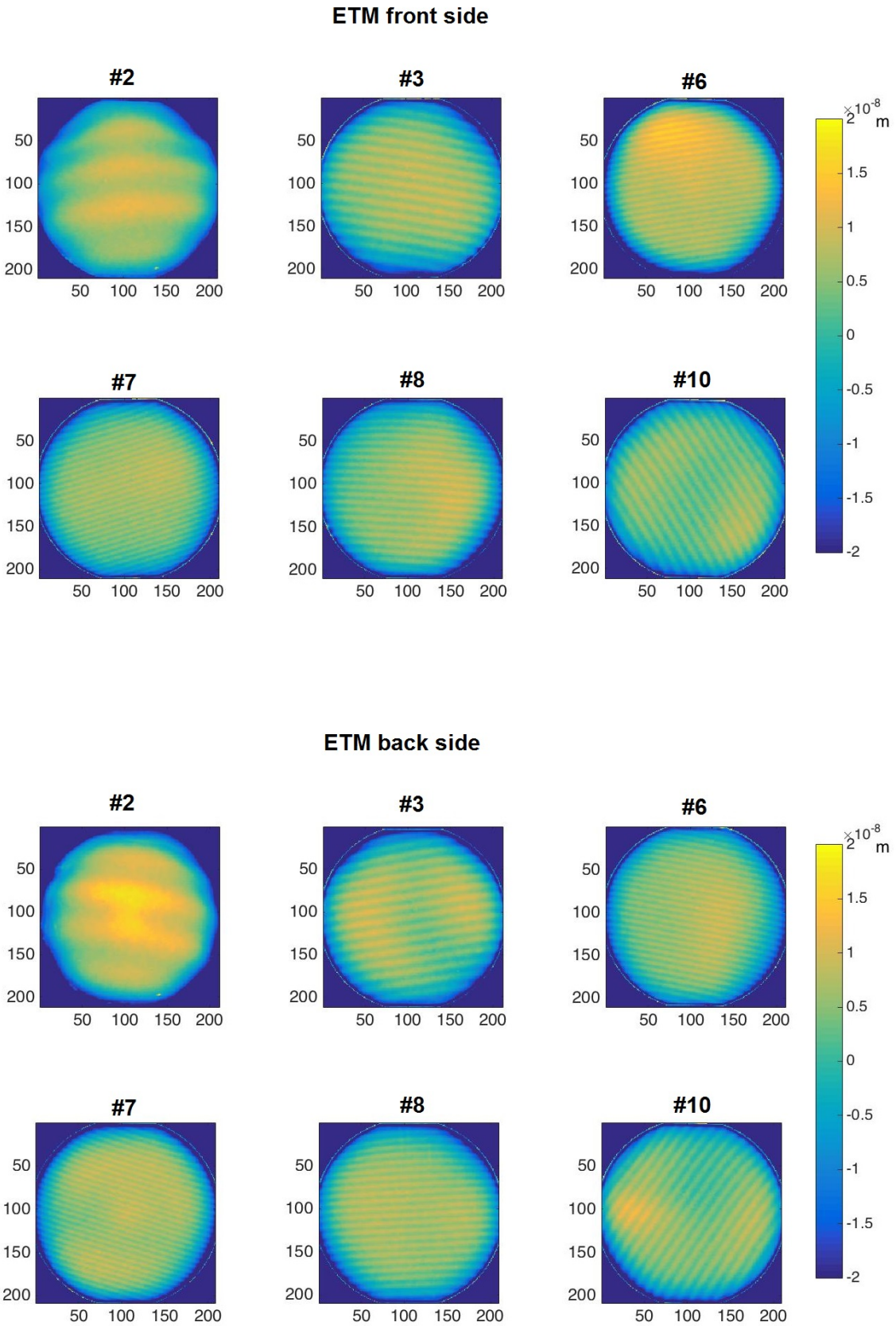

Figure B.6: Maps of the ETM front and back surfaces.

Appendix C

Specifications documents

In this appendix we report the specifications documents of the arm cavity mirrors of the Glasgow SSM experiment as they have been sent to the manufacture companies.

Specifications document of the ITM substrate of the Sagnac Speedmeter proof of principle experiment

Issue: 1
Date: July 9, 2015

SUPA
Institute for Gravitational Research
Department of Physics & Astronomy
University of Glasgow
Glasgow, G12 8QQ, United Kingdom

Contents

1 Aim of this document

The aim of this document is to describe the technical specifications of the input test masses of the Sagnac Speedmeter proof of principle experiment.

2 Specification zones

We define two different specification zones:

- Zone A: surface inside a radius of 3 mm;
- Zone B: surface outside a radius of 3 mm.

3 Material

The substrate material must be suprasil or equivalent.

4 Dimensions

We are flexible in regards to dimensions and leave to the producer whether to start from a cylindrical substrate (Option 1) or from a square substrate (Option 2).
Please quote the option you prefer.
For both options it is required that there is no wedge.

Option 1
The mirror must have a diameter of 10 mm ± 0.1 mm and a thickness of 5 mm ± 0.1 mm (see figure 1).

Option 2
The mirror must be square with dimensions 9 mm ± 0.1 mm x 9 mm ± 0.1 mm and a thickness of 5 mm ± 0.1 mm (see figure 2).

5 Lateral Flat

Option 1
The substrate must have 4 flat edge of dimensions 5 mm x 4 mm. They must be parallel with an accuracy of 0.1 mm.

Option 2
The lateral surfaces must be parallel with an accuracy of 0.1 mm.

In both cases on three sides there must be an area centered on the flat with dimensions 2 mm x 2 mm and with a roughness compatible with the silicate bonding (<1 nm) and a flatness PV of 60 nm and on the side without the bond area the serial number must be etch and there must be an arrow pointed to the curved surface (see figures 1 and 2).

6 Chamfers

All the sides of the substrate must have a polished chamfer of width 0.25 mm ± 0.05 mm at 45°.

7 HR Surface

7.1 Radius of curvature

The HR surface must be concave with radius of curvature of 7.91 m ± 0.02 m.

7.2 Microroughness

Microroughness must be < 0.1 nm ("super polish" best effort) for spatial frequencies above 750 mm^{-1}.

7.3 Surface defects

Digs

Zone A
No single point defects larger than 1 μm and total area of defects < 100 μm^2.

Zone B
No single point defects larger than 1 μm and total area of defects < 2000 μm^2.

Scratches

Zone A
No scratches with a width > 1 μm (5/L0x0.001 with ISO 10110 method 1).

Zone B
No more than 10 scratches with a width > 1 μm (5/L10x0.001 with ISO 10110 method 1).

7.4 Surface error (Low spatial frequencies)

Zone A
LSF error $< 2\,\text{nm}$ rms for spatial frequencies $0.3 - 1\,\text{mm}^{-1}$.
Astigmatism must be $< 8\,\text{nm}$.

7.5 Surface error (High spatial frequencies)

Zone A
HSF error $< 0.3\,\text{nm}$ pk-pk for spatial frequencies $1 - 750\,\text{mm}^{-1}$.

8 AR Surface

8.1 Radius of curvature

The AR surface must be flat ($RoC > 100\,\text{km}$).

8.2 Microroughness

Microroughness must be $< 0.1\,\text{nm}$ ("super polish" best effort) for spatial frequencies above $750\,\text{mm}^{-1}$.

8.3 Surface defects

Digs

No more than 100 point defects with size $> 2\,\mu\text{m}$.

Scratches

No more than 100 scratches with a width $> 5\,\mu\text{m}$ (5/L100x0.005 with ISO 10110 method 1).

8.4 Surface error (Low spatial frequencies)

LSF error must be $< 2\,\text{nm}$ rms.

8.5 Surface error (High spatial frequencies)

HSF error must be $< \lambda/8$.

9 Surface maps

If possible, the company should send the electronic files of the surface maps for future simulations.

10 Contacts

- Daniela Pascucci (d.pascucci.1@research.gla.ac.uk);
- Stefan Hild (Stefan.Hild@glasgow.ac.uk);

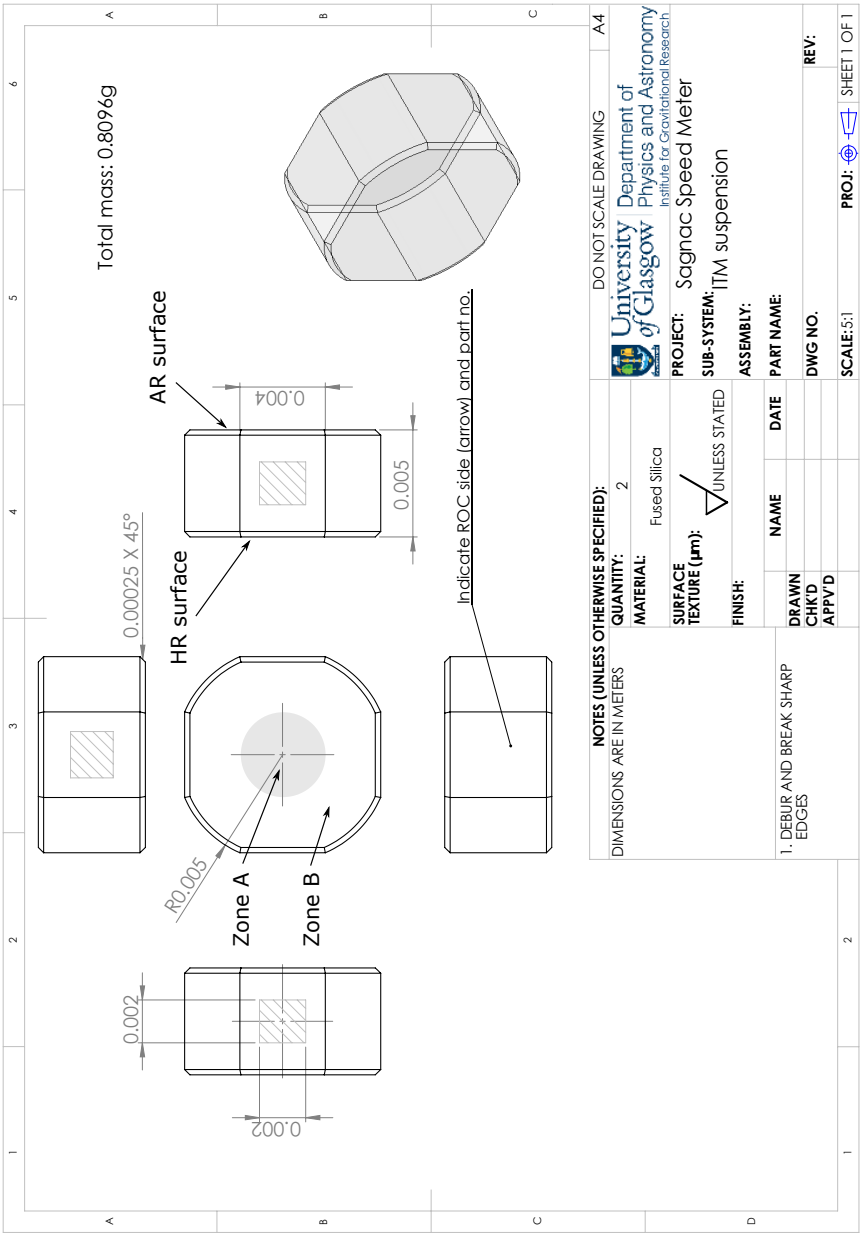

Figure 1: Drawing of the ITM (option 1).
page 6 of 7

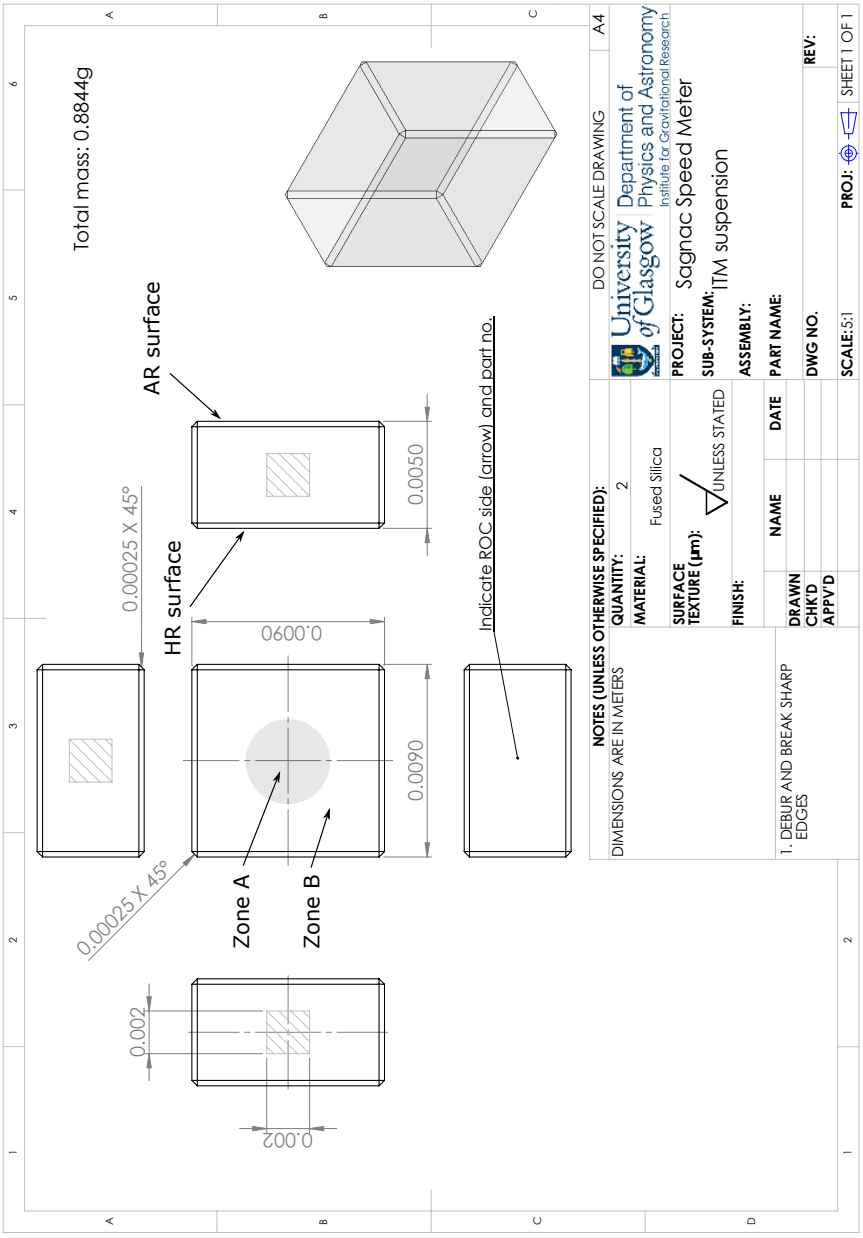

Figure 2: Drawing of the ITM (option 2).
page 7 of 7

Specifications document of the ETM substrate of the Sagnac Speedmeter proof of principle experiment

Issue: 1
Date: September 24, 2015

SUPA
Institute for Gravitational Research
Department of Physics & Astronomy
University of Glasgow
Glasgow, G12 8QQ, United Kingdom

Contents

1 Aim of this document

The aim of this document is to describe the technical specifications of the end test masses of the Sagnac Speedmeter proof of principle experiment.

2 Specification zones

We define three different specification zones:

- Zone A: surface inside a radius of 5 mm;
- Zone B: ring 5 mm from centre to 15 mm from centre;
- Zone C: surface outside a radius of 15 mm.

3 Material

The substrate material must be suprasil or equivalent.

4 Dimensions

The mirror must have a diameter of 48.8 mm ± 0.1 mm and a thickness of 24.5 mm ± 0.1 mm (see figure 1).
The parallelism must be 0.1°.

5 Lateral Flat

The substrate must have 2 flat faces of dimensions 15 mm x 24.5 mm., with a roughness compatible with the silicate bonding (<1 nm) and a flatness PV of 60 nm (see figure 1). They must be parallel with an accuracy of 0.4°.

On the curved barrel the serial number must be etched and there must be an arrow pointed to the front surface.

6 Chamfers

All the edges of the substrate must have a polished chamfer of width 0.25 mm ± 0.1 mm at 45°±15°.

7 Front surface

7.1 Radius of curvature

The front surface must be flat ($RoC > 10\,\mathrm{km}$).

7.2 Astigmatism

Astigmatism must be $< 16\,\mathrm{nm}$.

7.3 Microroughness

Microroughness must be $< 0.1\,\mathrm{nm}$ ("super polish" best effort) for spatial frequencies above $750\,\mathrm{mm}^{-1}$.

7.4 Surface defects

Digs

Zone A
No single point defects larger than $1\,\mu\mathrm{m}$ and total area of defects $< 600\,\mu\mathrm{m}^2$.

Zone B
No single point defects larger than $1\,\mu\mathrm{m}$ and total area of defects $< 3000\,\mu\mathrm{m}^2$.

Scratches

Zone A
No scratches with a width $> 1\,\mu\mathrm{m}$ (5/L0x0.001 with ISO 10110 method 1).

Zone B
No more than 10 scratches with a width $> 1\,\mu\mathrm{m}$ (5/L10x0.001 with ISO 10110 method 1).

7.5 Surface error (Low spatial frequencies: $0.3 - 1\,\mathrm{mm}^{-1}$)

Zone A
LSF error $< 1\,\mathrm{nm}$ pk-pk.

Zone B
LSF error $< \lambda/20$ rms (λ= 633nm).

Zone C
LSF error $< \lambda/5$ rms (λ= 633nm).

7.6 Surface error (High spatial frequencies: $1 - 750\,\mathrm{mm}^{-1}$)

Zone A
HSF error $< 0.25\,\mathrm{nm}$ pk-pk.

Zone B
HSF error $< \lambda/20$ rms (λ= 633nm).

Zone C
HSF error $< \lambda/5$ rms (λ= 633nm).

8 Back surface

8.1 Radius of curvature

The back surface must be flat ($RoC > 10\,\mathrm{km}$).

8.2 Microroughness

Microroughness must be $< 0.1\,\mathrm{nm}$ ("super polish" best effort) for spatial frequencies above $750\,\mathrm{mm}^{-1}$.

8.3 Surface defects

Digs

No more than 2 point defects with size $> 40\,\mu\mathrm{m}$ (5/2x0.04 with ISO 10110 method 1).

Scratches

No more than 2 scratches with a width $> 40\,\mu\mathrm{m}$ (5/L2x0.04 with ISO 10110 method 1).

8.4 Surface error

The surface error must be $< \lambda/20$ rms (λ= 633nm).

9 Surface maps

The company should send the electronic files of the surface maps for future simulations.

10 Contacts

- Daniela Pascucci (d.pascucci.1@research.gla.ac.uk);
- Stefan Hild (Stefan.Hild@glasgow.ac.uk);

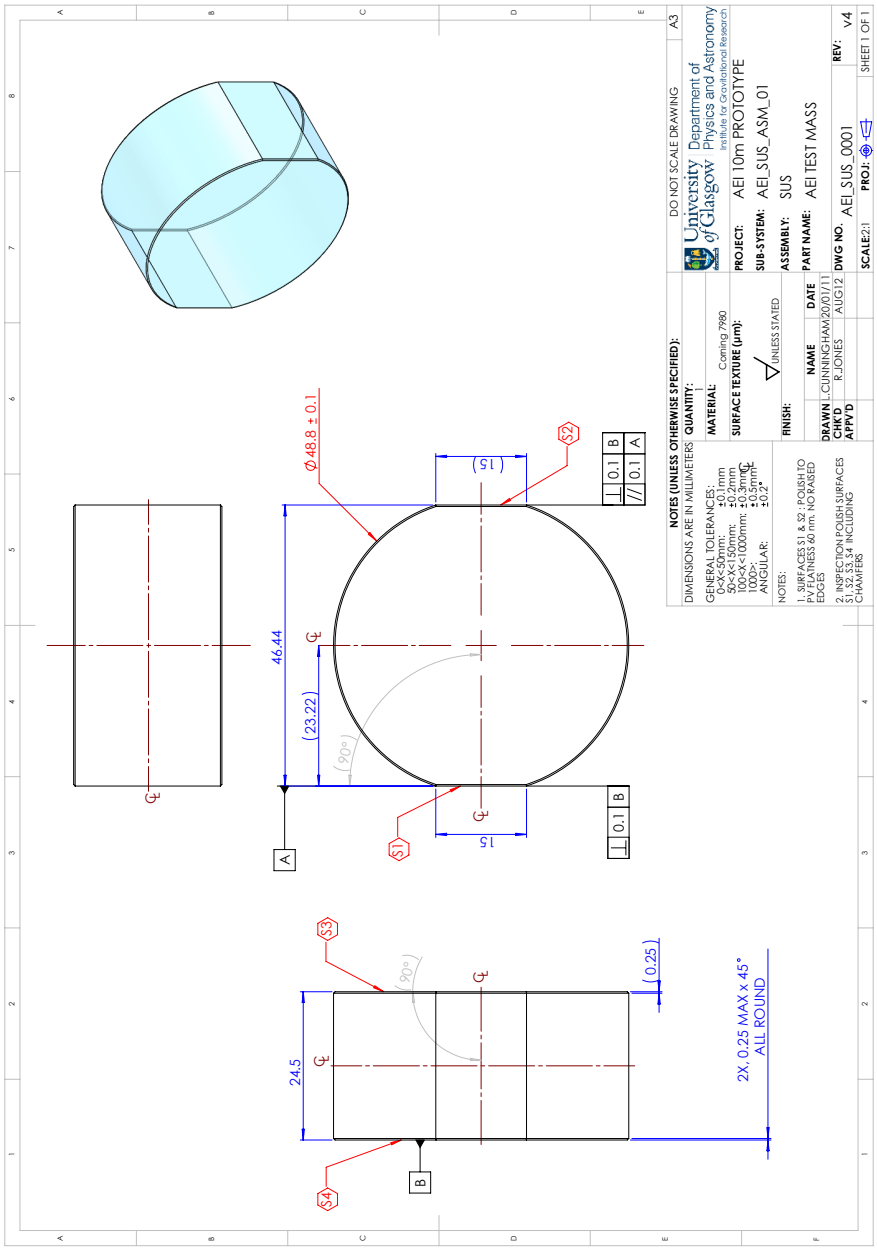

- v4.pdf

Figure 1: Drawing of the ETM.

Appendix D

Bonding of the test masses

In this section we will give an overview of the procedure of cleaning and bonding of the arm cavity mirrors of the Glasgow SSM proof-of-concept experiment. A more detailed description can be found in [83].

D.1 ETM

Before describing the cleaning and bonding of the ETM, we will show how the analysis of the ears flatness was made, in order to check that the requirements for the bonding surfaces were satisfied. We will show the results of the flatness measurements made for a set of 40 ears and the procedures followed to remove the spikes that we found on some of them.

D.1.1 Ears flatness

One of the crucial factors that determines the success of the bonding procedure is the flatness of the involved surfaces. In fact, the bonding procedure require a flatness of the surfaces involved of the order of 60 nm P-V and there must not be sharp spikes. So characterised the obtained ears with Zygo GPI XP/D™ in order to check that the ears surfaces satisfy these conditions. The technical drawing of the ears is shown in figure D.1.

A set of 40 ears has been measured and the values of the flatness obtained are listed in table D.1. Two examples of the Zygo measurements are shown in figure D.2, one of the best ears, with a flatness of ~ 12 nm rms, and one of the worst ears, with the presence of a spike with an height of ~ 300 nm.

As we can see from the results shown in the table, for some of them we notice the presence of spikes not compatible with the bonding requirements. So some polishing test were

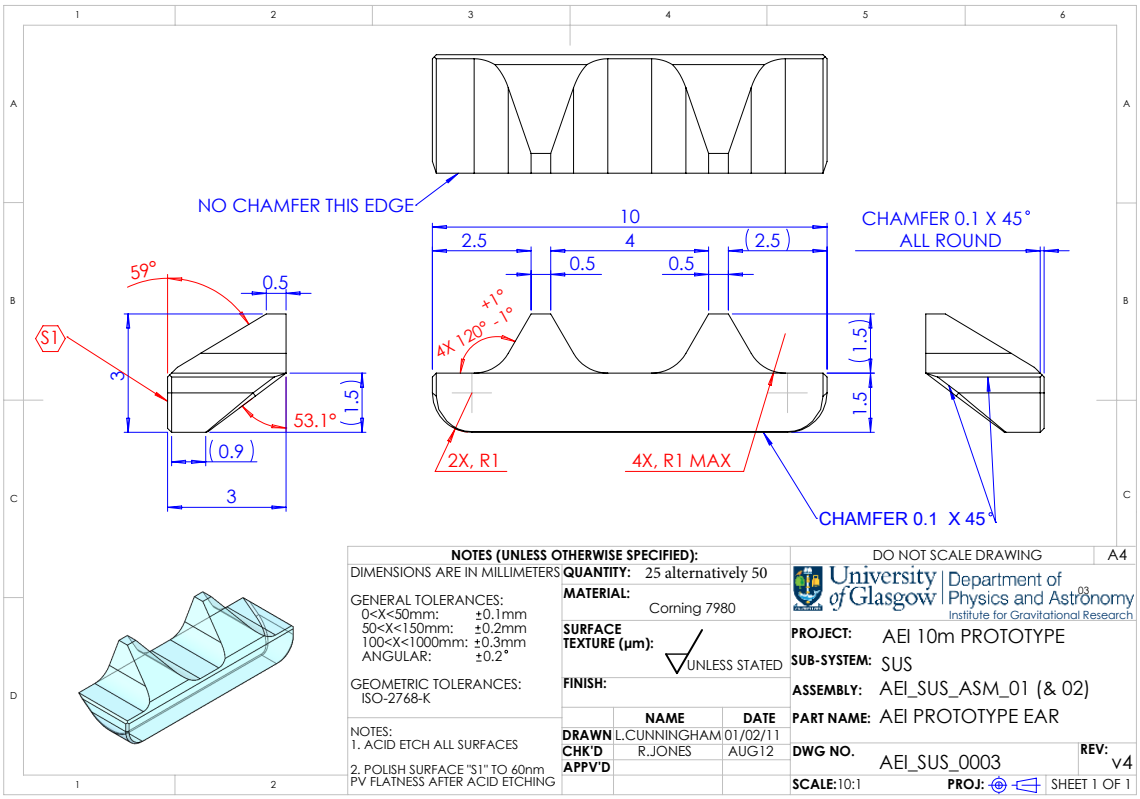

Figure D.1: Technical drawing of the ETM's ears.

performed in order to try to remove these peaks, without compromising the rest of the ear surface. Specifically we tried the following methods:

- isopropanol (C_3H_8O),
- cerium oxide (CeO_2),
- hydrofluoric acid (HF).

The first one was an attempt to clean the surface from dust particles, because isopropanol can only clean the surface without altering the surface itself. This procedure was made for 5 different ears, but none of them had any significant reduction of the spikes after the cleaning.

serial number	rms (nm)	P-V (nm)	comments
01	13.54	72.15	
02	18.62	110.99	
03	17.67	98.13	
04	24.51	424.64	spike with height of ∼ 250 nm
05	25.99	135.18	
06	22.76	145.16	
07	8.91	42.99	
08	18.93	111.72	
09	10.35	66.01	
10	17.74	236.50	
11	13.06	76.94	
12	26.02	120.42	
13	16.42	113.04	
14	16.43	94.40	
15	11.41	208.90	
16	25.62	252.94	spike with height of ∼ 150 nm
17	12.20	84.57	
18	22.53	118.71	
19	24.47	88.78	
20	24.43	124.40	
21	17.84	97.13	dig with depth of ∼ 80 nm
22	11.99	133.37	
23	22.33	162.24	spike with height of ∼ 80 nm
24	17.84	82.37	
25	16.89	168.05	spike with height of ∼ 40 nm
26	14.85	103.49	
27	11.58	94.65	

Continued on next page

Continued from previous page

serial number	rms (nm)	P-V (nm)	comments
28	15.91	186.00	spikes with max height of ~ 100 nm
29	13.72	75.08	
30	28.28	383.11	spike with height of ~ 250 nm
31	17.72	176.09	spike with height of ~ 50 nm
32	11.89	153.53	spikes with max height of ~ 70 nm
33	11.10	45.14	
34	10.84	77.92	
35	13.25	98.38	
36	16.50	89.64	
37	9.97	88.30	
38	28.61	616.11	spikes with max height of ~ 300 nm
39	9.66	76.80	
40	11.60	97.03	spike with height of ~ 40 nm

Table D.1: List of the values of the faltness obtaind for the ears

The second method is a common procedure of pre-bonding cleaning, because it can polish the surface without causing scratches [100]. The cerium oxide powder was wiped over the surface, then all remains of oxide were removed with soda bicarbonate and finally the mass was dried with methanol. We manually polished the surface for 10 seconds first and for 1 minute then, but none of them gave a significant change. So we decide to make a more drastic attempt wiping for 50 minutes. The spike disappeared, but, since the very small dimensions of the ears it was almost impossible to focus the pressure only on the spike position, then the surface around this position was damaged.

The third and last attempt that we made was using hydrofluoric acid, that is an acid able to dissolve silica [101]. We pushed on the spike with a cotton bud soaked with the acid for 90 seconds (since the etching rate for silica is 2.1 nm/s and the spike was about 200 nm), but we had again the same problem as before: the small dimensions of the part forced us to touch and affect the surrounding area. However what was interesting is that the spike was still there after the procedure (see figure D.3). This fact means that the spike was not made of silica but it was probably an organic contamination during the manufacturing procedure.

Finally, since none of these procedures has been found to be effective, the manufacturing company agreed to replace the ears that did not satisfy the requirements.

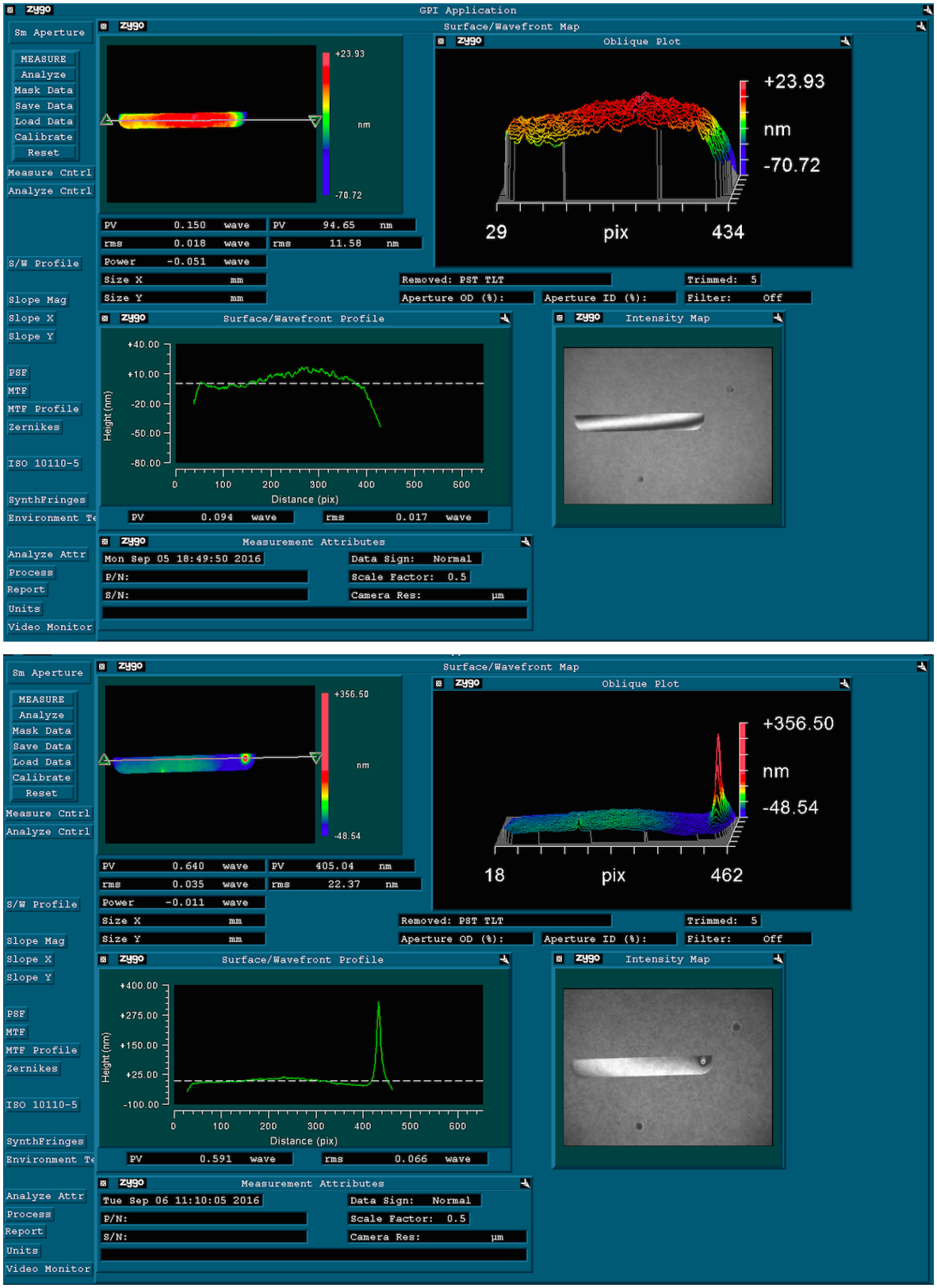

Figure D.2: Two examples of the measurements of the ears with Zygo interferometer (serial number #27 and #4): on the top the requirements are satisfied and on the bottom they do not, due to the presence of that huge spike on the right.

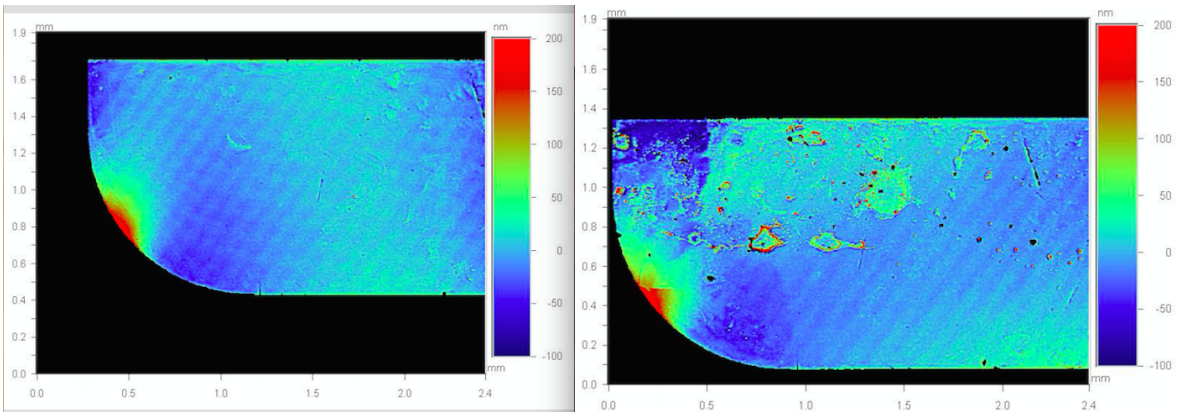

Figure D.3: Measurement of one of the ears with Veeco before and after the procedure with hydrofluoric acid.

D.1.2 Test masses cleaning

The coated surfaces of the arm cavity mirrors are very delicate and they must be protected during the successive procedures for the monolithic suspension assembly (like ears bonding and fibres welding). So once they arrived we cleaned and safely put them in caps specifically designed for this purpose.

The cleaning was done with methanol, without acting any pressure on the critical surfaces (coated surfaces and flat edges) and then the cap which covers and protects the coated surfaces was mounted (see figures D.4a and D.4b). The part, along with the ears, were then put in an ultraviolet/ozone (UV/O) chamber for the final cleaning as shown in figure D.4c. The UV/O cleaning procedure has been shown to be very effective to remove a lot of organic contaminants from the surfaces such as residues of methanol [102].

After that the test masses and the ears were ready for the bonding.

D.1.3 Hydroxide-catalysis bonding

The hydroxide-catalysis bonding consist in using a solution (in our case sodium silicate) which will be placed between the two surface that should be bonded. The chemistry process can be described by the following phases [103]:

- hydration and etching,
- polymerization,
- dehydration.

During the first phase the process is defined by the following reaction

$$SiO_2 + OH^- + 2H_2O \rightarrow Si(OH)_5^- \tag{D.1}$$

So the OH^- ions act as a catalyst and etch the two surfaces, which will emit silicate ions $Si(OH)_5^-$. This reaction entails a reduction of the number of OH^- ions and so a decrease of the pH of the solution and once it will be below 11 there will be the following reaction

$$Si(OH)_5^- \rightarrow Si(OH)_4^- + OH^-. \tag{D.2}$$

At this point we will have the second phase, i.e. the polymerization, described by the reaction

$$2Si(OH)_4^- \rightarrow (HO)_3SiOSi(OH)_3 + H_2O. \tag{D.3}$$

This means that two silicate ions will combine to form a so called siloxane chain plus water.

This leads us to the third and last phase: the dehydration. During this phase the water molecules created in the previous phase will evaporate or migrate to the bulk of the mass and the siloxane chain will form a 3D network that will attach the two surfaces.

The curing time needed for the whole process to complete and for the bond to have the maximum strength is four weeks at room temperature. [103]

D.1.4 Ears positioning

Two ears have to be bonded onto opposite flat edges of the test masses. In order to be sure that the ears will be in the right position we used a template, that is fixed on the cap and indicates the spot on the flat edge at which the ear must be placed (see figures D.4d and D.4e). A drop of 0.2 μl of bonding solution was applied on the flat edge and then the ear was placed in position as shown in figures D.4f, D.4g and D.4h.

After that we made a check of the position of the first bonded ear with Matlab Image Processing Toolbox, which allows to analyse an image pixel by pixel (see figure D.5). Through this method we found that the distance from the ear to the edge of the mirror is exactly the same at both sides and the distance from the ear to the edge of the flat differs by 28μm. The physical size of one pixel was found to be 28μm, which can be considered the error of our measurement.

This analysis was made only for the first one of the ears bonded in order to check the validity of the procedure and the accuracy of the template.

D.2 ITM

The procedure for the cleaning and the bonding of theITM was similar to that one of the ETM. The main difference is that in this case the caps to protect the coated surfaces were

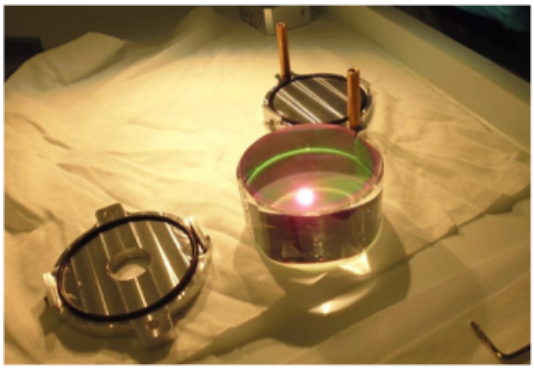

(a) *Mass cap and test mass.*

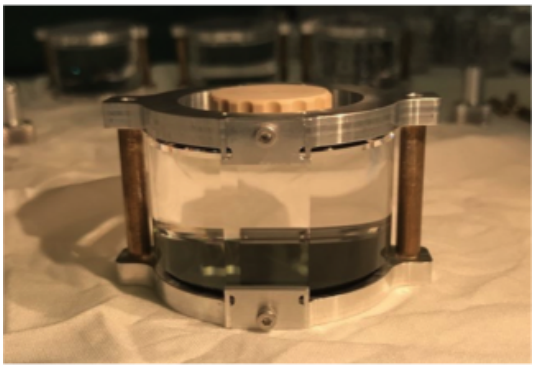

(b) *Mass with the mounted cap.*

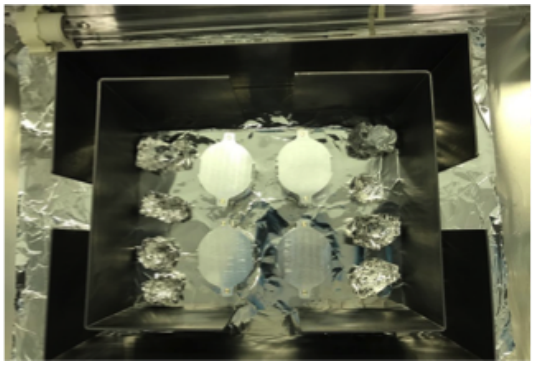

(c) *Test masses and ears placed in the ozone chamber.*

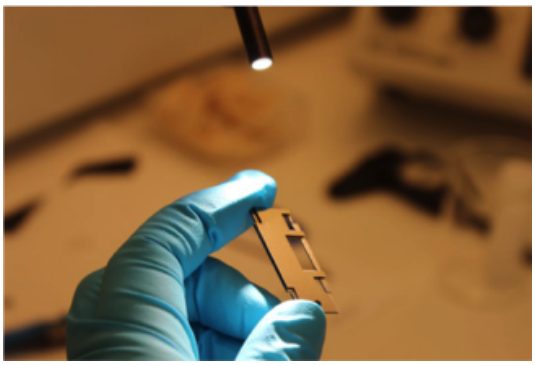

(d) *Template used for the right positioning of ears and prisms.*

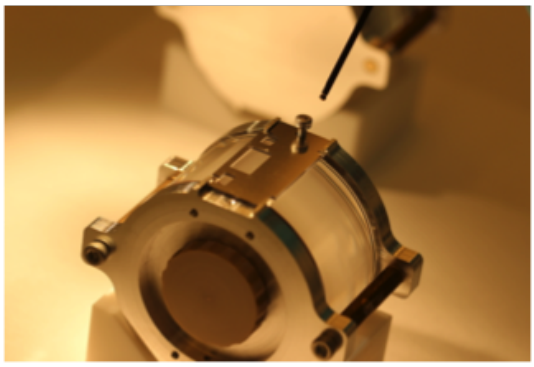

(e) *Positioning of the template.*

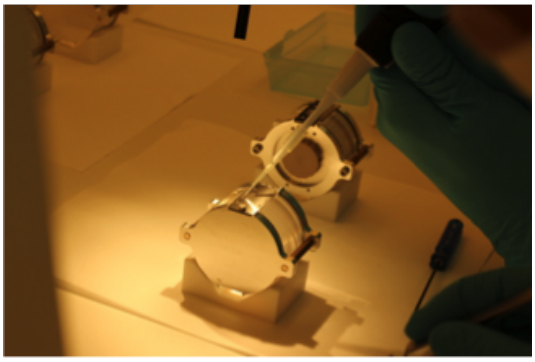

(f) *Bonding solution on the flat edge.*

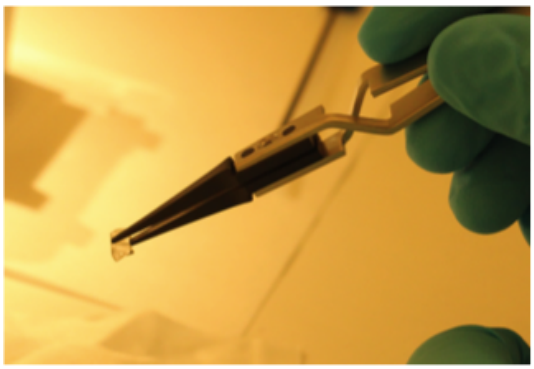

(g) *Positioning of the ear.*

(h) *Ear bonded on the flat edge.*

Figure D.4: Set of pictures that shows the whole process of cleaning and bonding of the ETM.

Figure D.5: Check of the ear position through Matlab Image Processing Toolbox.

mounted at the end of the process. In figure D.6 the main steps of the bonding procedure are shown. In this case the ear is placed in the jig, the bonding solution is put on it and then the test mass is placed over it. Then it has been left in the jig for a few hours and finally the mass cap is mounted. The mirrors were then placed in a vertical mount where they have been left in cure for 40 days.

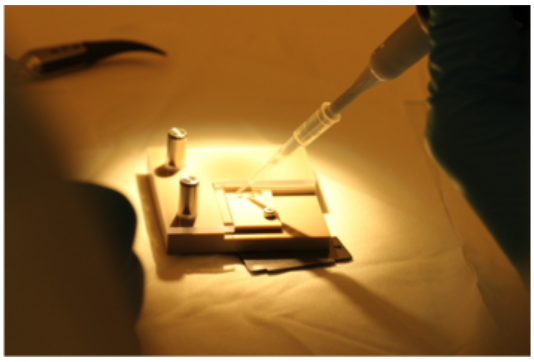

(a) Bonding solution on the ear.

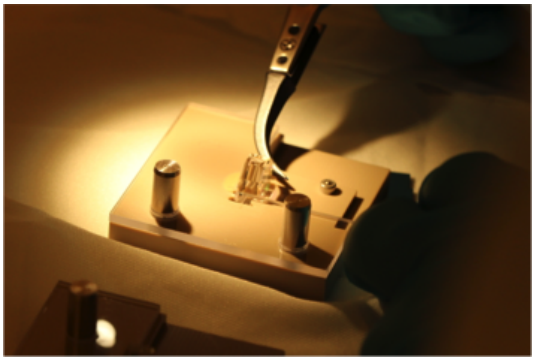

(b) Positioning of the test mass.

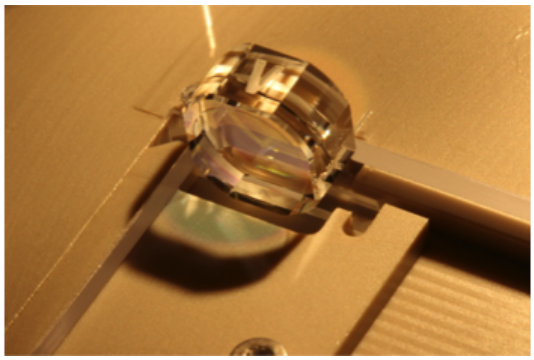

(c) Test mass in the jig.

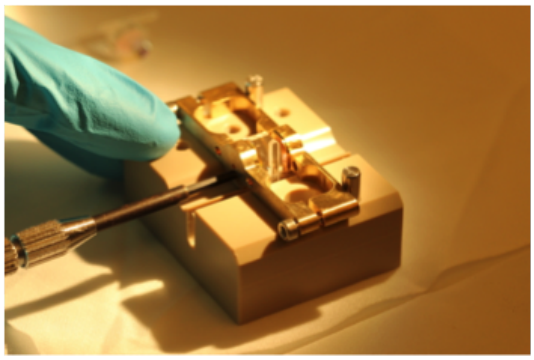

(d) Mounting of the cap.

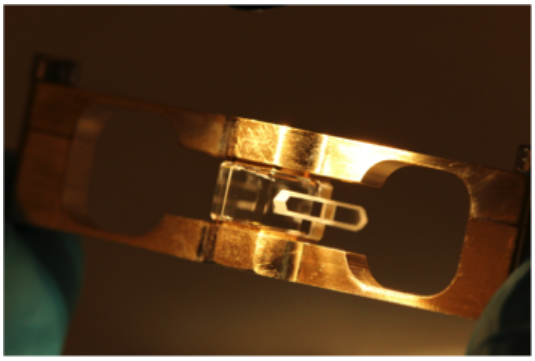

(e) Test mass in the cap.

(f) Two of the ITM in the vertical mount.

Figure D.6: Set of pictures that shows the whole process of bonding of the ITM.

Appendix E

MATLAB® script for backscattering calculation

```
function[chi_xx,Sx,Resp,QN]=SSM_QN_bs(p)
%
% function for the calculation of the quantum noise limited
% sensitivity of a Sagnac interferometer with triangular
% cavities when the backscattering effect is present.
%
% The argument of the function is a structure p with the
% following data:
%
% p.freq     -> frequency range [Hz]
% p.Pin      -> laser input power [W]
% p.L        -> half roudtrip length [m]
% p.lambda0  -> laser wavelength [m]
% p.etaPD    -> photodetector efficiency
% p.zeta     -> homodyne angle [rad]
% p.RBS      -> Power reflectivity of BS
% p.TBS      -> Power transmissivity of BS
% p.Tn       -> North cavity ITM power transmissivity
% p.mn       -> North cavity ITM mass [kg]
% p.Mn       -> North cavity ETM mass [kg]
% p.Te       -> East cavity ITM power transmissivity
% p.me       -> East cavity ITM mass [kg]
% p.Me       -> East cavity ETM mass [kg]
% p.kbN      -> North cavity backscattering coefficient
% p.kbE      -> East cavity backscattering coefficient

%% Constants
hBar     = 1.054572000000000e-34; %reduced Planck constant
c        = 299792458; %speed of light;

%% Experiment parameters
freq     = p.freq; %frequency range
Pin      = p.Pin; %laser input power
L        = p.L; %infrastructure length;
lambda0  = p.lambda0; %laser wavelength;
omega_p  = c/lambda0*2*pi; %laser angular frequency
k_p      = omega_p/c; %wave number for pump laser
```

```
etaPD    = p.etaPD; %photodetector efficiency
zeta     = p.zeta; %homodyne angle
tau      = L/c; %light single pass time

%% Beams plitter parameters
RBS      = p.RBS; %Power reflectivity of BS
TBS      = p.TBS; %Power transmissivity of BS

%% North arms parameters
Tn       = p.Tn; %ITM power transmissivity
Mn_ITM   = p.mn; %ITM mass
Mn_ETM   = p.Mn; %ETM mass
Mn       = 2*Mn_ITM*Mn_ETM/(Mn_ITM+2*Mn_ETM); %Effective mass
P_n      = RBS*Pin; %power entering N arm after the BS
eps_N    = p.kbN; %backscattering coefficient
Rn       = 1/(1+eps_N)-Tn; %ITM power reflectivity
Rn_eps   = eps_N*Rn; %backscattering in reflection
Tn_eps   = eps_N*Tn; %backscattering in transmission
Loss_N   = Rn_eps+Tn_eps; %Loss in the north arm

%% East arms parameters
Te       = p.Te; %ITM power transmissivity
Me_ITM   = p.me; %ITM mass
Me_ETM   = p.Me; %ETM mass
Me       = 2*Me_ITM*Me_ETM/(Me_ITM+2*Me_ETM); % Effective mass
P_e      = TBS*Pin; %power entering E arm after the BS
eps_E    = p.kbE; %backscattering coefficient
Re       = 1/(1+eps_E)-Te; %ITM power reflectivity
Re_eps   = eps_E*Re; %backscattering in reflection
Te_eps   = eps_E*Te; %backscattering in transmission
Loss_E   = Re_eps+Te_eps; %Loss

%% useful definitions
prop = @(f) exp(4i*pi*f*tau); %propagation factor

%% General purpose matrices
I = eye(2);
Pauli_mat = [0 1 ;-1 0];

Hv = [cos(zeta) sin(zeta)]; % Homodyne vector (row)

ScriptDn = @(f) (1-sqrt(Rn)*(1-Loss_N)*prop(f))^2+Rn_eps*(1-Loss_N)^2*prop(f)^2;
ScriptDe = @(f) (1-sqrt(Re)*(1-Loss_E)*prop(f))^2+Re_eps*(1-Loss_E)^2*prop(f)^2;

LMn     = @(f) (1-Loss_N) * prop(f) * sqrt(Tn) * (1-sqrt(Rn)*(1-Loss_N)*(eps_N+1)*prop(f)
    ) /ScriptDn(f) * Pauli_mat;
LMe     = @(f) (1-Loss_E) * prop(f) * sqrt(Te) * (1-sqrt(Re)*(1-Loss_E)*(eps_E+1)*prop(f)
    ) /ScriptDe(f) * Pauli_mat;
LMn_cp = @(f) (1-Loss_N) * prop(f) * (sqrt(Tn_eps) + sqrt(Tn*Rn_eps) - sqrt(Rn*Tn_eps) )
    /ScriptDn(f) * I;
LMe_cp = @(f) (1-Loss_E) * prop(f) * (sqrt(Te_eps) + sqrt(Te*Re_eps) - sqrt(Re*Te_eps) )
    /ScriptDe(f) * I;

LMn_vac     = @(f) -sqrt(1-Loss_N)*sqrt(eps_N)*(Rn+Tn) * prop(f) * (1-sqrt(Rn)*(1-Loss_N)
    *(eps_N+1)*prop(f)) /ScriptDn(f) * Pauli_mat;
LMe_vac     = @(f) -sqrt(1-Loss_E)*sqrt(eps_E)*(Re+Te) * prop(f) * (1-sqrt(Re)*(1-Loss_E)
    *(eps_E+1)*prop(f)) /ScriptDe(f) * Pauli_mat;
LMn_vac_cp = @(f) -sqrt(1-Loss_N)*Loss_N * prop(f) /ScriptDn(f) * I;
```

```
90  LMe_vac_cp = @(f) -sqrt(1-Loss_E)*Loss_E * prop(f) /ScriptDe(f) * I;
91
92  %% shot noise
93
94  T_sn_LN = @(f) (1-Loss_N) * ( sqrt(Rn)*I + sqrt(Tn)*Pauli_mat*LMn(f) + sqrt(Tn_eps)*
        LMn_cp(f) );
95  T_sn_RN = @(f) (1-Loss_N) * ( sqrt(Rn)*I + sqrt(Tn)*Pauli_mat*LMn(f) + sqrt(Tn_eps)*
        LMn_cp(f) );
96  T_sn_LE = @(f) (1-Loss_E) * ( sqrt(Re)*I + sqrt(Te)*Pauli_mat*LMe(f) + sqrt(Te_eps)*
        LMe_cp(f) );
97  T_sn_RE = @(f) (1-Loss_E) * ( sqrt(Re)*I + sqrt(Te)*Pauli_mat*LMe(f) + sqrt(Te_eps)*
        LMe_cp(f) );
98
99  T_sn_cp_LN = @(f) (1-Loss_N) * ( -sqrt(Rn_eps)*Pauli_mat + sqrt(Tn)*Pauli_mat*LMn_cp(f)
        + sqrt(Tn_eps) *LMn(f));
100 T_sn_cp_RN = @(f) (1-Loss_N) * ( -sqrt(Rn_eps)*Pauli_mat + sqrt(Tn)*Pauli_mat*LMn_cp(f)
        + sqrt(Tn_eps) *LMn(f));
101 T_sn_cp_LE = @(f) (1-Loss_E) * ( -sqrt(Re_eps)*Pauli_mat + sqrt(Te)*Pauli_mat*LMe_cp(f)
        + sqrt(Te_eps) *LMe(f));
102 T_sn_cp_RE = @(f) (1-Loss_E) * ( -sqrt(Re_eps)*Pauli_mat + sqrt(Te)*Pauli_mat*LMe_cp(f)
        + sqrt(Te_eps) *LMe(f));
103
104 N_sn_LN = @(f) (1-Loss_N)*sqrt(Tn) * ( Pauli_mat*LMn_vac(f) + sqrt(eps_N)*LMn_vac_cp(f)
        );
105 N_sn_RN = @(f) (1-Loss_N)*sqrt(Tn) * ( Pauli_mat*LMn_vac(f) + sqrt(eps_N)*LMn_vac_cp(f)
        );
106 N_sn_LE = @(f) (1-Loss_E)*sqrt(Te) * ( Pauli_mat*LMe_vac(f) + sqrt(eps_E)*LMe_vac_cp(f)
        );
107 N_sn_RE = @(f) (1-Loss_E)*sqrt(Te) * ( Pauli_mat*LMe_vac(f) + sqrt(eps_E)*LMe_vac_cp(f)
        );
108
109 N_sn_cp_RN = @(f) (1-Loss_N)*sqrt(Tn) * ( Pauli_mat*LMn_vac_cp(f) + sqrt(eps_N)*LMn_vac(
        f) );
110 N_sn_cp_LN = @(f) (1-Loss_N)*sqrt(Tn) * ( Pauli_mat*LMn_vac_cp(f) + sqrt(eps_N)*LMn_vac(
        f) );
111 N_sn_cp_LE = @(f) (1-Loss_E)*sqrt(Te) * ( Pauli_mat*LMe_vac_cp(f) + sqrt(eps_E)*LMe_vac(
        f) );
112 N_sn_cp_RE = @(f) (1-Loss_E)*sqrt(Te) * ( Pauli_mat*LMe_vac_cp(f) + sqrt(eps_E)*LMe_vac(
        f) );
113
114 M_LN = @(f) -sqrt(1-Loss_N)*sqrt(eps_N)*(Rn+Tn) * Pauli_mat;
115 M_RN = @(f) -sqrt(1-Loss_N)*sqrt(eps_N)*(Rn+Tn) * Pauli_mat;
116 M_LE = @(f) -sqrt(1-Loss_N)*sqrt(eps_E)*(Re+Te) * Pauli_mat;
117 M_RE = @(f) -sqrt(1-Loss_N)*sqrt(eps_E)*(Re+Te) * Pauli_mat;
118
119 M_cp_LN = @(f) -sqrt(1-Loss_N)*eps_N * (Rn+Tn) * I;
120 M_cp_RN = @(f) -sqrt(1-Loss_N)*eps_N * (Rn+Tn) * I;
121 M_cp_LE = @(f) -sqrt(1-Loss_N)*eps_E * (Re+Te) * I;
122 M_cp_RE = @(f) -sqrt(1-Loss_N)*eps_E * (Re+Te) * I;
123
124 %% Classical amplitudes
125
126 %%% Input fields
127 A_RN =  sqrt(2*P_n/(hBar*omega_p))*[1;0]; %North arm. Clockwise propagating (R) beam
128 A_LE =  sqrt(2*P_e/(hBar*omega_p))*[1;0]; %East arm. Counter clockwise propagating (L)
        beam
129
130 alpha_N =  T_sn_RN(0);
```

```
alpha_E =  T_sn_LE(0);
beta_N  =  T_sn_cp_RN(0);
beta_E  =  T_sn_cp_LE(0);

A_LN = (I-beta_E*beta_N)^-1*alpha_E*A_LE + beta_E*(I-beta_E*beta_N)^-1*alpha_N*A_RN; % North arm. Counter clockwise propagating (L) beam
A_RE = (I-beta_N*beta_E)^-1*alpha_N*A_RN + beta_N*(I-beta_N*beta_E)^-1*alpha_E*A_LE; % East arm. Clockwise propagating (R) beam

%%% Intra-cavity fields
E_RN =   LMn(0) * A_RN + LMn_cp(0) * A_LN; %North arm. Clockwise propagating (R) beam
E_LE =   LMe(0) * A_LE + LMe_cp(0) * A_RE; %East arm. Counter clockwise propagating (L) beam
E_LN =   LMn(0) * A_LN + LMn_cp(0) * A_RN; %North arm. Counter clockwise propagating (L) beam
E_RE =   LMe(0) * A_RE + LMe_cp(0) * A_LE; %East arm. Clockwise propagating (R) beam

%% Calculation

%%% optical response to the mirror displacement
R_arm_RN = @(f) 2*k_p*(1-Loss_N) * ( ( Pauli_mat*sqrt(Rn)*LMn(f) + sqrt(Rn_eps)*LMn_cp(f) )*E_RN + ( sqrt(Rn_eps)*LMn(f) + Pauli_mat*sqrt(Rn)*LMn_cp(f) )*E_LN - Pauli_mat*sqrt(Rn)*A_RN - sqrt(Rn_eps)*A_LN );
R_arm_LE = @(f) 2*k_p*(1-Loss_N) * ( ( Pauli_mat*sqrt(Re)*LMe(f) + sqrt(Re_eps)*LMe_cp(f) )*E_LE + ( sqrt(Re_eps)*LMe(f) + Pauli_mat*sqrt(Re)*LMe_cp(f) )*E_RE - Pauli_mat*sqrt(Re)*A_LE - sqrt(Re_eps)*A_RE );
R_arm_LN = @(f) 2*k_p*(1-Loss_N) * ( ( Pauli_mat*sqrt(Rn)*LMn(f) + sqrt(Rn_eps)*LMn_cp(f) )*E_LN + ( sqrt(Rn_eps)*LMn(f) + Pauli_mat*sqrt(Rn)*LMn_cp(f) )*E_RN - Pauli_mat*sqrt(Rn)*A_LN - sqrt(Rn_eps)*A_RN );
R_arm_RE = @(f) 2*k_p*(1-Loss_N) * ( ( Pauli_mat*sqrt(Re)*LMe(f) + sqrt(Re_eps)*LMe_cp(f) )*E_RE + ( sqrt(Re_eps)*LMe(f) + Pauli_mat*sqrt(Re)*LMe_cp(f) )*E_LE - Pauli_mat*sqrt(Re)*A_RE - sqrt(Re_eps)*A_LE );

%%% optical rigidity
K_arm_RN =  @(f) -2*hBar*k_p*2*k_p*sqrt(Rn)/sqrt(Tn) *  E_RN' * ( LMn(f)*E_RN + LMn_cp(f)*E_LN );
K_arm_LE =  @(f) -2*hBar*k_p*2*k_p*sqrt(Re)/sqrt(Te) *  E_LE' * ( LMe(f)*E_LE + LMe_cp(f)*E_RE );
K_arm_LN =  @(f) -2*hBar*k_p*2*k_p*sqrt(Rn)/sqrt(Tn) *  E_LN' * ( LMn(f)*E_LN + LMn_cp(f)*E_RN );
K_arm_RE =  @(f) -2*hBar*k_p*2*k_p*sqrt(Re)/sqrt(Te) *  E_RE' * ( LMe(f)*E_RE + LMe_cp(f)*E_LE );

%%% mechanical susceptibility function
chi_N = @(f) ( -1/(Mn*(2*pi*f)^2) );
chi_E = @(f) ( -1/(Me*(2*pi*f)^2) );
chi_new_N = @(f) chi_N(f) / ( 1+chi_N(f) * (K_arm_LN(f)+K_arm_RN(f)) );
chi_new_E = @(f) chi_E(f) / ( 1+chi_E(f) * (K_arm_LE(f)+K_arm_RE(f)) );

%%% radiation pressure force
F_RN_a_RN = @(f) 2*hBar*k_p * E_RN' * LMn(f); %coefficient of a_RN in F_RN
F_RN_a_LN = @(f) 2*hBar*k_p * E_RN' * LMn_cp(f); %coefficient of a_LN in F_RN

F_RN_n_RN = @(f) 2*hBar*k_p * E_RN' * LMn_vac(f); %coefficient of n_RN in F_RN
F_RN_n_LN = @(f) 2*hBar*k_p * E_RN' * LMn_vac_cp(f); %coefficient of n_LN in F_RN

F_LN_a_LN = @(f) 2*hBar*k_p * E_LN' * LMn(f); %coefficient of a_LN in F_LN
F_LN_a_RN = @(f) 2*hBar*k_p * E_LN' * LMn_cp(f); %coefficient of a_RN in F_LN
```

```
173
174 F_LN_n_LN = @(f) 2*hBar*k_p * E_LN' * LMn_vac(f); %coefficient of n_LN in F_LN
175 F_LN_n_RN = @(f) 2*hBar*k_p * E_LN' * LMn_vac_cp(f); %coefficient of n_RN in F_LN
176
177 F_RE_a_RE = @(f) 2*hBar*k_p * E_RE' * LMe(f); %coefficient of a_RE in F_RE
178 F_RE_a_LE = @(f) 2*hBar*k_p * E_RE' * LMe_cp(f); %coefficient of a_LE in F_RE
179
180 F_RE_n_RE = @(f) 2*hBar*k_p * E_RE' * LMe_vac(f); %coefficient of n_RE in F_RE
181 F_RE_n_LE = @(f) 2*hBar*k_p * E_RE' * LMe_vac_cp(f); %coefficient of n_LE in F_RE
182
183 F_LE_a_LE = @(f) 2*hBar*k_p * E_LE' * LMe(f); %coefficient of a_LE in F_LE
184 F_LE_a_RE = @(f) 2*hBar*k_p * E_LE' * LMe_cp(f); %coefficient of a_RE in F_LE
185
186 F_LE_n_LE = @(f) 2*hBar*k_p * E_LE' * LMe_vac(f); %coefficient of n_LE in F_LE
187 F_LE_n_RE = @(f) 2*hBar*k_p * E_LE' * LMe_vac_cp(f); %coefficient of n_RE in F_LE
188
189 F_a_RN = @(f) F_RN_a_RN(f) + F_LN_a_RN(f); %coefficient of a_RN in F_RN+F_LN
190 F_a_LN = @(f) F_LN_a_LN(f) + F_RN_a_LN(f); %coefficient of a_LN in F_LN+F_RN
191 F_a_RE = @(f) F_RE_a_RE(f) + F_LE_a_RE(f); %coefficient of a_RE in F_RE+F_LE
192 F_a_LE = @(f) F_LE_a_LE(f) + F_RE_a_LE(f); %coefficient of a_LE in F_LE+F_RE
193
194 F_n_RN = @(f) F_RN_n_RN(f) + F_LN_n_RN(f); %coefficient of n_RN in F_RN+F_LN
195 F_n_LN = @(f) F_LN_n_LN(f) + F_RN_n_LN(f); %coefficient of n_LN in F_LN+F_RN
196 F_n_RE = @(f) F_RE_n_RE(f) + F_LE_n_RE(f); %coefficient of n_RE in F_RE+F_LE
197 F_n_LE = @(f) F_LE_n_LE(f) + F_RE_n_LE(f); %coefficient of n_LE in F_LE+F_RE
198
199 %%% radiation pressure noise
200 T_rp_LN =    @(f) chi_new_N(f) * R_arm_LN(f) * F_a_LN(f);
201 T_rp_RN =    @(f) chi_new_N(f) * R_arm_RN(f) * F_a_RN(f);
202 T_rp_LE =    @(f) chi_new_E(f) * R_arm_LE(f) * F_a_LE(f);
203 T_rp_RE =    @(f) chi_new_E(f) * R_arm_RE(f) * F_a_RE(f);
204
205 T_rp_cp_LN = @(f) chi_new_N(f) * R_arm_LN(f) * F_a_RN(f);
206 T_rp_cp_RN = @(f) chi_new_N(f) * R_arm_RN(f) * F_a_LN(f);
207 T_rp_cp_LE = @(f) chi_new_E(f) * R_arm_LE(f) * F_a_RE(f);
208 T_rp_cp_RE = @(f) chi_new_E(f) * R_arm_RE(f) * F_a_LE(f);
209
210 N_rp_LN =    @(f) chi_new_N(f) * R_arm_LN(f) * F_n_LN(f);
211 N_rp_RN =    @(f) chi_new_N(f) * R_arm_RN(f) * F_n_RN(f);
212 N_rp_LE =    @(f) chi_new_E(f) * R_arm_LE(f) * F_n_LE(f);
213 N_rp_RE =    @(f) chi_new_E(f) * R_arm_RE(f) * F_n_RE(f);
214
215 N_rp_cp_LN = @(f) chi_new_N(f) * R_arm_LN(f) * F_n_RN(f);
216 N_rp_cp_RN = @(f) chi_new_N(f) * R_arm_RN(f) * F_n_LN(f);
217 N_rp_cp_LE = @(f) chi_new_E(f) * R_arm_LE(f) * F_n_RE(f);
218 N_rp_cp_RE = @(f) chi_new_E(f) * R_arm_RE(f) * F_n_LE(f);
219
220 %%% Transfer matrices
221 T_arm_LN =    @(f) T_sn_LN(f)    + T_rp_LN(f);
222 T_arm_cp_LN = @(f) T_sn_cp_LN(f) + T_rp_cp_LN(f);
223
224 T_arm_RN =    @(f) T_sn_RN(f)    + T_rp_RN(f);
225 T_arm_cp_RN = @(f) T_sn_cp_RN(f) + T_rp_cp_RN(f);
226
227 T_arm_LE =    @(f) T_sn_LE(f)    + T_rp_LE(f);
228 T_arm_cp_LE = @(f) T_sn_cp_LE(f) + T_rp_cp_LE(f);
229
230 T_arm_RE =    @(f) T_sn_RE(f)    + T_rp_RE(f);
```

```
231 T_arm_cp_RE = @(f) T_sn_cp_RE(f) + T_rp_cp_RE(f);
232
233 N_arm_LN =    @(f) N_sn_LN(f)    + N_rp_LN(f);
234 N_arm_cp_LN = @(f) N_sn_cp_LN(f) + N_rp_cp_LN(f);
235
236 N_arm_RN =    @(f) N_sn_RN(f)    + N_rp_RN(f);
237 N_arm_cp_RN = @(f) N_sn_cp_RN(f) + N_rp_cp_RN(f);
238
239 N_arm_LE =    @(f) N_sn_LE(f)    + N_rp_LE(f);
240 N_arm_cp_LE = @(f) N_sn_cp_LE(f) + N_rp_cp_LE(f);
241
242 N_arm_RE =    @(f) N_sn_RE(f)    + N_rp_RE(f);
243 N_arm_cp_RE = @(f) N_sn_cp_RE(f) + N_rp_cp_RE(f);
244
245 %% coefficients of the output functions
246 % b_x_z_y states for the coeffecient of z_y in the output function b_x
247
248 b_RE_b_RE = @(f) ( I-T_arm_cp_RN(f)*T_arm_cp_LE(f) )^-1 ;
249 b_RE_a_RN = @(f) T_arm_RE(f)*b_RE_b_RE(f) * T_arm_RN(f);
250 b_RE_a_LE = @(f) T_arm_RE(f)*b_RE_b_RE(f) * T_arm_cp_RN(f) * T_arm_LE(f) + T_arm_cp_RE(f
        );
251 b_RE_n_RN = @(f) T_arm_RE(f)*b_RE_b_RE(f) * N_arm_RN(f);
252 b_RE_n_LN = @(f) T_arm_RE(f)*b_RE_b_RE(f) * N_arm_cp_RN(f);
253 b_RE_m_RN = @(f) T_arm_RE(f)*b_RE_b_RE(f) * M_RN(f);
254 b_RE_m_LN = @(f) T_arm_RE(f)*b_RE_b_RE(f) * M_cp_RN(f);
255 b_RE_n_RE = @(f) T_arm_RE(f)*b_RE_b_RE(f) * T_arm_cp_RN(f) * N_arm_cp_LE(f) + N_arm_RE(f
        );
256 b_RE_n_LE = @(f) T_arm_RE(f)*b_RE_b_RE(f) * T_arm_cp_RN(f) * N_arm_LE(f) + N_arm_cp_RE(f
        );
257 b_RE_m_RE = @(f) T_arm_RE(f)*b_RE_b_RE(f) * T_arm_cp_RN(f) * M_cp_LE(f) + M_RE(f);
258 b_RE_m_LE = @(f) T_arm_RE(f)*b_RE_b_RE(f) * T_arm_cp_RN(f) * M_LE(f) + M_cp_RE(f);
259 b_RE_x_E  = @(f) T_arm_RE(f)*b_RE_b_RE(f) * T_arm_cp_RN(f) * R_arm_LE(f) + R_arm_RE(f);
260 b_RE_x_N  = @(f) T_arm_RE(f)*b_RE_b_RE(f) * R_arm_RN(f);
261
262 b_LN_b_LN = @(f) ( I-T_arm_cp_LE(f)*T_arm_cp_RN(f) )^-1 ;
263 b_LN_a_RN = @(f) T_arm_LN(f)*b_LN_b_LN(f) * T_arm_cp_LE(f) * T_arm_RN(f) + T_arm_cp_LN(f
        );
264 b_LN_a_LE = @(f) T_arm_LN(f)*b_LN_b_LN(f) * T_arm_LE(f);
265 b_LN_n_RN = @(f) T_arm_LN(f)*b_LN_b_LN(f) * T_arm_cp_LE(f) * N_arm_RN(f) + N_arm_cp_LN(f
        );
266 b_LN_n_LN = @(f) T_arm_LN(f)*b_LN_b_LN(f) * T_arm_cp_LE(f) * N_arm_cp_RN(f) + N_arm_LN(f
        );
267 b_LN_m_RN = @(f) T_arm_LN(f)*b_LN_b_LN(f) * T_arm_cp_LE(f) * M_RN(f) + M_cp_LN(f);
268 b_LN_m_LN = @(f) T_arm_LN(f)*b_LN_b_LN(f) * T_arm_cp_LE(f) * M_cp_RN(f) + M_LN(f);
269 b_LN_n_RE = @(f) T_arm_LN(f)*b_LN_b_LN(f) * N_arm_cp_LE(f);
270 b_LN_n_LE = @(f) T_arm_LN(f)*b_LN_b_LN(f) * N_arm_LE(f);
271 b_LN_m_RE = @(f) T_arm_LN(f)*b_LN_b_LN(f) * M_cp_LE(f);
272 b_LN_m_LE = @(f) T_arm_LN(f)*b_LN_b_LN(f) * M_LE(f);
273 b_LN_x_N  = @(f) T_arm_LN(f)*b_LN_b_LN(f) * T_arm_cp_LE(f) * R_arm_RN(f) + R_arm_LN(f);
274 b_LN_x_E  = @(f) T_arm_LN(f)*b_LN_b_LN(f) * R_arm_LE(f);
275
276 b_LN_i    = @(f)  sqrt(TBS)*b_LN_a_RN(f) - sqrt(RBS)*b_LN_a_LE(f);
277 b_LN_p    = @(f)  sqrt(RBS)*b_LN_a_RN(f) + sqrt(TBS)*b_LN_a_LE(f);
278 b_RE_i    = @(f) -sqrt(RBS)*b_RE_a_LE(f) + sqrt(TBS)*b_RE_a_RN(f);
279 b_RE_p    = @(f)  sqrt(TBS)*b_RE_a_LE(f) + sqrt(RBS)*b_RE_a_RN(f);
280
281 %%%
282 T_sag_i  = @(f) -sqrt(RBS)*b_RE_i(f)    + sqrt(TBS)*b_LN_i(f);
```

```
283 T_sag_p   = @(f) -sqrt(RBS)*b_RE_p(f)     + sqrt(TBS)*b_LN_p(f);
284
285 N_sag_RN = @(f) -sqrt(RBS)*b_RE_n_RN(f) + sqrt(TBS)*b_LN_n_RN(f);
286 N_sag_LN = @(f) -sqrt(RBS)*b_RE_n_LN(f) + sqrt(TBS)*b_LN_n_LN(f);
287 N_sag_RE = @(f) -sqrt(RBS)*b_RE_n_RE(f) + sqrt(TBS)*b_LN_n_RE(f);
288 N_sag_LE = @(f) -sqrt(RBS)*b_RE_n_LE(f) + sqrt(TBS)*b_LN_n_LE(f);
289
290 M_sag_RN = @(f) -sqrt(RBS)*b_RE_m_RN(f) + sqrt(TBS)*b_LN_m_RN(f);
291 M_sag_LN = @(f) -sqrt(RBS)*b_RE_m_LN(f) + sqrt(TBS)*b_LN_m_LN(f);
292 M_sag_RE = @(f) -sqrt(RBS)*b_RE_m_RE(f) + sqrt(TBS)*b_LN_m_RE(f);
293 M_sag_LE = @(f) -sqrt(RBS)*b_RE_m_LE(f) + sqrt(TBS)*b_LN_m_LE(f);
294
295 R_sag_E = @(f) -sqrt(RBS)*b_RE_x_E(f) + sqrt(TBS)*b_LN_x_E(f);
296 R_sag_N = @(f) -sqrt(RBS)*b_RE_x_N(f) + sqrt(TBS)*b_LN_x_N(f);
297
298 R_sag_diff = @(f) (R_sag_N(f)-R_sag_E(f))/2;
299
300 %% Mechanical susceptibility function
301
302 chi_xx=zeros(1,numel(freq));
303 for k=1:numel(freq)
304     chi_xx(k) =...
305         (abs(chi_new_N(freq(k)) ));
306 end;
307
308 %% Reponse of the cavity
309
310 Resp=zeros(1,numel(freq));
311 for k=1:numel(freq)
312     Resp(k) =...
313         (abs(Hv*R_sag_diff(freq(k)) ));
314 end;
315
316 %% Quantum noise
317
318 QN=zeros(1,numel(freq));
319 for k=1:numel(freq)
320     QN(k) =...
321         Hv*(...
322           T_sag_i(freq(k))*I*T_sag_i(freq(k))'+...
323           T_sag_p(freq(k))*I*T_sag_p(freq(k))'+...
324           N_sag_RN(freq(k))*I*N_sag_RN(freq(k))'+...
325           N_sag_LN(freq(k))*I*N_sag_LN(freq(k))'+...
326           N_sag_RE(freq(k))*I*N_sag_RE(freq(k))'+...
327           N_sag_LE(freq(k))*I*N_sag_LE(freq(k))'+...
328           M_sag_RN(freq(k))*I*M_sag_RN(freq(k))'+...
329           M_sag_LN(freq(k))*I*M_sag_LN(freq(k))'+...
330           M_sag_RE(freq(k))*I*M_sag_RE(freq(k))'+...
331           M_sag_LE(freq(k))*I*M_sag_LE(freq(k))'+...
332           (1-etaPD)/etaPD)*Hv';
333 end;
334
335 %% Displacement due to quantum noise
336
337 Sx =QN./(Resp).^2;
338
339
340 end
```

References

[1] B. P. Abbott et al. “Observation of Gravitational Waves from a Binary Black Hole Merger”. In: *Phys. Rev. Lett.* 116 (6 2016), p. 061102.

[2] B. W. Carroll and D. A. Ostlie. *An Introduction to Modern Astrophysics*. Ed. by S. F. P. Addison-Wesley. 2nd. 2007.

[3] B. F. Schutz. “Gravitational wave sources and their detectability”. In: *Class. Quant. Grav.* 6.12 (1989), p. 1761.

[4] B. P. Abbott et al. “Localization and Broadband Follow-up of the Gravitational-wave Transient GW150914”. In: *Astrophys. J. Lett.* 826.1 (2016), p. L13.

[5] B. P. Abbott et al. “Astrophysical Implications of the Binary Black-hole Merger GW150914”. In: *Astrophys. J. Lett.* 818.2 (2016), p. L22.

[6] B. P. Abbott et al. “Tests of General Relativity with GW150914”. In: *Phys. Rev. Lett.* 116 (22 2016), p. 221101.

[7] B. P. Abbott et al. “Characterization of transient noise in Advanced LIGO relevant to gravitational wave signal GW150914”. In: *Classical and Quantum Gravity* 33.13 (2016), p. 134001.

[8] J. Veitch et al. “Parameter estimation for compact binaries with ground-based gravitational-wave observations using the LALInference software library”. In: *Phys. Rev. D* 91 (4 2015), p. 042003.

[9] B. P. Abbott et al. “GW170817: Observation of Gravitational Waves from a Binary Neutron Star Inspiral”. In: *Phys. Rev. Lett.* 119 (16 2017), p. 161101.

[10] B. P. Abbott et al. “Multi-messenger Observations of a Binary Neutron Star Merger”. In: *Astrophys. J. Lett.* 848.2 (2017), p. L12.

[11] *GCN: The Gamma-ray Coordinates Network*. URL: `https://gcn.gsfc.nasa.gov`.

[12] B. P. Abbott et al. “Estimating the Contribution of Dynamical Ejecta in the Kilonova Associated with GW170817”. In: *Astrophys. J. Lett.* 850.2 (2017), p. L39.

[13] B. P. Abbott et al. “Gravitational Waves and Gamma-Rays from a Binary Neutron Star Merger: GW170817 and GRB 170817A”. In: *Astrophys. J. Lett.* 848.2 (2017), p. L13.

[14] B. P. Abbott et al. “A gravitational-wave standard siren measurement of the Hubble constant”. In: *Nature* 551.7678 (2017), pp. 85–88.

[15] B. P. Abbott et al. “GW151226: Observation of Gravitational Waves from a 22-Solar-Mass Binary Black Hole Coalescence”. In: *Phys. Rev. Lett.* 116 (24 2016), p. 241103.

[16] B. P. Abbott et al. “GW170104: Observation of a 50-Solar-Mass Binary Black Hole Coalescence at Redshift 0.2”. In: *Phys. Rev. Lett.* 118 (22 2017), p. 221101.

[17] B. P. Abbott et al. “GW170608: Observation of a 19 Solar-mass Binary Black Hole Coalescence”. In: *Astrophys. J. Lett.* 851.2 (2017), p. L35.

[18] B. P. Abbott et al. “GW170814: A Three-Detector Observation of Gravitational Waves from a Binary Black Hole Coalescence”. In: *Phys. Rev. Lett.* 119 (14 2017), p. 141101.

[19] R. Hulse and J. Taylor. “Discovery of a pulsar in a binary system”. In: *Astrophys. J.* 195 (1975), pp. L51–L53.

[20] J. Taylor and J. Weisberg. “A new test of general relativity: gravitational radiation and the binary pulsar PSR1913+16”. In: *Astrophys. J.* 253 (1982), p. 908.

[21] J. Weber. “Detection and Generation of Gravitational Waves”. In: *Phys. Rev.* 117 (1 1960), pp. 306–313.

[22] J. Weber. “Evidence for Discovery of Gravitational Radiation”. In: *Phys. Rev. Lett.* 22 (24 1969), pp. 1320–1324.

[23] M. Pitkin, S. Reid, S. Rowan, and J. Hough. “Gravitational Wave Detection by Interferometry (Ground and Space)”. In: *Living Rev. Relat.* 14.1 (2011), p. 5.

[24] The Royal Swedish Academy of Sciences. *Press Release: The Nobel Prize in Physics 2017*. 2017. URL: http://www.nobelprize.org/nobel_prizes/physics/laureates/2017/press.html.

[25] R. Weiss. *Electromagnetically coupled broadband gravitational antenna*. Quarterly progress report No.105, Massachusetts Institute of Technology. 1972.

[26] M. Gertsenshtein and V. Pustovoit. “On the detection of low frequency gravitational waves”. In: *Soviet Physics - JEPT* 16 (2 1963), pp. 433–435.

[27] F. A. E. Pirani. “On the Physical significance of the Riemann tensor”. In: *Acta Phys. Polon.* 15 (1956), pp. 389–405.

[28] P. R. Saulson. *Fundamentals of interferometric gravitational wave detectors*. World Scientific Publishing Co. Pte. Ltd., 1994. ISBN: 981-02-1820-6.

[29] *Gravitational wave interferometer noise calculator, v3.1*. 2016.

[30] G. Hammond, S. Hild, and M. Pitkin. "Advanced technologies for future ground-based, laser-interferometric gravitational wave detectors". In: *J. Mod. Opt.* 61.sup1 (2014), S10–S45.

[31] F Matichard et al. "Seismic isolation of Advanced LIGO: Review of strategy, instrumentation and performance". In: *Class. Quant. Grav.* 32.18 (2015), p. 185003.

[32] F. Acernese et al. "Advanced Virgo: a second-generation interferometric gravitational wave detector". In: *Class. Quant. Grav.* 32.2 (2015), p. 024001.

[33] J. Harms. "Terrestrial Gravity Fluctuations". In: *Living Rev. Relat.* 18.1 (2015), p. 3.

[34] M. W. Coughlin et al. *Implications of dedicated seismometer measurements on Newtonian-noise cancellation for Advanced LIGO*. In peer review. 2018.

[35] Y. Levin. "Theory of thermal noise in optical mirrors". In: *Optical coatings and thermal noise in precision measurement*. Ed. by G. M. Harry, T. Bodiya, and R. DeSalvo. Cambridge University Press, 2012, pp. 1–5.

[36] T. Akutsu et al. *The status of KAGRA underground cryogenic gravitational wave telescope*. arXiv:1710.04823 [gr-qc]. 2017.

[37] L. Wen and Y. Chen. "Geometrical expression for the angular resolution of a network of gravitational-wave detectors". In: *Phys. Rev. D* 81 (8 2010), p. 082001.

[38] T. Souradeep. *Status of LIGO-India*. LIGO-G1800433-v2. 2018.

[39] The LIGO Scientific Collaboration. *Instrument Science White Paper 2018*. LIGO -T1800133-v3. 2018.

[40] L. Barsotti, L. McCuller, M. Evans, and P. Fritschel. *The A+ design curve*. LIGO-T1800042-v5. 2018.

[41] A. Heptonstall et al. "Invited Article: CO2 laser production of fused silica fibers for use in interferometric gravitational wave detector mirror suspensions". In: *Rev. Sci. Instrum.* 82.1 (2011), p. 011301.

[42] B. P. Abbott et al. "Exploring the sensitivity of next generation gravitational wave detectors". In: *Class. Quant. Grav.* 34.4 (2017), p. 044001.

[43] M. Abernathy et al. *Einstein gravitational wave Telescope conceptual design study*. Tech. rep. No. ET-0106C-10. 2011.

[44] E. Hall. *Cosmic Explorer. A 40 km gravitational-wave detector*. LIGO-G1801336-v2. 2018.

[45] M. Evans, R. Sturani, S. Vitale, and E. Hall. *Unofficial sensitivity curves (ASD) for aLIGO, Kagra, Virgo, Voyager, Cosmic Explorer and ET*. LIGO-T1500293-v10. 2018.

[46] A. Einstein. “Die Grundlage der allgemeinen Relativitätstheorie”. In: *Ann. Phys.* 354 (1916), pp. 769–822.

[47] B. S. Sathyaprakash and B. F. Schutz. “Physics, Astrophysics and Cosmology with Gravitational Waves”. In: *Living Rev. Rel.* 12.1 (2009).

[48] C. M. Caves and B. L. Schumaker. “New formalism for two-photon quantum optics. I. Quadrature phases and squeezed states”. In: *Phys. Rev. A* 31.5 (1985), pp. 3068–3092.

[49] B. L. Schumaker and C. M. Caves. “New formalism for two-photon quantum optics. II. Mathematical foundation and compact notation”. In: *Phys. Rev. A* 31 (5 1985), pp. 3093–3111.

[50] S. L. Danilishin and F. Y. Khalili. “Quantum Measurement Theory in Gravitational-Wave Detectors”. In: *Living Rev. Relat.* 15.1 (2012), p. 5. ISSN: 1433-8351.

[51] H. Miao and Y. Chen. “Quantum theory of laser interferometer gravitational wave detectors”. In: *Advanced Gravitational Wave Detectors*. Ed. by D. G. Blair, E. J. Howell, L. Ju, and C. Zhao. Cambridge University Press, 2012, pp. 277–297.

[52] H. B. Callen and T. A. Welton. “Irreversibility and Generalized Noise”. In: *Phys. Rev.* 83 (1 1951), pp. 34–40.

[53] H. Yamamoto. *Effects of small size anomalies in a FP cavity*. LIGO-T1000154-v5. 2010.

[54] O. Svelto. *Principles of Lasers*. Springer US, 2010. ISBN: 978-1-4419-1302-9.

[55] E. Hecht. *Optics*. Addison-Wesley, 2002. ISBN: 9780805385663.

[56] F. Zernike. “Diffraction theory of the knife-edge test and its improved form, the phase-contrast method”. In: *MNRAS* 94 (1934), pp. 377–384.

[57] V. Lakshminarayanan and A. Fleck. “Zernike polynomials: A guide”. In: *J. Mod. Opt.* 58 (Apr. 2011), pp. 1678–1678.

[58] G. Billingsley, H. Yamamoto, and L. Zhang. *Characterization of Advanced LIGO Core Optics*. LIGO-P1700029-v5. 2017.

[59] *GPI Series™ Interferometer Operating Manual*. Zygo Corporation, 2007.

[60] H. Schreiber and J. H. Bruning. “Phase shifting interferometry”. In: *Optical shop testing*. Ed. by D. Malacara. John Wiley & Sons, Inc., 2007, pp. 547–666. ISBN: 978-0-471-48404-2.

[61] *SimTools*. 2006-2013. URL: `http://www.gwoptics.org/simtools/`.

[62] J.-Y. Vinet, P. Hello, C. N. Man, and A. Brillet. “A high accuracy method for the simulation of non-ideal optical cavities”. In: *J. Phys. I France* 2.7 (1992), pp. 1287–1303.

[63] *OSCAR: a Matlab based FFT code*. 2008. URL: http://www.mathworks.com/matlabcentral/fileexchange/20607-oscar.

[64] J. Degallaix. *OSCAR A Matlab based optical FFT code*. 2014.

[65] B. Bochner. "Modelling the performance of interferometric gravitational-wave detectors with realistically imperfect optics". PhD thesis. Massachusetts Institute of Technology, June 1998.

[66] W. H. Press, S. A. Teukolsky, W. T. Vetterling, and B. P. Flannery. *Numerical Recipes in FORTRAN; The Art of Scientific Computing*. 2nd. New York, NY, USA: Cambridge University Press, 1993. ISBN: 0521437164.

[67] J. Degallaix, M. Galimberti, R. Bonnand, and Q. Benoit. *Defining the arm cavity loss for Advanced Virgo*. VIR-706A-10. 2010.

[68] R. Bonnand. "The Advanced Virgo Gravitational Wave Detector: Study of the optical design and development of the mirrors". PhD thesis. Université Claude Bernard Lyon 1, Sept. 2012.

[69] L. Landau and E. Lifshitz. *Quantum Mechanics, Non-relativistic Theory. Course of Theoretical Physics, Volume 3*. 2nd ed. Pergamon press, 1965. ISBN: 3257227892.

[70] Y. Chen. "Topics of LIGO physics: quantum noise in advanced interferometers and template banks for compact-binary inspirals". PhD thesis. California Institute of Technology, May 2003.

[71] V. B. Braginsky, Y. I. Vorontsov, and K. S. Thorne. "Quantum Nondemolition Measurements". In: *Science* 209.4456 (1980), pp. 547–557. ISSN: 0036-8075.

[72] V. Braginsky and F. Khalili. "Gravitational wave antenna with QND speed meter". In: *Phys. Lett. A* 147.5 (1990), pp. 251 –256. ISSN: 0375-9601.

[73] V. B. Braginsky, M. L. Gorodetsky, F. Y. Khalili, and K. S. Thorne. "Dual-resonator speed meter for a free test mass". In: *Phys. Rev. D* 61 (4 2000), p. 044002.

[74] P. Purdue and Y. Chen. "Practical speed meter designs for quantum nondemolition gravitational-wave interferometers". In: *Phys. Rev. D* 66 (12 2002), p. 122004.

[75] P. Purdue. "Analysis of a quantum nondemolition speed-meter interferometer". In: *Phys. Rev. D* 66 (2 2002), p. 022001.

[76] A. R. Wade et al. "Polarization speed meter for gravitational-wave detection". In: *Phys. Rev. D* 86 (6 2012), p. 062001.

[77] Y. Chen. "Sagnac interferometer as a speed-meter-type, quantum-nondemolition gravitational-wave detector". In: *Phys. Rev. D* 67 (12 2003), p. 122004.

[78] A Freise et al. "Triple Michelson interferometer for a third-generation gravitational wave detector". In: *Classical and Quantum Gravity* 26.8 (2009), p. 085012.

[79] C. Gräf et al. "Design of a speed meter interferometer proof-of-principle experiment". In: *Class. Quant. Grav.* 31.21 (2014), p. 215009.

[80] *ERC Sagnac Speed-Meter Project*. URL: http://www.speed-meter.eu.

[81] R. Bork. *AdvLigo CDS Design Overview*. LIGO-T0900612-v2. 2010.

[82] S. S. Leavey. "Enhancing the sensitivity of future laser interferometric gravitational wave detectors". PhD thesis. University of Glasgow, Sept. 2016.

[83] J.-S. Hennig. "Mirror Suspensions for the Glasgow Sagnac Speed Meter". PhD thesis. University of Glasgow, Apr. 2018.

[84] J.-S. Hennig et al. "Demonstration of a switchable damping system to allow low-noise operation of high-Q low-mass suspension systems". In: *Phys. Rev. D* 96 (12 2017), p. 122005.

[85] S. Steinlechner et al. "Local-oscillator noise coupling in balanced homodyne readout for advanced gravitational wave detectors". In: *Phys. Rev. D* 92 (7 2015), p. 072009.

[86] T. Zhang et al. *Quantum noise cancellation in asymmetric speed meters with balanced homodyne readout*. arXiv:1806.05488 [quant-ph]. 2018.

[87] A. A. Michelson and E. W. Morley. "On the Relative Motion of the Earth and the Luminiferous Ether". In: *Am. J. Sci.* 34 (1887), pp. 333–345.

[88] G. Sagnac. "Sur la preuve de la réalité de l'éther lumineux par l'expérience de l'interférographe tournant cite". In: *C.R. Acad. Sci.* 95 (1913), pp. 1410–3.

[89] S. L. Danilishin et al. "Quantum noise of non-ideal Sagnac speed meter interferometer with asymmetries". In: *New J. Phys.* 17.4 (2015), p. 043031.

[90] A. V. Oppenheim and R. W. Schafer. *Discrete-Time Signal Processing*. 3rd. Upper Saddle River, NJ, USA: Prentice Hall Press, 2009. ISBN: 0131988425, 9780131988422.

[91] J. Stover and S. (Society). *Optical Scattering: Measurement and Analysis*. Press Monographs. SPIE Press, 2012. ISBN: 9780819492517.

[92] F. Raab and S. Whitcomb. *Estimation of Special Optical Properties of a Triangular Ring Cavity*. LIGO-T920004-00. 1992.

[93] J.-Y. Vinet. *Backscattering off MC end mirror*. VIR-NOT-OCA-1390-221. 2002.

[94] The Virgo Collaboration. *The Virgo Physics Book, vol. II. Optics and related topics*. 2006.

[95] E. Knyazev, S. Danilishin, S. Hild, and F. Khalili. "Speedmeter scheme for gravitational-wave detectors based on EPR quantum entanglement". In: *Phys. Lett. A* 382.33 (2018), pp. 2219 –2225.

[96] S. L. Danilishin et al. "A new quantum speed-meter interferometer: measuring speed to search for intermediate mass black holes". In: *Light: Science & Applications* 7.11 (2018).

[97] S. L. Danilishin. "Sensitivity limitations in optical speed meter topology of gravitational-wave antennas". In: *Phys. Rev. D* 69 (10 2004), p. 102003.

[98] D. Pascucci et al. *Quantum noise limitations due to backscattering in Sagnac speed meter with triangular cavities.* In preparation. 2018.

[99] R.X. Adhikari. *LIGO Voyager Upgrade: Design Concept.* LIGO-T1400226-v9. 2018.

[100] M. Yoshida et al. "Cerium oxide abrasive and method of polishing substrates". In: *United States Patent* US 6,221,118 B1 (2001).

[101] D. J. Monk, D. S. Soane, and R. T. Howe. "A review of the chemical reaction mechanism and kinetics for hydrofluoric acid etching of silicon dioxide for surface micromachining applications". In: *Thin Solid Films* 232 (1993), pp. 1–12.

[102] J. R. Vig. "Ultraviolet-ozone cleaning of semiconductor surfaces". In: *Handbook of Semiconductor Wafer Cleaning Technology. Science, Technology, and Applications.* Ed. by W. Kern. Park Ridge, NJ: Noyes Pubblications, 1993. Chap. 6, pp. 233–273.

[103] E. J. Elliffe et al. "Hydroxide-catalysis bonding for stable optical systems for space". In: *Class. Quant. Grav.* 22 (2005), S257–S267.